The
University
Of
Sheffield.

Access
To
Thesis.

- A bound copy of every thesis which is accepted as worthy for a higher degree, must be deposited in the University of Sheffield Library, where it will be made available for borrowing or consultation in accordance with University Regulations.
- All students registering from 2008–09 onwards are also required to submit an electronic copy of their final, approved thesis. Students who registered prior to 2008–09 may also submit electronically, but this is not required.

Author: Luke A. Marshal
Dept: Material Science and Engineering

Thesis Title: The influence of aluminium additions on titanium during machining through the application of a novel orthogonal cutting test method
Registration No: 100226300

For completion by all students:

Submit in print form only (for deposit in the University Library): ☐
Submit in print form and also upload to the *White Rose eTheses Online* server: In full ☑
Edited eThesis ☐

Please indicate if there are any embargo restrictions on this thesis. Please note that if no boxes are ticked, you will have consented to your thesis being made available without any restrictions.

Embargo details: (complete only if requesting an embargo to either your print and/or eThesis)	Embargo required?		Length of embargo (in years)
Print Thesis	Yes ☐	No ☑	
eThesis	Yes ☐	No ☑	

Supervisor: I, the supervisor, agree to the named thesis being made available under the conditions specified above.

Name: Dr. Martin Jackson
Dept: Materials Science and Engineering
Signed:
Date: 17/11/2014

Student: I, the author, agree to the named thesis being made available under the conditions specified above.

I give permission to the University of Sheffield to reproduce the print thesis in whole or in part in order to supply single copies for the purpose of research or private study for a non-commercial purpose.

I confirm that this thesis is my own work, and where materials owned by a third party have been used copyright clearance has been obtained. I am aware of the University's *Guidance on the Use of Unfair Means* (www.sheffield.ac.uk/lets/design/unfair)

I confirm that all copies of the thesis submitted to the University (including electronic copies on CD/DVD) are identical in content.

Name: Luke A. Marshall
Dept: Materials Science and Engineering
Signed:
Date: 17/11/2014

For completion by students also submitting an electronic thesis (eThesis):

I, the author, agree that the University of Sheffield's eThesis repository (currently WREO) will make my eThesis available over the internet via an entirely non-exclusive agreement and that, without changing content, WREO may convert my thesis to any medium or format for the purpose of future preservation and accessibility.

I, the author, agree that the metadata relating to the eThesis will normally appear on both the University's eThesis server and the British Library's EThOS service, even if the thesis is subject to an embargo. I agree that a copy of the eThesis may be supplied to the British Library.

I confirm that the upload is identical to the final, examined and awarded version of the thesis as submitted in print to the University for deposit in the Library (unless edited as indicated above).

Name: Luke A. Marshall
Dept: Materials Science and Engineering
Signed:
Date: 17/11/2014

THIS SHEET MUST BE BOUND IN THE FRONT OF THE PRINTED THESIS BEFORE IT IS SUBMITTED

The influence of alumnium additions on titanium during machining through the application of a novel orthogonal cutting test method

Luke Alan Marshall

A thesis submitted for the degree of Doctor of Philosophy

University of Sheffield
Department of Materials Science and Engineering
November 2014

ABSTRACT

Due to the high production rates of civil aircraft the demands for increased rates of production through high speed machining are ever increasing. A lack of consistency in the current practices for determining ‘machinability’ means that a bespoke trial is needed to ascertain whether a particular combination of material, tool and machining parameters yields a sufficiently beneficial outcome. The current approach of large scale trials, while effective, is inefficient and costly to OEMs. Most significantly, with the aerospace industries desire to build engines outside the capabilities of current alloys, conventional machining trials cannot be conducted on new alloys that have yet to reach production scale due to the material quantities required in large scale trials. With regard to titanium alloys, the majority of alloys contain some level of aluminium as a major addition.

A research programme has been undertaken to investigate the influence of aluminium on the sub-surface deformation of Ti-xAl binary alloys during high speed machining processes with a view to developing a testing method for determining ‘machinability’. Such a novel test method would fast track the current inefficient and uneconomical approach. Microstructural analysis of the region immediately below the machined surface has been performed for high speed milled material, focusing on quantifying the depth to which deformation occurs and the dominant plastic deformation mode by backscatter electron imaging and light microscopy. The influence of aluminium was measured through the penetration of the severe plastic deformation region and twin depth penetration and showed that the behaviour was parabolic, with Ti - 4 wt.% Al showing the maximum level of deformation. The resultant plastic deformation from high speed milling also causes the near surface material to undergo a crystallographic reorientation, demonstrating characteristics of a simple shear process. Comparisons were made with a well established simple shear test method, axisymmetric compression testing, analysing the deformation behaviour, from high speed milling, with the mechanical behaviour of axisymmetric compressions. Use of work hardening principles, traditionally applied to FCC materials, were used to identify characteristics that exhibit trends comparable to those observed during high speed milling, in contrast to conventional mechanical behaviours such as yield stress. A novel orthogonal cut test was successfully developed to generate deformation behaviour from high speed milling and flow behaviour from axisymmetric compression tests in a single test method. This suggests the potential to incorporate ‘machinability’ testing during alloy development rather then a final test once large scale production has commenced.

ACKNOWLEDGEMENTS

Throughout the course of my PhD I have been aided by a number of people who have willingly(!?) given their help and support. Special thanks are extended to Dr. Martin Jackson, who kept me going forward when things threatened to stop and helped my personal development as well as academic achievement. I would also like to thank Dr. Brad Wynne, who was always on hand to pick holes in everything, to the benefit of the work. I have received a large amount of help and support from my industrial supervisors Dr. Matthew Thomas (TIMET UK Ltd.) and Dr. Sam Turner (AMRC), for which I am very grateful; their help has been beneficial in aiding my understanding of an industry of which I know very little.

I thank all my colleagues in D1, Dr. Meurig Thomas, and especially my partner Mel, who had to listen to my many, many complaints about something and nothing, making helpful suggestions when it was something and just indulging me when it was nothing, also Dr. Andy Williams for proof reading.

I would would like to thank all the technical staff who have helped me carry out my experimental work: Ian Watts, Dean Haylock, Mike Bell and Kyle Arnold, who were always ready and willing to help. Thanks to the EPSRC (Engineering and Physical Sciences Research Council) and TIMET UK Ltd. for their financial support, which made this work possible.

Finally to my parents; you have provided everything I needed. Everything I have and will achieve is thanks to you and for that I am and will always be grateful.

> “All attempts at artificial aviation are not only dangerous to human life, but foredoomed to failure from the engineering standpoint.”
>
> - Engineering Editor, The Times, 1906

CONTENTS

LIST OF FIGURES

1. INTRODUCTION

With the level of air travel continuing to increase and a need to reduce emissions and cost, many resources have been focussed on improving design, materials selection, materials development, and manufacturing capability, with the latter areas receiving particularly high interest. Furthermore, the use of titanium alloys in the next generation of aircraft is projected to increase significantly, as shown in Figure 1.1.

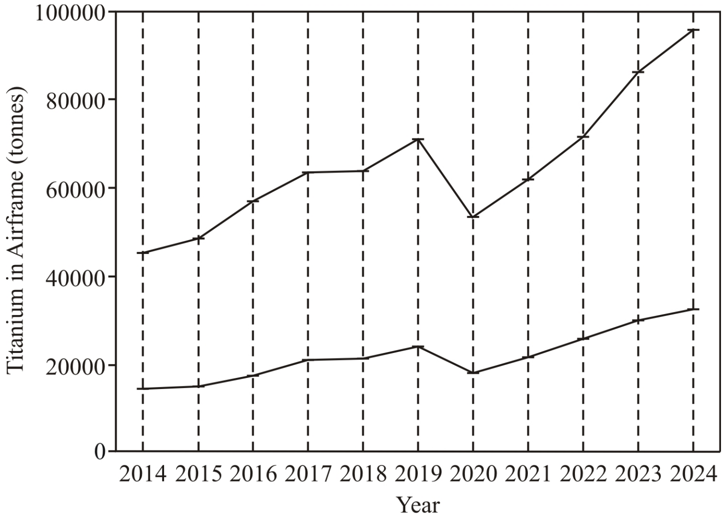

Figure 1.1: Plot showing the increase in percent of titanium alloys present in the Operating Empty Weight (OEW) of Boeing aircraft [1]

From a chemistry standpoint, the most widely used titanium alloy, Ti-6Al-4V, has been in use since the 1950s; to date, modern aerospace engines still rely on this alloy and after 60 years no alloy has replaced it. Ti-6Al-4V has been improved significantly over that time through closer control of tramp elements, improved processing practices and the development of a large range of microstructures. However, as with all technologies, each improvement is achieving smaller increases in performance as the limitations of the material begin to be reached. In order to achieve the properties that are desired for future generations of aero engines, a step change is required; which is most likely to be achieved through new alloy design. Therefore work on expanding the mechanistic understanding of the influence of aluminium on titanium is essential when trying to develop new titanium alloy systems.

From a manufacturing standpoint, the majority of titanium alloy components will require machining, through processes such as milling, turning and drilling. This has been highlighted by the European Union [2], Boeing [3] and Rolls-Royce [4]. The EU [2] currently has €24 million invested in current machining research projects for the aerospace and power generation sectors; Boeing [3] has seven major university partners, one being the emerging Advanced Manufacturing Research Centre (AMRC), whose principal purpose is to develop emerging machining technologies; and Rolls-Royce [4] have identified advanced machining as one of their primary areas of research development. The purpose of the funding and focus of these organisations is to increase the machining speeds and subsequently the rate of production, as a way of reducing manufacturing costs. The need for development and understanding of emerging machining practices on titanium alloys was highlighted by Airbus [5] at the World Titanium conference in Beijing, China, 2011, where they stated: "Improvement of economical impact of mechanical milling of titanium alloys - correlation between metallurgy and "machinability" (TIMETAL®54M)". Recent work on TIMETAL®54M, Ti-5Al-4V-1Fe, has highlighted that for changes in composition, similar mechanical properties can be achieved; however, the ability to manufacture that material can be significantly improved as demonstrated with TIMETAL®54M [6]. Also work performed by Thomas *et al.* [7] highlighted the microstructural damage caused by machining processes, such as high speed milling, in titanium alloys; TIMETAL®834, Ti-5.8Al-4Sn-3.5Zr-0.7Nb-0.5Mo-0.35Si-0.06C, and Ti-6Al-4V.

The aims of this project were to:

- Develop a mechanistic understanding of the influence of aluminium on the deformation behaviour of titanium alloys with respect to high strain rate processes. This work aims to examine several scales of deformation to form a holistic approach to understanding high strain rate deformation.
- Establish the key characteristics for the prediction of a materials 'machinability' and develop a more time and resource efficient method for prediction of 'machinability' to improve the rate of alloy development.

The first aim was achieved by using four polycrystalline binary alloys, 2, 4, 6 and 8 wt.% aluminium, to establish the influence of aluminum on the deformation and mechanical behaviour of titanium at intermediate strain rates, 10^{-1} - 10^{2} s^{-1}, through axisymmetric compression testing. Then using the same material, an industrial milling operation was conducted to analyse whether, at room temperature, the "complex" deformation behaviour correlates in the same manner.

The second aim was achieved by the development of a bespoke orthogonal cutting rig, which performed low speed orthogonal cutting operations. This enabled direct comparison of mechanical properties with those obtained from the intermediate strain rate testing and the deformation characteristics observed in both the intermediate strain rate testing and the high speed milling operation.

The first two aims of this project focus on the testing and analysis of the titanium binary alloy materials. The final aim of this project was to assess the 'machinability' using the orthogonal cutting rig and axisymmetric compression tests on three aerospace alloys. These alloys represent the current fan blade material, Ti-6Al-4V, a future fan blade material alternative, Ti-575, and a development alloy, Ti-407. In addition free cutting steel is investigated to provide an understanding of chip forming processes across the high aluminium content binary alloys, 6 and 8 wt.% Al.

The principal results expected from this work will help develop the understanding of the role of aluminium additions in titanium alloys on the 'machinability' during high speed milling followed by the production of a more time and resource efficient testing method for determining the 'machinability' of the next generation of titanium alloys. Finally, the testing of the process on the most widely used and researched titanium alloy, Ti-6Al-4V, and two alloys going through differing stages of the development and implementation process for aerospace applications will prove the suitability of the techniques developed in this work for future alloy developments.

2. LITERATURE REVIEW

As outlined in Section 1 there are two principlal focuses of this work; 1) the effect of aluminium and 2) development of a cost and time efficient method for determining the machinability of machinable materials, principally titanium alloys. This review first examines the deformation characteristics of close packed hexagonal, (CPH) metal, such as titanium, and the effect of aluminium additions on both the deformation and mechanical properties, followed by the influence of strain rate on deformation. Finally a review of the effects of high speed machining, turning and milling, with particular focus on titanium alloys is presented.

2.1 Titanium

Titanium is a transition metal and the ninth most abundant in the earth's crust, extracted from ores, such as rutile (TiO_2) and ilmenite, by the Kroll process, patented 1940, since the 1950s [8]. Other processes based upon electrochemical reduction of the oxide have been predicted since the 1940s [9] but while some remain promising possibilities [10] none have reached industrial scale production to date. Pure titanium exists as a CPH structure, Figure 2.1a), at room temperature and undergoes an allotropic phase transition to body centred cubic, BCC Figure 2.1b), at 882^{o}C.

The Burgers relationship, Figure 2.2, between β and α upon cooling occurs because the distance between respective closest packed planes in each phase, (0001) in α and $\{110\}$ in β, increases [11]. This increase leads to a distortion of this plane, contracting the c-axis relative to the a-axis and reducing the c/a ratio to 1.587, below the ideal 1.633.

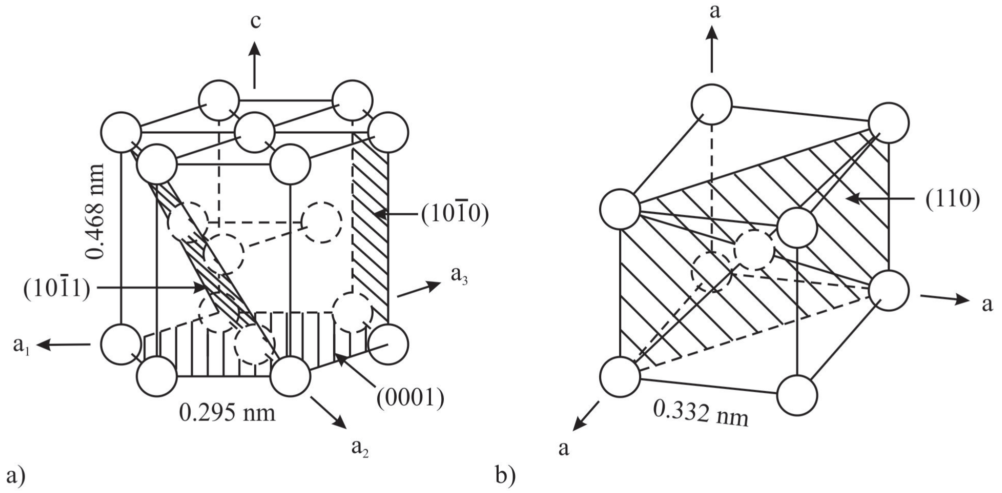

Figure 2.1: Schematic diagram showing the occurring phases of pure titanium 1) CPH and 2) BCC.

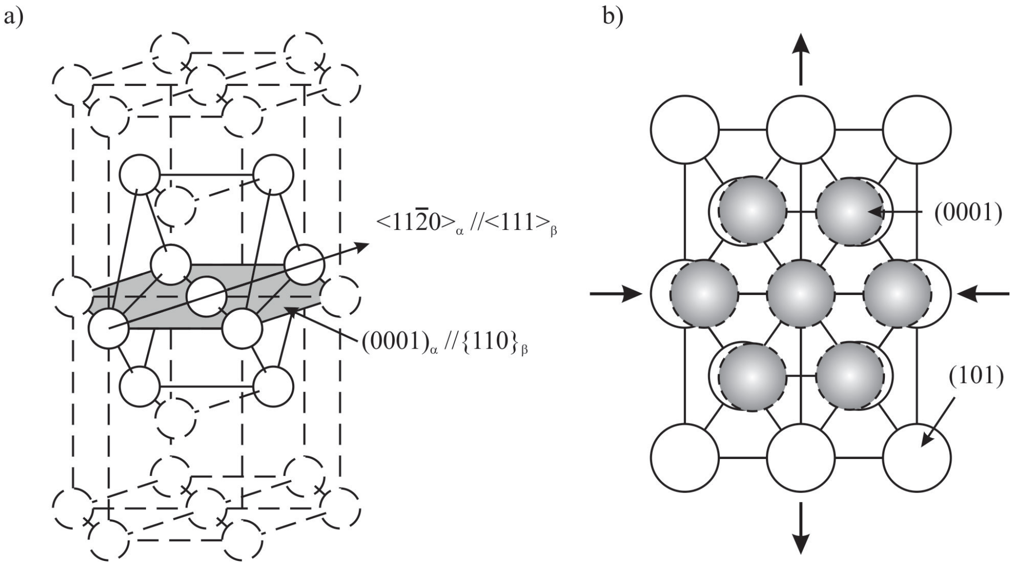

Figure 2.2: Schematic diagram showing a) BCC and CPH Burgers relationship and b) Schematic of the $(0001)_{\alpha} \setminus \backslash\{101\}_{\beta}$ plane distortion upon transition from $\beta \rightarrow \alpha$ in titanium.

Alloying elements added to titanium are categorised into four classes, Figure 2.3, depending how they influence equilibrium phase proportions. Neutral stabilizers show little influence on the transition temperature, initially decreasing it slightly before increasing it at higher temperatures [12]. Increasing the level of α stabilizers increases the temperature at which the $\alpha \rightarrow \beta$ occurs, due to their preferential solubility in the α. β stabilizers, preferentially soluble in the β phase, influence titanium in one of two ways. The first, β isomorphous, form a complete solid solution in the β field and lower the $\alpha \rightarrow \beta$ transitions with increasing concentration; the most common β stabilzers, Mo and V, are of this type. The second are β eutectoids; these elements have limited solubility and promote formation of precipitates and eutectiodally decomposing β in increasing concentrations, resulting in limited use compared to isomorphous additions such as Fe, Cr and W [12,13].

There are five alloy classes, α, near α, $\alpha + \beta$, near β and β [12]; they are classed based according to a pseudo-phase diagram proposed by Flower [14] in Figure 2.4. The phase fractions are controlled by the alloying additions present within the alloy.

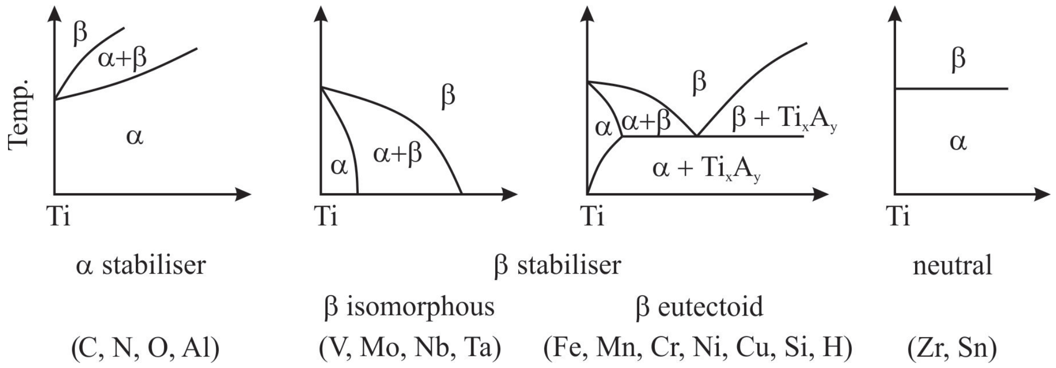

Figure 2.3: Schematic diagrams showing the influence of common elements found in titanium alloys [12].

2.1.1 α and Near α Alloys

These alloys are characterised by single phase structures, CPH α phase, at room temperature [14]. The final microstructure consists of equiaxed grains or 'transformed β', depending on the final deformation process relative to the $\alpha \rightarrow \alpha + \beta$ transition temperature [14]. The size of the equiaxed grains can be refined with small quantities of Fe, which pins prior β grain boundaries and therefore reduces the transformed β grain size [12]. This does, however, mean they are ideal candidates for welding applications [15], resulting from no phase transition occurring from heating generated by welding. An example of an α alloy is CP (Commercially Pure) titanium, where titanium is purposely alloyed with oxygen to increase strength. Applications of CP titanium revolve around its high corrosion resistance, regularly being used for reaction and cryogenic vessels, condensers and many other chemical and marine applications. This is the most significant alloy class

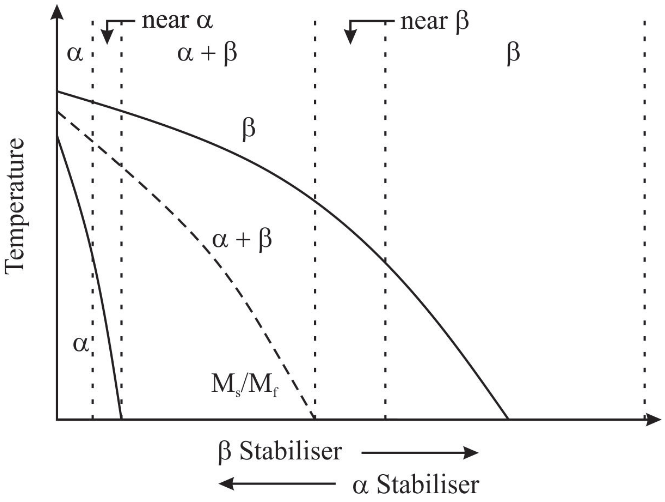

Figure 2.4: Pseudo-phase diagram of isomorphous β isomorphous [12].

for this work as the major alloying addition is aluminium and all the binary alloys will be classified as α alloys.

In near α alloys small levels of β stabilisers are intentionally added to broaden the α+β phase field to allow hot working to be performed in a large process window. Due to the β stabiliser additions a small volume fraction of β is retained at room temperature [11,14]. An example of this alloy is TIMETAL 834, which is primarily used in components that require high cycle fatigue resistance at temperatures approaching 600^{o}C and providing oxidation protection and better in-service stability [14].

2.1.2 $\alpha + \beta$ Alloys

$\alpha + \beta$ alloys contain additions of both α and β stabilising elements, this permits the extension of the $\alpha + \beta$ all the way down to room temperature, as shown schematically in Figure 2.4. This alloy class includes the most widely used alloy, Ti-6Al-4V [11], developed in the 1950s. One of the main reasons for widespread use of Ti-6Al-4V is the excellent range of mechanical properties achievable due to the wide range of two phase microstructures that can be generated during thermomechanical processing and cooling to room temperature. These can be broken down into three individual groups; fully lamellar, bi-modal and fully equiaxed [12].

2.1.3 Metastable β and β Alloys

β and metastable β alloys, also known as near β alloys [16], have sufficient β stabilisers to suppress the martensite start/finish (M_s/M_f on Figure 2.4) temperature to allow the martensite to be suppressed down below room temperature and as a result the material does not transform under quenching [11, 14]. This means that 100% β can be retained all the way down to room temperature, through quenching for near β, by air-cooling due to the slow kinetics of α formation [14, 16]. However, martensite (α') can be induced through deformation. A processing advantage of β alloys are the low temperature flow stresses: metastable β alloys are forged at ≈760°C, compared to Ti-6Al-4V which would be processed at ≈900°C. In the aged condition, the near β alloys, such as Ti-6V-2Fe-3Al, exhibit the highest strength of all titanium alloys, showing yield strengths above 1200 MPa [14]. It must be noted that all the 'β' alloys used in airframes are actually near β as true β alloys would be expensive, have high density and low strength.

Fully Lamellar Microstructure

This microstructure is readily achieved through annealing in the β phase, as a result it is also known as β annealed. The rate of cooling from the annealing temperature dictates the α colony size, the thickness of the α lamella and the α layer present at the β grain boundary [14], as demonstrated in Figure 2.5. These microstructures are generated when high fracture toughness and fatigue crack growth resistance are required and the level of each is dependent on the size of the prior β grains. If the β grain size is coarse, the fracture toughness is enhanced and the creep resistance is also improved. With a finer β grain size strength and ductility are improved as is the fatigue initiation resistance [17].

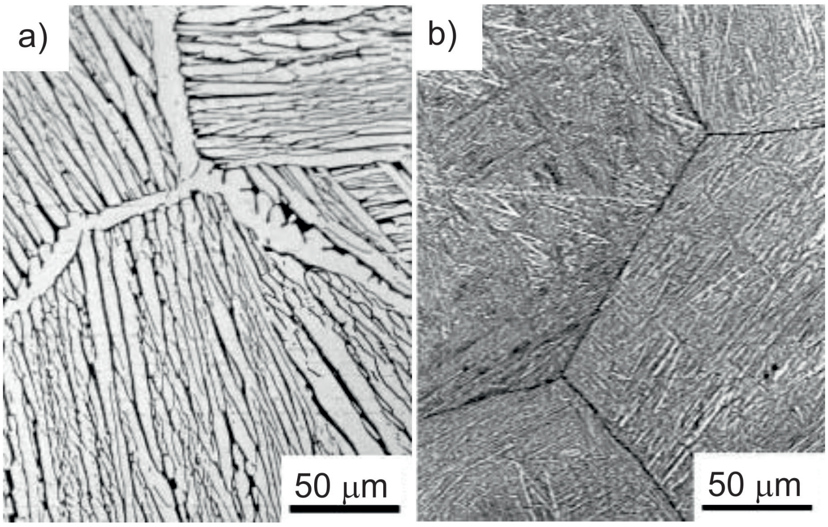

Figure 2.5: Light micrograph of a Ti-6242 lamella structure with varying cooling rate from the β phase (a) 1°C min^{-1} and (b) 8000°C min^{-1} [12].

Bi-Modal Microstructure

Sometimes refered to as a duplex structure, this microstructure contains both a primary α and transformed β; it also contains a large fraction of 'untransformed' β at room temperature, with these β grains largely interconnected at the prior β grain boundaries [12], Figure 2.6. The advantages of a bi-modal structure is that good ductility, high strength, fatigue initiation resistance and low cycle fatigue resistance can be obtained [17]. There are an increased number of key processing variables with bi-modal structures depending on the volume fraction of the phases, average grain size required and level of alloy addition segregation, all of which are critical when designing this microstructure depending on the application [12].

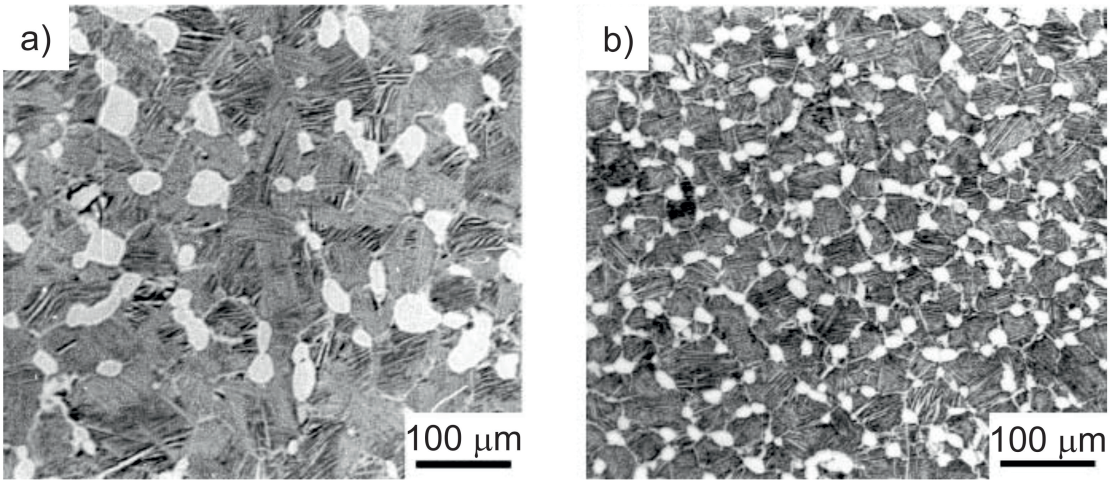

Figure 2.6: Light micrograph of TIMETAL 834 bi-modal structure with varying cooling rate from the β phase (a) slow cooling rate (b) fast cooling rate [12].

Equiaxed Microstructure

The processing to achieve a fully equiaxed structure is very similar to that of a bi-modal structure except that the cooling rate after recystallisation is sufficiently slow that only α_p grains grow and the α lamella in β does not. This leads to a structure which has equiaxed grains and at triple points between adjacent α grains a small volume fracture of β is retained [12], Figure 2.7. This microstructure gives rise to good strength and ductility, low cycle fatigue resistance, and fatigue crack initiation resistance [17].

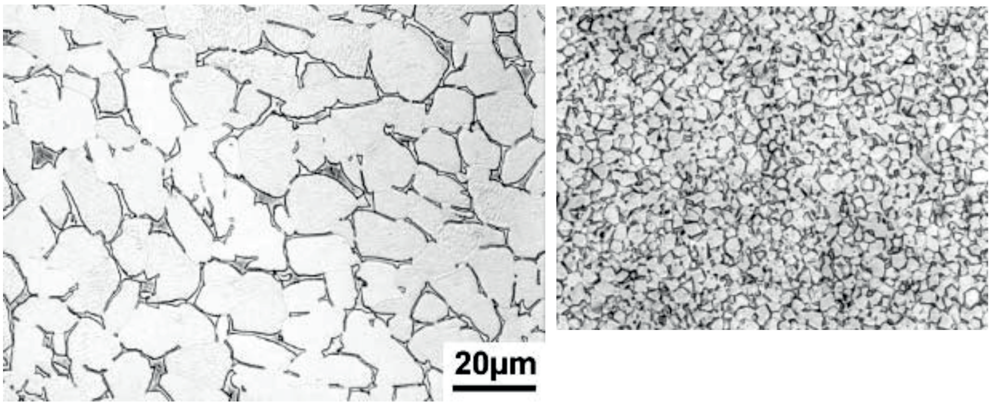

Figure 2.7: Light micrograph of Ti-6242 alloy a) slow cooled b) fast cooled from bi-modal recrystallisation annealing temperature [12].

Microstructure Review

As the work is centred on the effect of aluminium on titanium, it is clear that an equiaxed microstructure is going to be observed. The advantage of a single phase equiaxed structure is that it is the simplest microstructure and therefore ideal for this fundamental study.

2.2 Deformation Modes

The process of unrecoverable, plastic, deformation in α titanium occurs by two modes, slip and twinning [18–22]. Each of these mechanisms contributes to the accommodation of plastic strain and is fundamental to any study of subsurface damage as both of these mechanisms occur regardless of surface finish quality [7]. This section aims to review deformation behaviour of commercially pure (CP) titanium before discussing the influence of aluminium.

2.2.1 Slip

Slip is the process by which deformation occurs through dislocation motion. The plane in which the dislocation resides and the direction in which the dislocation moves are known as the slip plane and the slip direction respectively. Slip preferentially occurs in the direction of shortest lattice translation and on the planes of high packing density [23]. In titanium this corresponds to $\langle 11\bar{2}0 \rangle$ direction and one of three slip planes with this $\bar{a}$ Burgers vector: (0001), the three $\{10\bar{1}0\}$ and the six $\{10\bar{1}1\}$. Due to the preference for slip to occur on the closest packed plane - which with pure titanium and its less than ideal c/a ratio of 1.587, where ideal is 1.633, is the $\{10\bar{1}0\}$ plane - this has been observed as the principle slip system in subsequent studies [20, 24]. This is in contrast to materials with a closer to ideal c/a ratio, such as in magnesium with 1.623 [18], which demonstrates a preference for basal slip as a result [25].

It is known that to cause homogeneous plastic deformation, five independent systems are required under the Von Mises criterion. Titanium has eight independent systems with $\bar{a}$ Burgers vectors; however, this is further reduced to four as the net effect of system types one and two, Table 2.1, is type three [12]. This means in order to achieve Von Mises criterion a $\bar{c}+\bar{a}$ system needs activating. $\bar{c}+\bar{a}$ has been observed using TEM [22,24,26] but has a large CRSS (critically resolved shear stress) [27], and therefore its activation is difficult at room temperature owing to the preferential activation of twinning for c-axis deformation. This is further supported by the work performed by Gurao [28], who determined through experimentation and modeling that the activity, inversely proportional to CRSS, of $\bar{c}+\bar{a}$ is very low in weak textured CP titanium, demonstrated in Figure 2.8. The suggested cause for this is that because titanium has a less than ideal c/a ratio, the spacing between close packed planes is reduced, increasing the energy, CRSS, required to cause glide. This has been observed with more than ideal c/a ratio CPH materials, Zn and Cd (c/a = 1.86 and 1.89 respectively), where slip occurs almost completely on the basal plane at room temperature [29]. The less than ideal c/a ratio not only leads to the possibility of multiple slip systems but in titanium leads to the $\{10\bar{1}0\}$ system being energetically favourable at room temperature [30]. There are two types of slip system listed in Table 2.1, $\bar{a}$ and $\bar{c}+\bar{a}$. They are named depending on the slip direction, i.e. $\bar{a}$ slip has a slip direction in the a direction ($\langle 11\bar{2}0\rangle$), as defined in Figure 2.1, and $\bar{c}+\bar{a}$ ($\langle 11\bar{2}3\rangle$) slip has a slip direction with vectors in both the a and c direction. The possibility of non-basal slip systems, those containing planes and directions of lower density packing, is relevant due to these planes and directions being 'close to full', i.e. a plane or direction with a high atomic packing but less than the ideal packing seen in the $(0001)\langle 11\bar{2}0\rangle$ system. Rosi *et al.* [21] observed that $\{10\bar{1}0\}$ is the dominant slip system, with isolated occurrences of $\{10\bar{1}1\}$ in coarse α titanium grains and that in no conditions tested did basal slip occur. The suggestion is made, and later confirmed by Anderson *et al.* [30], that this is due to the large grains tested having orientations towards the $\{11\bar{2}0\}$ and $\{10\bar{1}0\}$ planes, according to the stereographic projection in Figure 2.9a). This perception would agree with the theory that slip along the basal plane would not accommodate the extension induced during deformation in a single crystal, and subsequent work by Anderson and others [20, 30], Figure 2.9b), shows basal slip as the secondary slip system. Results by Churchman demonstrate, however, that an increase in the oxygen content from around 0.01 wt.% as achieved in some work [20,30,31] to 0.1 wt.% leads to a change in propensity and pyramidal slip superseding basal slip as the secondary slip system [20]. This is also comparable to the observation as a function of temperature, where at 500^{o}C pyramidal slip again superseded the room temperature secondary slip system, basal slip [31]. Due to the CRSS of slip in CPH material and the need to comply with the Von-Mises criterion it is apparent that homogeneous deformation via only slip deformation is not realistic at room temperature, illustrating the importance of twinning in the environment under which machining occurs.

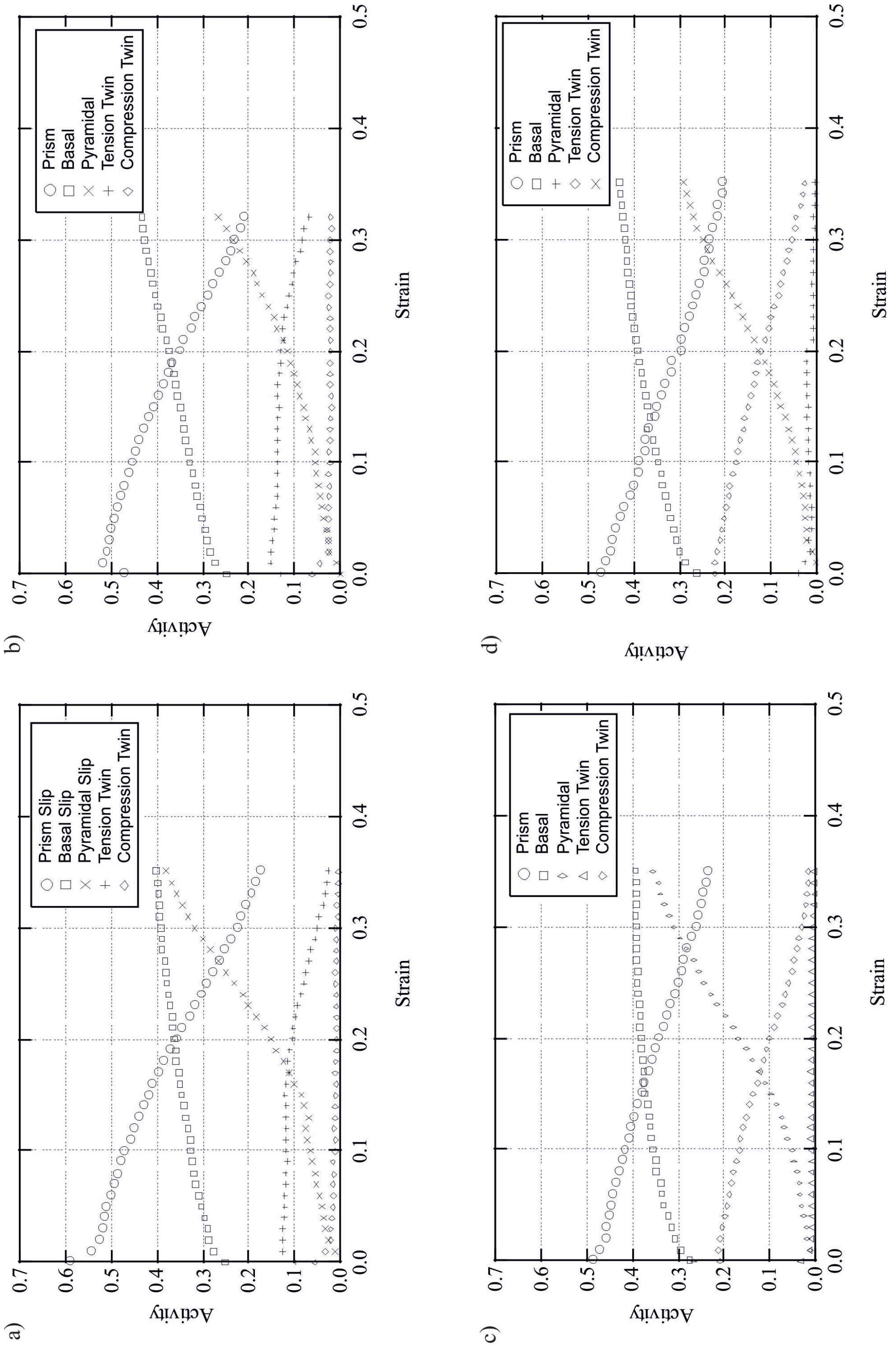

Figure 2.8: Activity of slip and twin systems for samples, with weak crystallographic texture, deformed at a) and b) 3×10^{-4} and c) and d) 1.5×10^{3} [28].

TABLE 2.1: OBSERVED SLIP MODES IN α-TITANUM [12, 24].

Slip system type	Burgers vector type	Slip Plane	Slip Direction	No. of slip systems		minimum CRSS, kg/mm^2	
				Total	Independent	O + N $\approx$ 0.1%	O + N $\approx$ 0.01%
1	$\bar{a}$	(0001)	$\langle 11\bar{2}0\rangle$	3	2	10.9	6.3
2	$\bar{a}$	$\{10\bar{1}0\}$	$\langle 11\bar{2}0\rangle$	3	2	9.19	1.4
3	$\bar{a}$	$\{10\bar{1}1\}$	$\langle 11\bar{2}0\rangle$	6	4	9.90	
4	$\bar{c}+\bar{a}$	$\{11\bar{2}2\}$	$\langle 11\bar{2}3\rangle$	6	5		

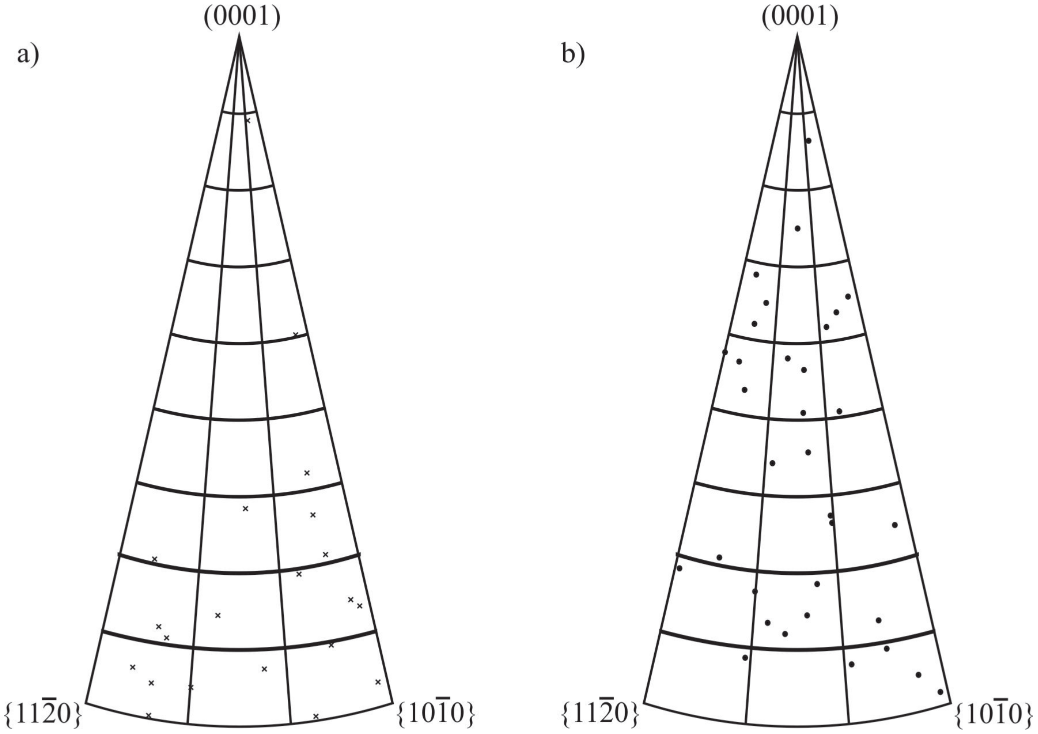

Figure 2.9: Stereographic projection of titanium specimen axes, points indicating a) large crystal orientations from Rosi [21] and b) single crystal orientations from Anderson [30].

2.2.2 Twinning

Twinning is the mechanism by which a rapid reorientation of a grain, or section of a grain, occurs [32]. It is induced by mechanical shear (mechanical twin) or by annealing heat treatments (annealing twin). A complete definition of a twin was used by Dana [32]: “A lattice is twinned when one or more parts, regularly arranged, are in reverse position with reference to the other part or parts”. This means that a twin boundary is a plane of reflection from which both sides are identical but reflected, as shown in Figure 2.10. A table of the three most commonly observed twinning modes in α titanium has been compiled in Table 2.2. There are four terms to fully characterise a twin; these are K_1, K_2, η_1 and η_2, and less significantly K_2' and η_2' [33]. The shear in twinning leaves two lattice planes undistorted; this is termed the K_1, which lies along the twin boundary. The line that intercepts the shear plane and K_1 has the direction $\eta 1$. The $K2$ plane, which becomes K_2' after twinning has occurred [33], represents the shear plane before and after twinning. The η_2 and η_2' represent the direction of the $K2$ and $K'2$, respectively. The same relationship applies to K_2 and η_2, as well as K_2' and η_2', as is seen in the K_1 and η_1. To determine a twins identity either the K_1 and η_2 or K_2 and η_1 are required [33].

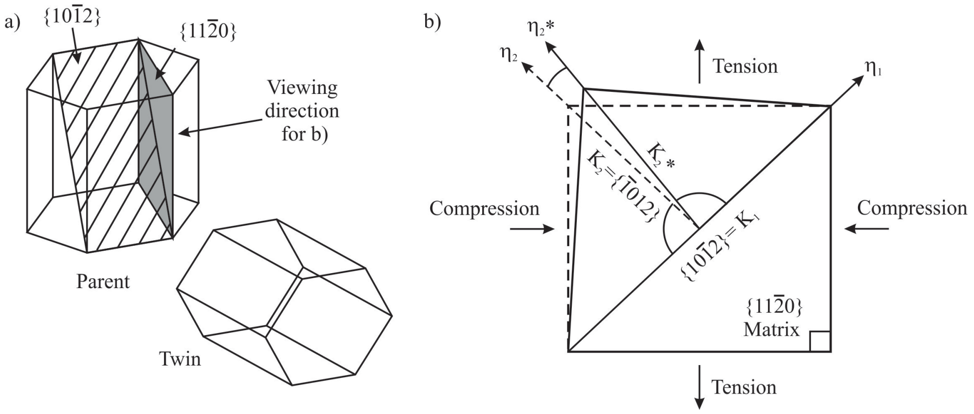

Figure 2.10: Schematic diagram showing a) the orientation relationship between a parent CPH crystal having twinned on $\{10\bar{1}2\}$ plane and b) the relative geometry for a $\{10\bar{1}2\}$ twin in α titanium. Adapted from Partridge [18].

In CP titanium the occurrence of twinning is a significant mechanism for deformation, particularly the $\{10\bar{1}2\}$ tensile twin in compression testing [22, 26]. The reason for this twins significance is because the most common slip planes observed are all have a slip direction of $\langle 11\bar{2}0 \rangle$. This direction contains no c-axis vector meaning a homogeneous deformation is not possible, therefore requiring twinning to accommodate c-axis deformation. Its dominance over the other three modes listed in Table 2.2 is that under compression tensile twins are preferential due to e

TABLE 2.2: OBSERVED TWIN MODES IN α TITANIUM [34].

Mode	K_1 Plane	η_1 Direction	Misorientation* (Angle/Axis)	Shear
Tensile type-1	$\{10\bar{1}2\}$	$\langle\bar{1}011\rangle$	$85^o\langle 1\bar{2}10\rangle$	0.171
Tensile type-2	$\{11\bar{2}1\}$	$\langle\bar{1}\bar{1}26\rangle$	$35^o\langle 1\bar{1}00\rangle$	0.629
Compression type-1	$\{11\bar{2}2\}$	$\langle 11\bar{2}\bar{3}\rangle$	$65^o\langle\bar{1}100\rangle$	0.221
Compression type-2	$\{10\bar{1}0\}$	$\langle 10\bar{1}2\rangle$	$54^o\langle\bar{1}2\bar{1}0\rangle$	0.101

2.3 Influence of Aluminium

Aluminium is an integral part of all the major commercially available titanium alloys. Work has been done to determine the effect of aluminium content on titanium at low strain rates [20, 22, 26]. This section reviews the influence of aluminium on properties ranging from atomic level to macroscopic mechanical properties. The influence of aluminium as an α stabiliser and substitutional addition has been discussed in Section 2.1 and makes the Ti-Al phase diagram of significant importance, Figure 2.11.

2.3.1 Lattice Parameters

As can be seen from Figure 2.12 the substitutional behaviour of aluminium influences the lattice parameters of α-titanium. Firstly, the a parameter reduces linearly up to approximately 21 wt.% Al. This coincides reasonably well with the onset of titanium aluminide formation (TiAl) which begins to occur just above 21 wt.% Al. Secondly, the c parameter initially remains relatively constant, up to approximately 6 wt.% Al, before decreasing linearly until approximately 21 wt.% Al, in the same fashion as the a parameter. The overall result on the c/a ratio is an initial increase, up to approximately 5 wt.% Al, before plateauing at 1.60, up from 1.588 initially. Such change in a and c parameters is responsible for the increase in CRSS values for virtually all the slip mechanisms described in Section 2.2.1 due to decrease in plane separation with the increasing presence of the smaller aluminium atoms within the unit cell. This reduction in plane separation, while remaining mostly titanium atoms, will mean that the strain required to cause glide between these planes will increase as the strain induced by the smaller atoms needs to be overcome in addition to the other barriers to dislocation motion.

2.3.2 Stacking Faults

Stacking faults in CPH materials are energetically unfavourable compared to twins. However, they do occur, and most of the work surrounding them has focused on FCC metals as these materials demonstrate the highest propensity for their formation [36]. In a CPH material the stacking sequence of planes is $A\ B\ A\ B$, Figure 2.13 and Figure 2.14a). The introduction of a stacking fault into CPH influences the stacking sequence and generally

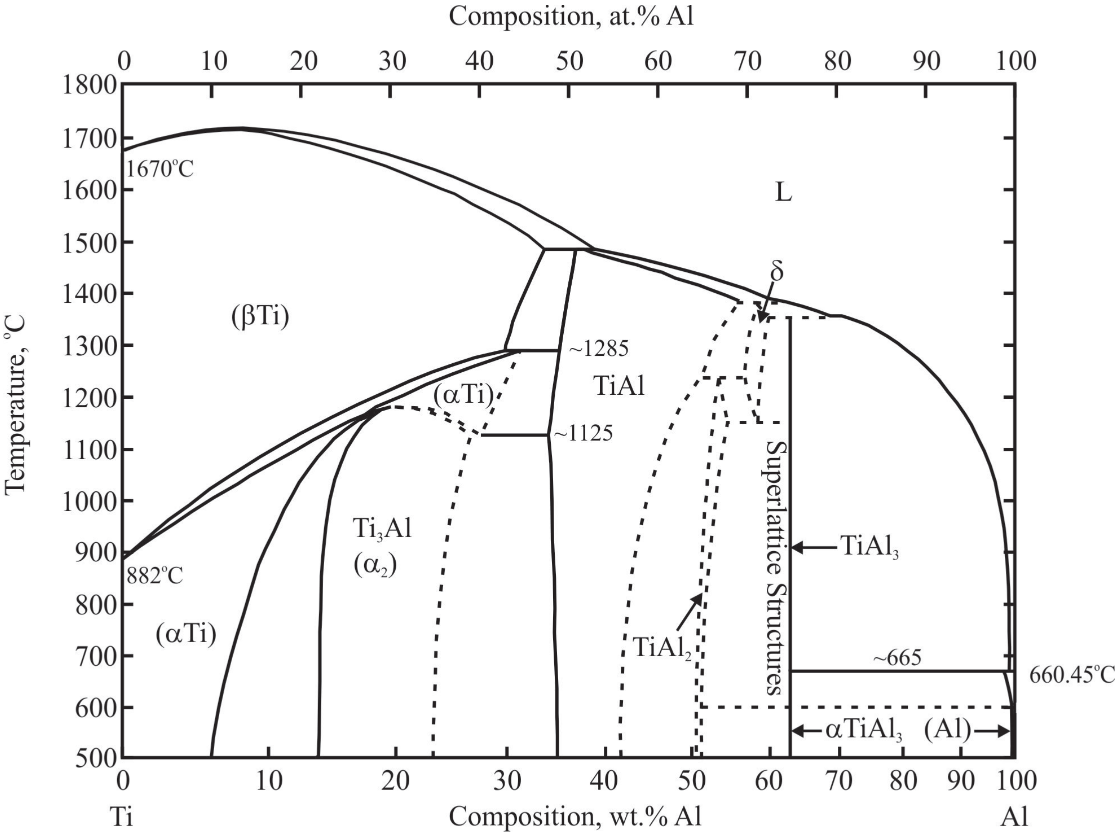

Figure 2.11: Titanium - aluminium phase diagram [11].

creates a FCC region, sequenced *A B C A*, within the CPH parent structure, bounded by two partial dislocations, Figure 2.14b). The separation of these two partial dislocations is determined by the stacking fault energy; a low stacking fault energy, such as in most alloyed materials, has high partial dislocation separation (or wide stacking fault), Figure 2.15, and the reverse is true of a high stacking fault energy, also Figure 2.15. This means that the energy required to generate a stacking fault is low resulting in a higher propensity for stacking faults. Conversely a high stacking fault energy results in a low partial dislocation separation and narrow stacking fault, and is observed more frequently in pure material such as copper [36–38].

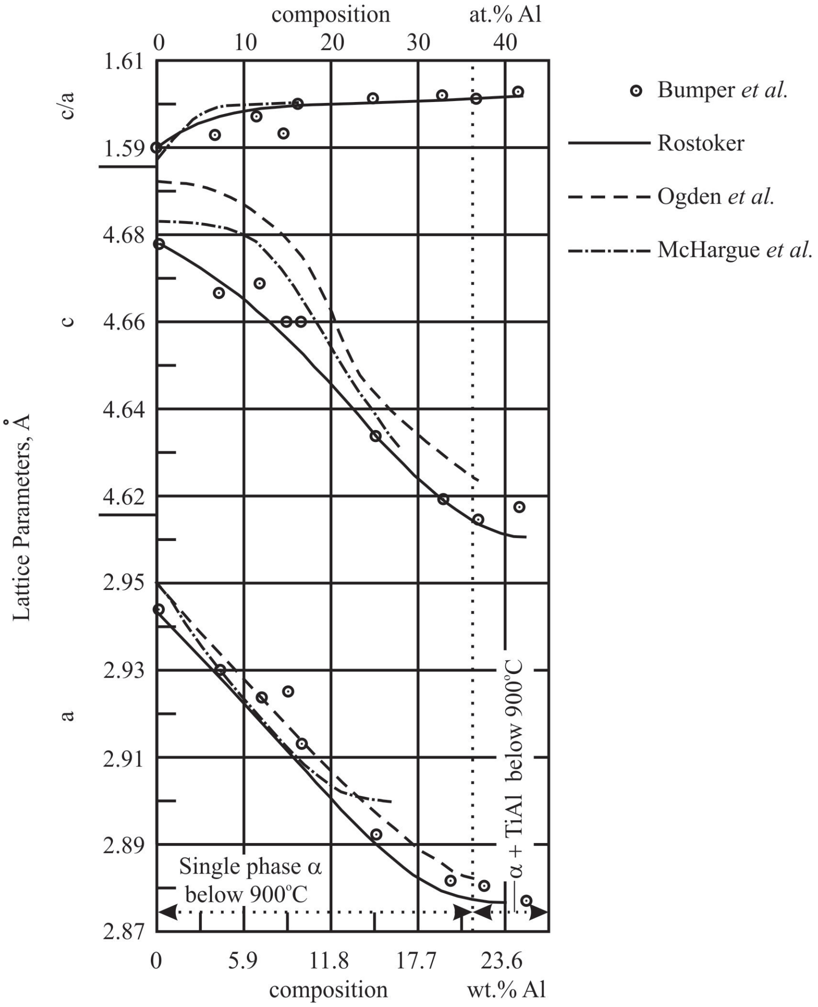

Figure 2.12: Graph depicting the influence of aluminium on the lattice parameters of α titanium. Adapted from McQuillan [35].

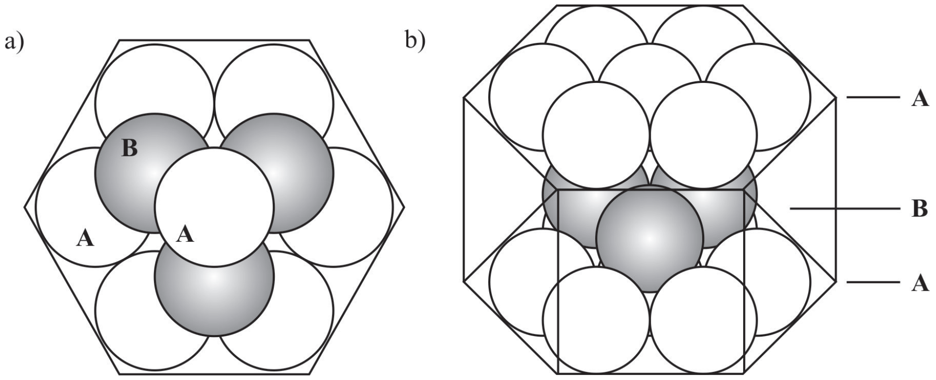

Figure 2.13: Stacking sequence of titanium viewed from a) [0001] direction and b) $\langle 1\bar{1}02 \rangle$ direction.

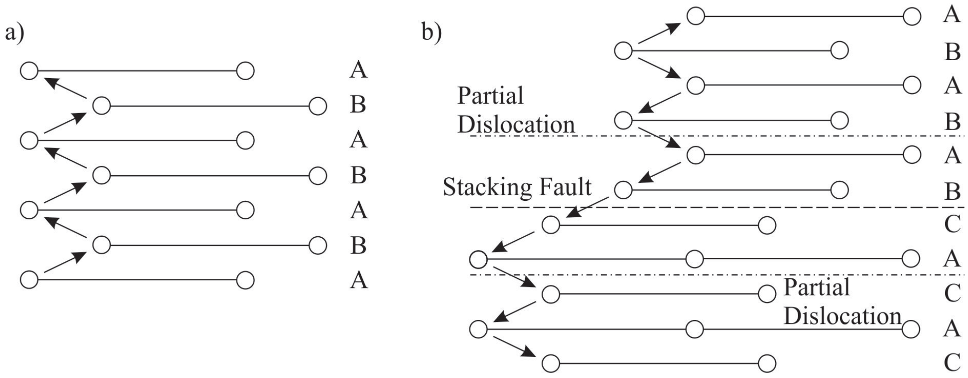

Figure 2.14: Schematic demonstrating a) Faultless CPH structure and b) CPH exhibiting a stacking fault, bounded by partial dislocations.

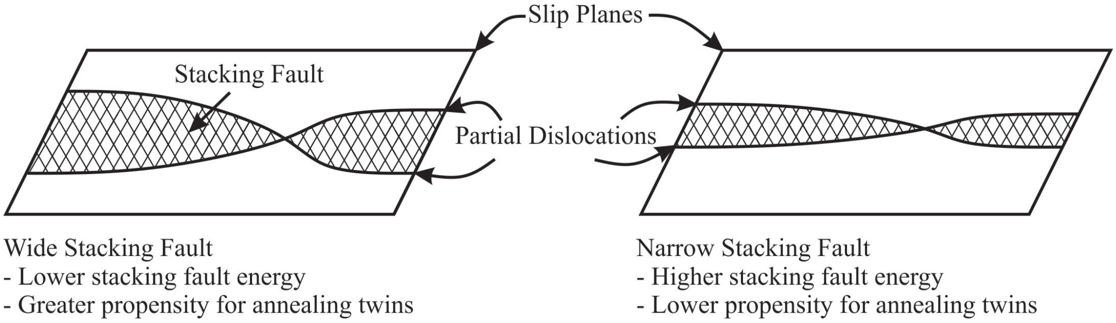

Figure 2.15: Schematic stacking faults sequence of titanium listing properties associated with left, wide stacking faults and right, narrow stacking faults.

The partial dislocation separation has a very large effect on the observed dislocation behaviour. In FCC metals there is a theory that cross-slip occurs because partial dislocations 'pinch' in the plane of origin and extension continues along the slip plane [37]. This means that a pure material, e.g. copper or titanium, would have a high stacking fault energy and subsequently few stacking faults and a low partial dislocation separation, meaning cross-slip is more readily formed than in alloyed material, such as Ti-6Al-4V or the higher aluminium Ti-Al binary alloys examined in this work.

2.3.3 Slip

Slip in titanium, and CPH structures generally, has been widely observed and researched [7, 24, 26, 39, 40]. As discussed in Section 2.2.1, in CP titanium at room temperature the most commonly observed slip system is prismatic, namely $\{10\bar{1}0\}\langle11\bar{2}0\rangle$, with $\{10\bar{1}1\}\langle11\bar{2}0\rangle$ and $\{0001\}\langle11\bar{2}0\rangle$ as secondary and tertiary systems. As aluminium content increases, the CRSS value for all of the observed slip systems increases, Figure 2.18, due to having to overcome the added lattice strain, discussed in Section 2.3.1. Figure 2.16 shows us that there is a linear relationship between Al content and the CRSS and, apart from the absolute values, the only change in the relationship is the gradient of the line. It should be noted that one of the compositions proposed in this work will be close to the $\alpha Ti \rightarrow Ti_3Al$ (α_2) phase boundary; however, this work aims to avoid the formation of this embrittling phase.

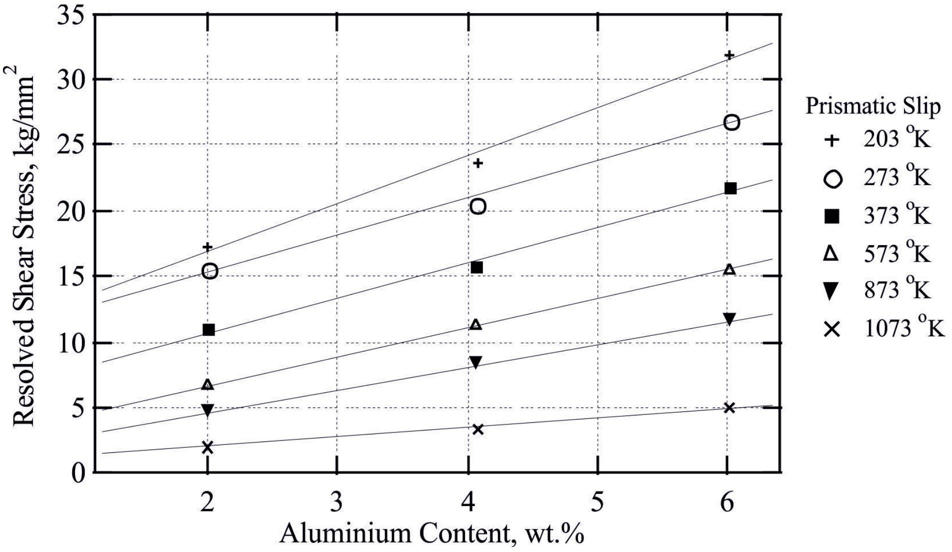

Figure 2.16: Graph showing the critically resolved shear stress of prismatic slip as a function of aluminium content in titanium. Adapted from Paton [24].

As aluminium content increases the $\bar{a}$ slip presence is increasingly confined, Figure 2.17. This confinement has a strong orientation dependence. It could be suggested that the cause of this is the increased level of order associated with increasing aluminium content with regards to its appearance within the crystal structure [41]. The less common $\bar{c}+\bar{a}$ slip systems, which require higher CRSS values to occur, only do so when a favourable orientation arises. It is shown by Paton *et al.* [22] that if the crystal orientation is approximately 15^o off the loading angle then $\bar{c}+\bar{a}$ slip does occur, but maintains a comparably high CRSS values compared to the principal $\bar{a}$ slip system (approximately 2.5 times).

Williams [26] indicated that prism slip would dominate in polycrystalline materials at room temperature, Figure 2.18, but at 1000 K (≈730°C) the CRSS values have converged; this effect is replicated at room temperature once the aluminium content reaches 11 wt.%. From Patons work [24], after extrapolating the trends in Figure 2.19, it would support the observations by Williams and suggests that if the temperature of the material reached >500°C (873 K), at least locally, then the propensity for $\bar{c} + \bar{a}$ slip and the principal $\bar{a}$ slip system would be almost equal according to the CRSS value. Although the window for this to occur could be limited, as shown by Figure 2.19, at temperatures of 900°C an unstable shear process overtakes and $\bar{c} + \bar{a}$ ceases to be observed [22]. This is supported by Williams [26] who also indicated that the behaviour of slip is relatively straight forward in the absence of twinning compared to once twinning occurs. Furthermore, as the aluminium content increases there is a substantial decrease in the presence of twinning. The complication arises with the behaviour of slip in the same environment as twinning. With $\{11\bar{2}2\}$ twins, extensive $\bar{c} + \bar{a}$ slip occurs in the surrounding material, believed to be an accommodation mechanism. However, a higher density of $\bar{a}$ slip exists within the twin than in the adjacent parent material, which provides evidence to suggest that the twin is orientated favourably for slip.

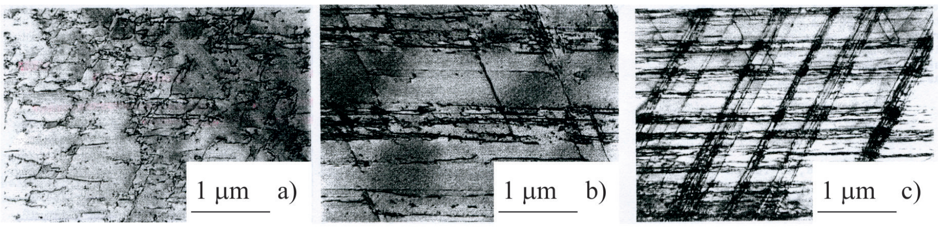

Figure 2.17: Micrographs demonstrating the increasing level of slip line confinement from (a) 2.1 wt.% Al, (b) 4.0 wt.% Al and (c) 6.1 wt.% Al [24].

It must be noted that, as discussed in Section 2.7.1, significant temperatures may be achieved during shear band formation and as temperature rises there is a convergence of the CRSS values [26] for the slip systems across the aluminium contents examined, Figure 2.19.

2.3.4 Twinning

With twinning being the main deformation mechanism observed in low aluminium content material, < 5 wt.% Al, and at progressively higher temperatures, with decreasing aluminium [26], identifying the particular system becomes prudent. The main system to be indexed was $\{11\bar{2}1\}$ twins; this contrasts with what was observed by Paton [24] who observed $\{10\bar{1}2\}$ twins, especially as this was the case in both 5 and 2.9 wt.% Al in Williams [26] and 3.5 wt.% Al in Paton [24]. The most obvious explanation for this contrast in observations would be that the orientation of the grains observed was more

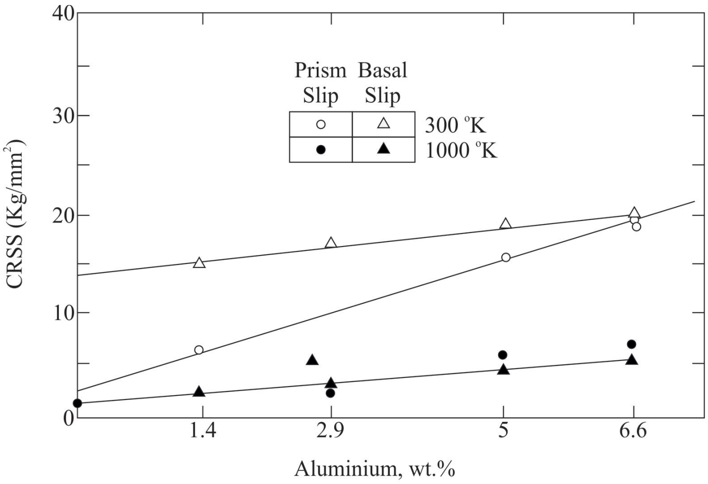

Figure 2.18: Critically resolved shear stress for prism and basal slip as a function of aluminium content for crystals deformed at temperatures of 300 K and 1000 K [26].

favourable for the opposing twins systems; $\{11\bar{2}1\}$ occurred in single crystal specimens orientated for basal slip and $\{10\bar{1}2\}$ were observed in a polycrystalline material. However, the observed twins remained $\{10\bar{1}2\}$, even in grains orientated favourably for basal slip in the polycrystalline material. This would lead to the suggestion that the stresses and strains induced by the polycrystalline material as opposed to in the single crystal, i.e. for a given grain the constraining effect of neighbouring grains, force the system to prefer $\{10\bar{1}2\}$ over $\{11\bar{2}1\}$. This is because if both twins possessed similar CRSS values then both would be present in significant quantities, rather than the significant dominance of one over the other that is observed. Work by Chichili [42] further supports the findings of Paton [24].

2.3.5 Deformation Mechanism Summary

The overall result on the deformation of titanium is complex due to the large number of systems in operation. The influence of stacking fault energy, with respect to slip, is that a low stacking fault energy would lead to the prediction that favourable slip systems would be a more prevalent deformation mechanism in CP titanium than in an alloyed system of the same phase. This would be because the higher propensity for cross-slip, due to narrow stacking fault, means a reduced requirement for twinning to occur to achieve the required five independent deformation modes for homogeneous deformation. This has clearly been demonstrated by a number of studies which show an increase in the critically resolved shear stress, CRSS, with an increase in alloying additions [26, 43]. But as even CP titanium, alloyed with oxygen, possesses a lower stacking fault energy, wider stacking fault, than pure titanium a subsequent reduction in slip occurs and the requirement for twinning increases. It must be noted that these observations only hold

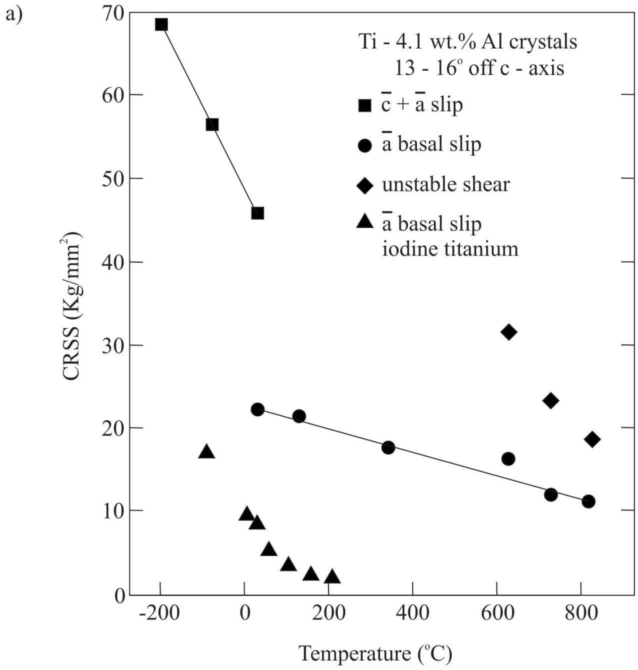

Figure 2.19: Critically resolved shear stress vs. temperature iodine Ti and Ti - 4.1wt% Al single crystals for slip and unstable shear mechanisms [24].

qualitative analysis of deformation as a quantitative analysis suggests that there is an overall reduction in deformation occurrence, hence the occurrence of shear bands.

2.3.6 Ti_3Al, α_2 Phase

Examination of the α_2 precipitate in titanium alloys has been extensively studied with much effort in determining an accurate phase diagram [44–49]. This has resulted in a widely accepted $\alpha \rightarrow \alpha + \alpha_2$ phase boundary somewhere around 5 - 6 wt.% Al. This value is dependent on oxygen content as an increase in oxygen shifts the boundary to higher temperatures and lower aluminium contents [50, 51]; this has been attributed to a preference for oxygen to partition preferentially into the α_2 phase [50]. α_2 particles, with the chemical formula of Ti_3Al, form the superlattice structure $D0_{19}$, Figure 2.20. This structure exhibits the same CPH structure as α titanium, so undergoes a congruent transition between $\alpha \rightarrow \alpha_2$, but has a lattice mismatch, Table 2.3. As can be obtained from Figure 2.12 at the proposed transition concentration, 5 - 6 wt.% Al [44–49], the c parameter agrees with the value given by Banerjee [52]; however the value for the a parameter is significantly different. The cause for this is not clear; the influence of common interstitial impurities has been investigated, and three of the most common impurities (oxygen, carbon and nitrogen) all influence the c parameter more than the a parameter, Table 2.4, but data presented by Banerjee suggests the reverse. Suggestions have been

TABLE 2.3: α-α_2 PRECIPITATE MISMATCH ALONG a AND c DIRECTIONS [52, 54].

α-α_2 mismatch			
	Calculated Ti-Al Solid solution, Å	Ti_3Al, Å	mismatch, %
a parameter	2.904	5.761 - 5.765*	0.74 - 0.81
c parameter	4.665	4.625 - 4.649	0.34-0.86

*Due to superlattice structure $a_{D0_{19}} \approx 2a_\alpha$.

made as to the influence of short range ordering, SRO, [50,53,54]. Lim [50] observed that not only did an increase in oxygen lead to increased volume fraction of α_2 particles, for a given aluminium content and heat treatment, but that the distribution of these particles became more uniform compared to the heterogenous distribution found at lower oxygen contents, illustrated in Figure 2.21. In the low oxygen specimens the α_2 precipitated almost exclusively on low-angle grain boundaries, Figure 2.21b), but as the oxygen level increases particles become observable in the matrix initially with heterogenous distribution and size, Figure 2.21c), before becoming more homogenous, Figure 2.21d) and growing linearly with time Figure 2.21e) and f).

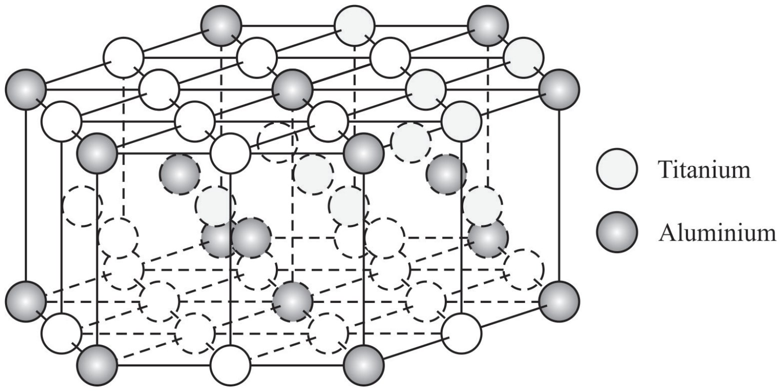

Figure 2.20: Schematic of α_2, $D0_{19}$ superlattice, showing sites occupied by titanium and aluminium.

As discussed previously, Section 2.3.1, the influence of the aluminium in the ordered phase is comparable to that observed in the solid solution, α, phase because a larger reduction in the a direction occurs than in the c direction and there is a marked increase in the CRSS for all slip, similar to that observed by Paton [24]. Confinement of the type observed by Paton [24] and by Blackburn [43] is the manifestation of the increasing aluminium content and therefore decreasing plane separation and increased short range ordering and ordered particles (α_2) [43]. The result of this confinement is that it becomes increasingly easy for shearing, and shear band formation to occur, observed in IMI 834 [55], Ti-6Al-4V [56] and most importantly, with regards to this work, Ti-Al

TABLE 2.4: EFFECT OF SMALL QUANTITIES OF IMPURITY ELEMENTS ON LATTICE PARAMETERS ON α TITANIUM [35].

Addition elements	Parameter change per wt.% of addition element, Å	
	a	c
Oxygen	0.000	0.015
Nitrogen	0.002	0.023
Carbon	0.013	0.049

binary alloys [43]. This is because it increases the CRSS for all systems and reduces the number of operating slip systems. For example $\bar{c}+\bar{a}$ and twinning is present in lower aluminium content material [22, 24, 26, 27, 43] but as aluminium content increases to 17 at% Al (~10 wt.% Al) then its occurrence decreases and in 25 at.% Al (~ 16 wt.% Al), on the $\alpha+\alpha_2 \rightarrow \alpha_2$ boundary, it was not detected at all [43]. The expected result of this would be a reduction in ductility and increased occurrence of cleavage fracture, which is also the conclusion reached by Blackburn [43].

All of these observations lead to the macroscopic behaviour effects, shown in Figure 2.22, where yield stress shows small influence by the presence, and increasing size of, α_2 compared to the heavily reduced net area fracture stress. This suggests that the inclusion of these particles may have an effect that is not immediately obvious. It is also possible that these particles behave comparably to how MnS (manganese sulphide) particles do in free cutting steels, examined in Section 6.6. Blackburn [43] also noted that from measurements made from Figure 2.23 the author calculated that the displacement measures ~3000 Å, equivalent to ~700 $\langle 11\bar{2}0\rangle$ dislocations. It is suggested that this may be enough to cause fracture as a band of this size may be large enough to make specific dislocation interactions redundant.

2.4 Work Hardening Behaviour

Work hardening behaviour has been rigorously explored for FCC [38, 57] but, due to the complex deformation, exploration of CPH materials has only begun in the last decade or so [40, 58–60]. Work on copper has shown that at low strains, <0.05, behaviour is determined by whether the material is single crystal or polycrystalline, illustrated in Figure 2.24. Polycrystalline materials, examined in this work, are characterised by an initally high work hardening and progress as a decay curve.

Examination of CPH work hardening shows a three region curve, comparable to those seen in low stacking fault FFC materials [38]. Nemat-Nasser [58] qualitatively showed flow curves that appeared to exhibit three distinct regions for CP titanium in a range of conditions from room temperature, 298 K, to between 473 and 698 K depending upon

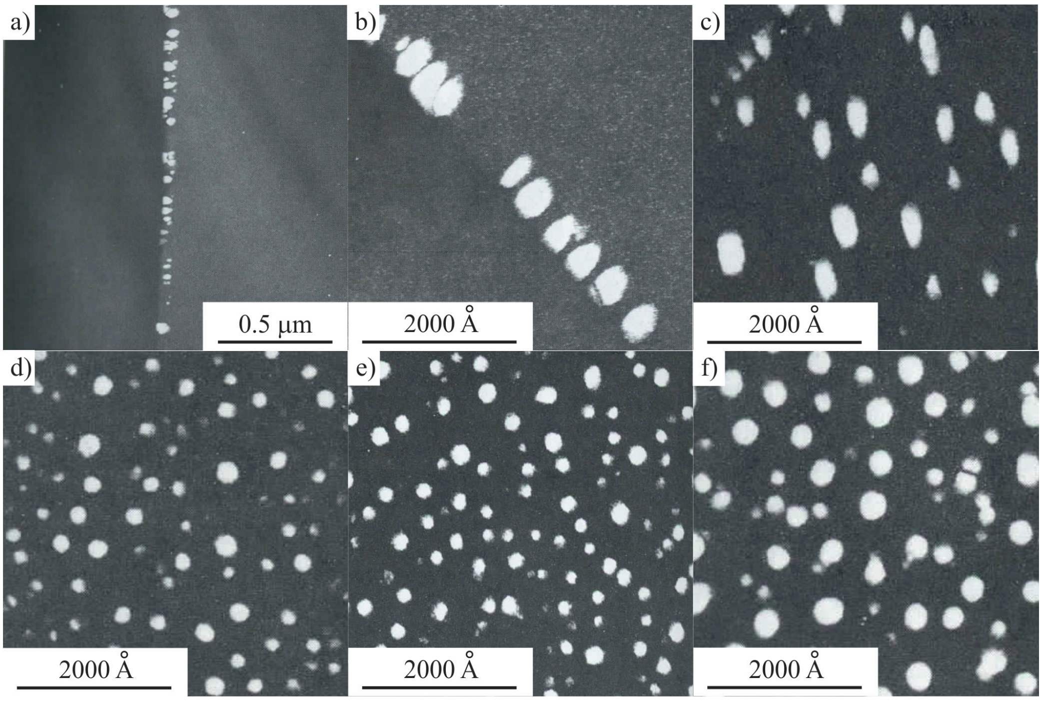

Figure 2.21: α_2 particles observed in Ti-8 wt.% Al particles, aged for 200 hours at 695^{o}C, by TEM containing a) and b) 580 ppm, c) 1060 ppm, d) 1300 ppm, e) 1780 ppm and f) 2900 ppm oxygen [50].

strain rate and 10^{-3} to 8×10^3 and possibly beyond, whereas 8×10^3 was the fastest strain rate tested. Further work by Salem [59] progressed the idea by quantitatively describing this three region curve by generation of a normalised, using shear modulus, work hardening curve against strain for high purity α-titanium, Figure 2.25. These results show that three region curves are the likely form work hardening curves will take in this work, as testing will occur in the window determined by Nemat-Nasser. The early work performed by Salem [59] performed a systematic metallographic analysis of high purity α-titanium progressively strained to higher strains and examining deformation behaviour and correlating the observed results to positions along the work hardening curve.

2.4.1 *Region* I

Region *I* is the region that occurs at the lowest strain values. It is characterised by a large decrease before reaching a minima, comparable to a decay curve. This region is comparable to the dynamic recovery region observed in many metals [59]. High stacking fault energy materials, such as copper, exhibit work hardening curves which essentially exhibit only Region *I* in contrast to low stacking fault materials, such as brass, which exhibit their minima before transition to Region *II*. Comprehensive work on FCC material [61] has shown that this correlates to dynamic strain recovery and deformation

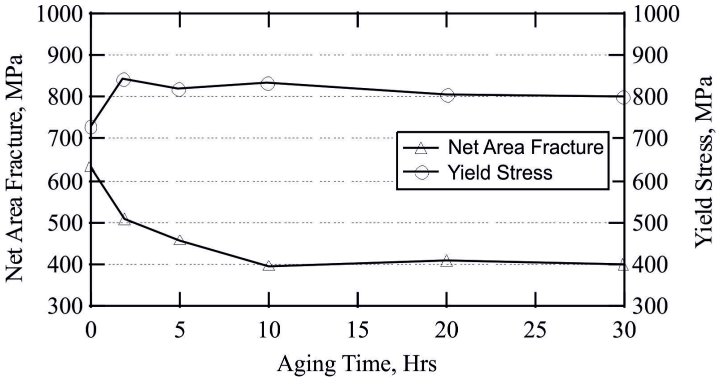

Figure 2.22: Variation of net area fracture stress for Ti-8.6 wt.% Al (notched specimens) quenched and aged at 700°C and corresponding yield stress [43].

by slip only as samples strained only to values in Region *I* exhibit no twinning [59], illustrated in Figure 2.26. The work hardening in this region can be expected to vary inversely as a function of the Hall-Petch relationship, i.e. smaller grain size results in lower work hardening.

2.4.2 *Region* II

This region is where the behaviour of work hardening varies between compression and tension. Under tension the work hardening rate continues to fall but at a lower rate than in Region *I* [62]. In compression Region *II* is characterised by an increase in the work hardening rate to a maxima and occurs at intermediate strain ranges. This region microstructurally has been characterised by the formation of deformation twins and the subsequent twin volume saturation, illustrated by Figure 2.27 which shows a sharp increase in the twin volume fraction at corresponding strains as an increase in the work hardening to the maxima. Continuing to strain beyond the work hardening peak causes no further increase in the measured twin volume fraction.

2.4.3 *Region* III

Region *III* is comparable to Region *I*, showing a decrease in the work hardening rate at high strain values. This demonstrates a region of dynamic recovery, at the end of which titanium alloys could be considered as failing as there is a large load drop due to shear band fracture.

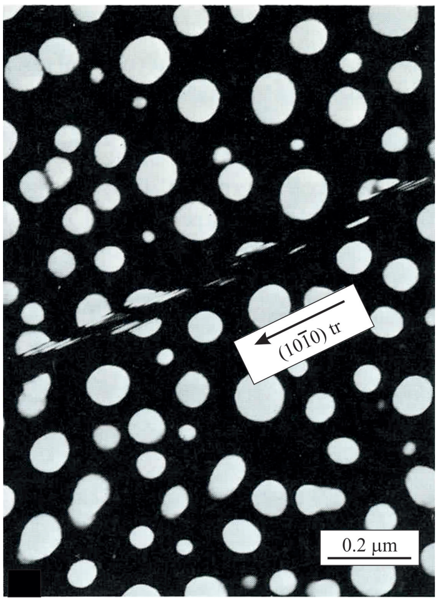

Figure 2.23: Prism slip particle shearing in Ti-10.3 wt.% Al aged for 48 hours at 840^{o}C [43].

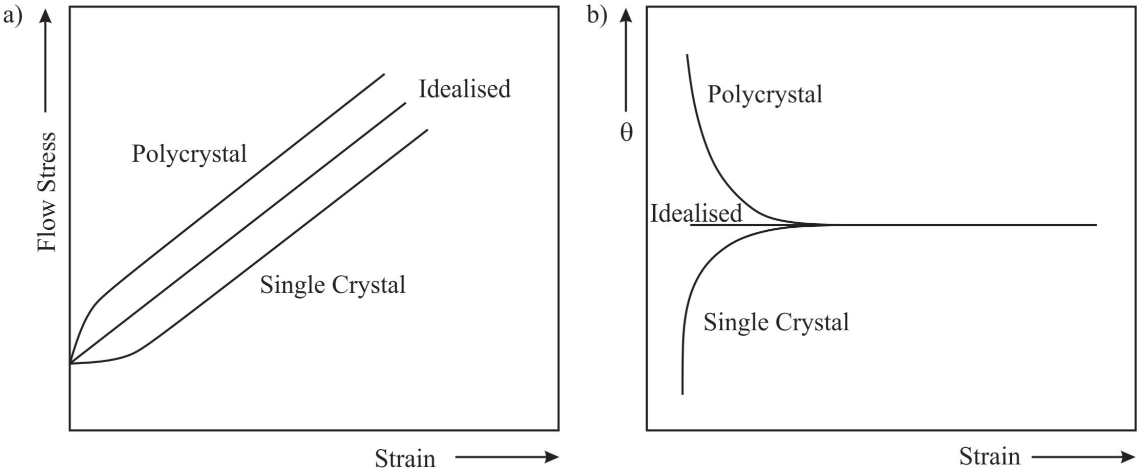

Figure 2.24: Schematic diagrams of a) simple flow curves and b) work hardening against strain of idealised, polycrystal and single crystal [57].

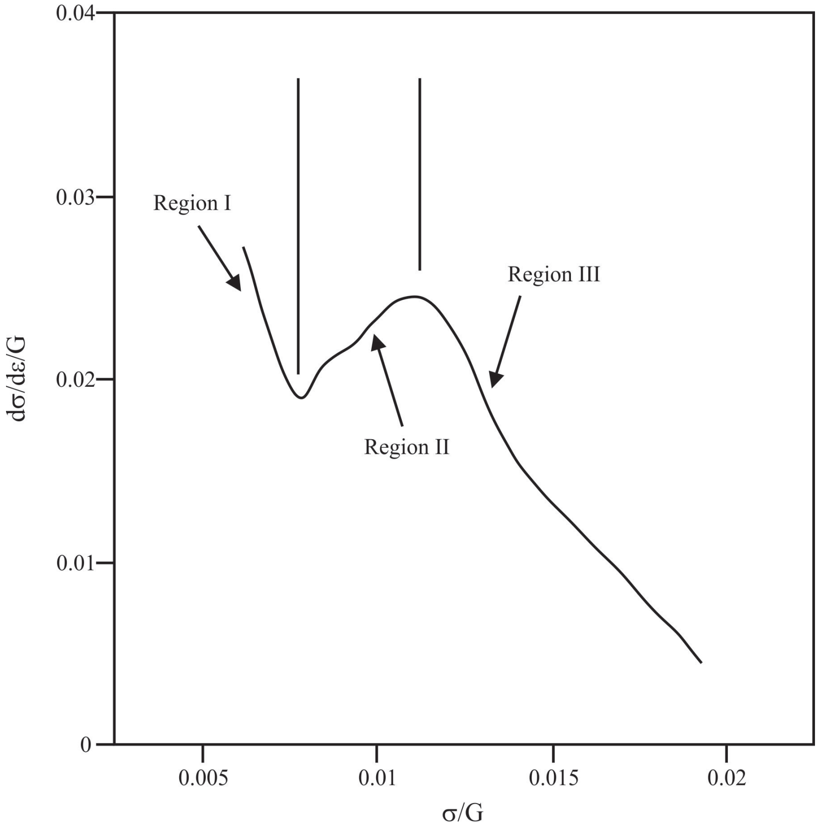

Figure 2.25: Normalised strain hardening response of α-titanium in simple compression [40].

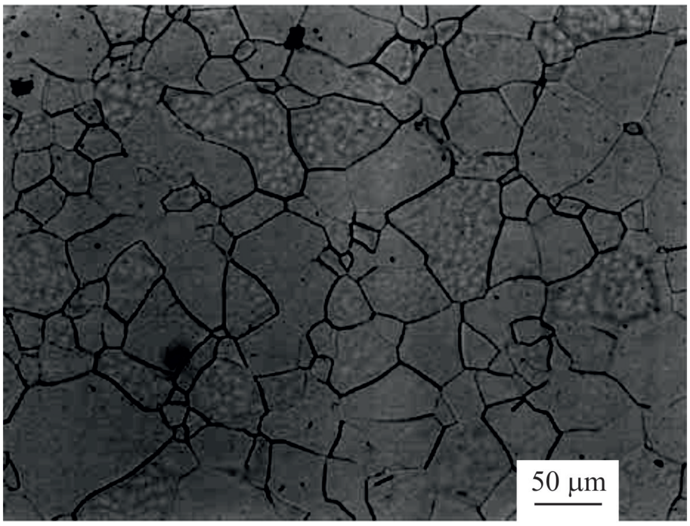

Figure 2.26: Optical micrographs of high purity α-titanium deformed to ϵ=0.025 by simple compression [59].

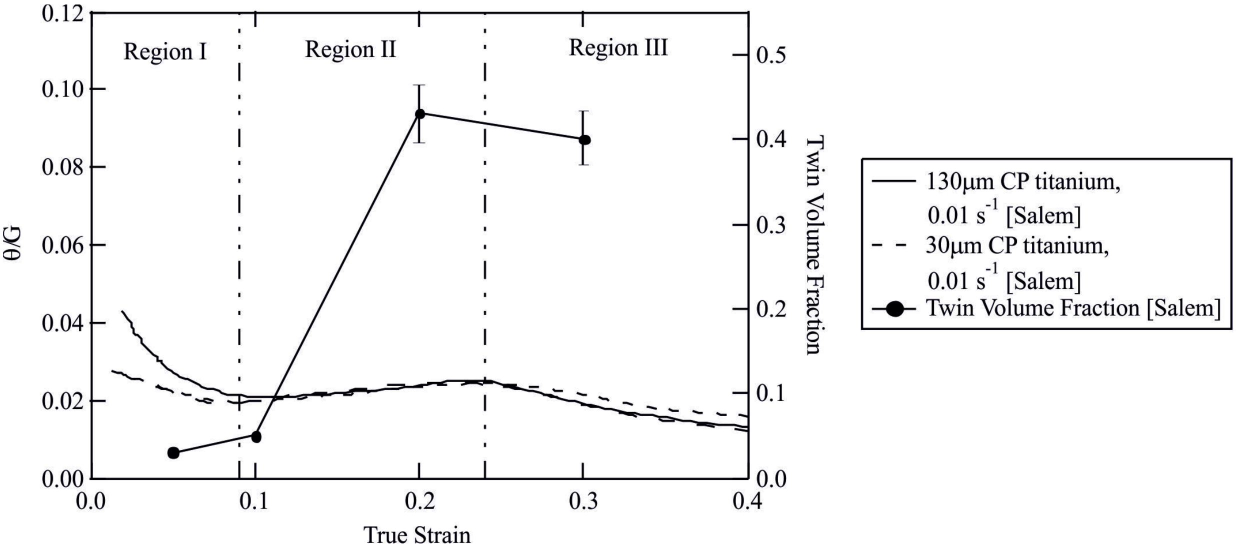

Figure 2.27: Plot of twin volume fraction and work hardening rate against true strain for high purity titanium under axisymmetric compression [60].

2.5 *Textural Effects*

The anisotropic nature of the CPH structure means there will be significant variation as a result of any macroscopic textures that are present in any product. Wang illustrated the influence of texture [63] on a magnesium alloy, showing that for material orientated with the basal plane perpendicular to the compression direction very limited work hardening is observed, indicating the material exhibits little twinning based on work hardening phenomena [38, 58, 59] discussed in Section 2.4, the likely cause of this is due to the ability to accommodate extensive slip due to the favourable orientation of the most common slip direction, $\langle 11\bar{2}0\rangle$, to the direction of deformation. In contrast, with the basal plane parallel to the compression direction the flow curve shows significant work hardening, indicating extensive twinning. As texture is not a selected variant for this work it highlights that any results generated during this work must make consideration of the texture to ensure any comparisons take account of its potential influence.

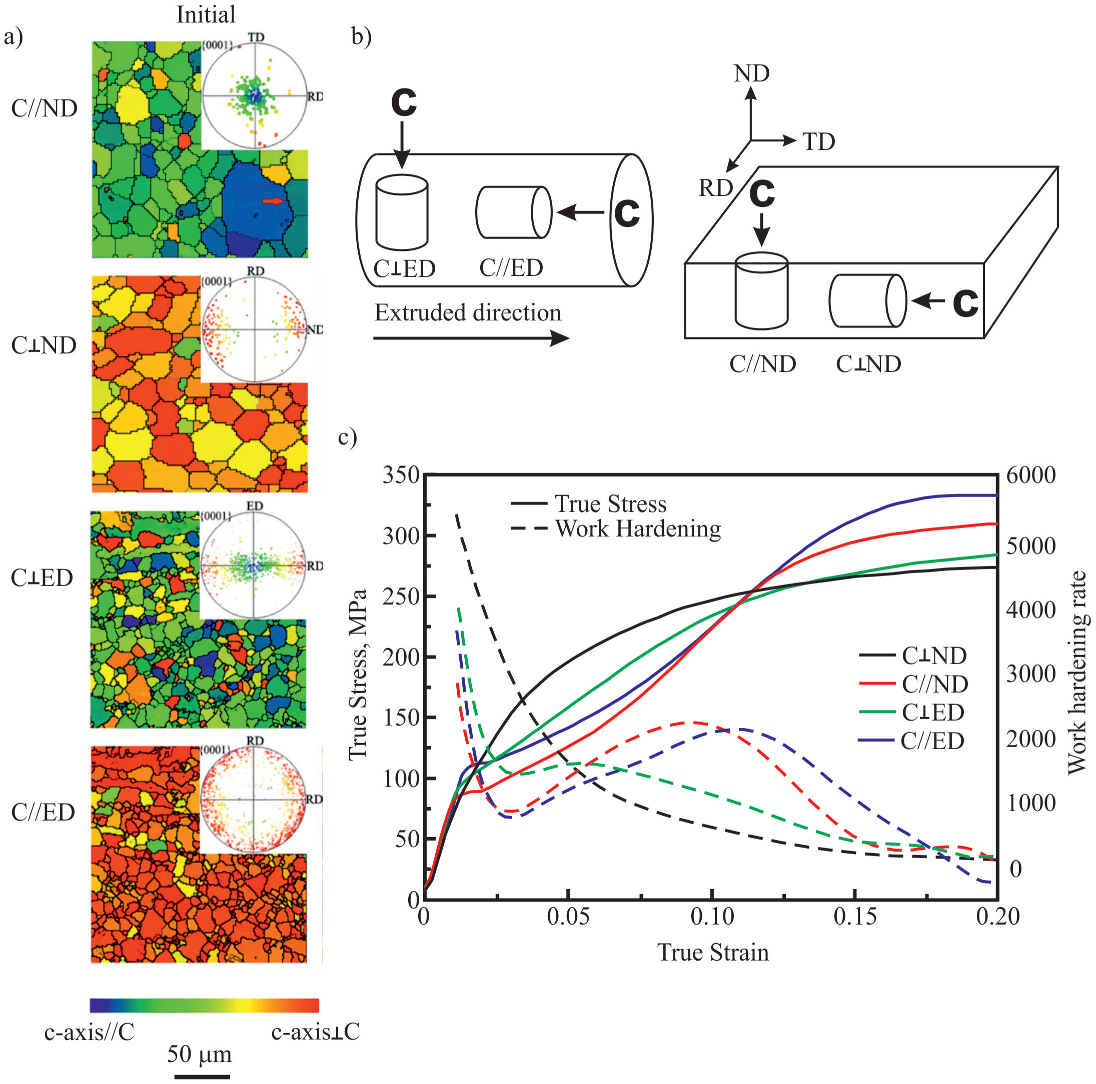

Figure 2.28: Magnesium alloy AZ31 a) EBSD IPF images and pole figures for *c*-axis texture of the specimen orientations tested, b) schematic illustrating the specimen orientations relative to the starting material and c) true stress versus true strain plots (flow curves) and work hardening curves for the four orientations tested [63].

2.6 High Strain Rate Deformation

To date much of the work performed with regards to high strain rate testing on titanium and its alloys is based around the macroscopic behaviour of the material, i.e. flow stress, high and low cycle fatigue and only, microscopically, as detailed as the presence of shear bands [64–66]. This information, while useful, does not significantly aid the understanding of the deformation mechanisms which this work is based on, as it only indicates what behaviour might occur macroscopically, and even then, knowing this behaviour of titanium and its alloys means the combination of mechanisms that could produce the same result is extensive. However, work by Chichili [42] gives some insight and this shall be discussed here. As would be expected, the propensity for different mechanisms changes, not only as a function of the material composition, but also the strain rates at which it is subjected to. The first note in this work [42] is that as the strain rate is increased, the occurrence of twinning increases, and that the cause for this increase is two-fold. Firstly, the number fraction of grains that contain twinning has greatly increased. Secondly, the number of individual twin systems present in an individual grain has also increased, Figure 2.29. It is also apparent that if they are strained to increasing levels, the same behaviour remains true. In almost all cases the twinning was identified as $\{10\bar{1}2\}$ type. There is, however, a saturation type effect where once the strain rate is increased sufficiently, 10^5 – 10^6 s^{-1}, then the increase in twinning reduces significantly, due to a saturation of the number of grains that contain twins. This supports the conclusion that the level of strain is the dominant factor in twin formation at high strains, rather than strain rate. However, at low strain rates the reverse is true [42] as this saturation effect has not occurred. It must also be noted that there was no observation of any basal slip at any strains or strain rates tested. However, the behaviour differs in that at the high strain rate, 10^5 – 10^6 s^{-1}, the twin density continued to increase with secondary populations forming and extensive twin interactions; normally it would be prudent to discuss these interactions but this is beyond the scope of this work. Slip behaved similarly to twinning in that increasing strains and strain rates produced an increasing population of slip bands with the same two-fold behaviour, with $\{10\bar{1}0\}$ being the most commonly observed. Whether 10^{-5} - 10^0 s^{-1}, under compression testing, or 10^2 - 10^6 s^{-1}, using impact based testing [42], basal slip was not observed, but was observed in low strain rate work [24, 26] when testing occurred under tensile conditions, which could account for the discrepancy in observations. Unlike with the high strain rate work there was no documented appearance of unstable shear. While all this information is useful in understanding when and where shear bands may be predisposed to occur, there is almost no work trying to understand mechanistically how the initiation process proceeds. From the literature it could be suggested that increasing already high absolute CRSS values for all types of deformation mechanism means a less homogenous deformation. This leads to the strain localisation that is widely accepted as responsible for the formation of shear bands, a view supported by Williams [26].

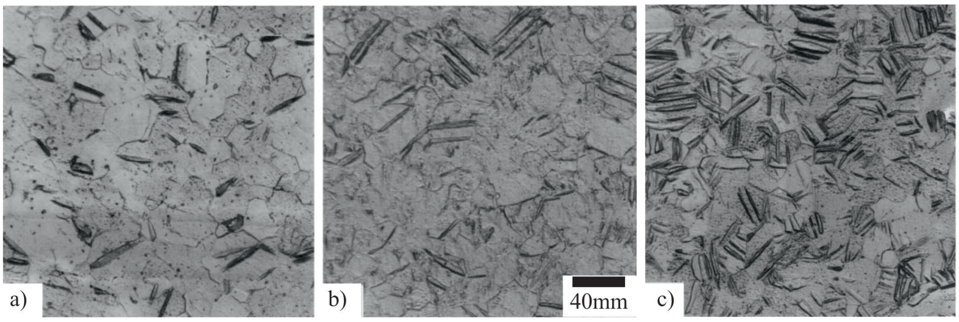

Figure 2.29: Light micrographs of α titanium strained to 6.5% at (a) 10^{-5} s^{-1} (b) 1.0 s^{-1} (c) 6 x 10^3 s^{-1} [42].

2.7 Shear Band Theory

Shear Band Initiation

It is widely accepted in each of the presented propagation theories that the initial strain localisation is a result of material microstructural inhomogenities [26], or geometric concentrators [67], such as corners or physical constraints [68], which cause localised heating [66] and therefore softening. In Sections 2.7.2 - 2.7.5 it is assumed that this strain localisation has already occurred and that all of the theories diverge from the same localised strain initiation scenario.

2.7.1 Shear Band Failure

Shear band formation is of key importance when examining the machinability of titanium and its alloys, due to its extensive presence in chips formed during high speed machining. Its presence in a material essentially signifies the impending failure of the component, with failure propagating from the shear band. There are several competing theories for the formation of shear bands with varying levels of detail; each of these will be discussed, compared and contrasted here. The following theories will be discussed from a microstructural evolution standpoint and the start point for each of these theories will be immediately after strain localisation. All work discussed is based upon impact of steel balls on Ti-6Al-4V plates, at ballistic speeds, i.e. up to $10^5 s^{-1}$, unless stated.

2.7.2 Localised Melting

On the formation of a region of strain concentration, the stresses experienced locally are higher than those experienced elsewhere. This localised cold working causes a temperature rise as dislocations are created and begin to diffuse through the material. As this process continues the temperature rise continues, allowing the formation of more dislocations as the CRSS for formation drops with temperature, creating a self perpetuating cycle of heating and thermal softening. As the deformation is happening at ballistic speeds [67–71], strains of 1000% can be reached [71], and as the thermal conductivity of titanium alloys is low [72], it can lead to high levels of almost complete adiabatic heating [70]. It predicts that the rapid increase in temperature outweighs the quench cooling of thermal diffusivity, achieving a temperature rise of $>$1600^{o}C. This means that within a shear band, a second band of superheated material is either liquid or, due to short duration of this temperature [71], extremely thermally softened. This results in an observed smooth fracture surface, Figure 2.30. While melting may have been observed in aluminium alloys [73], where the melting point is lower than in titanium alloys, it seems unlikely that a temperature of 1600^{o}C has been reached in order for localised melting to occur. This is supported by working using infrared demonstrating temperatures of up to 550^{o}C [74, 75]. This, coupled with the lack of recrystallisation present, requiring a temperature of $>0.5\mathrm{T}_m$, would be expected towards the edge of the shear band; however, literature has measured temperatures of up to 1250^{o}C using pyrometry techniques [76, 77]. This leads to the alternate theory suggested in the work seeming more realistic.

2.7.3 Micro-void Coalescence

This theory starts in the same manner as localised melting and is based on observations of fracture surfaces propagating through shear bands. It suggests that the concentration and lack of heat transfer away from the shear band cause adiabatic heating, the same as localised melting theory (Section 2.7.2), however, with a lower level of adiabatic heating. This theory was developed for Ti-6Al-4V by Timothy and Hutchings [69], who showed that shear bands formed within a number of different parent microstructures, listed in Table 2.5. Shear band regions thermally softened by adiabatic heating cause voids to form and coalesce along the shear band, which is also the direction of shear displacement. Coalescence occurs as voids line up in the shear band (Figure 2.31b). The ligaments experience intense shear in the direction of the shear stress. The ligaments then undergo necking (Fig 2.31c), or possibly brittle failure if temperature is insufficient. The temperature rise caused by the shearing and adiabatic heating process is dominated by strain rate [71]. This contributes to a large variation in the extent of the heating processes; however, what has been observed are heating rates of 2.7×10^7 - 4.4×10^7 Ks^{-1} and cooling rates of approximately 2×10^7 Ks^{-1} [74]. This is also in agreement with theoretical values obtained through principles of heat transfer [71]. Firstly, this theory works on the principle that the temperature rise is insufficient to cause dynamic

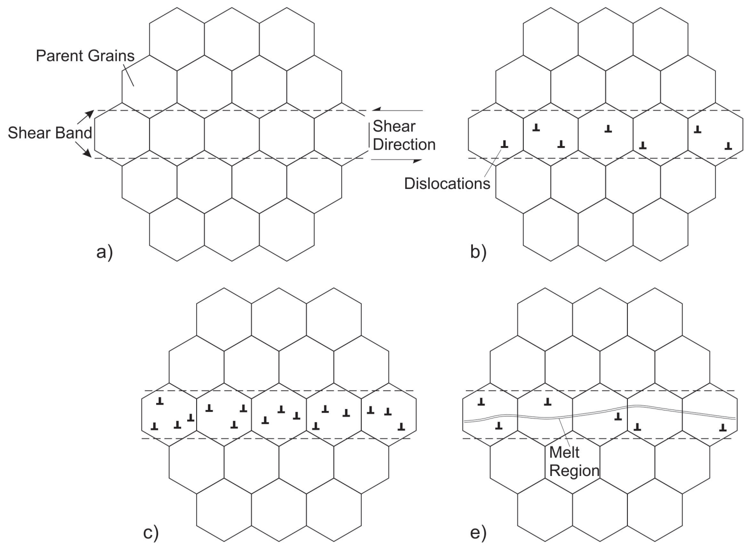

Figure 2.30: a) Intense shear localised stress in shear band b) Shear causes a build up of dislocations c) Dislocation annihilation rate slower than formation rate and build continues, simultaneously with adiabatic heating d) Build of dislocations and heating reach critical level, localised melting occurs, increasing diffusion and annihilating large volumes of the built up dislocations.

TABLE 2.5: Ti-6Al-4V ALLOY MICROSTRUCTURES EXAMINED BY TIMOTHY AND HUTCHINGS [69].

Heat Treatment	Mean Vickers Hardness (GPa)	Microstructure
As Received	3.42 ± 0.05	Fine equiaxed α + transformed β
$\frac{1}{2}$h at 950^{o}C, FC	3.12 ± 0.02	Fine equiaxed α + intragranular β
24h at 950^{o}C, FC	2.98 ± 0.02	Coarse equiaxed α + transformed β
$\frac{1}{2}$h at 1050^{o}C, FC	3.08 ± 0.10	Colonies of transformed β
$\frac{1}{2}$h at 1050^{o}C, WQ	3.77 ± 0.09	Grains of α/ martensite

recrystallisation, i.e. T<0.5T$_m$ [78], which is below 830^{o}C for this material. Also, there is no evidence that deformation twinning plays a significant role in shear band formation and subsequent failure, as none are observed in the region of a shear band [71]. There is the possibility that twins form and then anneal out, meaning that they form in the early phases of shear band formation and as time progresses, and the temperature rises, they are removed during recrystallisation, Figure 2.35. Another possibility is that a temperature rise above the $\alpha \rightarrow \alpha + \beta$ transus and the level of quenching causes the transformation to α' martensite to occur [79]. As has been shown by Liao [74] the cooling rate achieves such a rate that the formation of martensite is possible, provided the initial temperature rise is sufficient. This would also be difficult to distinguish from α as the crystal structure is the same, requiring TEM to distinguish each.

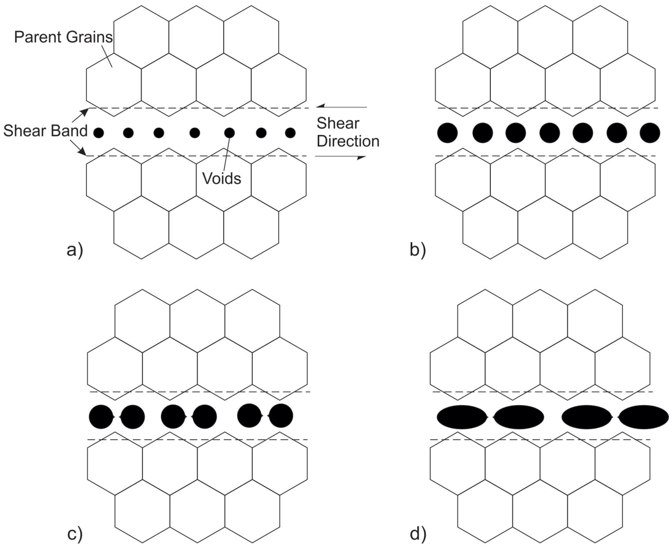

Figure 2.31: a) Small voids form due to intense shear b) Voids grow with increased strain and adiabatic heating c) Ligaments between voids begin 'neck' d) Voids coalesce and necking continues to form a continuous crack.

Microcrack Coalescence

There is a further subdivision to this form of failure propagation. This is where voids do not coalesce parallel to the shear band direction, but instead at an angle to it. Figure 2.32b) shows this formation of small cracks, from voids, and their subsequent rotation due to the shear stress experienced in the shear band. Once rotation has reached a critical level, i.e. the cracks become sufficiently parallel to the shear band, then fracture occurs to connect the individual microcracks, Figure 2.32c). There is sufficient evidence to see this as a viable mechanism of shear band failure as demonstrated by Figure 2.33.

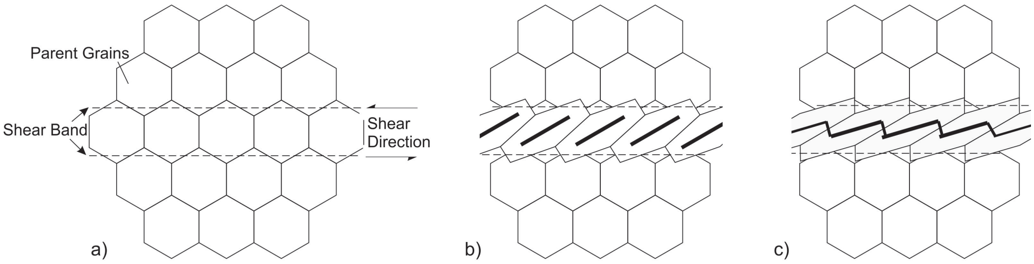

Figure 2.32: a) Strain localisation occurs forming the shear band b) Microcracks form within the shear band c) continued straining causes cracks to rotate, becoming closer to parallel to the shear band direction. These cracks once they become sufficiently close that fracture causes the microcracks to coalesce.

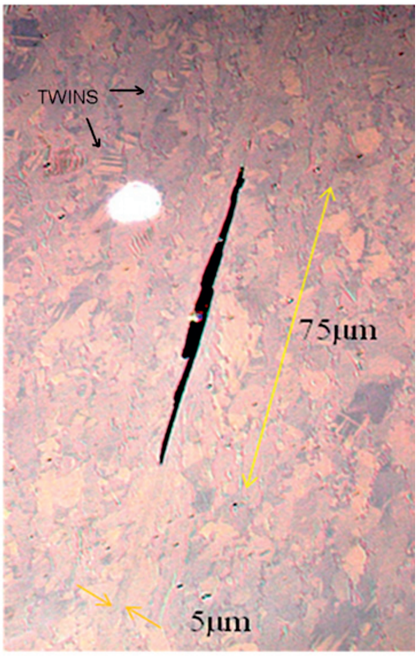

Figure 2.33: Several micro-cracks are linked; the resulting crack surface looks fragmented. Twins are observed in the vicinity of the shear band [67].

2.7.4 Recrystallisation and Micro-void Coalescence

Work by Me-Bar [71] made the suggestion that some recrystallisation of the β phase occurs. They observed a refined β structure, in the order of a magnitude smaller than in the bulk, within the shear band. The cause for this is adiabatic heating, resulting in temperatures exceeding the β transition ($\sim$990^{o}C). However, it is believed that this is inaccurate; if the temperature was sufficient to cause β recrystallisation then it was sufficiently high for α to recrystallise also. The images used to draw such conclusions show no such α recrystallisation, leading to the idea that the refined β is a result of heavy cold work and the breakup of β into the observed, refined, structure. This corroborates more recent work by Liao [74] showing that the peak temperature in Ti-6Al-4V ballistic deformation is $<$550^{o}C. However, there are examples of genuine α recrystallisation within shear bands in other works [69, 80].

2.7.5 Twin Softening

Another theory which has been formed, unlike the previous theories, is largely dependent upon twinning to allow what is alternatively termed "unstable shear" to occur. It states that the region that will become the shear band undergoes intense twinning, Figure 2.35a; this reorientation of material within the twins has an increased Schmid factor for $\langle a \rangle$ slip than the parent material. This increases the amount of slip that occurs within the twins,

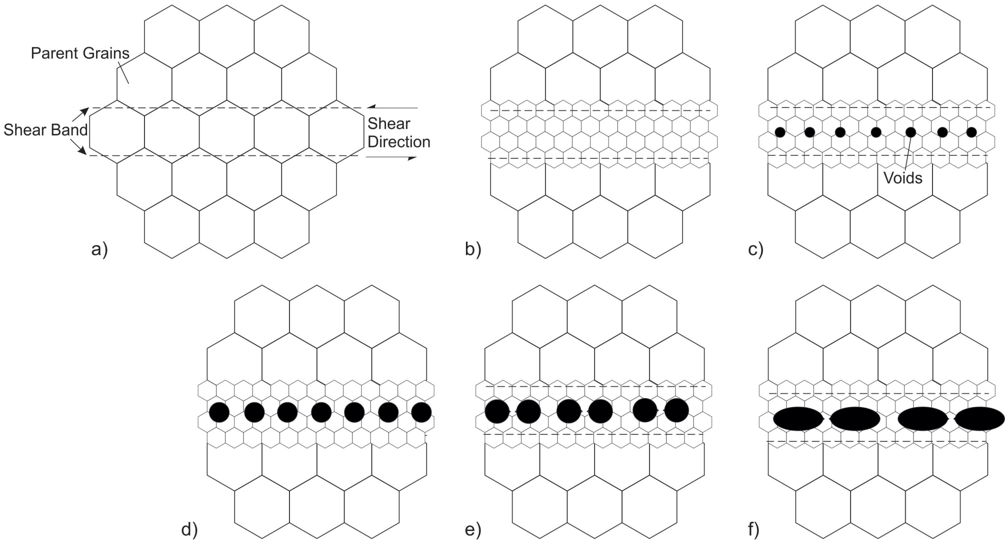

Figure 2.34: a) Intense shear localised stress in shear band b) Shear causes sufficient stressing to cause dynamic recrystallisation c) Small voids form due to intense shear d) Voids grow with increased strain and adiabatic heating e) Ligaments between voids begin 'neck' f) Voids coalesce and necking continues to form a continuous crack.

increasing susceptibility to void nucleation. It has also been demonstrated that twin boundaries are areas where dislocation pile up occurs; this could also be a source of void nuclei [26]. This theory, while plausible, seems improbable as many other sources [67,71] have shown that the region surrounding shear bands is generally twin free whereas the bulk, away from the shear band, contains twins. This leads to the suggestion that the shear band is also twin free.

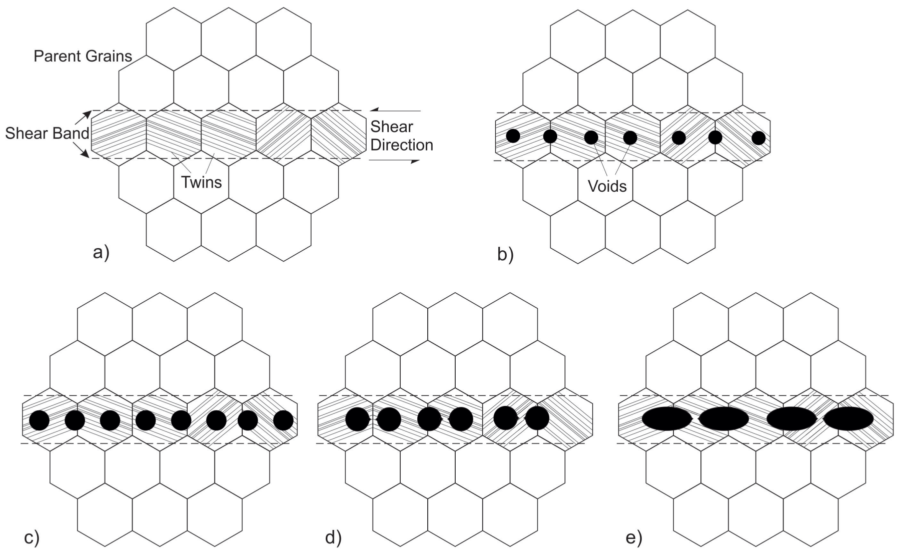

Figure 2.35: a) Shear stress causes twinning b) Continued shear causes rotation and 'alignment' of twins within the shear band c) Material inside twins now more susceptible to slip, concentrating strain localisation further d) Voids form with increased strain and adiabatic heating e) Ligaments between voids begin 'neck' f) Voids coalesce and necking continues to form a continuous crack.

2.8 Machining

Work on machining has focused on two areas, one focusing on the perceived less complex turning, as opposed to milling [6,39,81–84]. This is due to the perception that milling is a more complex three dimensional operation, whereas turning can be considered almost two dimensional [85], although work in recent years has begun to incorporate the perceived more complex milling process [7,86]. The second area is the focus on increasing the 'mechanical machinability', i.e. increased cut speed, tool, etc. [6,82,84,87–92], with some examining the induced stress in the subsurface region and hardness [87,93–96]. However, only a handful of work has been performed on the, ultimately more important, 'material machinability' such as microstructural modification and introduction of deformation system, etc. [7,39,93,94].

The earliest work focused in the first area, on understanding the physics of metal cutting [85,97]. Merchant developed a force diagram, Figure 2.36, showing the relationship between the forces generated during continuous chip generation. The generation and subsequent validation in this work mean that, as expected, the mechanics of machining have a strong physical base and a location for future developments of any machining processes to progress from.

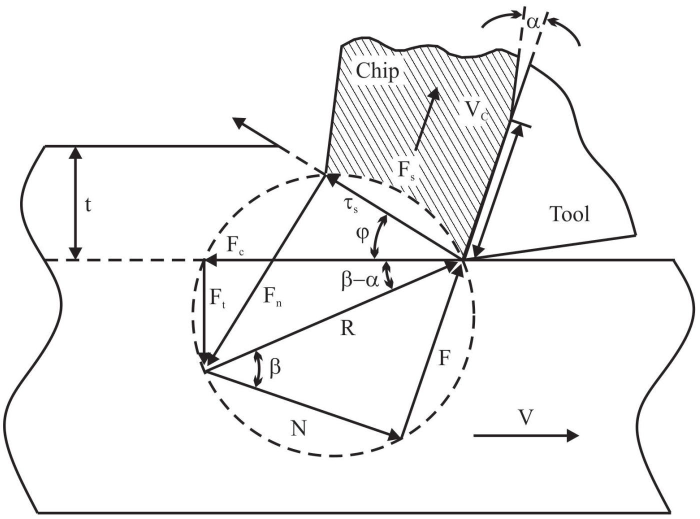

Figure 2.36: Force diagram showing relationship between component forces in orthogonal cutting environment. Adapted from Merchant [85].

Merchant took the two dimensional approach one step further in determining the force diagram for turning in three dimensions also, highlighting the added complexity introduced by the oblique angle the cutting tool is held at relative to the cutting direction [85]. This complexity possibly implies the reason for a similar diagram not being available for milling, the added complexity of a helically moving tool, and the cause for, theoretically, turning being a less complex system to understand.

The work that has focused on subsurface damage incorporates several areas. There are three commonly depicted regions [87, 93, 94, 98] illustrated in Figure 2.37, known in this work as severe plastically deformed region (SPD), sub-surface deformed region and undeformed bulk. However due to the techniques employed, mainly light and BSE microscopy, a fourth region can be observed using EBSD, illustrated in Figure 2.38, where the material has experienced lattice rotation or slip band formation. Each region will now be discussed in further detail.

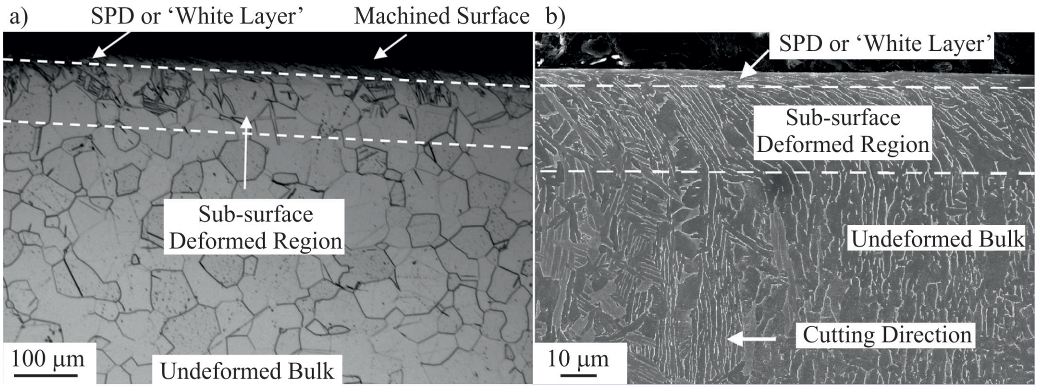

Figure 2.37: BSE images of three observable regions of subsurface damage in a) CP titanium $V_c = 0.6$ m.min^{-1} [93], and b) Ti-6Al-4V, $V_c = 260$ m.min^{-1} [94].

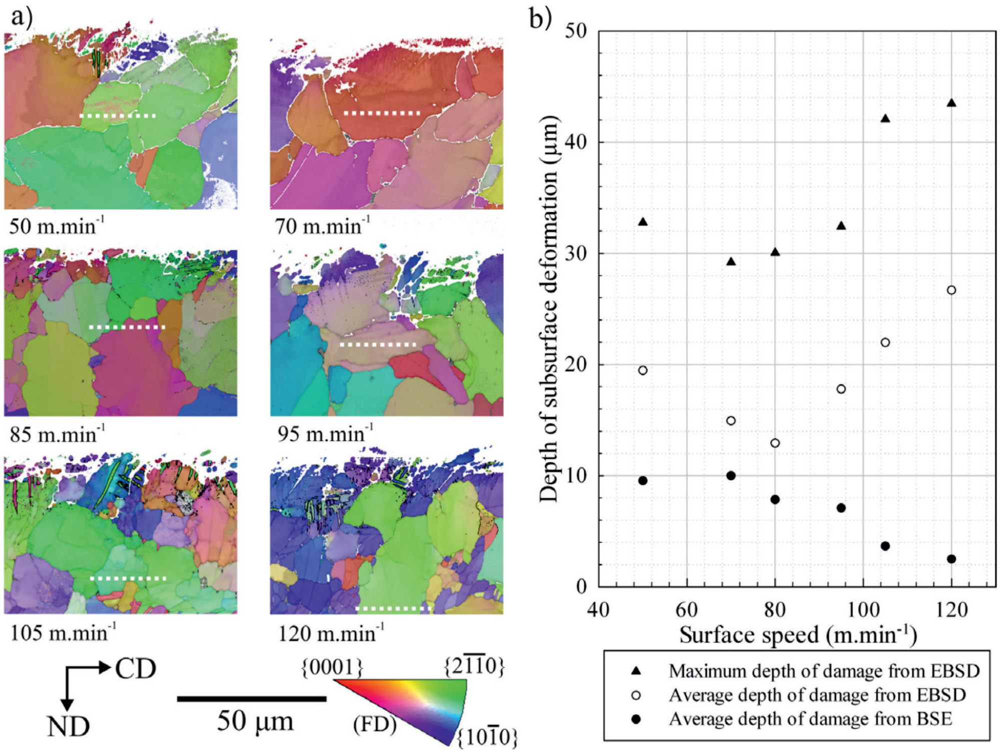

Figure 2.38: a) EBSD inverse pole figure (IPF) maps of the machined surface with increasing surface speed. The white delineated line signifies the interface between the undeformed bulk material and the maximum depth of damage. b) Graph illustrating the effect of surface speed on the depth of surface deformation assessed by measuring beta distortion using backscatter electron (BSE) images and EBSD [39].

The SPD region is a region in which under light, BSE and EBSD microscopy no microstructural features can be discerned. Described by Shankar as ‘featureless’ [93], what is meant is that the region has undergone such high levels of strain that the microstructure has been refined to ultrafine grained (UFG) material, beyond the level of resolution of techniques used. The cause for this region being so heavily strained and therefore deformed is thought to result from this being a small component of the shear band, formed during cutting, that is observed in chip, illustrated by Figure 2.39. This means that as examination of sub-surface deformation from machining operations has only limited coverage, much can be learned from shear band formation and examination, which is more substantially examined in Sections 2.6 and 2.7 [26, 67–74, 78–80]. The presence of the SPD region varies with a large number of parameters including, but not limited to, plastic deformation, chemical reactions, high temperature gradients, rapid heating/cooling, thermal softening, cutting speed, feed rate, tool and work piece [99].

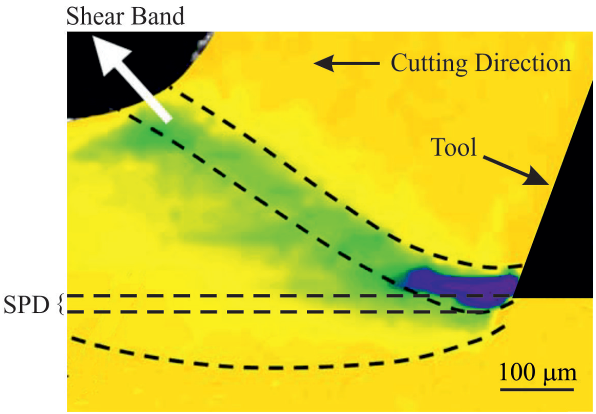

Figure 2.39: Shear strain rate field obtained using PIV (particle image velocity) demonstrating chip shear band extending into cut surface of CP titanium cut at 0.6 m.min^{-1}. Adapted from Shankar [93].

The subsurface deformation region is the most well explored of the three deformation regions. Substantial amounts are already known about mechanical twinning, discussed in Section 2.2.2. The formation of twinning occurs at relatively low strain values both in tension and compression, and during the cutting processes twinning occurs in front of the cutting processes, illustrated in Figure 2.40. As can be observed, the region in front of the tool, where twins are being formed, has a fan shape, Figure 2.40a). This fan shape matches that generated by PIV (particle image velocity) data of the same cut, shown in Figure 2.40b). While the PIV data does not inform us about the level of strain experienced, the presence of a strain rate naturally implies the presence of some level of strain, below a value of approximately 0.6 as determined by Shankar [93]. The subsurface deformation region does not only contain twins; in many $\alpha + \beta$ alloys little or no twinning is observed at all. Thomas [7] observed intense slip bands, Figure 2.41a), or more commonly in the case of others [39, 87, 93, 94, 100, 101], grain ‘sweeping’, Figure

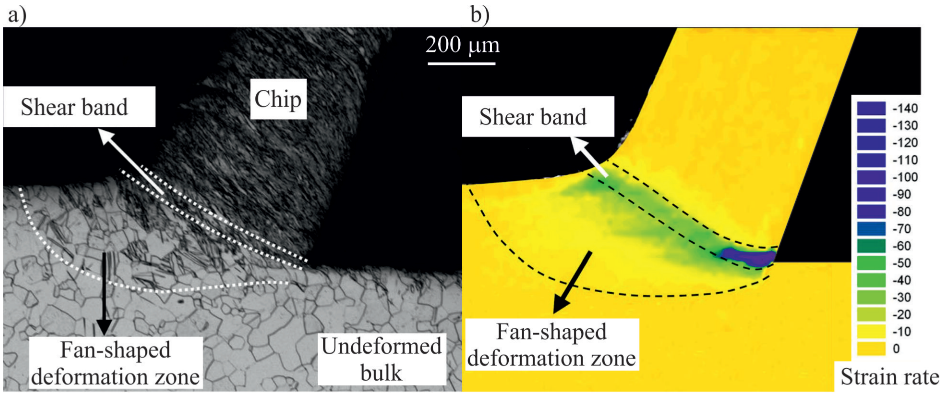

Figure 2.40: Shear strain rate field obtained using PIV demonstrating chip shear band extending into cut surface, indicating likely SPD depth of CP titanium cut at 0.6 m.min^{-1} [93].

2.41b) - f). The depth of this region has been quantified as a function of many parameters, such as cutting speed, tool condition, lubrication condition and material to name a few; however, a clear understanding is currently not possible as there is no consistency across these works in constant parameters. This means while some compare their work to others, variation in parameters such as type of lubricate, feed and tool geometry, material and coatings means some results show, for example, an increase in subsurface deformation depth as a function of machining speed; another shows a decrease, and a third shows no conclusive influence, demonstrated by Figure 2.42.

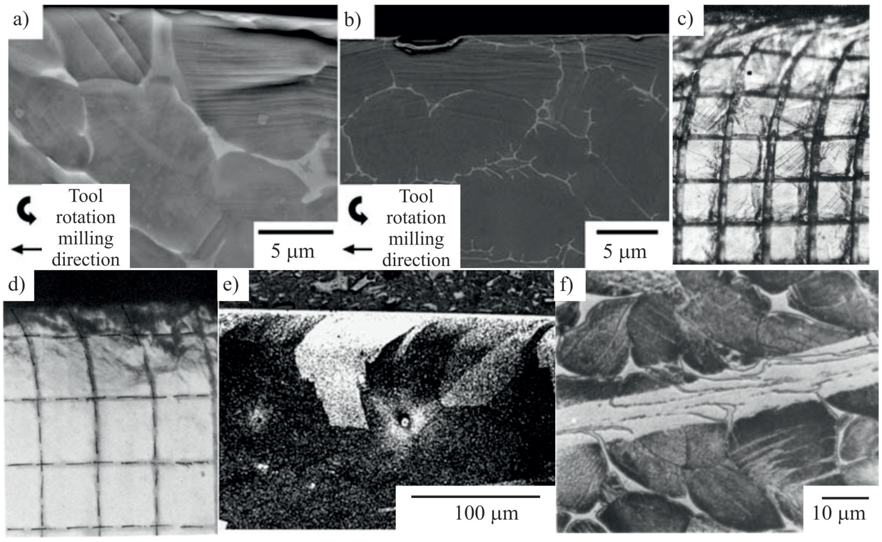

Figure 2.41: BSE micrographs showing intense slip bands below the milled surface in a) Ti-6Al-4V [7], b) Ti-834 [7] and grain 'sweeping' in c) Copper [102], d) Ti-6Al-2Sn-4Zr-2Mo [101], e) Inconel-718 [95] and f) 'swept' grains inside an adiabatic shear band of Ti-6Al-4V [103].

The final region of the microstructural damage is the lattice rotation, towards the edge of the strain field, highlighted in Figure 2.41c). There is very little available work which applies EBSD analysis to subsurface damage of high speed machining. However the work performed shows clearly that increasing machining speed increases the depth to which this region occurs, even in contradiction to the damage generated in sub-surface deformed region [39], which is observable in backscatter electron imaging. Full analysis of all of the observed regions described here will not be comprehensively analysed during this work as this is not a focus of the work; however, appreciation of what is to be observed is key to understanding any trends and causes from both quantitative and qualitative perspectives.

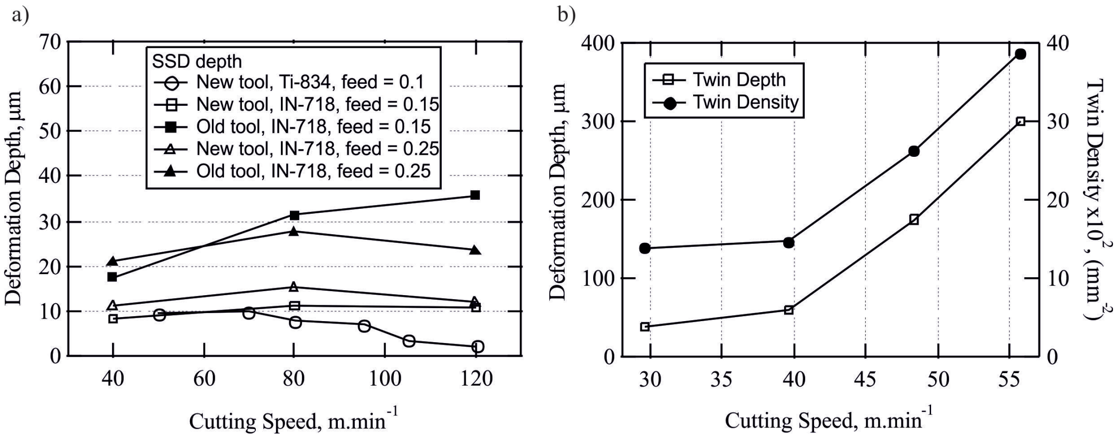

Figure 2.42: a) Plot showing that subsurface deformation depth depth can increase, decrease or remain constant as a function of cutting speed, Ti-834 data [39] and Inconel-718 data [95] b) Plot of subsurface deformation twin depth and density in dry machining of CP titanium [104].

The orthogonal cutting test to be developed in this work is based upon an approach developed by Sutter [105]. Figure 2.43 shows an orthogonal cut experiment utilising the SHPB (Split Hopkins Pressure Bar) test to produce cutting speeds of between 1020 - 3600 m.min^{-1}. This test has modified the conventional SHPB test by replacing the striker bar from a conventional SHPB setup. Also by attaching the specimen to the front of the projectile it is possible to adjust the specimen geometry and as a result the depth of cut is also adjusted.

The “openness” of the manufacturing area, i.e. the position in which the cutting occurs, allows positioning of a camera close to the cut, making *in-situ* imaging possible. The disadvantage of modifying the SHPB in this manner is that the load measuring capability of the test is removed. The method proposed in this work would use an hydraulic actuator to propel the specimen. This means that load and displacement information can be obtained during testing as both are measured from the actuator. This means while comparable speeds cannot be obtained, sufficient accessibility for imaging equipment and greater control over deformation rate are possible.

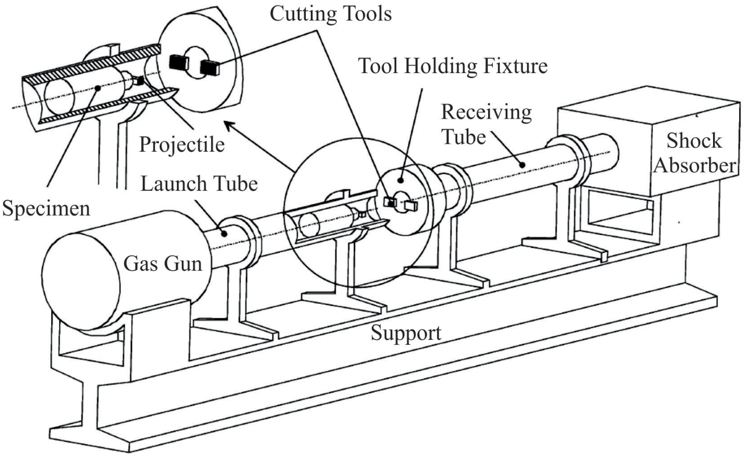

Figure 2.43: Schematic of modified Split Hopkins Pressure Bar test, as used by Sutter [105].

2.9 Literature Review Summary

This chapter has highlighted the areas of research that have to date been explored. No work currently exists that has attempted to combine fundamental knowledge of titanium behaviour with the mechanical approach traditionally applied to researching machining processes. As machining is a deformation process the potential to determine the machinability from more conventional testing methods and property characterisation techniques exists. Application of work hardening behaviour analysis is a relatively new approach for CPH structures and could be used to help predict potential levels of subsurface deformation. To date very little work has been performed on the influence of material characteristics, i.e. composition, microstructure and texture, on subsurface deformation induced during machining processes, with almost all of the limited work examining the influence of machining parameters on tool life and forces rather than the, ultimately, more important in service material condition. Development of a testing method that uses similar principles applied by Sutter [105] would allow generation of pseudo flow curves, meaning mechanical properties, such as yield strength, and machining properties could be obtained from the same test, which ultimately would require significantly less than the 240 kg currently required for conventional machining trials.

3. EXPERIMENTAL METHODS

This chapter aims to outline all the processing, testing and analysis techniques used during this project.

3.1 Alloy Production

Four titanium - aluminium binary alloys containing 2, 4, 6 and 8 wt.% Al were produced at TIMET UK Ltd. Binary alloy ingots were generated from super pure α-titanium powder (1-12 mm) sponge from Osaka Titanium Technologies and high purity aluminium shot used by TIMET UK Ltd. Two separate 200 g square bars of each binary alloy were processed, denoted as lots *I* and *II*, using a vacuum arc double melt process in a water cooled copper crucible; Tables 3.1 and 3.2 display chemical information. Ingots were forged, at 900^{o}C, into a bar from a coffin shape, Figure 3.1b) to 3.1c), and then hot rolled at 900^{o}C, from approximately 26 mm^2 down to 13 mm^2 with a reheat stage halfway through. Stages of the process route are summarised in Figure 3.1.

Each bar *I* alloy was heat treated 40^{o}C below its $\alpha \rightarrow \alpha + \beta$ transus for five hours. Temperature adjustments for bar *II* were made with a view to achieving a more consistent average grain size than in bar *I*. Heat treatment temperatures, transus temperatures and grain sizes are listed in Tables 3.1 and 3.2. A commercially pure α-titanium (grade 2), obtained from bar stock provided by TIMET UK Ltd.was also used as part of this study.

TABLE 3.1: ALLOY COMPOSITION, MICROSTRUCTURE AND HEAT TREATMENT DATA FOR BAR *I* BINARY ALLOYS.

Alloy	Ti-2Al *I*	Ti-4Al *I*	Ti-6Al *I*	Ti-8Al *I*	Ti - CP
Aluminium, %wt.	2.00	3.956	5.95	7.94	0.00
Oxygen, %wt.	0.1328	0.0579	0.1034	0.0660	0.1416
Nitrogen, ppm	34	17	36	23	33
$\alpha \rightarrow \alpha + \beta$ Transus, ^{o}C	920	955	990	1025	882
Annealing Temp., ^{o}C	880	915	950	985	n/a
Avg. Grain Size and Standard Error, μm	114 ± 19	90 ± 22	80 ± 9.5	75 ± 5.6	45

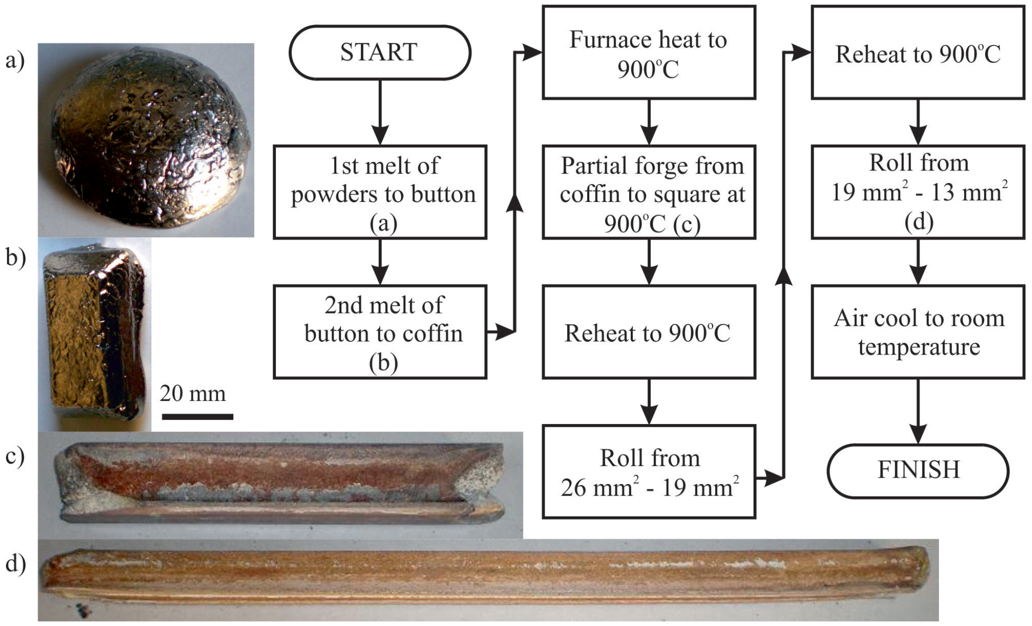

Figure 3.1: Photos of the binary product at various stages; a) button after first melt, b) coffin after second melt, c) bar after forge at 900^{o}C and d) bar after rolling at 900^{o}C completed.

3.2 Materials Characterisation

The examined materials were subjected to a series of characterisation techniques. These techniques and the associated preparations are described.

3.2.1 X-Ray Energy Dispersive Spectroscopy

The technique used for analyzing the aluminium content in the binary alloys was x-ray energy dispersive spectroscopy (X-EDS) on a JOEL JSM6400 scanning electron microscope. Precision was determined over an area of at least 0.75 mm^2, an area equivalent to approximately 55 grains, broken into three area scans and distributed through half the cross section of the binary bar. These values were subsequently confirmed and interstitial elements analysed by ICP mass spectrometry, at TIMET Ltd., Savioue. The starting microstructure was examined using polarised light microscopy, as illustrated in Figure 3.2, where grain size was determined using the linear intercept method, see Tables 3.1 and 3.2. The microstructure was also examined for the presence of β phase using SEM backscatter electron (BSE) detection. The β phase would appear bright under BSE detector due to aluminium deprived nature of β phase compared to α phase; however, no β phase was visible up to magnifications of x20k. This was expected as rolling was performed in the single α phase at a temperature below the $\alpha \rightarrow \alpha + \beta$ phase field.

TABLE 3.2: ALLOY COMPOSITION, MICROSTRUCTURE AND HEAT TREATMENT DATA FOR BAR *II* BINARY ALLOYS.

Alloy	Ti-2Al *II*	Ti-4Al *II*	Ti-6Al *II*	Ti-8Al *II*
Aluminium, %wt.	1.89	3.90	5.84	7.83
Oxygen, % .	0.0768	0.0651	0.0590	0.0526
Nitrogen, ppm	7	20	12	6
$\alpha \rightarrow \alpha + \beta$ Transus, ^{o}C	920	955	990	1025
Heat Treatment Temp., ^{o}C	895	933	968	992
Avg. Grain Size and Standard Error, μm	101 ± 6	91 ± 5	93 ± 3	77 ± 3

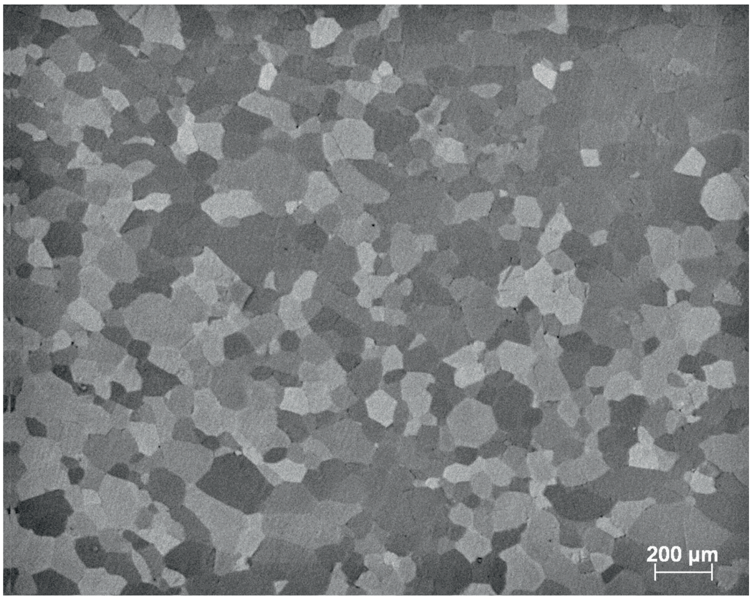

Figure 3.2: Light micrograph of Ti - 2 wt.% Al *I* microstructure after heat treatment.

3.2.2 Electron Backscatter Detection Mapping

Electron backscatter detection (EBSD) mapping was used to examine more closely the subsurface damage generated during milling. The machine used was FEI Sirion electron microscope, used at 20 kV and 10 nA probe current throughout, and a step size of 0.1 μm was used. Automatic indexing and diffraction data post-processing was performed using Oxford Instruments HKL Channel 5 software [106]. The reason for such a small step size for a microstructure with substantially larger grains of approximately 100 μm was to determine which of the subgrain deformation features could be identified, i.e. slip or twin deformation mechanisms had occurred. If the step size had been greater than 0.1 μm the resolution of the map might have been insufficient to enable slip traces and fine scale mechanical twins to be observed. Schmid factor maps were generated using the Channel 5 software [106], using the orientation of the parent twin and the slip plane and direction, for slip, or the K_1 plane and η_1 direction, for twinning, the resolved stress acting on a system is calculated by Equation 3.1 [107]. Where τ_R is the resolved shear stress, P is load, A is the area upon which the load acts and ϕ and λ are the angles the slip plane and slip direction are with the loading axis.

$$\tau_R = \frac{P}{A} \cos\phi \cos\lambda \tag{3.1}$$

3.3 High Speed Machining

3.3.1 Mechanical Preparation

Mechanical preparation was performed on milled specimens, including an Abramin automatic polishing machine beginning at 1200 grit size paper, for three minutes, then polishing on a MD-Largo using 9 μm water based diamond solution. The final stage used an MD-Chem with 0.025 μm silica suspension mixed with 10% H_2O_2 and water alternately for four, two, four and ten minutes. The two minute water stage was to prevent chemical etching of the surface occurring and the ten minute water stage ensured the surface had no residual silica as this obstructs high resolution electron microscopy imaging.

3.4 High Speed Milling

Each alloy was subjected to a series of slot milling operations. The process of reaching the finishing pass was achieved by first milling slots of 6 mm wide and 8 mm deep in four incremental steps of 2 mm up to the final depth, theses steps were carried out at the roughing speed of 25 m.min^{-1}. Each slot was then subjected to a finishing pass on both walls of the slot, down the full depth of the slot with a 1 mm depth of cut (DOC), Figure 3.3, resulting in a total slot width of 8 mm. Each slot contains one wall of climb type milling and the other of conventional type milling, as depicted in Figure 3.4. A list of the milling speeds and associated machine parameters is given in Table 3.3. The reason 188 m.min^{-1} was used as the maximum cutting speed is that the maximum tool speed of the machine is 10,000 RPM, in accordance with Equations 3.2 and 3.3. Where V_c is cutting speed, m.min^{-1}, D_T is tool diameter, mm, and Fpt is feed per tooth, mm. V_c is given in m.min^{-1} to comply with machining convention and accommodate the rotational frequency standard measure, ν in RPM. All milling operations used a coolant and due to subsequent chip fracture mechanics the chip was not retrieved after milling. The viewing direction for milled specimens is down the axis of tool rotation, Figure 3.3; specimens were sectioned in reference to this viewing direction, Figure 3.4.

$$\nu = \frac{V_c \times 1000}{D_T \times \pi} \tag{3.2}$$

$$Feed = \nu \times Fpt \times T_c \tag{3.3}$$

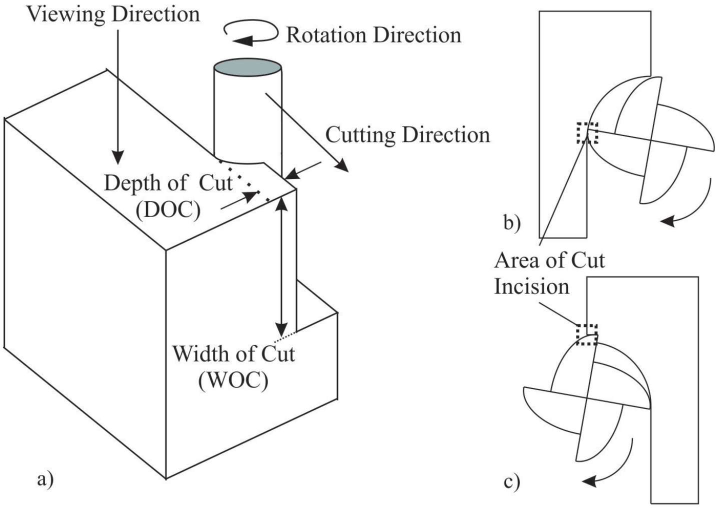

Figure 3.3: Schematic depicting a) milling, b) conventional type milling and c) climb type milling.

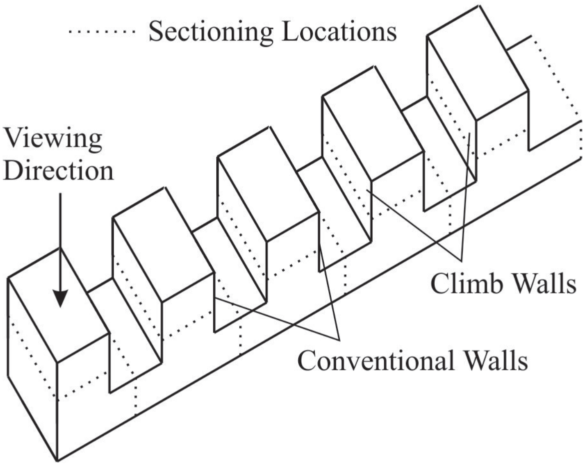

Figure 3.4: Schematic showing the location of sample section cuts on the milled bar.

3.4.1 *Measurement of Deformed Severe Plastic Deformation Depth*

The severe plastic deformation (SPD) region, sometimes referred to as the 'white layer' in industry, is a region immediately below the new cut surface in which deformation is so severe that it is not possible to distinguish any microstructural features under SEM. An example of this region is depicted in Figure 3.5. Under BSE imaging the SPD region has a higher luminescence, and appears brighter, than the undeformed parent grain. The

TABLE 3.3: PARAMETERS USED IN MILLING TRIALS.

$V_c, m.min^{-1}$	25	100	125	150	188
Tool Speed, RPM	1326	5305	6631	7958	9974
Feed Rate, m.min^{-1}	159	636	796	955	1197

SPD region depth was determined from the BSE micrographs first, converting the image to 32-bit colour type and introducing a colour threshold whereby brightness and hue limits were introduced to create a definitive boundary between the SPD region and the parent microstructure, illustrated in Figure 3.6.

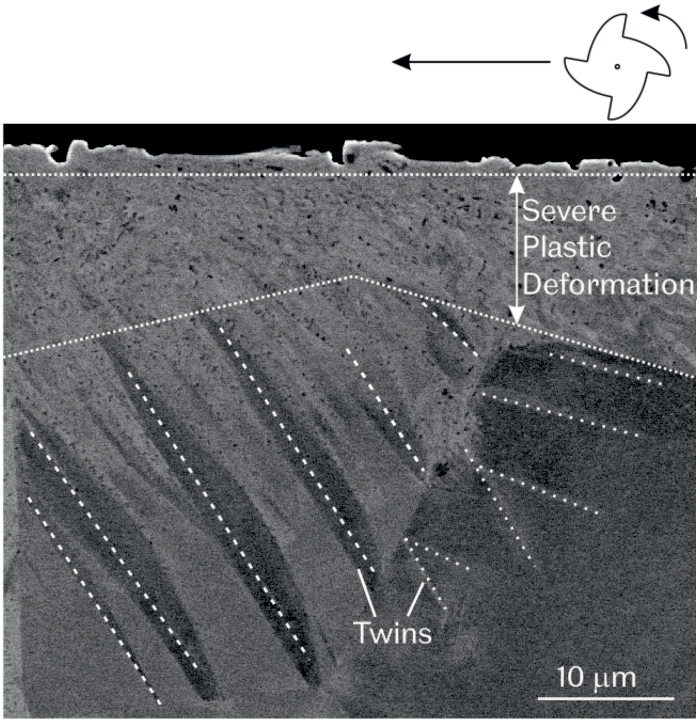

Figure 3.5: Backscatter electron micrograph with markers indicating the severe plastic deformation region. Material is Ti-4Al climb milled at 125 m.min^{-1}.

3.4.2 Measurement of Twin Penetration Depth

Twin depth measurements were calculated by using cross polarized light micrographs and using a grid method for calculating twin volume fraction as described by Ghaderi [108]. An alternate method described by Ghaderi [108] was available also but a further development of the twin geometry function, or the inclusion of a further function relating to twin orientation, would have been required. The reason for this is that due to the unidirectionality of the twins, i.e. the long axis of the twins running parallel to each other,

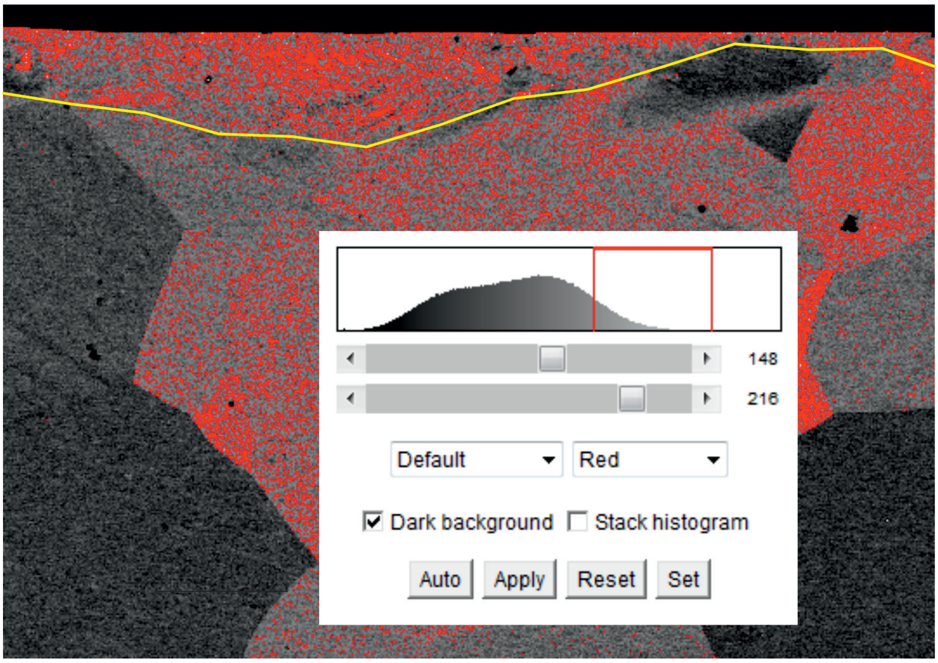

148

216

Default

Red

☑ Dark background ☐ Stack histogram

Figure 3.6: Backscatter electron micrograph with threshold filter highlighting SPD / parent material boundary. Material is Ti-8Al climb milled at 125 m.min^{-1}.

resulted in twin volume fractions greater than one. This was seen as an unnecessary process as the grid method did not falter due to this issue and was therefore superior for the conditions observed in milled material.

3.4.3 Measurement of Twin Volume Fraction

As the twin penetration depths, described in Section 3.4.2, only indicate the depth of penetration and no indication of the twins frequency it was necessary to consider a second method for quantifying twin occurence. Two methods were considered, a grid and a line method, both described by Ghaderi [108]. A comparison of the two methods was performed and the line method was deemed inappropriate because unrealistic values, $V_f < 1$, were calculated, similar to twin penetration depth. This is due to the unidirectional nature of the observed twins, i.e. perpendicular to the milled surface and the lines required to perform the technique. The grid method, due to counting in an area, is not susceptible to the same failings of the unidirectional line method. The full methods are described comprehensively by Ghaderi [108].

3.5 Axisymmetric Compression Testing

3.6 Axisymmetric Compression

In order to understand the complex three dimensional load state experienced during high speed milling, axisymmetric compression testing was performed on each alloy. A compression of a cylinder can be considered two dimensional; this allows simple examination of occurring mechanisms and permits extrapolation of observed deformation events/microstructure evolution compared to the more complex milling system.

The axisymmetric compression testing was performed on a thermomechanical compression machine (TMC), Figure 3.7. It consists of an upper and lower M22 steel tool post. The lower tool post remains stationary and the upper is ram driven; both are usually contained within a test furnace. For the testing performed at room temperature, the furnace was removed to allow access to the tools and allow retrieval of all specimens. The specimens were loaded into the robot arms and held between the tools. Upon compression occurring the spring loaded robot arms remain gripped the sample and moved with the deformation of the specimen; once compression was complete the sample was withdrawn. The machine has working parameters of up to 500 kN and tool velocity of $0.01 - 2.9 \times 10^2$ mm.s^1. The ram also possesses a ± 0.1 mm accuracy for stopping points at low speeds, which increases slightly with higher speeds.

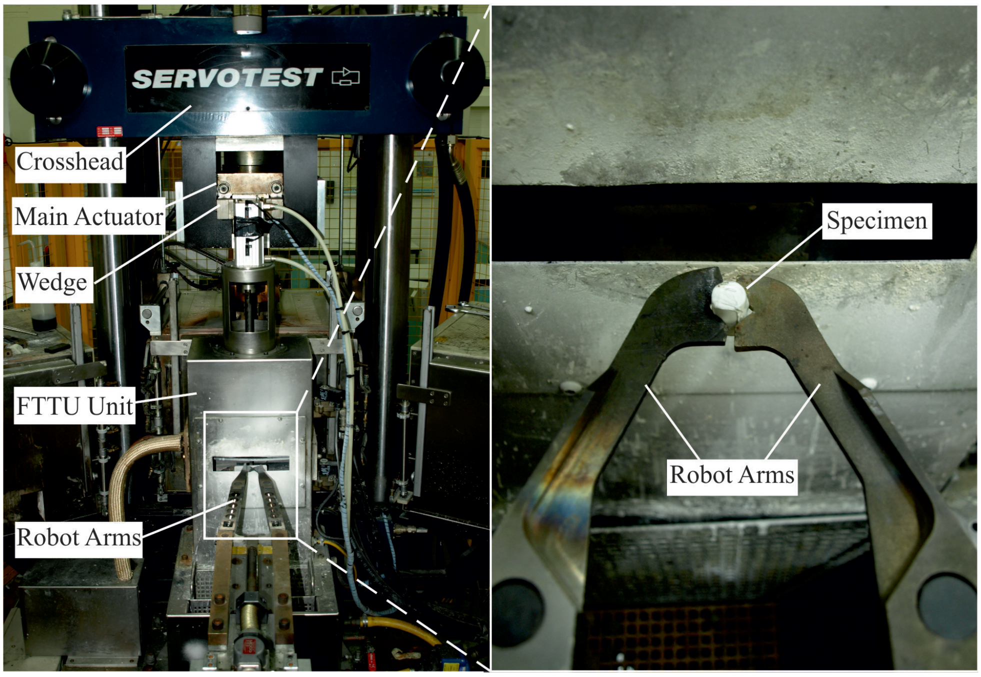

Figure 3.7: Image showing a) the TMC used during testing with parts labeled and b) the robot arms holding a specimen prior to testing.

Specimens have a cylindrical geometry, 10 mm diameter by 15 mm height, both with a tolerance of ±0.1 mm. Figure 3.8 shows the orientation of the compression specimens relative to the rolled bar. Specimens from binaries *I* were tested at strain rates of 0.01 s^{-1} to 100 s^{-1}. Specimens from binaries *II* were only tested at 0.1 s^{-1} to confirm comparative behaviour between binaries *I* and *II*. Each specimen was wrapped in PTFE (polytetrafluoroethylene) tape to prevent sticking of specimens to the tools. PTFE is not the most effective lubricant, but as discussed in Section 2.7, one of the requirements for shear bands to form is via inhomogeneous strain, therefore a reduction of friction just below the sticking point is all that is required. Thermocouples were not used during testing as the hole in the specimen induces premature shear band formation.

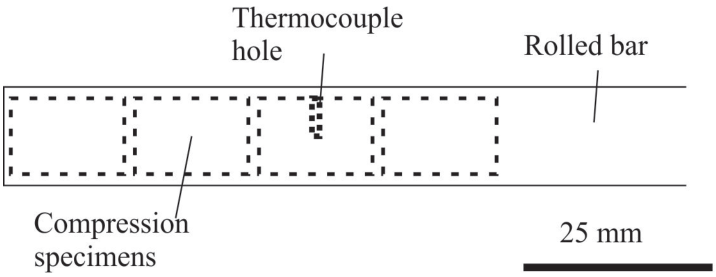

Figure 3.8: Schematic depicting compression specimens orientation with regards to the binary bar.

3.6.1 Electropolish Preparation

Due to the varying levels of work hardening experienced throughout the compression specimens, subsequent mechanical polishing would have been undesirable, therefore electropolishing, illustrated in Figure 3.9, was applied. A stainless steel vessel was placed inside a bath of liquid nitrogen with methanol, to prevent the liquid nitrogen freezing. The steel vessel contained the polishing solution (1 part perchloric acid, 10 parts methanol and 12 parts butan-1-ol) and specimens were cooled to -40 °C. Specimens were held using stainless steel tweezers and lacomit varnish was used as a stop-off. The polishing solution was continually stirred using a magnetic stirrer and a voltage of 6 V was applied.

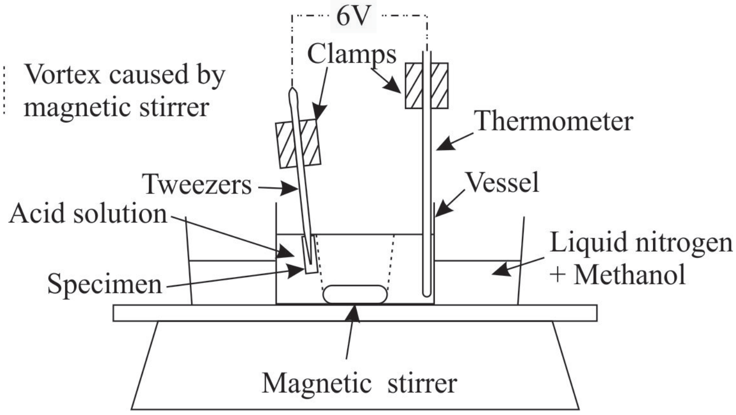

Figure 3.9: Schematic depicting equipment set up used for electropolishing.

3.6.2 Axisymmetric Specimen Sectioning

Specimens from axisymmetric compression testing were sectioned down the plane of compression, Figures 3.10a) and 3.10c). As shown in Figure 3.10b) this is the plane in which shear bands would form, allowing observation of them. Figure 3.10a) shows how barrelled specimens were sectioned, in any plane down the c-axis, and Figure 3.10c) how the sheared specimens were section perpendicular to the shear failure, allowing observation along the failure and at the tips of the crack to obtain propagation and nucleation mechanism information.

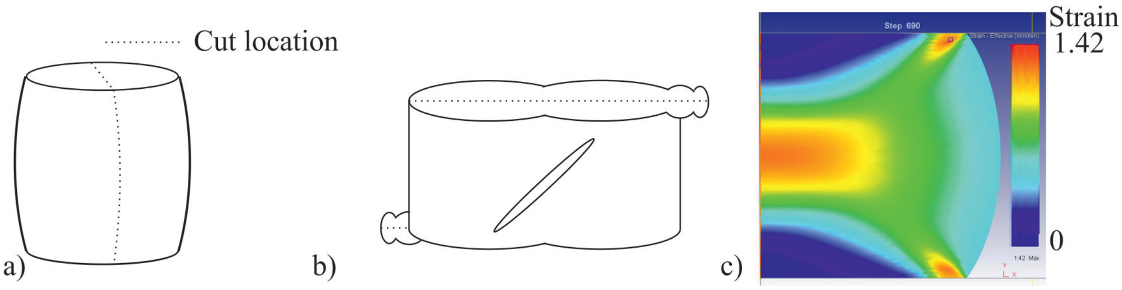

Figure 3.10: a) Schematic showing sectioning cuts on barreled axisymmetric compression specimens b) schematic showing sectioning cuts on sheared axisymmetric compression specimens and c) FEM of half a barreled axisymmetric compression test showing area where adiabatic heating occurs.

3.6.3 Flow Curves

To determine the materials' flow curve the data collected from each test included load, displacement and time. These are manipulated using Equations 3.4-3.6 to obtain strain rate vs time plots, to check the actual strain rate during testing, and stress-strain graphs (flow curves). The full process is described by Roebuck [109] and this was followed throughout data analysis.

$$\epsilon = \log H/H_o \tag{3.4}$$

$$\sigma = F/A \tag{3.5}$$

$$\dot{\epsilon} = \Delta d/t \tag{3.6}$$

$$V = h_i\pi(2({R_1}^2) + {R_2}^2) \tag{3.7}$$

Yield stress and yield strain were subsequently determined at 0.2% stress. First the gradient of the elastic region was obtained, using a line of best fit through the straightest section of the elastic region, Figure 3.11a). A line of this gradient is offset by 0.2% strain and the point of intersection with the flow curve is the yield stress, Figure 3.11b). The yield strain is the strain value at which this intersection takes place.

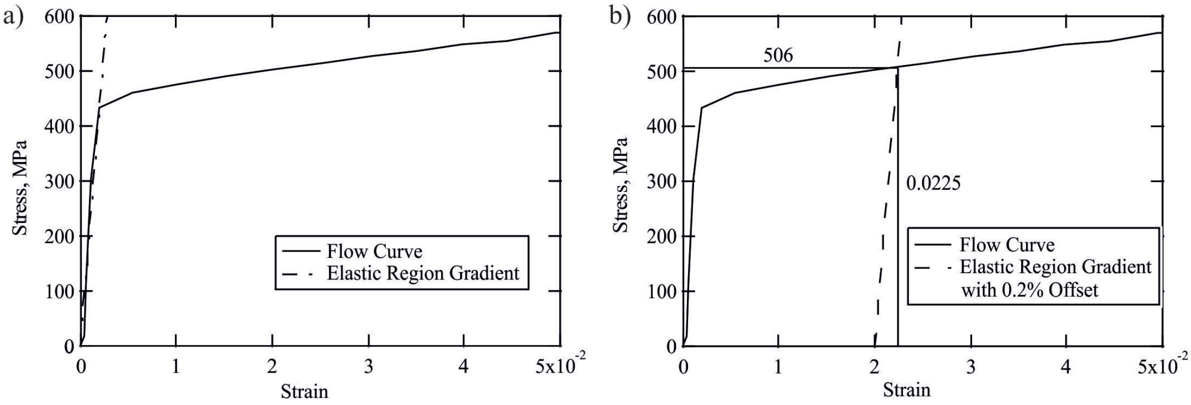

Figure 3.11: Example flow curves showing a) determination of the elastic gradient, and b) the inclusion of the 0.2% offset and yield stress and strain.

TABLE 3.4: CALCULATED SHEAR MODULI FOR BINARY ALLOYS.

	Ti-2Al	Ti-4Al	Ti-6Al	Ti-8Al
Calculated Shear Modulus, GPa	40.8	40.3	39.8	39.3

3.6.4 Work Hardening

Once conventionally analysed as described in Section 3.6.3 further analysis of work hardening behaviour followed. The equation for calculating work hardening, Θ, is shown in Equation 3.8. The inclusion of the shear modulus, a common method for normalisation of non-similar materials, is not necessary as according to Equation 3.9 the calculated variation in G values is less than 4%, Table 3.4. Where G_i is shear modulus and C_i is concentration.

$$\Theta = \frac{\delta\sigma}{\delta\epsilon} \tag{3.8}$$

$$G_{alloy} = sum\{G_i C_i\} \tag{3.9}$$

3.6.5 Axisymmetric Shear Stress

There are three different equations available for calculating shear stress: Von Mises, Tresca and Octahedral, and all of these are Equations 3.10, 3.11 and 3.12 respectively [110]. Each of these were applied to flow stress values to generate alternate curves of shear flow stress.

$$k_{VM} = \frac{1}{\sqrt{3}}\sigma_0 \tag{3.10}$$

$$k_T = \frac{\sigma_0}{2} \tag{3.11}$$

$$k_O = \frac{\sqrt{2}}{3}\sigma_0 \tag{3.12}$$

3.6.6 Work Done During Compression Testing

Calculating the work done during compression is achieved using the Equation 3.13; this determines the area under the flow curve. Integration calculation were performed in Igor Pro [111] and used a trapezoidal algorithm to determine the values. This equation also represents the Cockcroft-Latham damage criterion, discussed in more detail in Section 3.10.3.

$$W = \int_0^{\epsilon_f} \sigma \mathrm{d}\epsilon \tag{3.13}$$

This data was subsequently manipulated to determine 1) Strain to failure and 2) Work done to failure, where failure is determined as $\Theta = 0$, which occurs at the point of maximum stress, as methods to identify first approximations of a given material's 'machinability'.

3.7 Orthogonal Cutting

This section looks at the machine used during the orthogonal cutting tests. The cutting rig attachment design is discussed in Section 3.9.

3.7.1 Utilisation of the Abitrary Strain Path Machine

The process of rig design is covered in Section 3.9; the equipment the rig is fitted to is described here. The machine used is a Servotest arbitrary strain path (ASP) machine and is designed to perform tests using tension, compression, torsion or any combination thereof. It consists of a fixed lower tool post and a ram driven upper, with both vertical and torsional capabilities. Using the compression capabilities of this machine, which allows ±30 mm tool displacement up to 100 $\mathrm{mm.s^{-1}}$ and has a load capacity of up to 100 kN, linear displacement was measured using a linear variable differential transformer (LVDT) positioned above the upper tool crosshead. The lower tool is fitted to the load cell, which in turn is attached to the machine frame.

The specimen geometry used for the tests is shown in Figure 3.12, allowing orthogonal cutting to occur on both sides of the specimen. Further discussion of specimen geometry can be found in Section 3.9. The data obtained from this test method were time, load, and displacement. During testing torque and angular displacement were not recorded; however, they were monitored to ensure that no lateral loads were experienced, causing failure of equipment and tests.

3.8 Tool Selection

The tool selected for initial testing was a Sandvik Coromat tool with product code 'SNMA 15 06 16-KR 3215'. This tool is a simple square tool with a 15 mm inscribed inner diameter, meaning that a consistent cut can occur along the entire test specimen. The tool has a rake angle and clearance angle of 0^o, Figure 3.13, which generates the simplest conditions for testing and with a 0^o rake angle ensures an ideal orthogonal cut. The tool material is grade 3215 designed for cast iron, not for cutting titanium, but as

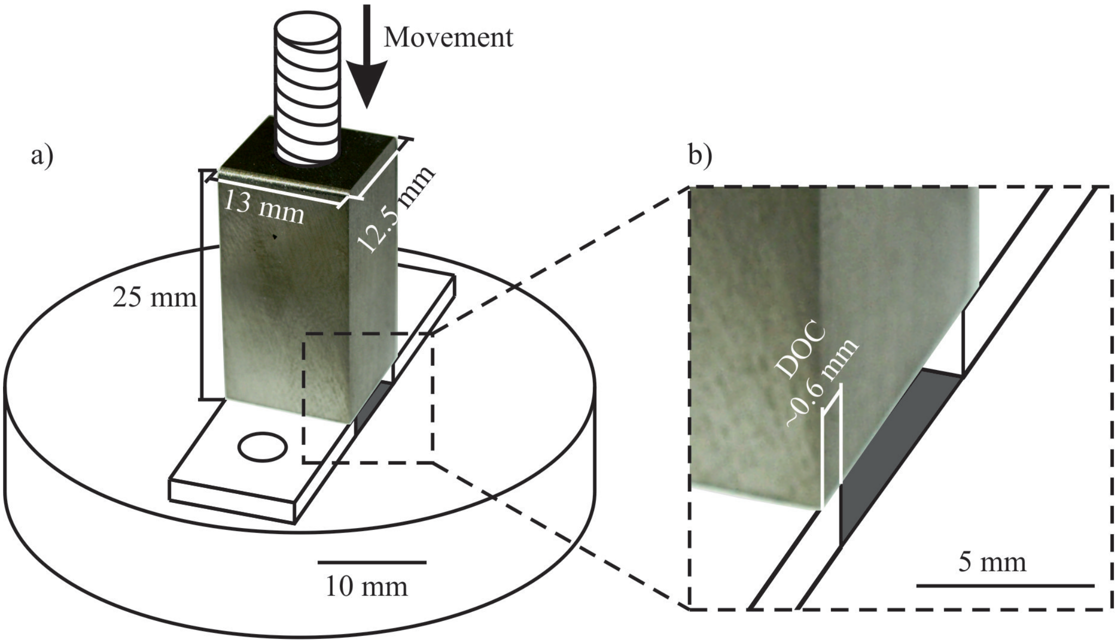

Figure 3.12: a) Schematic and photo composition showing sample geometry and b) Illustrating specimen/tool interaction with respect to depth of cut.

the cut length is so short, 5 mm, it is not envisaged to impact too heavily upon the results.

3.9 Rig Design

The first requirement for the orthogonal cutting rig (OCR) is its compatibility with the ASP. This meant both upper and lower tools must have six mounting points in a hexagonal arrangement with point centres separated by 70.6 mm, distance measured through hexagon centre, Figure 3.14a), and each point is secured using a 10.5 mm bolt. Additionally, any deformations would be required to occur at the centre of the mounting points; this is to prevent shear loads being applied to the tools. Finally, the need for orthogonal cutting requires the tool and the specimen to be perpendicular, utilising the compression or tensile abilities of the ASP. These considerations lead to Mk *I* of the rig Figures, 3.14b) and 3.14c). Mk *I* was designed in tension; it was thought that this would prevent deflection of the tools as would be possible in compression. However, it was deemed that to permit recording of the cutting process, the support structures in the rig would be insufficiently strong to prevent torsion if specimens were aligned incorrectly.

Mk *II* was built with the aim of using the simplest possible design, with considerations of the cutting tool to be used. A square tool with no rake angle, or chip breaker, was selected. Also due to the insufficient support required, if recording was to be possible, redesign to a compression testing method was necessary. Compression testing could

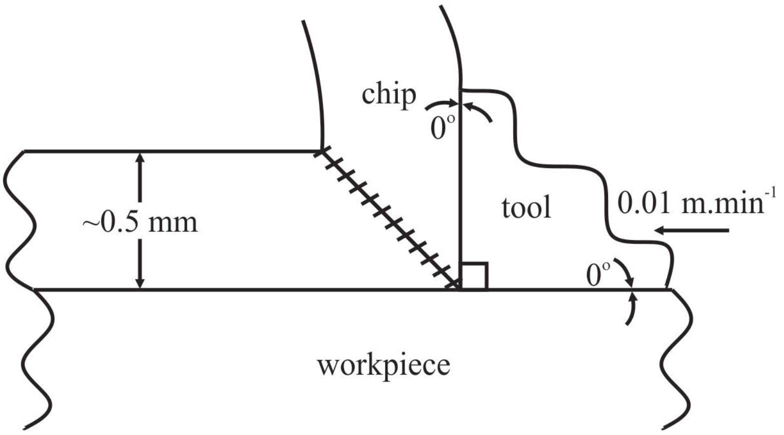

Figure 3.13: Schematic depicting key orthogonal cutting parameters.

utilise a solid lower tool to provide the stability lacking in Mk *I*. Consideration of tool shape was made with the intention to include a recess into the lower tool where the tool would sit, preventing tool movement during testing and allowing accurate and reproducible alignment of the tools. Figure 3.15 shows OCR Mk *II*.

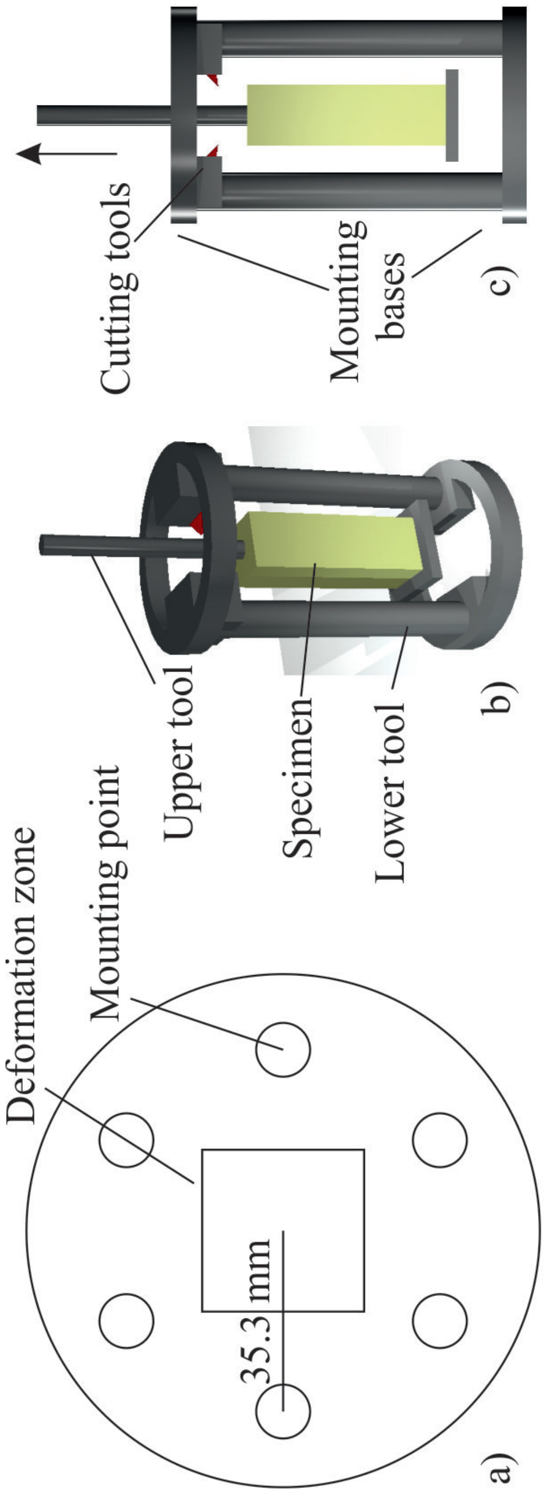

Figure 3.14: a) Schematic depicting mounting base and mounting point arrangement b) perspective view of CAD design Mk *I* OCR c) Cross section of Mk *I* OCR, indicating direction of movement.

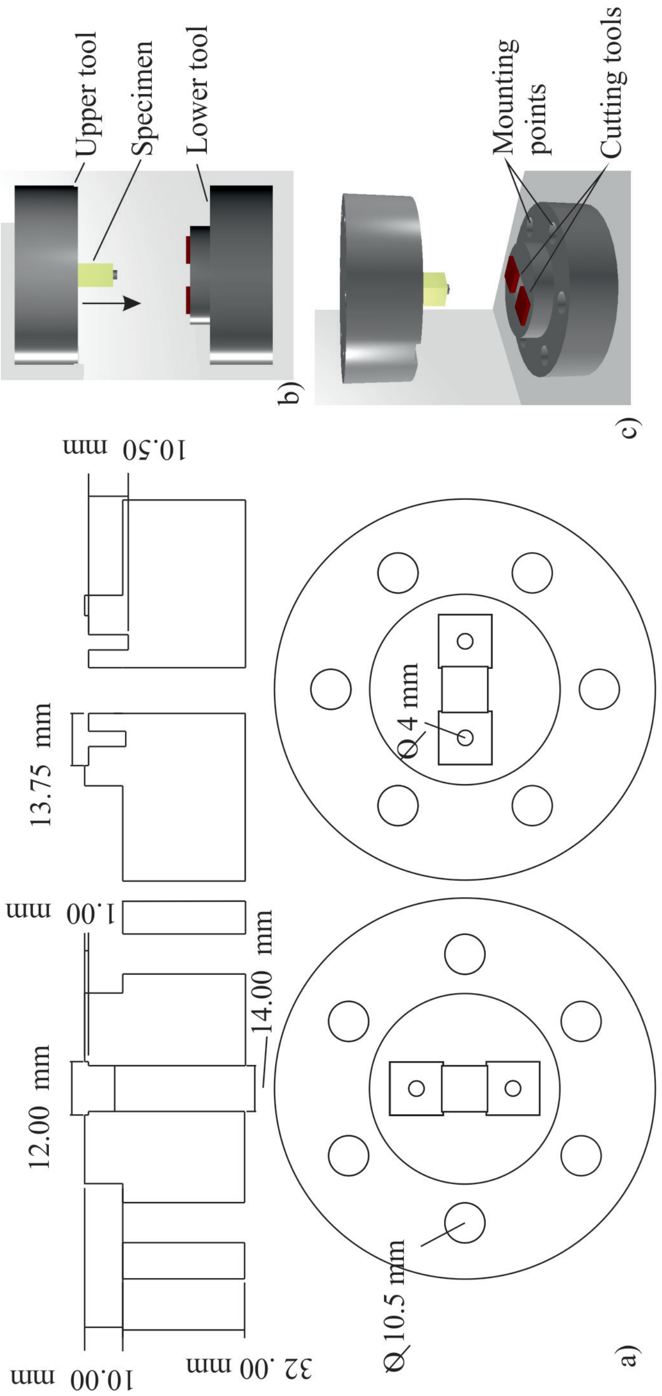

Figure 3.15: a) Schematic depicting mounting base and mounting point arrangement b) Cross section of Mk *II* OCR, indicating direction of movement and c) perspective view of CAD design Mk *II* OCR.

3.9.1 Tool Damage

A measure of the tool damage was performed. The damaged tools were imaged using low magnification microscopy. Figure 3.16 shows the location where tool failure occurred relative to the cutting interface. The damaged area, Figure 3.17a), had a silhouette created using imaging software, Corel Draw [112], and the area of the silhouette, Figure 3.17b), measured using ImageJ [113]. Damage was normalised as a function of cut area, to account for the any variation between individual tests.

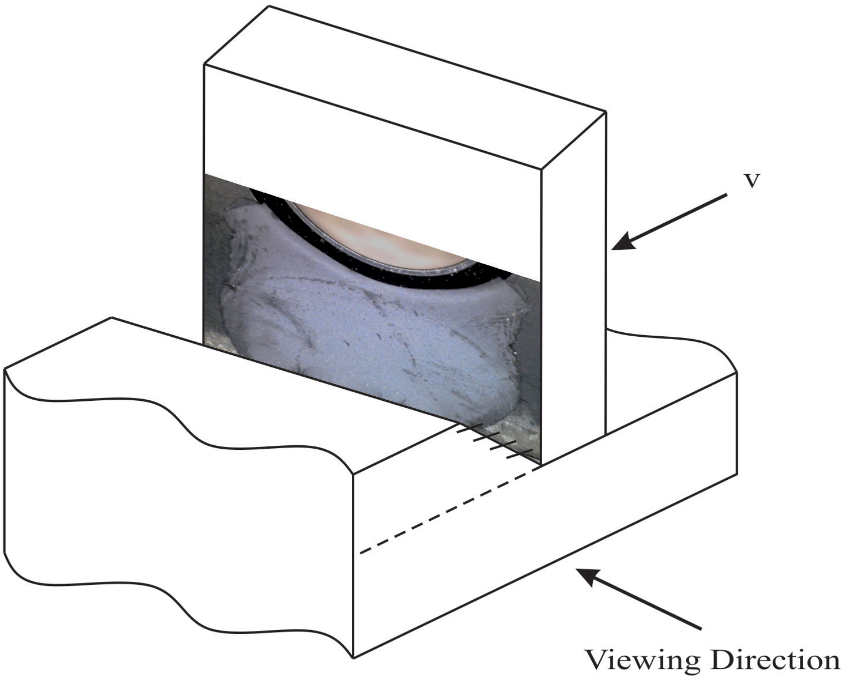

Figure 3.16: Schematic diagram illustrating the location of the tool fracture area relative to the orthogonal cut.

3.9.2 Shear Band Angle

Shear band angle is an important parameter for aiding determination of shear stresses generated during the cutting process. Determination of this angle was performed using a macro image and measuring the angle between the machined surface and the shear band, shown in Figure 3.18.

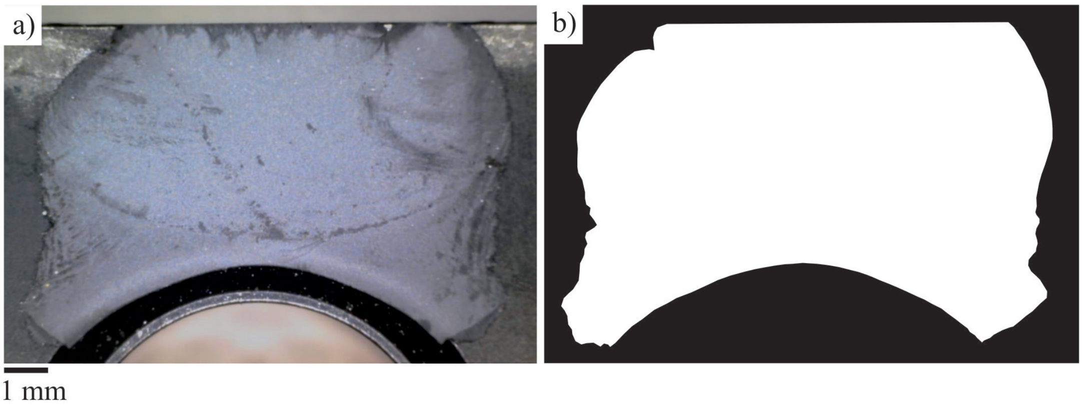

Figure 3.17: a) Marcoimage of tool damage induced during orthogonal cutting tests b) silhouette of damaged area used to measure tool damage area.

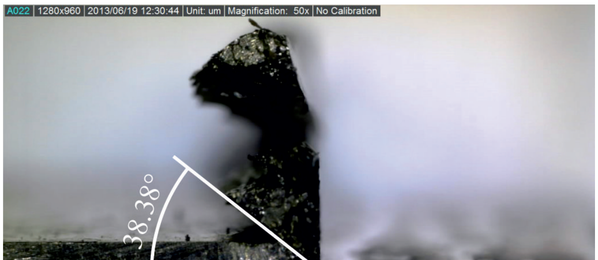

Figure 3.18: Macro image, showing Ti-2Al cut at 0.01 m.min^{-1}, showing measurement of the shear band angle relative to the cut surface.

3.9.3 Shear Stress Calculation

Axial load versus displacement measurements were made during cutting. These were converted to shear stress versus strain, described below. Shear stress was determined in the manner described in Section 3.6.5; the instantaneous contact area was defined as the cut area, cut width multiplied by cut depth. Force circle analysis [114] and the measured shear band angle were used, through Equations 3.18-3.16, to determine the stress experienced in the direction of the shear band, Figure 3.19. This allowed direct comparison to the values determined for shear stress in the axisymmetric compression specimens. From the force circle in Figure 3.19, Equations 3.14 and 3.15 are generated. As the rake angle (α) in these equations is 0 the result is that $N = F_c$ and $F = F_t$ as $\cos\alpha = 1$ and $\sin\alpha = 0$, respectively. Where N and F are the normal and friction components of the resultant force R, F_c is the measured cutting force and F_t is the unmeasured tangential force. This means that once Equation 3.16 is solved for $\alpha = 0$ [115], where ϕ is the shear band angle, Equation 3.17 can be used to determine F and by extension F_t, where β is the angle between N and R. F_c and F_t are then used to determine F_s and F_n in Equation 3.18 and 3.19, where F_s and F_n are the shear and normal components of the resultant force R'. These two resultants are then used to determine the shear stress, τ_s, where A_s, the shear plane area, is described in Equation 3.21 and t and w are the uncut chip thickness and width respectively.

$$N = F_c \cos\alpha - F_t \sin\alpha \tag{3.14}$$

$$F = F_c \sin\alpha + F_t \cos\alpha \tag{3.15}$$

$$\beta = \frac{\pi}{4} + \alpha - \phi \tag{3.16}$$

$$\beta = \tan^{-1}\mu = \tan^{-1}\frac{F}{N} \tag{3.17}$$

$$F_s = F_c \cos\phi - F_t \sin\phi \tag{3.18}$$

$$F_n = F_c \sin\phi - F_t \cos\phi \tag{3.19}$$

$$\tau_s = \frac{F_s}{A_s} \tag{3.20}$$

$$A_s = \frac{tw}{\sin\phi} \tag{3.21}$$

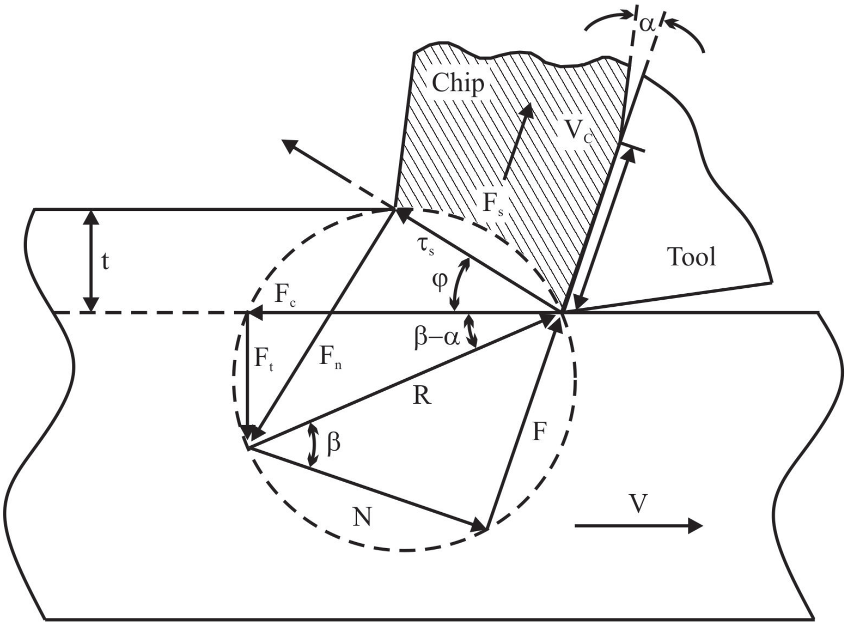

Figure 3.19: Cutting mechanism shown in relation to a force circle diagram [114].

3.9.4 Digital Image Correlation

Digital Image Correlation (DIC) is a optical technique developed to track motion for measurement of image changes for two and three dimensions. The technique works through registering of two, or more, images of the same environment, in this work the orthogonal cutting of a specimen. Displacement measurements are made by tracking the movement of a pixel or, as is the case in this work, subset of pixels between a first image, known as the reference image, and a second image. Strain is determined by calculating the change in separation between pixel subsets using the mathematical relationships previously described [116].

3.9.5 Digital Image Correlation Strain Determination

In order to apply DIC analysis to the material being deformed a high contrast speckle is required to generate the points to be tracked by the software. In the first instance a white primer layer was applied followed by a black speckle pattern; ideally a range of speckle diameters is required to generate a sufficiently high number of unique points, illustrated in Figure 3.20a). For the first specimen, of free cutting steel grade EN1A, the speckle size generated was in the range of 10 - 350 μm. After performing the cut on the first EN1A specimen the images captured were examined. The image shown in Figure 3.20b) is of the EN1A specimen at various stages of the cutting operation. It is apparent that as the chip forming process occurs, the white primer layer has stronger self adhesion properties than to the EN1A substrate, which resulted in the white layer peeling and folding out of the plane of the images around the cutting tool face. This led into examination of a method of generating a speckle pattern that will displace coherently with the substrate when the chip is forming.

The first method to prevent film formation was to generate a double speckle. This meant instead of applying white primer base, immediately applying a white speckle then overlaying a black speckle. Examination of this scenario generated what appeared to be the necessary result, where a combination of white and black speckle and substrate could be observed, illustrated in Figure 3.21. However, when used during the orthogonal cut experiment it became clear that this approach was not ideal. As can be observed in Figure 3.22 the right side of the specimen shows that sufficient separation of paint particles can be achieved, however on the left, this is not the case, where a more solid film appears to have formed, this appears to be due to a slightly thicker layer and as a result the white has wetted the surface more effectively to form a film.

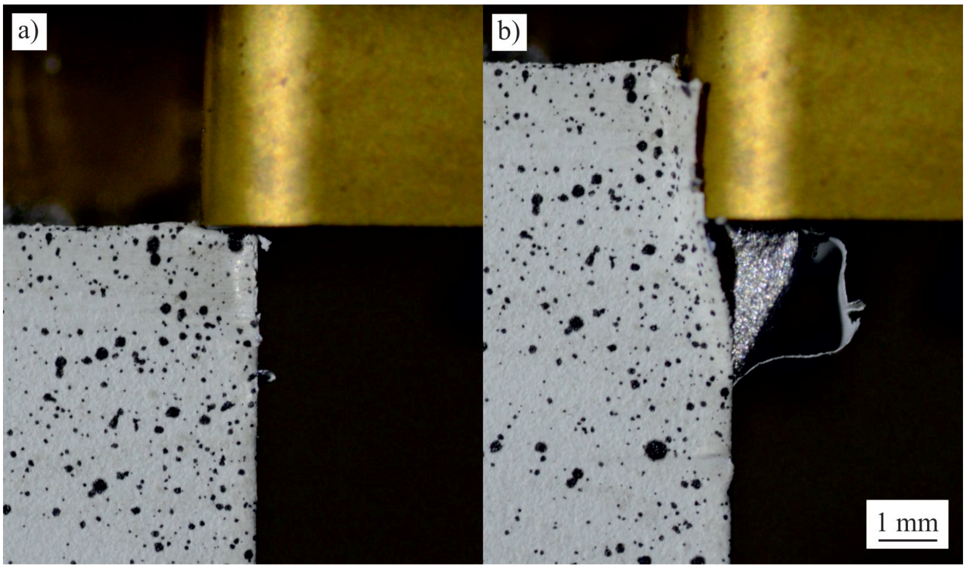

Figure 3.20: Macrographs of steel grade EN1A taken of a) speckle pattern prior to testing and b) of speckle film moving independantly of the substrate during orthogonal cut, performed at 0.01 m.min^{-1}.

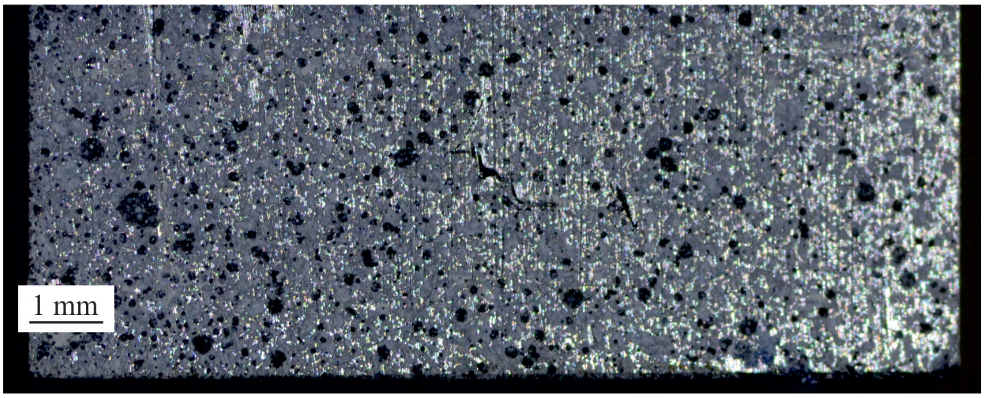

Figure 3.21: Macrograph of specimen which has been speckled with both white and black speckles prior to orthogonal cutting.

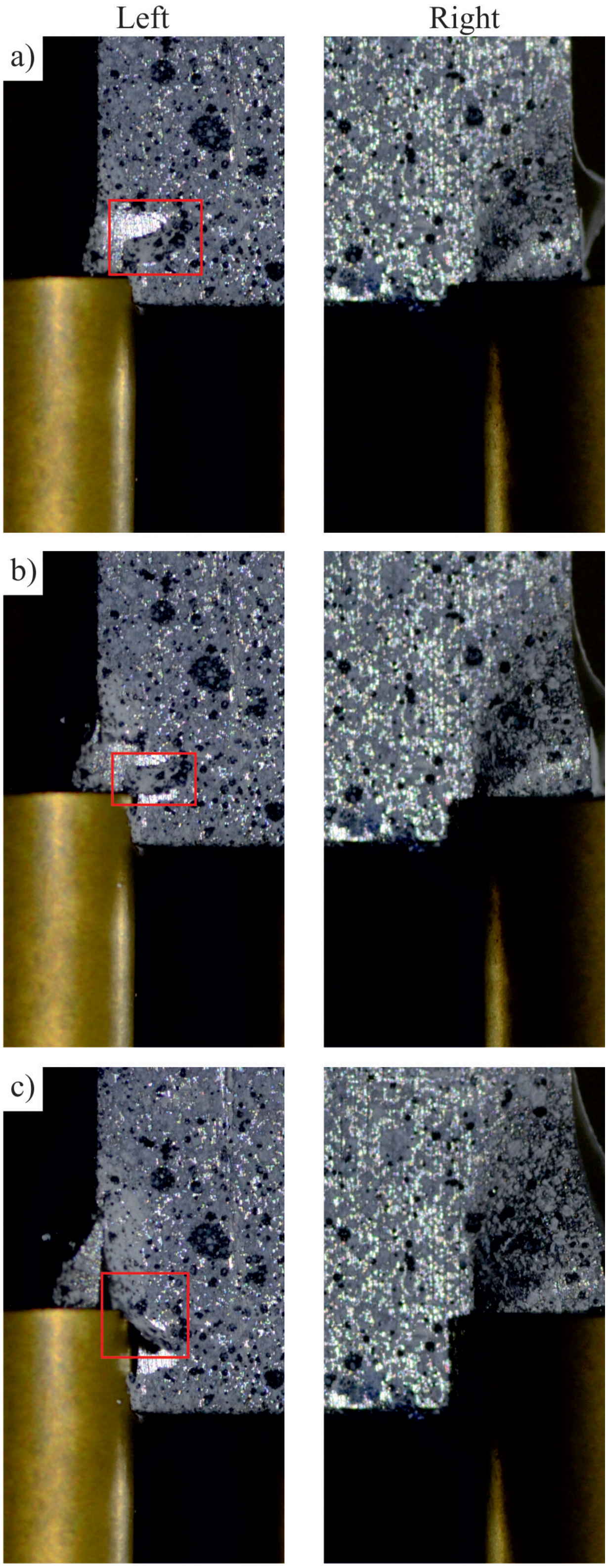

Figure 3.22: Macrograph taken in-situ during orthogonal cut of 0.01 m.min^{-1}of specimen which has been speckled with both white and black speckles prior to orthogonal cutting.

The second attempt was to replace the white primer with a white plastic particle spray. This had been seen to bond more effectively to the substrate material than itself, meaning the particles would move with any chips that formed. Much work has been performed on determining the ideal speckle size and distribution [117, 118]. It was also considered that due to the scale of the deformation occurring during cutting, a finer speckle would be preferable. In order to achieve this the speckles were applied through a sieve with mesh size of 150 μm, this limited the speckle size, measured between $<$10 and 150 μm but also upon examination Figure 3.23 combined the plastic particle spray with the mesh, which generated a non circular speckle compared to the circular speckle when the mesh was not used. This meant in compensation for a lack of unique speckle sizes a much larger set of unique speckle geometries was created resulting in a subset size of $\sim$45μm.

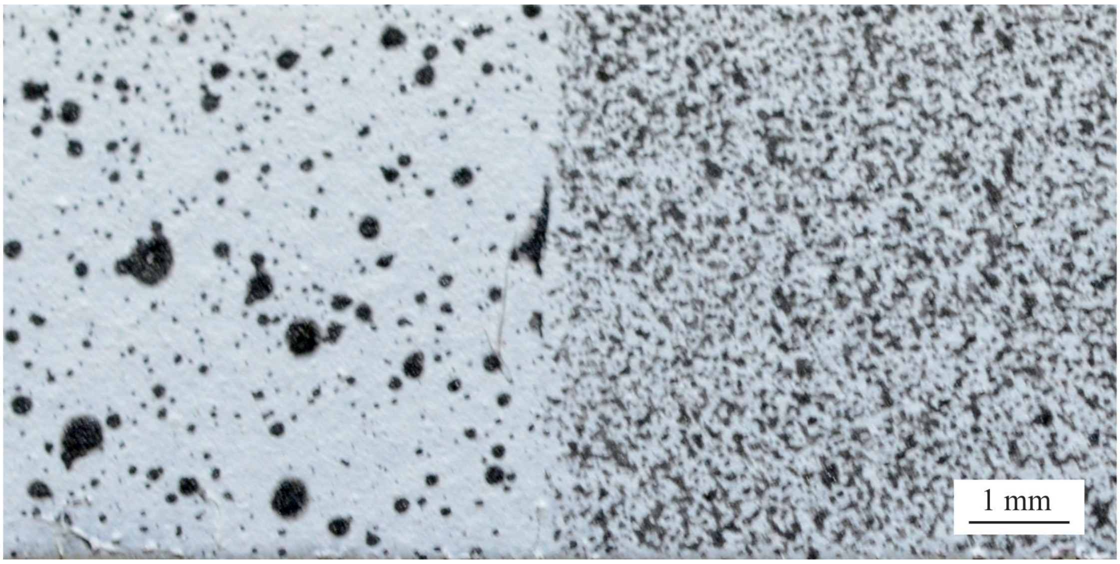

Figure 3.23: Macrograph of specimen primed using white and without use of a mesh, left, and with use of the mesh, right.

Testing of this speckle pattern was performed on the second EN1A specimen, images from that test, with DIC determined strain overlay, are shown in Figure 3.24. This figure shows successful movement of the speckle pattern with deformation. This was then analysed, using VIC-2D digital image correlation software [119], and the generated strain values were comparable to those observed by Shankar [93].

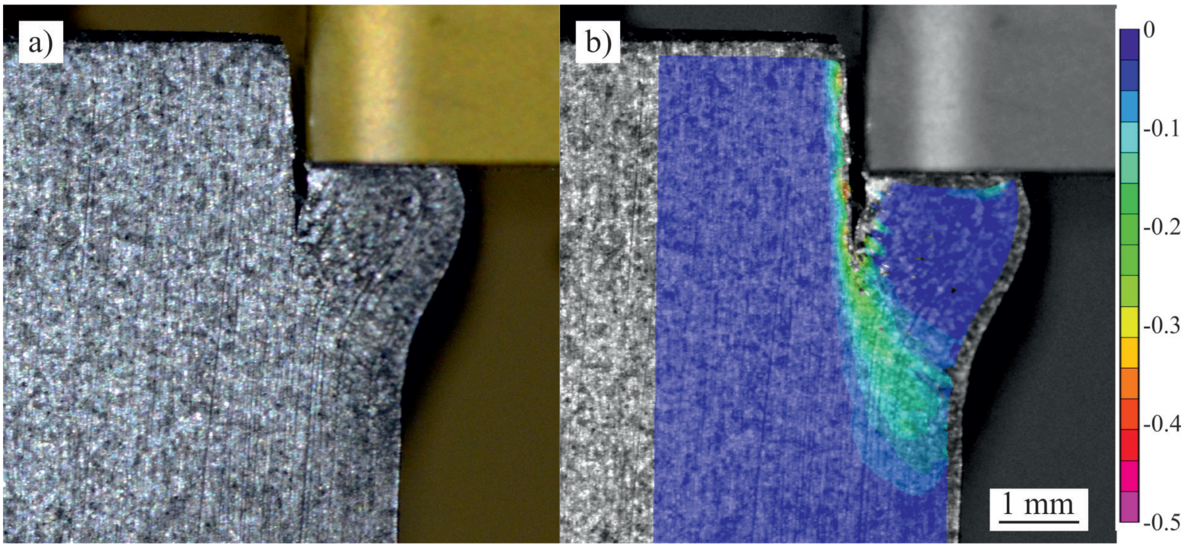

Figure 3.24: Macrograph of steel grade EN1A during orthogonal cutting, at 0.01 m.min^{-1}, a) from during the test and b) corresponding image to a) with DIC strain profile overlayed.

3.10 Materials Data

Experimental data taken from the axisymmetric compression testing was used to generate materials constants for application to two phenomenological flow stress models. These were then applied to finite element modeling (FEM) models to aid proof of concept that the machinability of a given material is predictable through established testing methods, in this case axisymmetric compression testing. The results of these FEM models will be compared to results obtained from the orthogonal cutting experiments. The test conditions used to determine the materials' parameters for both equations were 298 K, $\dot{\epsilon} = 0.1$, $\epsilon = 0.05$ (where applicable). The reason for the selection of the Power Law and Johnson-Cook equations were that Power Law represents the simplest equation for expressing flow stress, while the Johnson-Cook is the equation most widely employed industrially.

3.10.1 Power Law Constitutive Equation

The Power Law constitutive equation works on the principle of perfect viscoplasticity. This means that the effects of elasticity are neglected in the model meaning the effective yield strength is equal to zero. This equation is given in Equation 3.22. For application in this study the equation was simplified to Equation 3.23 and as can be seen, there is no strain rate or temperature dependence. The model was simplified as the test matrix required to fully determine each parameter in Equation 3.22 was too large for the material available. Determination of the materials' constants $\ln K$ and n is achieved by rearranging Equation 3.23 into the form $y = mx + c$ resulting in Equation 3.24. Plotting of this equation allows extraction of the materials' parameters from the plot in Figure 3.25; the gradient of the line is n, $\ln K$ is the intercept and K is derived from Equation 3.25.

$$\bar{\sigma} = K\bar{\epsilon}^{n}\dot{\bar{\epsilon}}^{m}\exp\left(\frac{Q}{RT}\right) \tag{3.22}$$

$$\bar{\sigma} = K\bar{\epsilon}^{n} \tag{3.23}$$

$$\ln\bar{\sigma} = n\bar{\epsilon} + \ln K \tag{3.24}$$

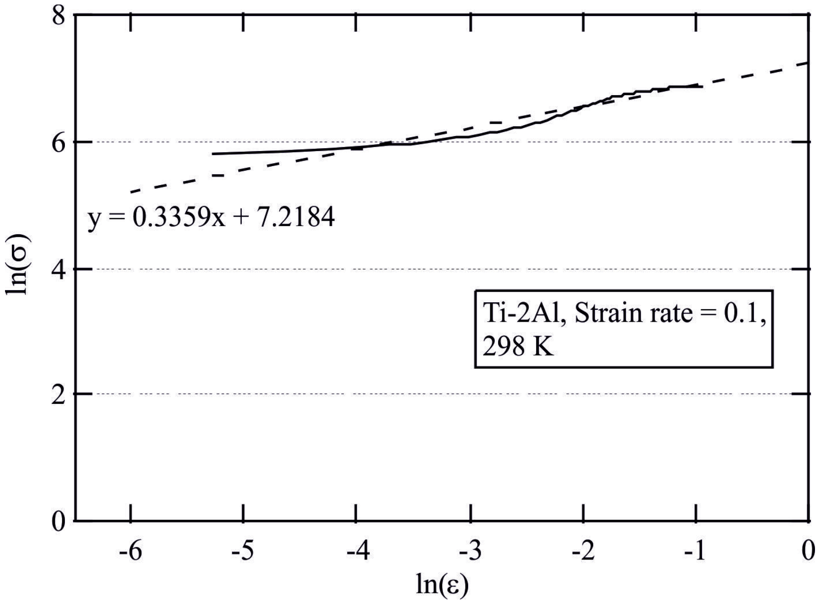

Figure 3.25: Plot used to determine the K and n materials parameters from the Power Law equation.

$$\exp^{\ln K} = K \tag{3.25}$$

3.10.2 Johnson-Cook Equation

The Johnson-Cook equation is a phenomenological model, meaning parameters are generated based on empirical observations. For the purpose of this work, where temperature effects are expected to be limited, a constant value for all material from literature has been used. It must be noted that while the strain term for both the Power Law and Johnson-Cook appear similar, $K\bar{\epsilon}^n$ and $B\bar{\epsilon}^n$, they differ in that K includes elastic contributions whereas B does not as these have already been accounted for by the presence of A. A is defined as the yield stress, as determined in Section 3.6.3.

$$\bar{\sigma} = (A + B\bar{\epsilon}^n)(1 + C\ln\dot{\bar{\epsilon}}^\star)(1 - T^{\star m}) \tag{3.26}$$

$$\dot{\bar{\epsilon}}^* = \frac{\dot{\bar{\epsilon}}}{\dot{\bar{\epsilon}}_0} \tag{3.27}$$

Parameter B and n are functions of the observed hardening behaviour. In order to determine B and n it is necessary to use conditions so that Equations 3.28 and 3.29 are true, so Equation 3.26 becomes Equation 3.30. For this to occur the strain rate must be 0.1 s^{-1}, so using Equation 3.27, results in $\ln\dot{\bar{\epsilon}}^* = 0$. Applying similar processes to Equation 3.29 to achieve T*=0, T=25^{o}C. Thus the flow curve for $\dot{\bar{\epsilon}} = 0.1$ s^{-1} at 25^{o}C test was used to determine both B and n. Rearranging Equation 3.30 to the general form $y = mx + c$ gives Equation 3.31 and plotting of this results in Figure 3.26a). From this the gradient of the line is n, $\ln B$ is the intercept and B is derived from Equation 3.32.

$$(1 + C\ln\dot{\bar{\epsilon}}^*) = 1 \tag{3.28}$$

$$(1 - T^{*m}) = 1 \tag{3.29}$$

$$\bar{\sigma} = A + B\bar{\epsilon}^n \tag{3.30}$$

$$\ln(\bar{\sigma} - A) = n\ln\bar{\epsilon} + \ln B \tag{3.31}$$

$$\exp^{\ln B} = B \tag{3.32}$$

The parameter C indicates the strain rate sensitivity of the material. It is determined by plotting the dynamic stress to static stress ratio at 5% (0.05 strain) plastic strain against the $\ln(\dot{\bar{\epsilon}}/\dot{\bar{\epsilon}}_0)$. 5% plastic strain is selected as, in experimental curves, stress values alter considerably as the strain increases until failure as different deformation mechanisms become dominant. However, as can be seen from Figure 3.27 the computational flow curves show a high level of agreement with experimental curves up to a strain of 0.2 - 0.4 depending on the point of failure. For determining parameter C, 5% dynamic

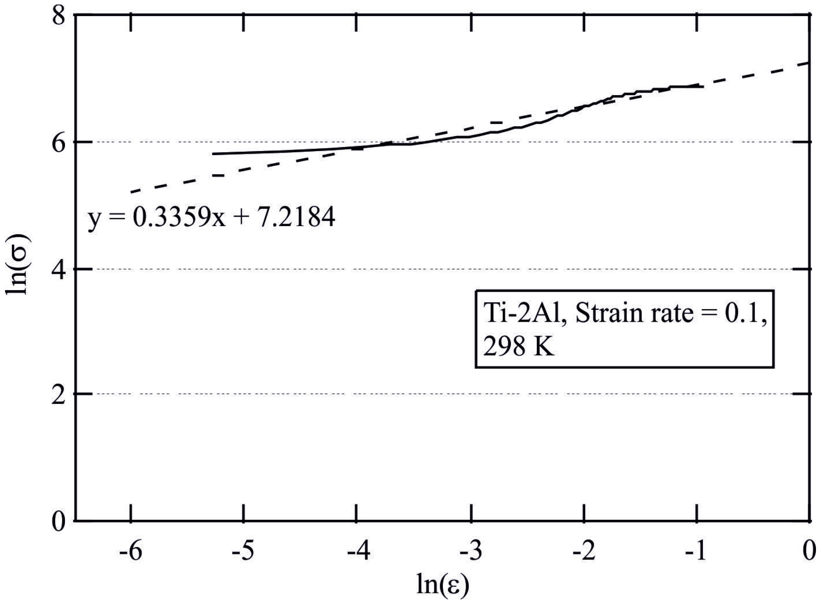

Figure 3.26: Plot used to determine a) the B and n, and b) C materials parameters from the Johnson-Cook equation.

stress is the 5% plastic stress at all of the strain rates tested, and the static stress is the 5% plastic stress value at a strain rate of 0.1 s^{-1}. The static stress is defined at a strain rate of 0.1 s^{-1}. This means that as Equation 3.29 is still true, but Equation 3.28 $\neq$ 1, it forms Equation 3.33 as a result and Equations 3.34 and 3.35 are assumed. This means Equation 3.35 can be rewritten as Equation 3.36 after manipulation to achieve $y = mx + c$ form resulting in Figure 3.26b).

$$\bar{\sigma} = (A + B \ln \bar{\epsilon}^n)(1 + C \ln \dot{\bar{\epsilon}}^*) \tag{3.33}$$

$$\dot{\bar{\epsilon}} = \dot{\bar{\epsilon}}_0 \therefore \dot{\bar{\epsilon}}^* = \frac{\dot{\bar{\epsilon}}}{\dot{\bar{\epsilon}}_0} = \frac{\dot{\bar{\epsilon}}_0}{\dot{\bar{\epsilon}}_0} = 1 \tag{3.34}$$

$$\bar{\sigma} = (A + B \ln \bar{\epsilon}^n)(1 + C \ln \dot{\bar{\epsilon}}^*), \qquad when(3.34) \rightarrow \bar{\sigma}_0 = A + B \ln \bar{\epsilon}^n \tag{3.35}$$

$$\frac{\bar{\sigma}}{\bar{\sigma}_0} = 1 + C \ln \dot{\bar{\epsilon}}^* \tag{3.36}$$

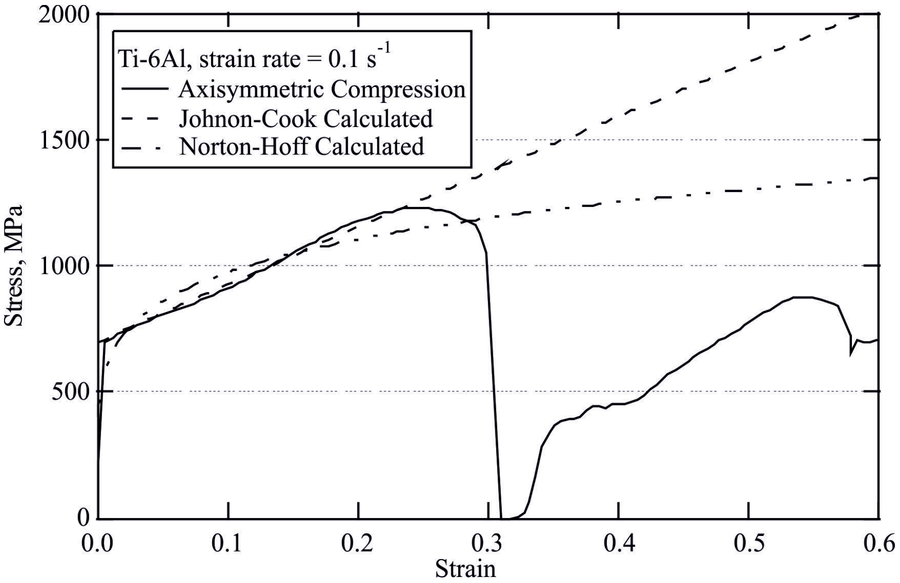

Figure 3.27: Plot showing the stress strain curve for Ti-6Al deformed at $\dot{\epsilon} = 0.1$ s^{-1} from experiment and calculated using both the Johnson-Cook and Power Law equation.

3.10.3 Cockcroft-Latham Damage Criterion

The Cockcroft-Latham criterion is a damage criterion first proposed in 1968 by Cockcroft and Latham [120]. It describes how fracture occurs once the plastic strain energy per unit volume reaches a critical value, expressed in Equation 3.37. For application in finite element modeling a modified version is applied, whereby once the critical strain energy per unit volume is reached the material undergoes softening, as opposed to fracture, to percentage of the flow stress prior to softening. This facilitates strain localisation, the precursor to shear band formation.

$$\int_0^{\epsilon_f} \bar{\sigma} d\bar{\epsilon} = W \tag{3.37}$$

3.10.4 Orthogonal Cut FEM Model

FEM model for orthogonal cut tests were performed to generate load - displacement data to compare directly to data generated by equivalent experiment. DEFORM™V10.2 was used and the materials data file "Ti6Al4V-machiningSFTC" was selected as a first comparison to the Ti-6Al-4V orthogonal cut test, with properties listed in Table 3.5. Generation of materials databases for the four binary alloys used the same initial database, but modified the Cockcroft-Latham damage criterion, using Table 3.6. The flow stress was also modified and used the experimentally generated parameters for 1) Power Law, Table 3.7, 2) Johnson-Cook, Table 3.8, and 3) direct value input, for comparison. The modification of the same initial materials database was done as it would mean that other

TABLE 3.5: MATERIALS DATA AND SIMULATION VARIABLES

Variables	Applied Values
Environment temperature (^{o}C)	20
Workpiece temperature (^{o}C)	20
Poissons Ratio	0.31
Mechanical work to heat	0.9
Damage criteria	Cockcroft - Latham
Softening of original flow stress (%)	10
Heat capacity (N/mm^2/^{o}C)	2.4
Thermal conductivity (N/s/^{o}C)	7.1
Time step (sec/step)	0.02
Step increments to save (no. of steps)	10
Total simulation length (mm)	5
Interference depth (mm)	0.003
Convergence error Limit, velocity (mm/s) & force (N)	0.001 & 0.01

TABLE 3.6: EXPERIMENTALLY DETERMINED COCKCROFT-LATHAM PARAMETERS FOR TITANIUM - ALUMINIUM BINARY ALLOYS

Al content, wt.%	damage criterion
0	329
2	259
4	204
6	245
8	276

properties, such as shear modulus, discussed in Section 3.6.4, and Poissons ratio would be comparable to those expected within the binary alloys and means that only flow stress is altered between models, allowing direct comparison.

TABLE 3.7: EXPERIMENTALLY DETERMINED POWER LAW PARAMETERS FOR TITANIUM - ALUMINIUM BINARY ALLOYS

Al content, wt.%	K	n
2	1364	0.3359
4	1307	0.2211
6	1476	0.1805
8	1227	0.0974

TABLE 3.8: EXPERIMENTALLY DETERMINED JOHNSON-COOK PARAMETERS FOR TITANIUM - ALUMINIUM BINARY ALLOYS

Al content, wt.%	A	B	n	C
2	334	2352	0.9751	0.0092
4	467	3196	1.0834	0.0076
6	705	2224	0.9737	0.0066
8	812	1174	0.9695	0.0305

The simulation was setup using the Lagrangian incremental method and using DEFORM™Skyline solver with direct iteration. Other variables such as time step and error limits are listed in Table 3.5. The tool geometry used was the same as for the orthogonal cut experiments, discussed in Section 3.8, and was rigid and fixed, decreasing the simulation time but meaning no heat transfer occurred between the workpiece and the tool. The workpiece geometry was set suitably large, 50 mm depth by 100 mm length, ensuring containment of all deformation comfortably within the workpiece. Movement of the workpiece was induced using boundary conditions along the opposite edges, in both x and y, to the point where cutting is initiated, as illustrated in Figure 3.28. The mesh for the workpiece used 3000 square shaped elements in six mesh windows centred on the cutting corner of the tool, which increase in relative size as the distance from the cutting corner increases, illustrated in Figure 3.28, initially starting at 0.008 mm (8 μm), and increasing to 0.02, 0.04, 0.08, 0.3 and 1 mm in size.

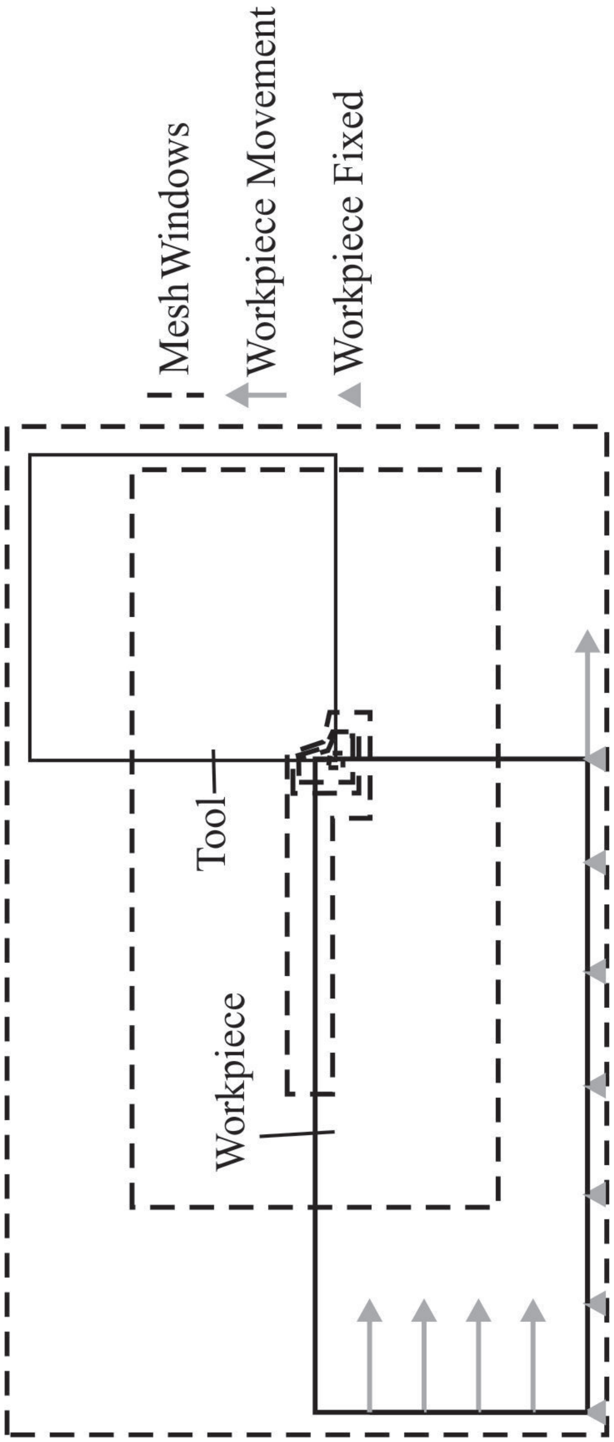

Figure 3.28: Image from DEFORM™ model preprocessor window showing boundary conditions and mesh windows.

4. HIGH SPEED MILLING RESULTS AND DISCUSSION

As discussed previously, in Section 2.8, milling is a widely used process but very little research has focussed on understanding the mechanics of the process, with most research focussing on turning. Since the 1930s work has attempted to understand all facets of turning from the mechanics [85,97,121] all the way through to the influence on machining temperature [122] and coolant conditions [104].

4.1 Twin Depth

After completion of the milling processes, described in Section 3.4, the subsurface deformation generated was examined using light microscopy. Figure 4.1 illustrates the typical form that the observable deformation takes. The first observation is the orientation of the twins, the majority of which show a long axis running along a twin plane that lies (close to) perpendicular to the machined surface. The twins then exhibit a 'sweeping' in the cutting direction. Figure 4.2 illustrates this schematically describing how this morphology is likely to have resulted. Starting from an undeformed structure, Figure 4.2*I*, as machining initiates, a strain affected zone is generated ahead of the tool (Figure 4.2*II*); this zone generates sufficient strain to form mechanical twins. As the tool passes over the mechanical twins, accumulating higher strain, the entire region undergoes plastic deformation which causes the material nearest the surface to 'smear', Figure 4.2*III*. Such smearing is hypothesised to be due to friction forces being generated perpendicular to the cutting direction. As shown in Figure 4.2*IV*, the level of sub-surface deformation generated as the tool passes is dependent on the local crystallographic structure where 'hard' orientations deform less and 'soft' orientations more. This is likely to be dependent on not just the orientation of an individual grain but neighbour orientations also.

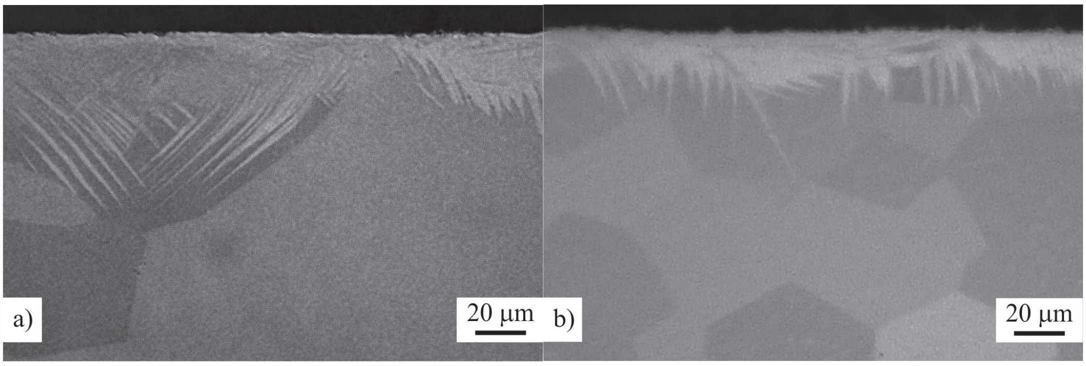

Figure 4.1: Light micrograph showing subsurface deformation in the form of twinning in down milled material with a DOC = 1 mm on a) Ti - 4 wt.% Al, V_c = 188 $m.min^{-1}$ and b) Ti - 2 wt.% Al, V_c = 150 $m.min^{-1}$.

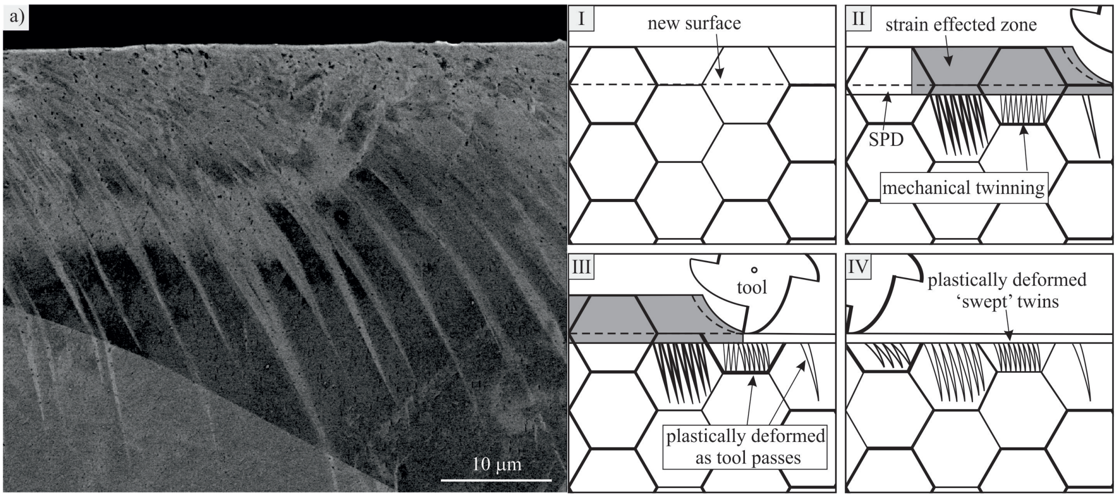

Figure 4.2: a) BSE image of Ti - 4 wt.% Al down milled at 25 $m.min^{-1}$ illustrating plastically deformed twins in the subsurface region, *I* - *IV* schematic illustrating route for formation of 'swept' twins. *I*) Unmachined surface containing no mechanical deformation, *II*) Machining progresses, generating a strain affected zone ahead of the tool which forms mechanical twins, *III*) as the tool progresses and passes the mechanical twins generated in *II* it generates more twins ahead and plastically deforms already formed twins in the direction of the cutting edge movement. *IV*) Upon completion of machining all mechanical twins are plastically deformed and appear 'swept'.

A comparison between up milled and down milled, also known as conventional and climb respectively, surfaces is provided. Figure 4.3 illustrates qualitatively the difference between down milling and up milling in Ti - 8 wt.% Al. The first observation is the increased surface roughness and presence of chip fragments still attached in the up milled specimen, better illustrated in Figure 4.4. The higher surface roughness was expected as industrial convention is to down mill rather than up mill, as it produces a high quality surface finish. Results here support that theory; however, very little research has examined the influence of up versus down milling and the only literature on titanium [123,124] comparing surface roughness is inconclusive as to which produces a more desirable surface finish and suggests that the machining conditions dictate which is preferable. It has been suggested that the occurrence of the chip fragments observed in up milled material is due to chips readhering back to the surface through what is thought to be high chip temperatures in combination with high frictional forces. The observation of chip fragments has been seen practically elsewhere, but no documentation of its presence exists in the open literature.

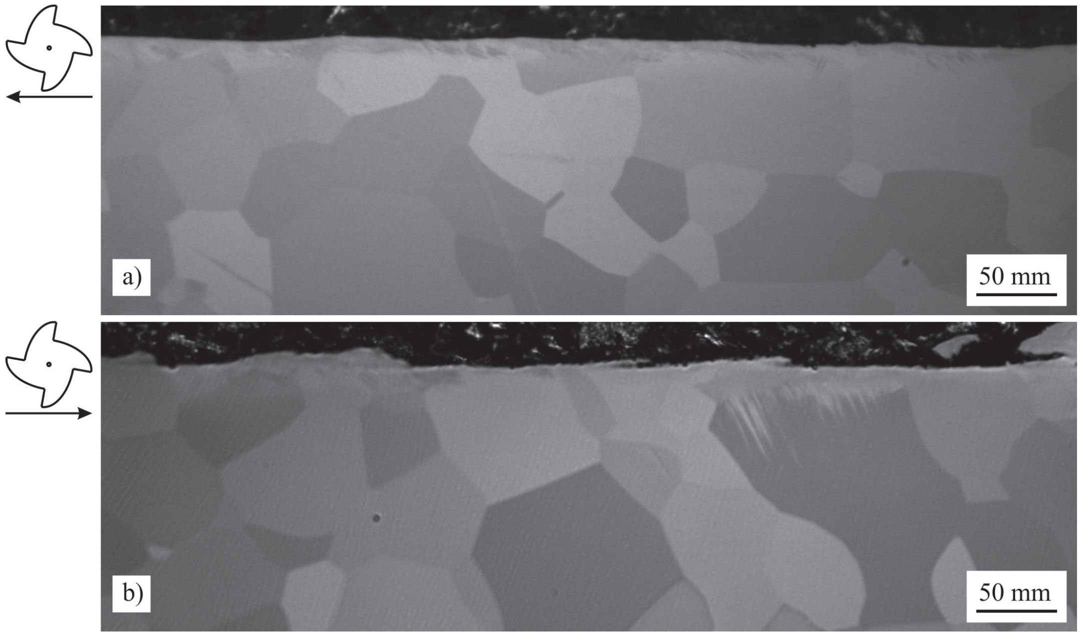

Figure 4.3: Light micrograph showing subsurface deformation in the form of twinning in Ti - 8 wt.% Al milled with a DOC = 1 mm at 125 m.min^{-1} by a) climb milling and b) up milling.

The second observation is the increased depth and reduced regularity with which the observed twins penetrate the bulk material. This is more than likely linked to the surface roughness already described, and also suggests a reason for the dominance of down milling over up milling industrially. This is supported further by observations made using EBSD, Figure 4.5, which illustrates an increased level of observable damage, but

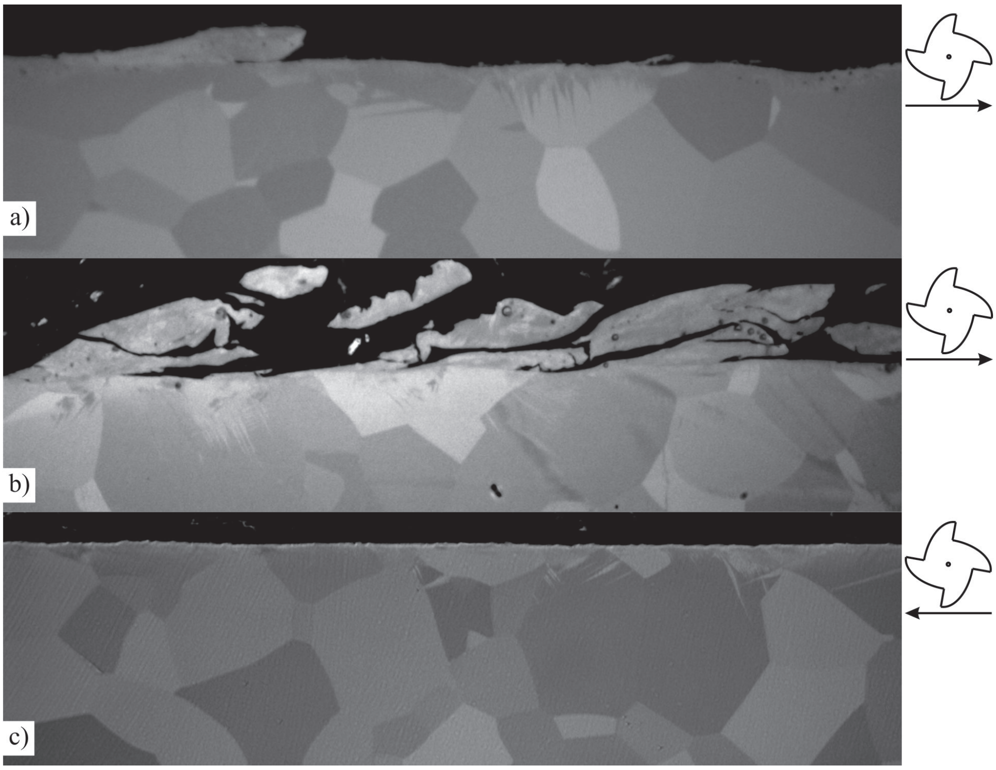

Figure 4.4: Light micrographs showing chip fragments adhered to the machinined surface of up milled specimens at a) 100 m.min^{-1} on Ti - 4 wt.% Al, b) 125 m.min^{-1} on Ti - 6 wt.% Al and c) a down milled specimen of Ti - 4 wt.% Al milled at 100 m.min^{-1} for comparison.

also a significantly increased variation in deformation in the up milled material. One similarity between the two milling types is the twin types generated. Both systems are dominated by $\{10\bar{1}2\}$ tensile twins, which are widely observed as the most common twin system during room temperature deformation with secondary twin mechanism of $\{11\bar{2}1\}$, Figure 4.5. This is in good agreement with the literature and examination of work by Rosi [31] suggests temperatures in the near sub-surface could be reaching 500^{o}C based on the propensity order described. This is also in good agreement with work by Liao [74], which measured shear band temperatures of up to 550^{o}C comparable to results here, if Rosi's [31] propensity order is correct.

Closer examination of twin depth penetration is focused on down milling as the industrial convention. Measurements of the average twin depths were made and the results are illustrated in Figure 4.6. Figure 4.6a) shows a plot of twin depth as a function of the milling speed, but there is not clear correlation between the cutting speed and the average twin depths observed. Figure 4.6b) show a consistent behaviour across all speeds where an initial increase in twin depth peaks at Ti - 4 wt.% Al before decreasing. These

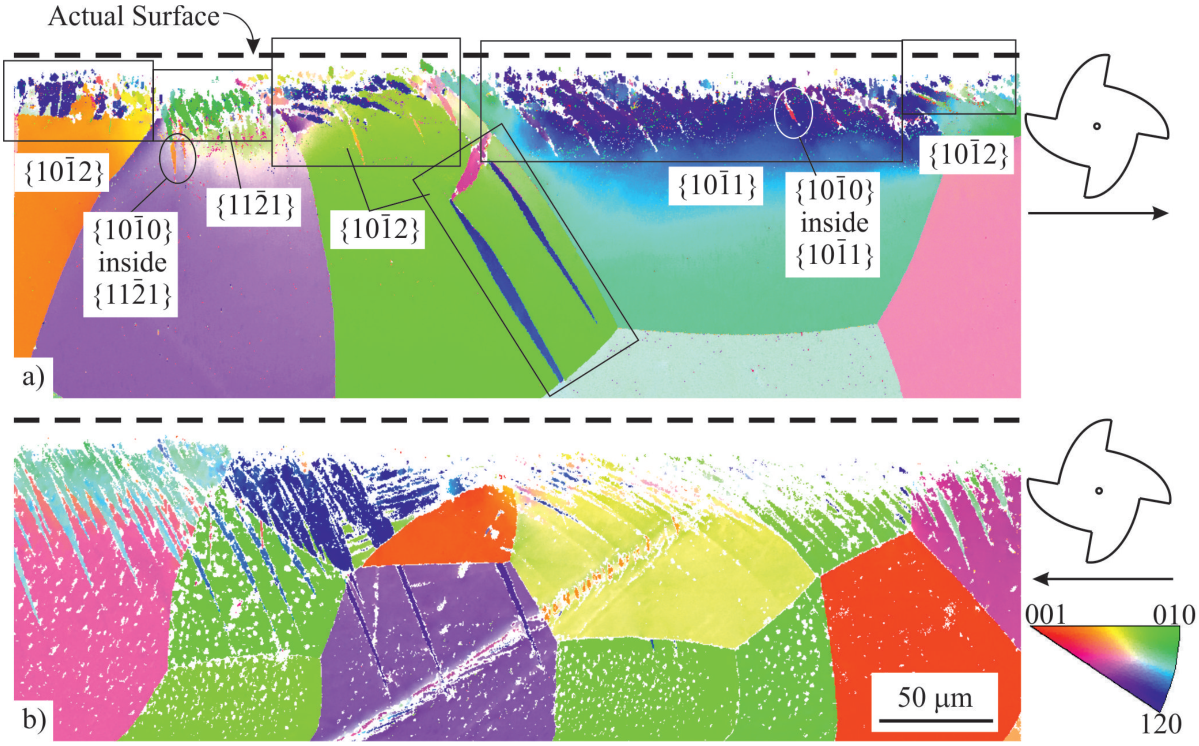

Figure 4.5: IPF EBSD map showing the subsurface damage generated in Ti - 4 wt.% Al through milling at V_c = 188 m.min^{-1} in the a) down milling and b) up milling condition.

results do not include errors, as these are large; however, they provide a good qualitative understanding of the occurring deformation. This is further supported by measurements of the SPD, which do include errors as results were more consistent and many more measurements were possible due to the more regular behaviour of this region. The same behaviour is observed in the SPD region, described by Figure 3.5 in Section 3.4, in the immediate sub-surface, illustrated in Figure 4.7, where there is no visible correlation between milling speed and SPD penetration but there is a maximum occurring at Ti - 4 wt.% Al before a reduction in the SPD penetration depth. The more reliable nature of the SPD results, due to the much larger data set, adds support to the observations made on the twin depth.

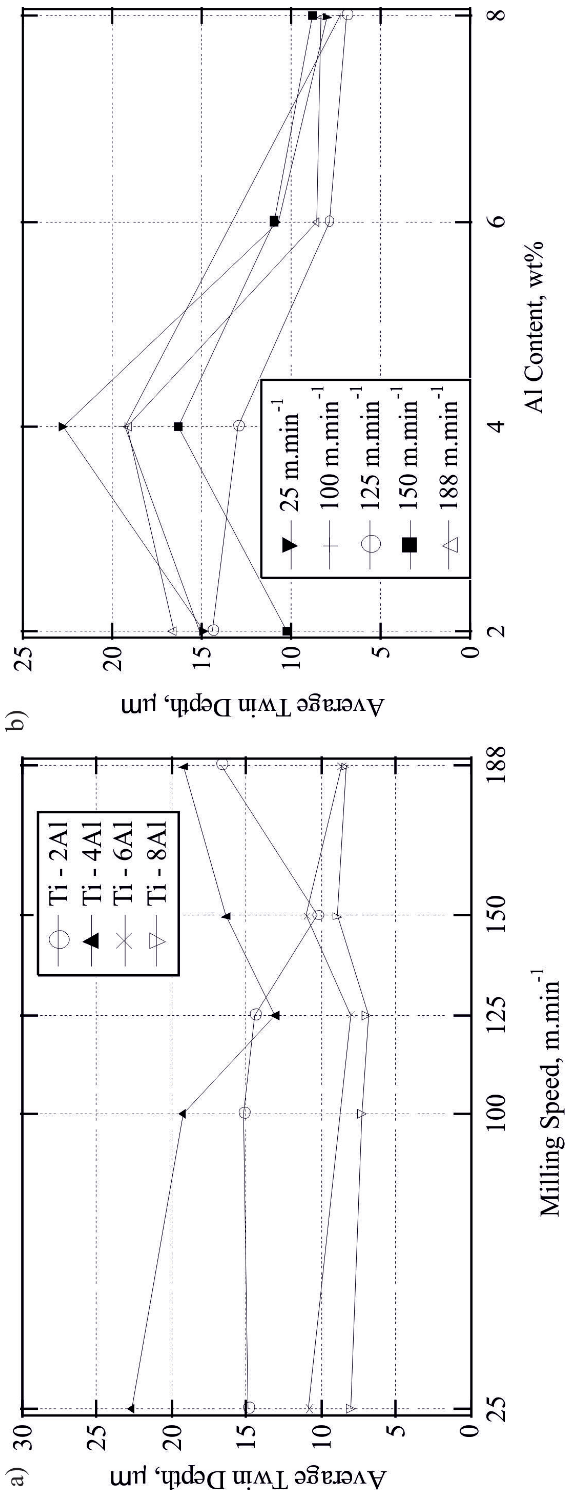

Figure 4.6: Graph showing the influence of a) aluminium content and b) cutting speed on twin penetration, DOC = 1 mm.

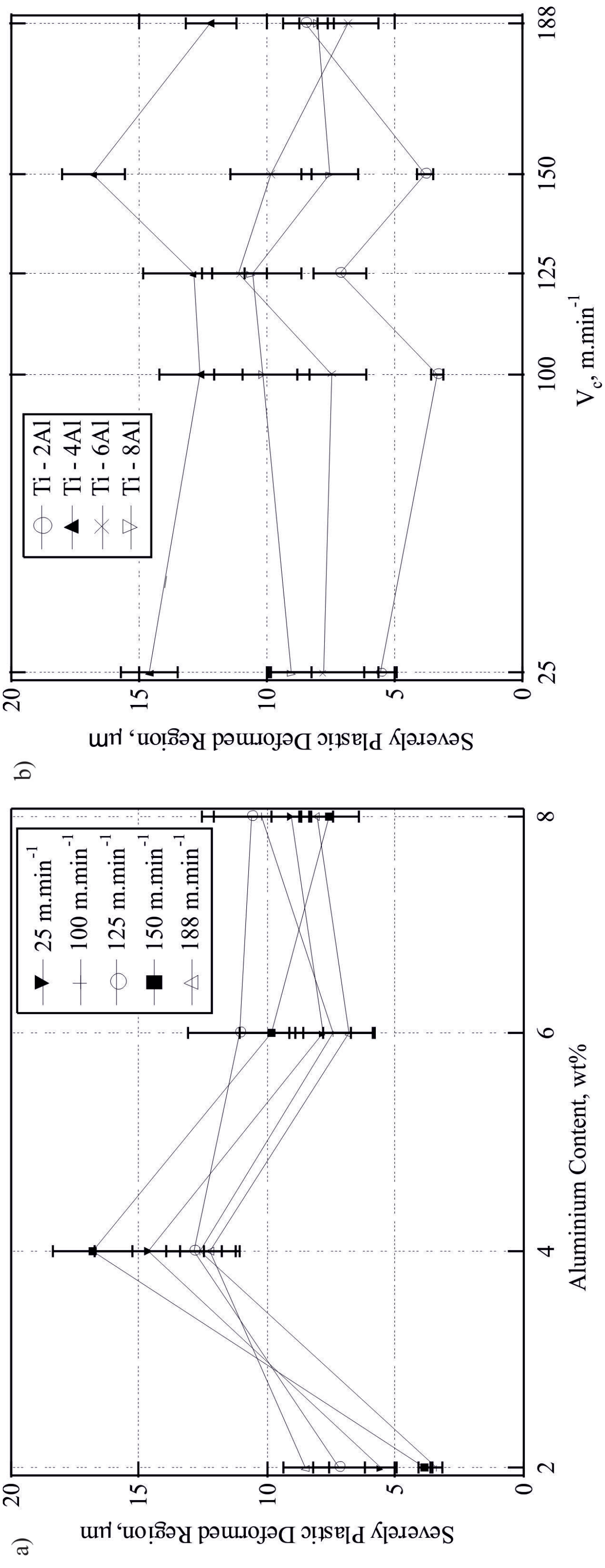

Figure 4.7: Graph showing the influence of a) aluminium content and b) cutting speed on SPD penetration, DOC = 1 mm.

4.2 Lattice Rotation

Observations made on EBSD maps in Figure 4.5 show that there appears to be a change in the texture, based on the gradiation of colour from the IPF map, of grains in contact with the surface of the down milled specimen after machining is completed. Firstly, the lattice rotation occurs to a greater average depth than twinning, shown in Figure 4.8, and that it appears to have a linear correlation with the twin penetration within a parent grain. While it is difficult to distinguish this rotation in the Ti - 2 and Ti - 8 wt.% Al samples it is present in the near surface regions that have indexed successfully. It is also clear from these maps that the depth of deformation does not follow the trends described in Figures 4.6 and 4.7. This is due to high indexing rates during analysis of the twinned region in Ti - 4 and Ti - 6 wt.% Al, compared to low indexing rates for Ti - 2 and Ti - 8 wt.% Al. The reason for this is not fully understood; a possible cause is that for Ti - 2 wt.% Al a significant portion of the deformation is accommodated through slip networks and dislocation forests in the bulk meaning indexing is difficult. This reduces in Ti - 4 wt.% Al, although there is an increased volume of twinning. However when the aluminium content increases, the CRSS values also increase, making deformation sufficiently difficult, so that when twins do form, there is a cascade effect when dislocations build up at the twin boundary; as a result the Kikuchi patterns are distorted making indexing difficult. There is insufficient evidence to conclusively prove this and further work would require an extensive TEM study to confirm.

Closer examination of the lattice rotation observed in Figure 4.8 for Ti - 4 wt.% Al, in Figure 4.9, shows that the overall lattice rotation is consistently reorientated to approximately 45^o from the cutting direction, when viewed down the axis of tool rotation. Further examination of individual grains and twins, Figure 4.9, shows that the lattice rotation shows generally minor rotations, in contrast to the twins which are all orientated within a couple of degrees of the apparently ideal 45^o. It also appears that the grains which exhibit the most pronounced lattice rotation, grains *1* and *3* in Figure 4.8, have prior parent grain orientations close to 45^o. This suggests that this is the 'soft' orientation and is more easily forming dislocations. This is in contrast to grain *2* which is almost 90^o from the 'soft' orientation of grains *1* and *3* and exhibits very little lattice rotation, with the exception of a small region that could almost be considered a sub-grain, due to segregation from the rest of the grain by surrounding twins. It is unlikely that it is coincidence that this is the grain that exhibits the largest twins, penetrating the bulk considerably more than the majority of the subsurface twins. The cause of this is clear: the 'harder' orientation of the grain is preventing dislocation formation, resulting in a need for lattice strain energy release in the form of large twins. This supported by Figure 4.10, which shows that all of the grains have a relatively high likelihood, high Schmid factor, of twinning via $\{10\bar{1}2\}$ or $\{11\bar{2}1\}$, the two most common twins observed here and the tensile twins. In contrast prism slip, the most common slip system, has a relatively low Schmid factor, which is increased by the lattice rotation, in the grains in contact with the surface; however the twins that have been introduced, both $\{10\bar{1}2\}$ and $\{11\bar{2}1\}$, are orientated ideally for prismatic slip. Interestingly, the grains in contact with the surface have a significantly high Schmid factor for basal slip, possibly encouraging the formation of twins as the CRSS for basal slip is higher then that for the preferential prism slip. It is no coincidence that grains *2* and *3*, which have low Schmid factors for slip are the grains that contain the highest amount of twinning, both in terms of number and size of twin. Grain *1* appears to be anomalous due to is very high Schmid factor for basal slip yet it exhibits twinning, a possible cause of this is the relatively small area of the grain in contact with the surface compared to the actual size of the grain and therefore the geometric constraints imposed upon it by the neighbouring grains. This is suggested as work by Barnett [125] on a magnesium alloy shows that a reduction in grain size encourages deformation via slip rather than by twinning. The possible comparison with a simple shear process, such as rolling, is an unexpected result, but one that has been observed in high speed turned industrial alloys in unpublished work by Crawforth [126]. This leads to the conclusion that even though machining, such as milling and turning, is a complex system of forces, it essentially results in a simple shear system. This unique result continues to add support to the application of axisymmetric compression as a method for prediction of high strain behaviour generated using these high speed machining processes.

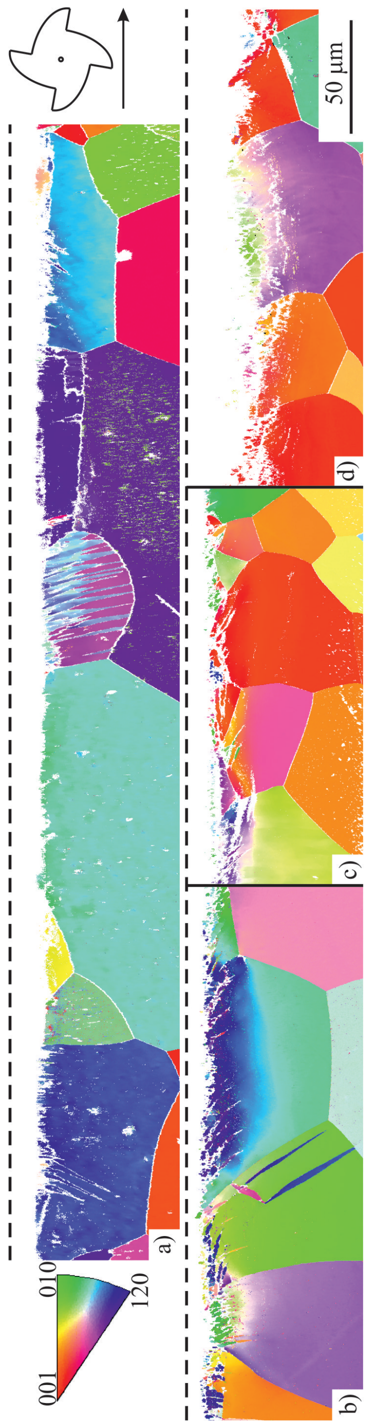

Figure 4.8: IPF EBSD map of 188 m.min^{-1} down milled material of a) Ti - 2 wt.% Al, b) Ti - 4 wt.% Al, c) Ti - 6 wt.% Al and d) Ti - 8 wt.% Al.

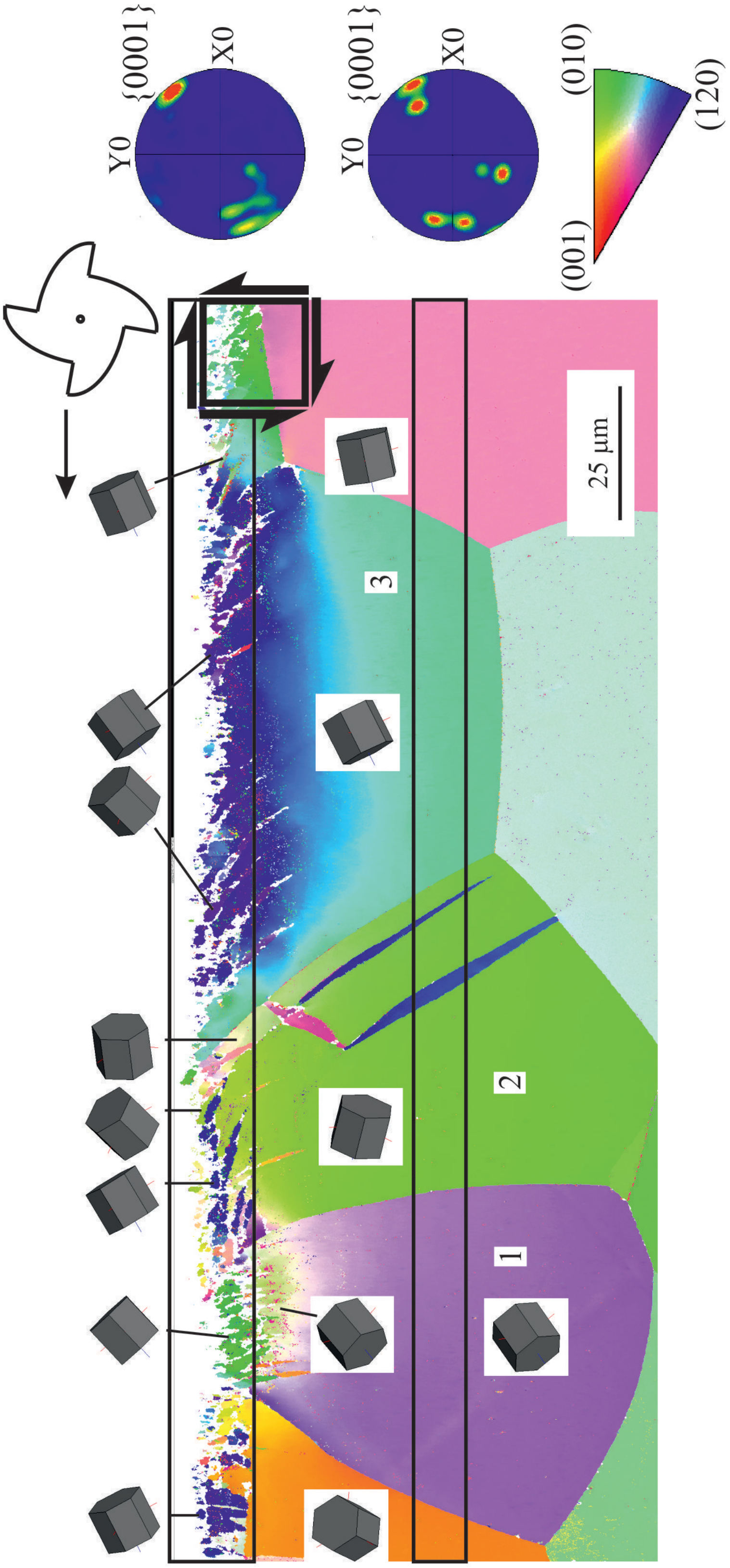

Figure 4.9: IPF EBSD map and pole figures showing the lattice rotation from the bulk to the surface post milling with individual crystal orientations in Ti - 4 wt.% Al down milled at 188 m.min^{-1}.

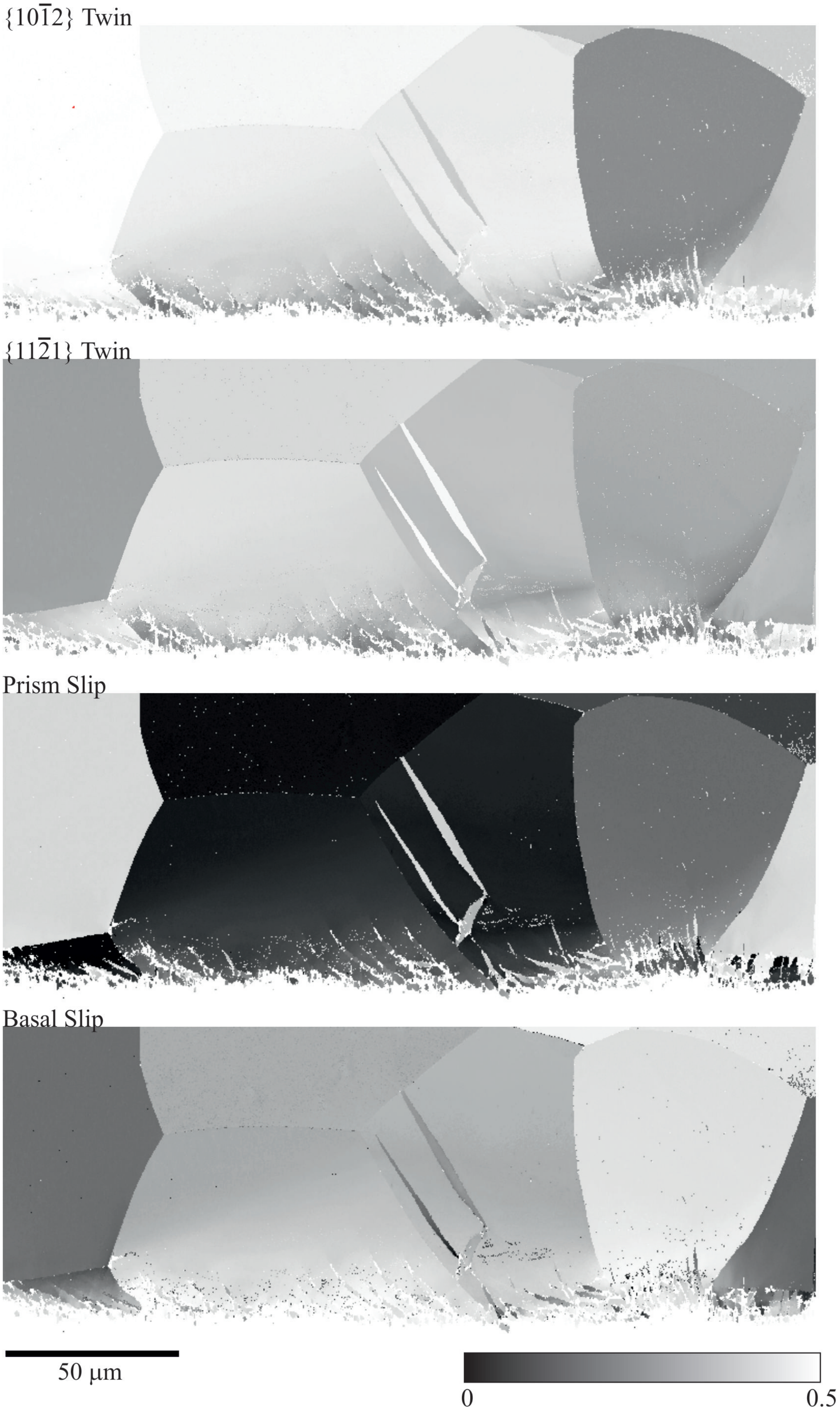

Figure 4.10: Schmid factor maps for the two most common twin types, $\{10\bar{1}2\}$ and $\{11\bar{2}1\}$, and slip types, prismatic and basal, observed in Ti - 4 wt.% Al down milled at 188 $\mathrm{m.min^{-1}}$.

5. AXISYMMETRIC COMPRESSION RESULTS AND DISCUSSION

This section details all the results generated from axisymmetric compression testing in order to understand the influence of aluminium and strain rate upon mechanical deformation of titanium.

5.1 Macrostructural Deformation

Upon completion of the compression testing, the test specimens were examined. On the macroscopic scale a qualitative trend was observed, illustrated in Figure 5.1, and increases in aluminium content and strain rate resulted in an increased shear localisation and increased severity of shear band formed. Also at each of the strain rates tested, the chips generated at the edge of each specimen become more pronounced and the length of the fracture observed in the centre increases as a function of the increase in aluminium as well as strain rate. As can be seen the transition to shear band failure from conventional 'barreling' in the 2 and 4 wt.% Al samples occurs in the strain rate range tested. This transition does appear to occur at a lower strain rate for Ti - 4 wt.% Al, at 10^0 s^{-1}, compared to Ti - 2 wt.% Al, which becomes apparent at 10^1 s^{-1}. The Ti - 2 wt.% Al specimens demonstrate a clear transitional path for shear band formation as a function of strain rate. Specimens tested at 10^{-2} and 10^{-1} s^{-1} exhibit what could be described as 'ideal' barreling followed by 'leaning', as observed in the 10^0 s^{-1} specimen, which has progressed to chip generation by 10^1 s^{-1}. Finally, bulk failure occurs due to cracking at 10^2 s^{-1}. This same progression is also apparent as a function of aluminium content in specimens tested at 10^{-1} s^{-1}. This suggests an increase in propensity for off axis instability, illustrated in Figure 5.1. The complete failure observed in the Ti - 8 wt.% Al specimen tested at 10^{-1} s^{-1} is an anomaly with the conclusion of increasing shear band propensity but failure occurred during sectioning and was equally likely to occur in all of the Ti - 8 wt.% Al specimens due to the extent of the bulk fractures observed.

The results observed in Figure 5.1 are in good agreement with observations in the literature as to the influence of aluminium content and strain rate, discussed in Sections 2.3 and 2.6. With regard to aluminium content an increase in content increases the CRSS for deformation of any type [24,26]. This causes strain accumulation, concentrating predominantly in regions experiencing the highest strain in a compression specimen under high friction condition, Figure 5.2. This strain accumulation would appear to cause failure as load dissipation becomes increasingly difficult, as the CRSS values rise to an extent that

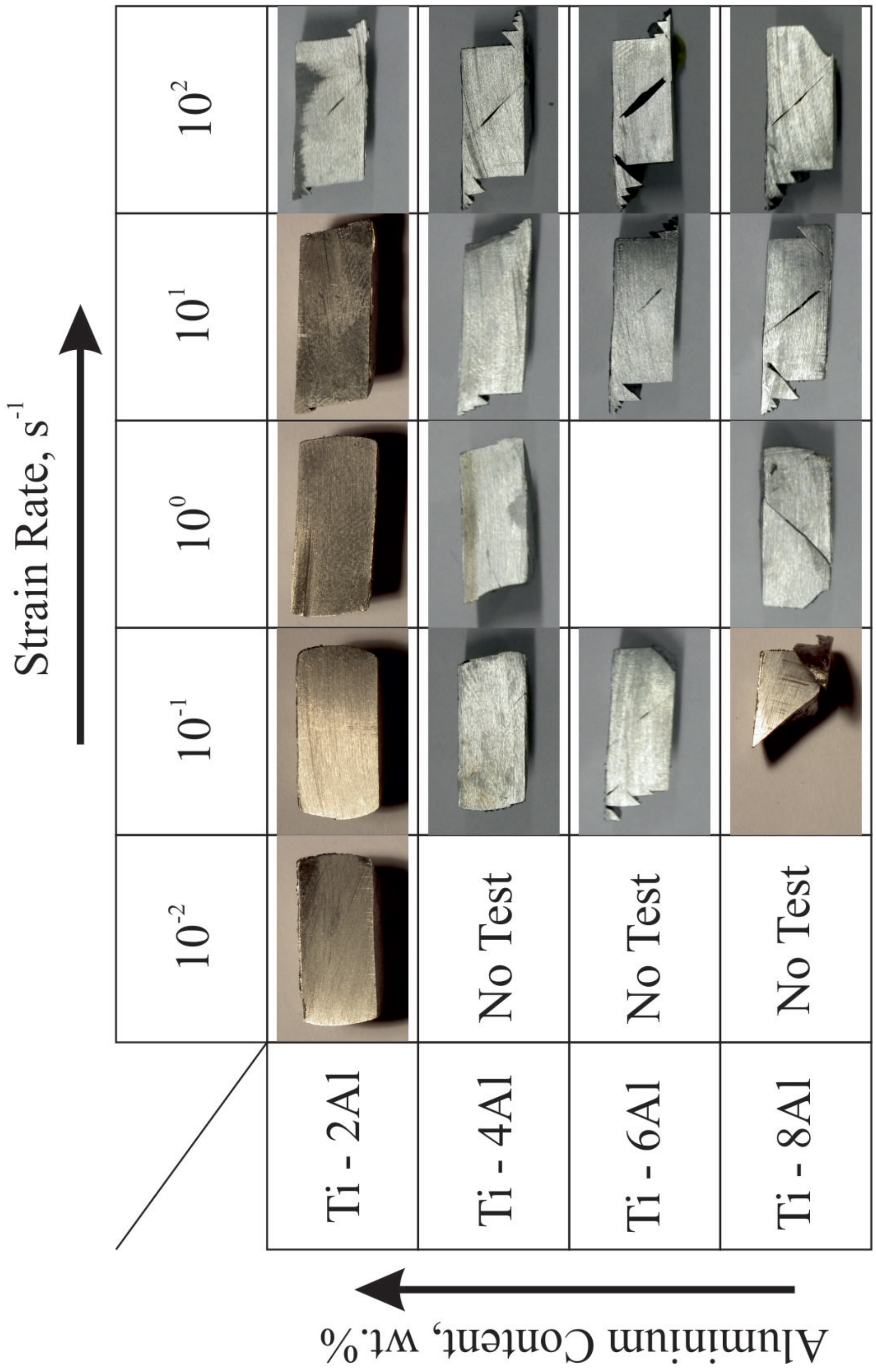

Figure 5.1: Map showing the effect of strain rate and aluminium content on the shear band characteristics. Strain rate 10^{-2} - 10^{2} s^{-1} s^{-1}, horizontal, and aluminium content 2 - 8 wt.% Al, vertical. $\epsilon = 0.7$.

(i), they are substantially more difficult to generate and (ii), the rise is so large for some individual deformation modes that the Von Mises criterion for homogeneous deformation becomes extremely difficult [26].

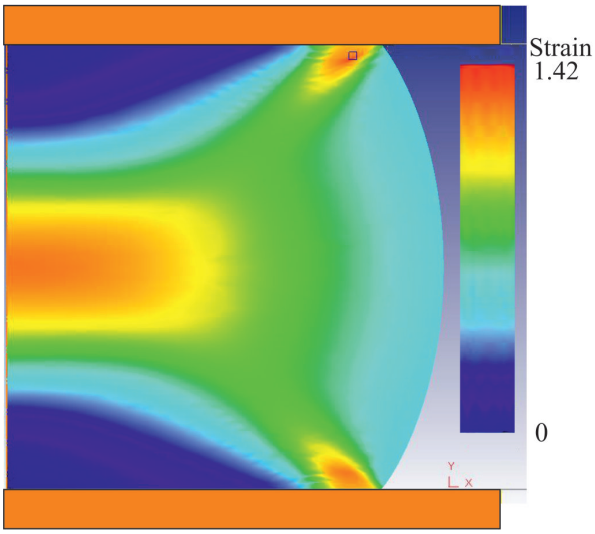

Figure 5.2: FEM model showing strain distribution in a compression cylinder, $\mu = 0.3$, 50 % reduction.

The cause of the specimen shape after compression is in contrast to that observed by Asgari [38] in α-brass, illustrated in Figure 5.3a) and b); investigation of the specimen shape suggested geometric constraint, caused by the robot arms used to insert the specimen prior to testing. When a specimen was loaded manually, meaning no constraint by the robot arms during deformation, the deformed shape of the specimen, Figure 5.3c) and d), is unchanged compared to when the robot was used. This eliminates geometric constraining, by the robot arms, as the cause for the unexpected deformed shape. This suggests that the most likely cause of the deformed shape is due to crystal structure, where α brass is face centred cubic (FCC) and α titanium is CPH; therefore, the inherent anisotropy of CPH could be responsible.

5.2 Failure Mechanism

Features inherent of the multiple theories of shear band initiation were observed. Figure 5.4 shows Ti - 2 wt.% Al specimen deformed at a strain rate of 10^1 s^{-1}, where voids have formed and are parallel to the shear bands. The elliptical shape of the voids, and the wavy morphology of the twins that intersect the shear bands, show that the material on each side of the shear band has generated a localised tensile strain, even though the macroscopic system is under compression. Figure 5.4 suggest that for this specimen the

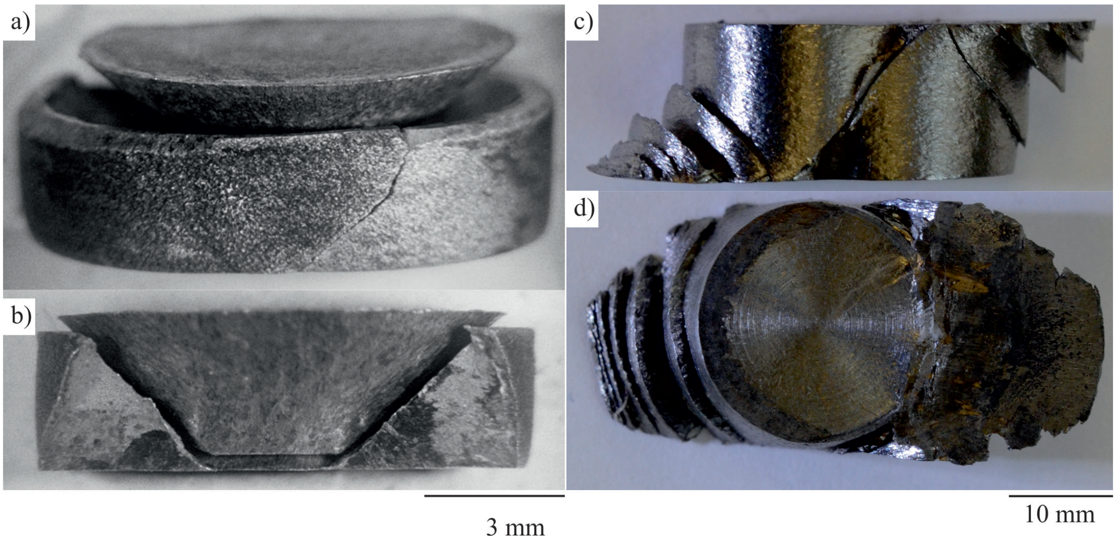

Figure 5.3: Macro images showing unconstrained axisymmetric compression specimen of a) and b) α-brass tested to $\epsilon = 1.5$ [38] and c) and d) Ti - 4Al $\dot{\epsilon} = 10^{-1}$ s^{-1}, $\epsilon = 0.7$ loaded unconstrained by robot arms.

method of failure propagation appears to be void coalescences.

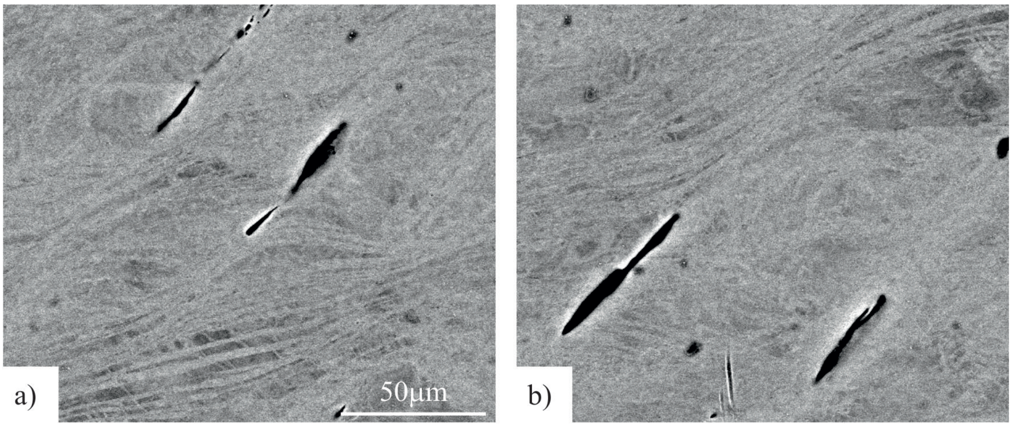

Figure 5.4: Backscatter electron micrograph depicting elongated voids formed within a shear band. a) and b) Ti-2Al, $\epsilon = 0.7$ and $\dot{\epsilon} = 10^1$ s^{-1}.

In contrast the Ti - 4 wt.% Al specimen deformed at 10^2 s^{-1} shows signs of recrystallisation, an observation that occurred in isolation, in Figure 5.5. The likely cause is not clear, as observations made on the milled specimen, in Section 4.1, show that Ti - 4 wt.% Al exhibits the highest level of twin depth penetration. It appears that, at the strain rates tested, insufficient adiabatic heating is generated to cause localised melting, in agreement with experimental literature [74]. There is sufficient evidence to support the micro-void coalescence theory. The presence of recrystallisation suggests sufficient adiabatic heating may be occurring to surpass the $0.5T_m$ temperature, required for the onset of recrystallisation, and indicates dislocation pile up is occurring in material adjacent to the shear band failure. The occurrence of this dynamic recrystallisation suggests that strain is accommodated by high levels of slip, as opposed to via twinning, suggesting that a change in dominant deformation mode occurs, from slip to twinning with increasing strain rate. From the observations made it is not possible to determine whether any failure is occurring through the proposed twin softening mechanism; a more focused testing and analysis program would be required to determine whether this mechanism is occurring.

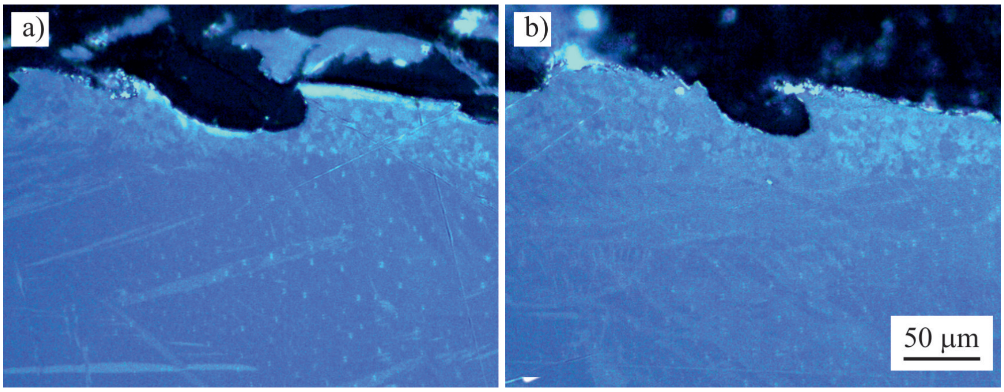

Figure 5.5: a) and b) Optical micrograph depicting recrystallised grains formed in material adjacent to shear band failure in Ti-4Al, $\epsilon = 0.7$ and $\dot{\epsilon} = 10^2$ s^{-1}.

5.3 Flow Curves

Flow curves were generated using the method described in Section 3.6.3, and are shown in Figure 5.6-5.7. Figure 5.6 illustrates the influence of strain rate. There are a number of observations, the first is that the majority of specimens exhibit a drop in flow stress at a value of between 0.3 - 0.4 strain. There is also a change in the flow stress drop off observed in the Ti - 2 wt.% Al specimens: in Figure 5.6a), the 10^1 and 10^2 s^{-1} specimens experience a drop to approximately 50% of the maximum flow stress value. As Figure 5.1 illustrates these two 2 wt.% Al specimens show clear 'leaning', and therefore shear band formation on the macroscale. A small drop in flow stress was observed in the 10^0 s^{-1} specimen, which demonstrates a transitional between the barrel behaviour at the low strain rates and the 'leaning' barrel of the higher strain rates. This suggests that the drop in flow stress indicates the point at which the shear band becomes the significant contributor for strain accommodation, and for the purpose of mechanical analysis the point of failure. It is possible that it also indicates the point at which fracture occurs; however, cracking was not observed in all the specimens that generated a significant flow stress drop. The theory of shear band strain dominance corresponding with the flow stress drop is demonstrated in the Ti - 2 wt. % Al, 10^0 s^{-1} specimen, where there is definitely no fracture and the drop in flow stress is not so much a drop, more a steady reduction. This leads to suggestions that the gradient of the flow stress drop may be an indication of the shear band severity. The tests carried out at 10^2 s^{-1} exhibit an oscillatory function on what would be considered the flat curve; the cause of this is explained in Section 3.6.3.

Across the four materials tested there appears to be minimal strain rate sensitivity for the strain rate range tested. Only a 5% variation of yield strength was observed across the range tested and the work hardening behaviour appears to be consistent across all of the test strain rates. The two other noticeable observations for 4, 6, 8 wt.% Al specimens, Figure 5.6b)-d), are that the reduction of the strain at which the flow stress drop occurs appears to be a function of the strain rate and secondly, for all the Al contents, Figure 5.6a)-d), the change in the shape of the curves, which can be more clearly explained using work hardening characteristics in Section 5.6.

Examination of the curves in relation to aluminium content, (Figure 5.7a)-d)), shows that the yield strength increases as aluminium content increases, as expected due to the increased solid solution strength imparted [127,128]. However, each of the systems clearly exhibits differing work hardening behaviour, where 4 and 6 wt.% Al show much higher rates of work hardening than seen in 2 and 8 wt.% Al. This gives an indication that while mechanical properties, such as yield strength, increase with increasing aluminium content, deformation characteristics such as work hardening show a non-linear correlation with aluminium content. For all of the curves shown in Figures 5.6-5.7, after initial failure between 0.3 - 0.4 strain the specimen begins to work harden again before undergoing a minor flow stress drop. Examination of the number of 'failures', or flow stress drops, correlates well with the number of chips observed on each specimen in Figure 5.1. This further supports the theory that shear stress drop correlates with shear band formation.

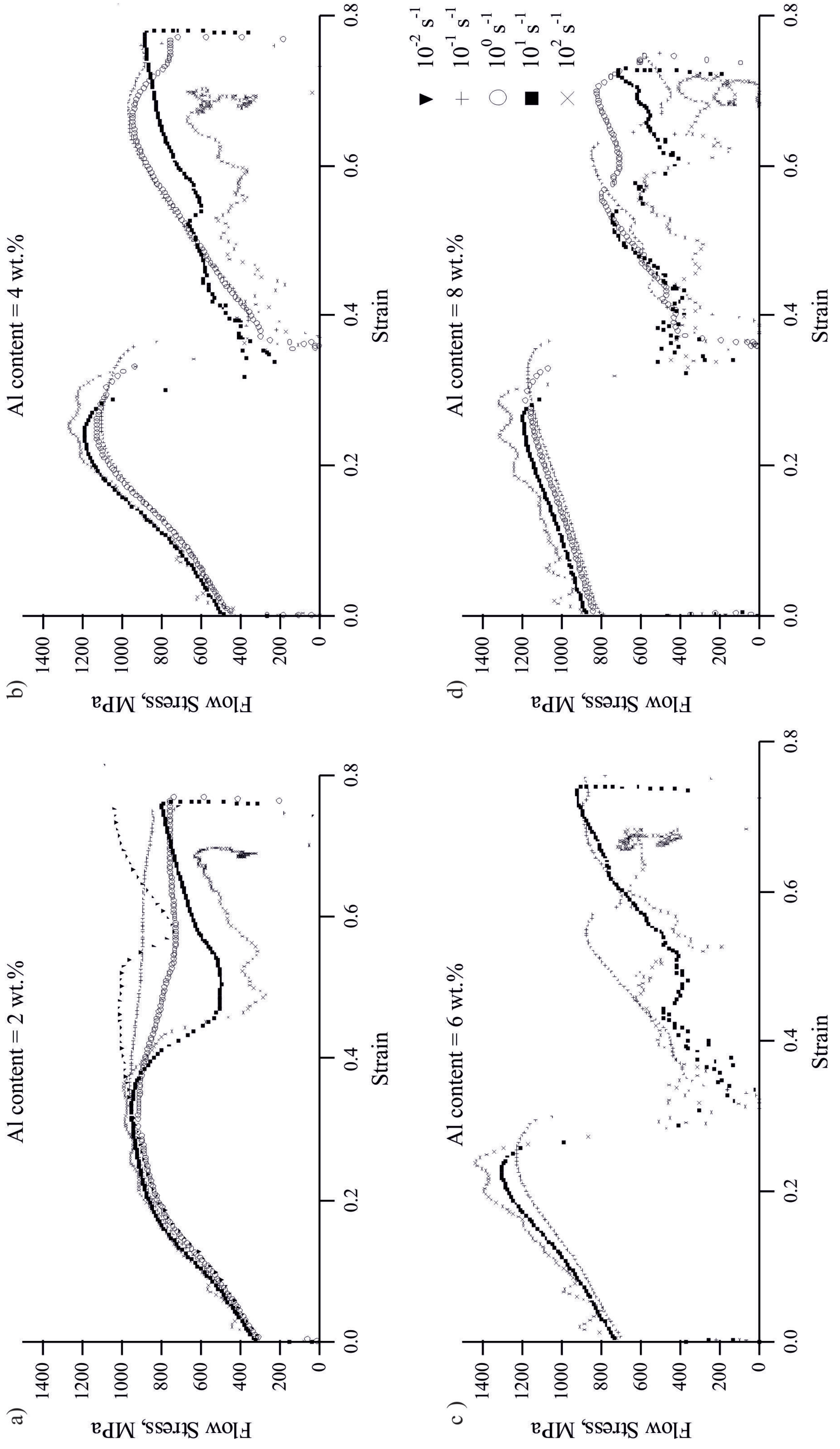

Figure 5.6: True stress vs true strain curves for strain rate ranges of 10^{-2} - 10^{2} s^{-1} for a) Ti - 2 wt.% Al, b) Ti - 4 wt.% Al, c) Ti - 6 wt.% Al and d) Ti - 8 wt.% Al.

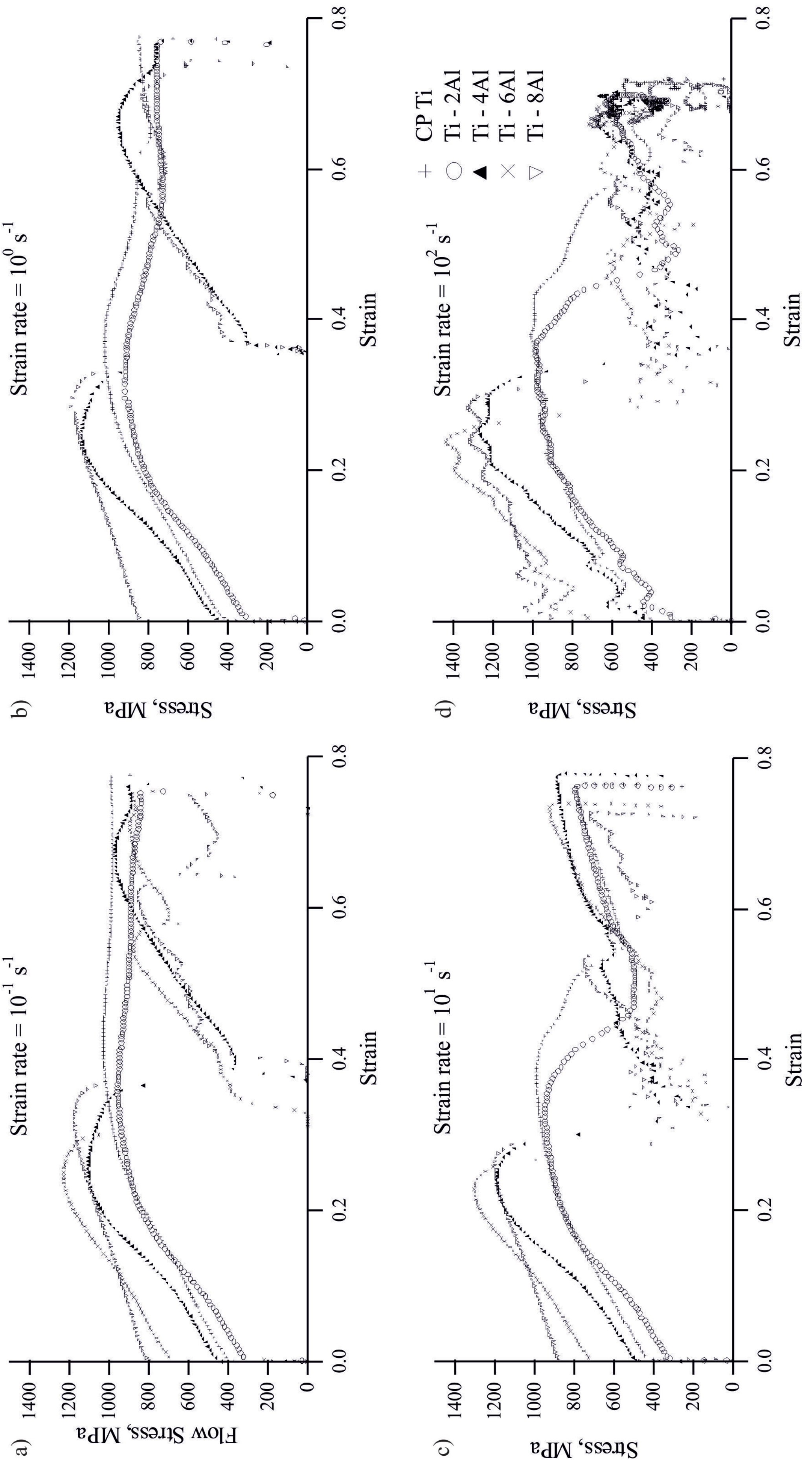

Figure 5.7: True stress vs true strain curves for aluminium contents 2 - 8 wt.% Al for a) 10^{-1} s^{-1}, b) 10^{0} s^{-1}, c) 10^{1} s^{-1} and d) 10^{2} s^{-1}.

5.4 Binary Batch 1 vs. Binary Batch 2

Two lots of binary alloys were produced and due to slight inconsistencies in the titanium production route, Lots *I* and *II* had varying compositions. Figure 5.8 shows the effect of composition differences, highlighted in Tables 3.1 and 3.2. The most important observation is that the shape of the curve remains the same even with the variation in aluminium and oxygen content. As expected, considering lot *I* has consistently higher aluminium contents than lot *II*, the lot *II* flow curves are slightly lower compared to lot *I*. Further examination of the chemistry shows that there is an 'anomaly' when examining the aluminium equivalence of the two lots. The aluminium equivalency equation, Equation 5.1, suggests that due to the oxygen contents in Ti - 4 wt.% Al, lot *II*, the curve should have a higher, or at least comparable, flow stress, considering the difference, 4.5 and 4.6 for lot *I* and *II* respectively. As an aside this result suggests that the aluminium equivalency equation may contain an overestimation of the influence of oxygen. The final observation is that the lot *II* Ti - 2 wt.% Al alloy appears to undergo shear band deformation, indicated by the stress drop in Figure 5.8 and observed in Figure 5.9; the cause of this is not clear. Chemistry suggests that if either is to shear then it should be lot *I*. Further examination of literature indicates that the difference in grain size does not account for the variation in failure [60], and by extension shear band behaviour. Ghaderi [108] showed in AZ31 magnesium alloy that an increase in grain size shows a lowering of experienced stress during compression but also a reduction in the failure strain, which is a contradiction to what is observed here. As there is no reproduction of experiments in this work, due to quantities of the alloys produced, it is difficult to identify the exact cause, but as has been highlighted in Section 2.7 the potential causes are numerous such as alloy inhomogeneity and variation in specimen geometry (corner radius rather than height and diameter).

$$Al_{eq} = Al + \frac{Sn}{3} + \frac{Zr}{6} + 10(O + N) \tag{5.1}$$

Examination of aluminium segregation occurred and the results are represented in Figure 5.10. This shows that there is no clear variation in aluminium content induced by, or a cause of, shear band formation. However, this result does not rule out aluminium segregation occurring on a much finer scale than the resolution of the SEM microscope used and a more detailed examination using TEM would be needed to confirm that no segregation is occurring on the nano to micro scale, as opposed to the micro to macro scale possible using SEM.

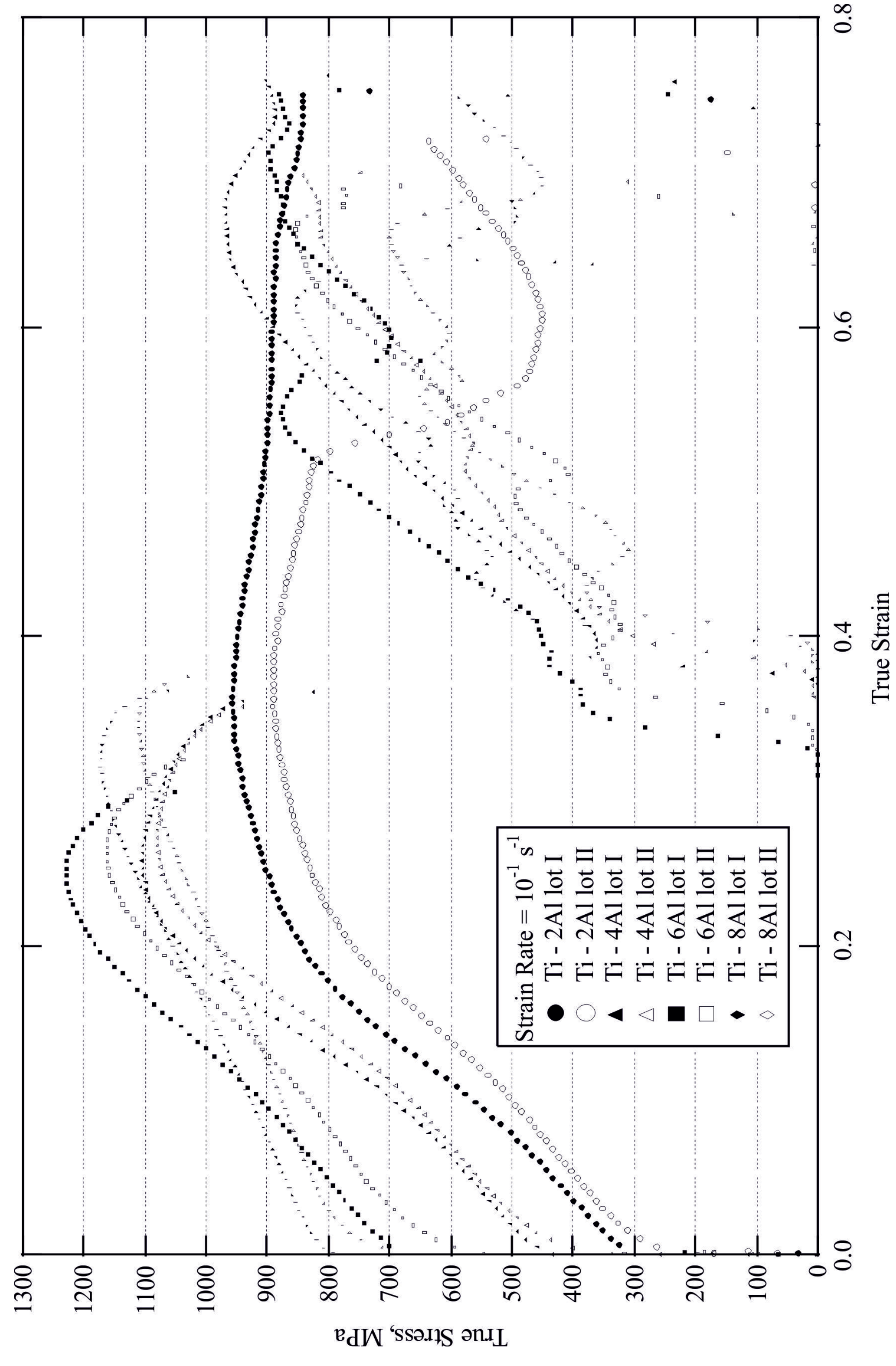

Figure 5.8: Flow curve comparison of lot *I* and lot *II*, $\dot{\epsilon}$ 10^{-1} - 10^{1} s^{-1}. Lot *I* $\epsilon = 0.7$, lot *II* $\epsilon = 0.3$ - 0.4.

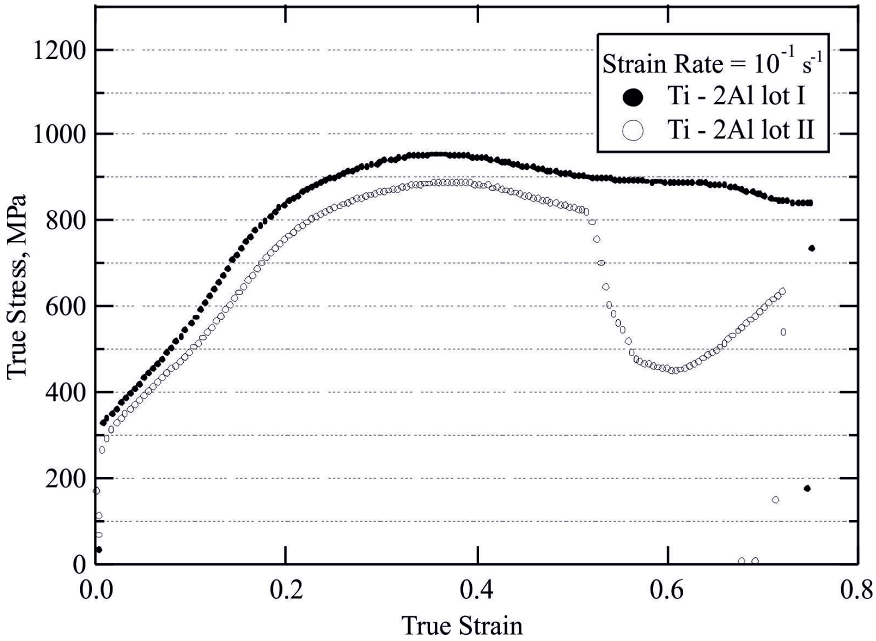

Figure 5.9: Flow curve comparison of Ti - 2 wt.% Al batch 1 and batch 2, $\dot{\epsilon}$ 10^{-1} - 10^{1}. Batch *I* $\epsilon = 0.7$, batch *II* $\epsilon = 0.3$ - 0.4.

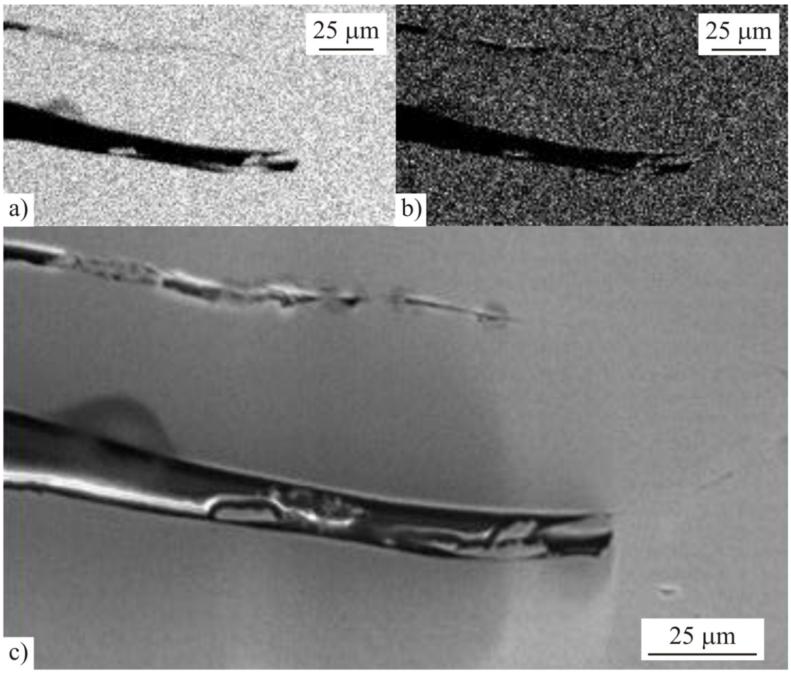

Figure 5.10: EDAX mapping showing qualitative distribution of aluminium and oxygen in shear band region for *I* of Ti - 8 wt.% Al specimens compressed to 0.7 true strain.

5.5 Strain to Onset of Failure

From the flow curves in Figures 5.6-5.7 it is possible to extract a number of material behaviours, which could indicate how the material will behave when machined. The first behaviour is the strain to onset of failure. This is defined as the strain at which maximum stress occurs; from this point the material exhibits flow softening before failure. These curves, illustrated in Figure 5.11, show that a minima occurs at Ti - 6 wt.% Al; however, the values for Ti - 4 wt.% Al are only marginally higher. Ti - 8 wt.% Al shows an unexpected result, based on the literature, which demonstrates continually increasing CRSS values for all deformation modes, because it shows an increased strain to failure compared to 4 and 6 wt.% Al.

Results from the literature would suggest that the increases in CRSS would increase the propensity for deformation via strain localisation in higher aluminium content material. This should lead to higher quantities of strain accommodation within the shear band, ultimately leading to failure at lower strains compared to lower aluminium contents. Some of this unexpected behaviour of Ti - 8 wt.% Al, shown in Figure 5.12, is mitigated in that the maximum stress values occur at strain values very close to failure, demonstrating a very low amount of work softening prior to complete failure. This is in contrast to Ti - 4 wt.% Al, which shows an extended softening regime compared to the other compositions. This leads to examination of strain when $\sigma = 0$ (for CP titanium the strain value used is when stress is at mininimum) in Figure 5.13. This plot shows a very similar trend to that observed in Figure 5.11. The largest difference is the shift of lower aluminium contents, CP, 2 and 4 wt.% Al, to higher strain values, which indicates a larger strain region of work softening in contrast to the higher aluminium contents of 6 and 8 wt.% Al. At the lowest strain rate, the CP titanium material undergoes no failure and either continues to work hardening or plateau up until the test is terminated at the predetermined end point of 0.7 true strain. However, this alteration in approach still shows consistently lower strain values for Ti - 6 wt.% Al and equal values for Ti - 4 wt.% Al in comparison to Ti - 8 wt.% Al. This shows that while some of the behaviour observed in Figure 5.11 has been accounted for, Ti - 8 wt.% Al is still ‘overachieving’ based on the predicted behaviour. As discussed in Section 3.6.4, the cause could be a variation in the deformation behaviour which is linked to the work hardening behaviour, which has previously been identified as variant with aluminium content.

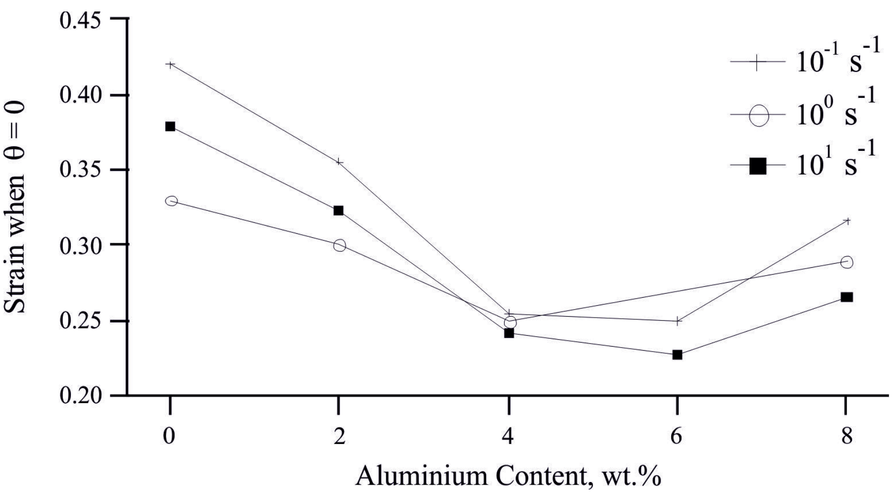

Figure 5.11: Graph showing strain at work hardening rate (θ) = 0 as a function of aluminium content, 2 - 8 wt.% Al, for a range of strain rates, 10^{-1} - 10^{1} s^{-1}. $\epsilon = 0.7$.

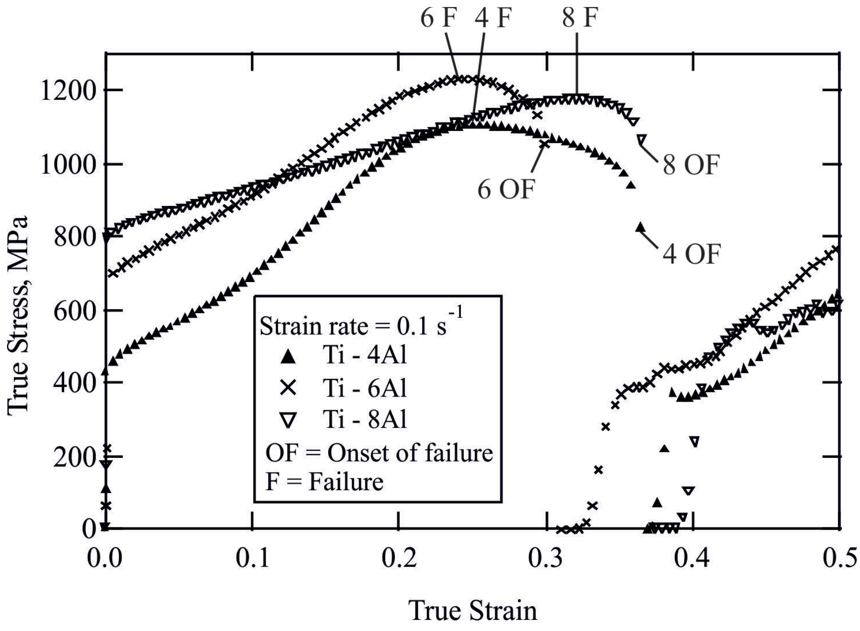

Figure 5.12: Graph showing variation of failure and onset of failure for titanium 4, 6 and 8 wt.% Al alloys. Strain rates 10^{-1} s^{-1}.

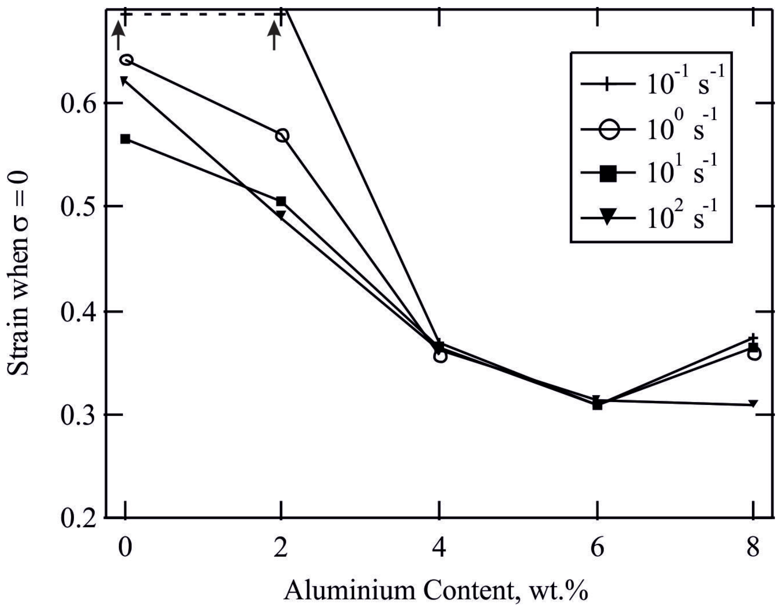

Figure 5.13: Graph showing strain at failure, $\sigma = 0$ as a funct ion of aluminium content, 2 - 8 wt.% Al, for a range of strain rates, 10^{-1} - 10^{1} s^{-1}. $\epsilon = 0.7$.

5.6 Work Hardening

The work hardening behaviour, Figure 5.14, of the alloys shows a three stage work hardening profile, identified in Figure 5.15. As has been highlighted previously by Salem [40, 59, 60], in CPH material, and Asgari [38], in FCC material with low stacking fault energy, each of the regions is associated with a particular deformation mode. Region *I* of the work hardening curve is characterised by dynamic recovery, Region *II* has been shown to indicate the onset of mechanical twinning, and Region *III* demonstrates dynamic recovery (comparable to Region *I*). The 10^2 s^{-1} experiments were not included as the load cell 'ringing' oscillations give a hugely fluctuating curve that does not represent the materials actual behaviour. Previous work has shown that the three stages of work hardening observed here have been widely observed in CPH materials, in CP titanium and magnesium most notably [40, 58–60, 108]. Examination of the work hardening behaviour demonstrates minimal change as a function of strain rate in the range tested. Ti - 4 wt.% Al, Figure 5.14b), in particular demonstrates that at the strain rates tested the material has an even lower strain rate dependency as there is no accelerated reduction in work hardening rate in Region *III*, as observed in 2, 6 and 8 wt.% Al. This indicates that the strain of maximum stress, $\epsilon_{\sigma_{max}}$, extracted from the curves in Figure 5.7, is independent of strain rate for the tested strain rates. This is unexpected as with 2, 6 and 8 wt.% Al an increasing strain rate correlates to a decreasing $\epsilon_{\sigma_{max}}$. This is clearest in the 2 and 8 wt.% Al specimens, Figure 5.14a) and d). Ti - 6 wt.% Al follows this trend but may be spurious as there are only two usable flow curves.

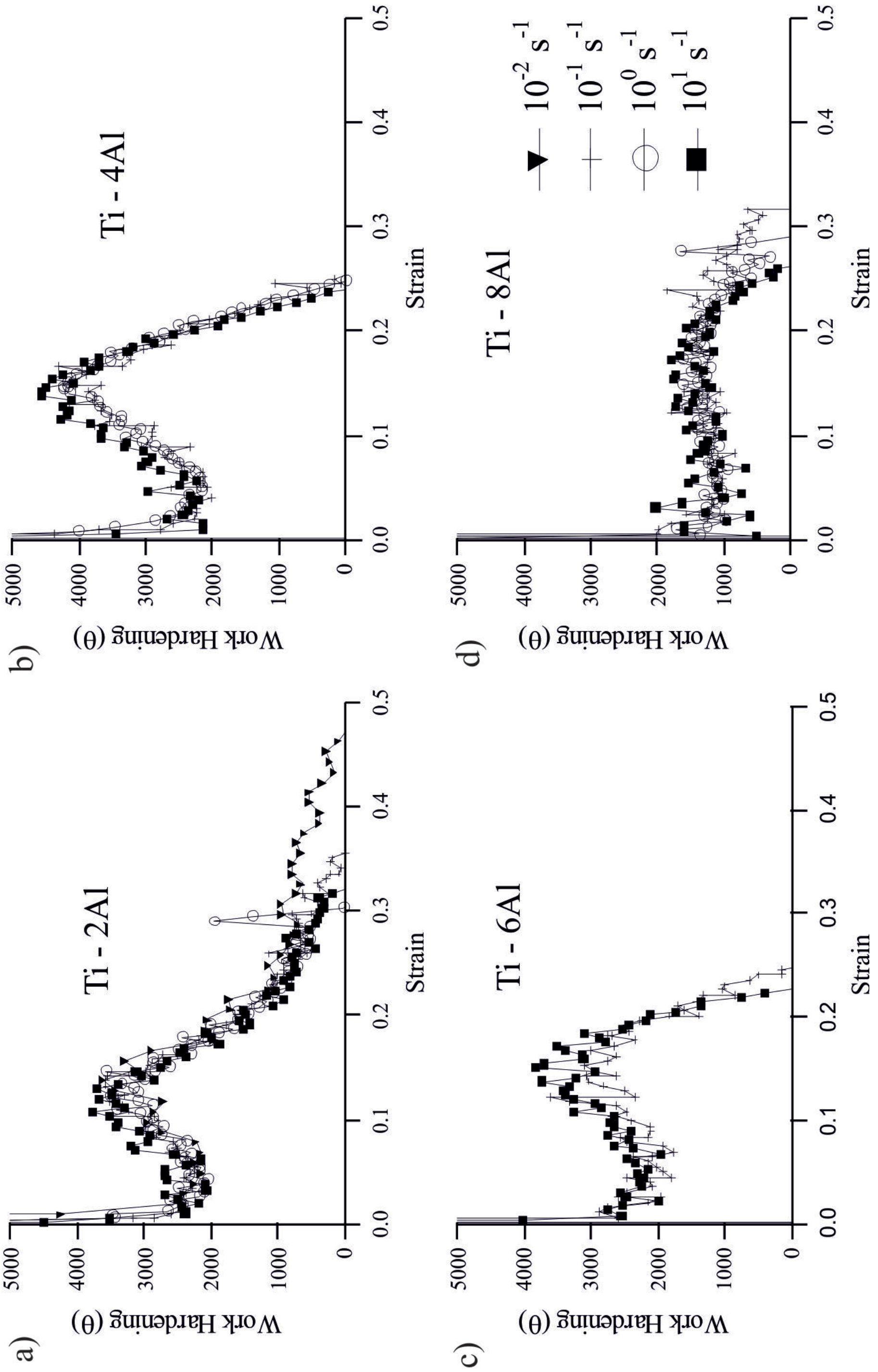

Figure 5.14: Work hardening (θ) behaviour of axisymmetric compression tests for titanium alloys containing 0 - 8 wt.% Al at strain rates a) 0.1 s^{-1} b) 1 s^{-1} and c) 10 s^{-1}. $\epsilon = 0.7$.

Comparison of results from Salem [60], illustrated in Figure 5.16, to the CP titanium tested here shows that the curves are similar: both show the three region shape but exhibit a large difference in the strains at which region boundaries occur and the magnitude of work hardening. The transition Region $I \rightarrow II$ is comparable for both Salem and this work; however, the transition Region $II \rightarrow III$ is noticeably higher for Salem, and the level of work hardening is significantly lower in Region II. Examination of the grain size, which shows some influence in Salem's work, is not the cause as the grain size tested here is comparable to the 30 μm specimen of Salem, thus grain size is not the source of the discrepancy. Examination of chemistry also shows little to no influence: Salem's material contained 95 ppm oxygen compared to 1400 ppm for the CP titanium tested here. This leads to examination of lots *I* and *II* of the binary alloys. Tables 3.1 and 3.2 show that all the alloys contain similar differences in aluminium content between lots *I* and *II* but a greater variation in oxygen content. For example: the extremes, lot *I* being 700 ppm higher for Ti - 2 wt.% Al and *II* being 70 ppm higher for Ti - 4 wt.% Al. As can be observed in Figure 5.17a) - d) there appears to be no significant variation in the behaviour of lot *II* compared to *I*. With all plots there appears to be an offset. Firstly the strain at which Region $I \rightarrow II$ and $II \rightarrow III$ transition occurs are lower for lot I; it also exhibits an increased work hardening rate. The shift to lower strains is likely caused by slight inconsistencies in testing. A variation in the elastic behaviour for each alloy, characterised in Region *I*, shows that lot *II* exhibits more elastic behaviour than *I*, characterised by the boundary between Region $I \rightarrow II$, therefore yield occurs at slightly higher strains. The drop to lower gradient values, therefore lower rates of work hardening, is another behaviour observed in both scenarios. The cause of this is unclear but rules out oxygen variation being the dominant cause for the variation between this work and Salem's because the shift is consistent between both lots of alloys but the oxygen variation is not. A similar observation is made with grain size, where there is differing variation between lot *I* and *II* which is inconsistent with the shift observed in the curves, supporting the grain sizes relative lack of influence. The consistent shift in Figure 5.17 seems most likely due to aluminium levels as they consistently measure approximately 0.1 wt.% higher in lot *I* compared to lot *II*. However, this provides no insight into the cause of the two sets of CP titanium results; closer examination of the texture of each shows a potential cause, as is observed in Figure 5.18.

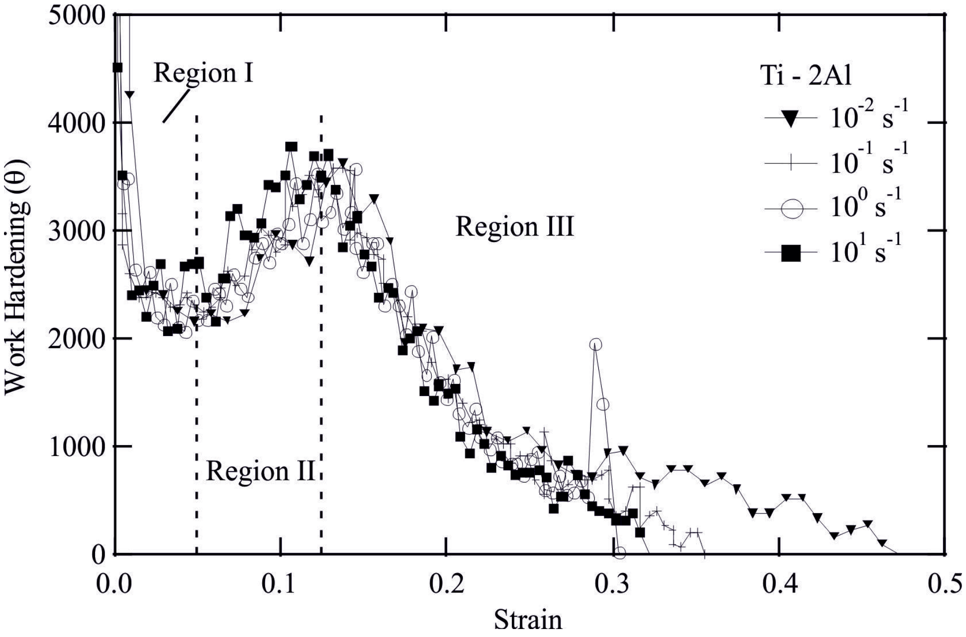

Figure 5.15: Work hardening (θ) of Ti - 2 wt.% Al at a range of strain rates between 10^{-1} - 10^{1} s^{-1} with each of the three regions identified.

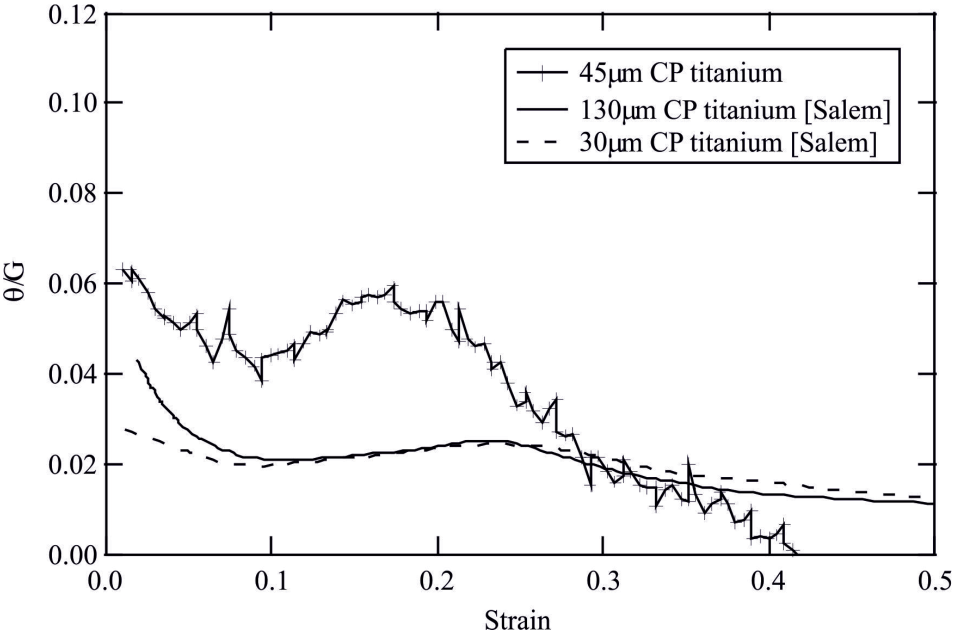

Figure 5.16: Plot showing work hardening of CP-Ti with grain size 45, 130 and 30 μm, 130 and 30 μm results from Salem [60].

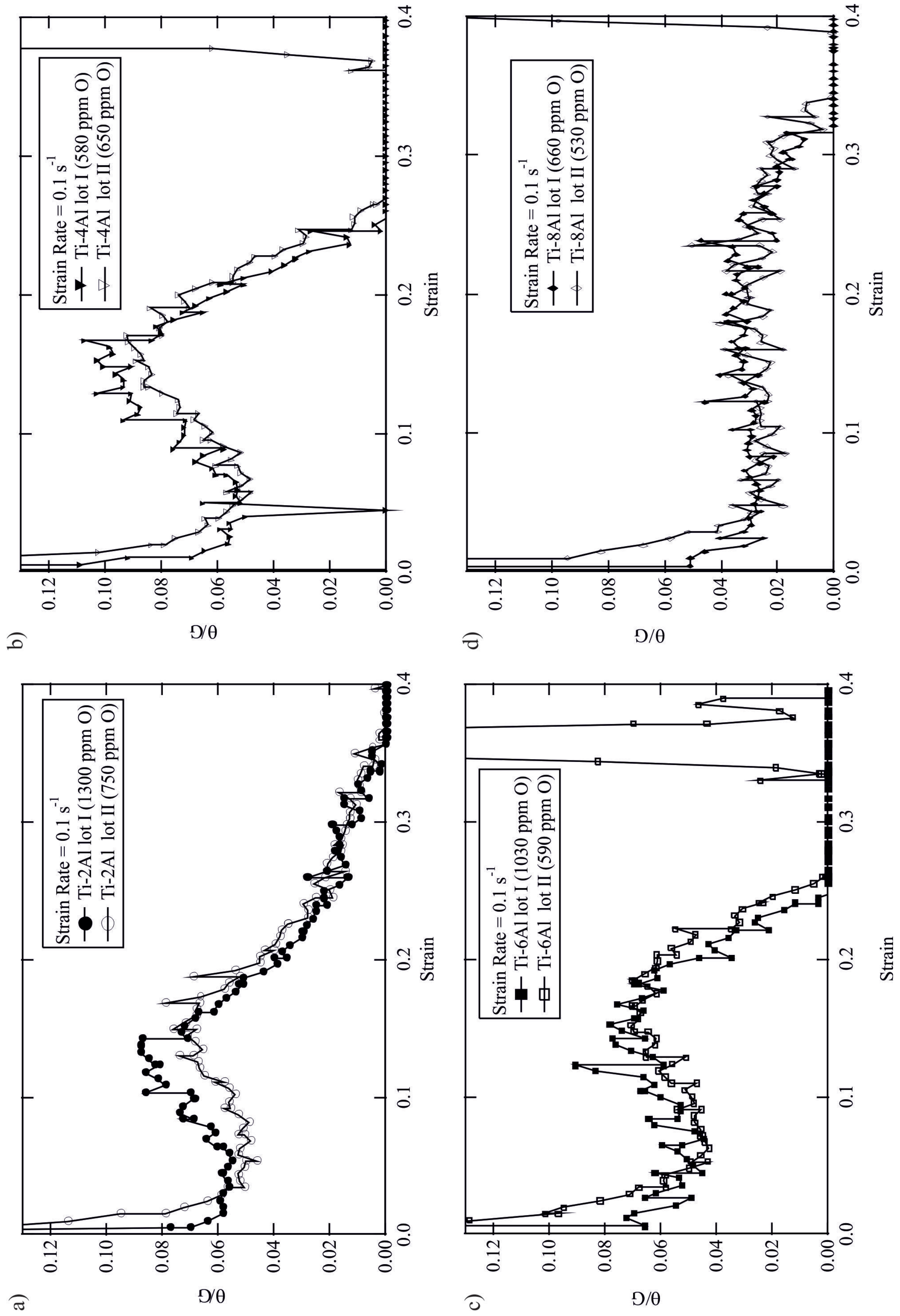

Figure 5.17: Plots showing a) work hardening of Ti - 2 wt.% Al from lots *I* and *II* with different oxygen contents, 1300 and 750 ppm respectively, b) work hardening of Ti - 4 wt.% Al from lots *I* and *II* with different oxygen contents, 580 and 650 ppm respectively, c) work hardening of Ti - 6 wt.% Al from lots *I* and *I* with different oxygen contents, 1030 and 590 ppm respectively, d) work hardening of Ti - 8 wt.% Al from lots *I* and *II* with different oxygen contents, 660 and 530 ppm respectively.

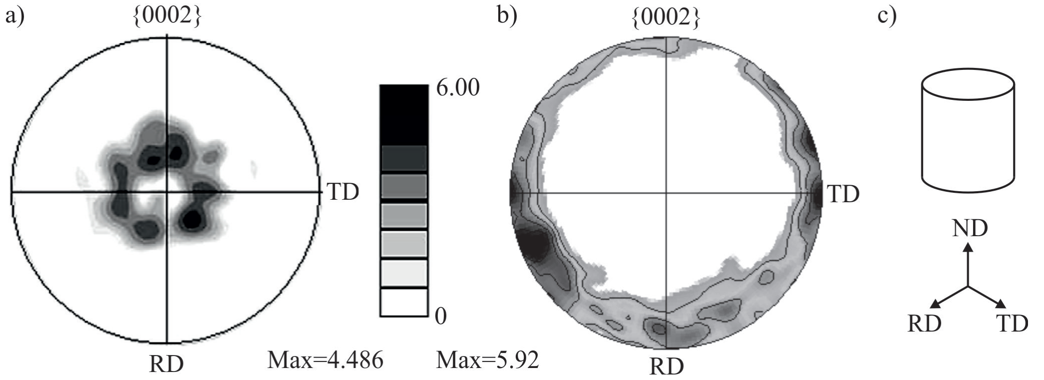

Figure 5.18: Pole figures for {0002} plane for a) CP titanium tested by Salem [40] and b) CP titanium tested here. c) shows pole figure directions relative to direction of compression.

Each material shows a different starting texture; Salem shows an as-forged texture with the *c*-axis perpendicular to the forging direction and parallel with the *c*-axis of the compression specimen, which is consistent with a disk sliced from billet. In contrast, the texture observed in the CP titanium bar used here is an extrusion texture so the *c*-axis is perpendicular to the extrusion direction and also the *c*-axis of the compression specimens. This contrasting texture appears the likely cause as work performed on magnesium alloy AZ31 [63] showed a significant variation in flow and work hardening behaviour as a function starting texture. Based on this work the CP titanium tested by Salem [40] is most comparable to the specimen $C//ND$ and the CP titanium from this work comparable to the $C//ED$, according to their texture. As was observed by Wang [63] the extrusion texture observed shows a higher work hardening rate in contrast to the as-forged texture which demonstrates low levels of work hardening behaviour. The biggest variation observed when compared to Wang is for the as-forged texture and the CP titanium tested by Salem: Wang shows a magnesium alloy that demonstrates a curve that comprises only Region I, meaning no work hardening occurs, where Salem shows a weak work hardening Region II followed by Region III. The cause for this is likely to be the more significant role basal slip plays in magnesium compared to titanium where $\{10\bar{1}0\}$ is dominant. However, the result appears to confirm that textural variation is the dominant contributor to the large difference in behaviour observed between this work and Salems.

Exploration of work hardening as function of aluminium content, illustrated in Figure 5.19, shows that all the alloys exhibit comparable $I \rightarrow II$ transitions, a trend of increasing levels of work hardening to a maximum and then a reduction beyond that. In all the strain rates tested Ti - 4 wt.% Al showed the highest work hardening yet comparable strain values for the $II \rightarrow III$ transition. Another observation is the comparable behaviour of the 2 and 6 wt.% Al alloys, where the curves are coherent until after the onset of Region *III*, where 6 wt.% Al reaches zero work hardening, a plateau on the flow curve, at a lower strain than Ti - 2 wt.% Al indicating lower levels of work softening. Finally Ti - 8 wt.% Al exhibits a much lower work hardening rate in Region II compared to the other three compositions but also a much later Region $II \rightarrow III$ transition. Based upon literature results [40], which show a saturation of twin volume fraction with increasing strain. Figure 5.20 shows that the saturation appears to coincide with the transition between Region $II \rightarrow III$. This leads to the possibility that the lower work hardening rate means that higher strain values are required to reach saturation, the knock on effect meaning failure is suppressed until saturation has been achieved. This also suggests why Ti - 4 wt.% Al fails earliest as the work hardening rate is much higher achieving saturation earlier.

5.7 Cockcroft-Latham Damage Criterion

Cockroft-Latham damage criterion, also the work done, as described in Section 3.10.3, is the energy imparted on the work piece by the tool. One potential method for assessing machinability would be to analyse the work imparted on the work piece for a cut to occur. Newtons third law states that 'when one body exerts a force on a second body, the second body simultaneously exerts a force equal in magnitude and opposite in direction to that of the first body'. Assuming a situation of constant machining conditions, a material which possesses a lower work done threshold to cause failure would also allow an improvement in tool life, either increased speed or longer life at lower speeds, as according to Newton's Third Law, less work on the work piece means equally less work being imparted on the tool. After determination of work to failure values, a clear trend that shows a minima occurs at Ti - 4 wt.% Al. This would have been predictable based on the strain to failure, illustrated in Figure 5.13, as 4 and 6 wt.% Al have comparable strain failure values, but Ti - 6 wt.% Al exhibits higher stresses. This suggests that the root cause of TIMETAL™54M improved machinability over Ti-6Al-4V, reported by Armendia [6], could be the reduced level of aluminium causing a reduced work threshold to chip formation and therefore less damage on the tool.

Both of these behaviours appear consistent with the deformation behaviour observed in the axisymmetric compression specimens in Chapter 4. This result is significant because it indicates that the deformation behaviour is constant across the axisymmetric compression test and the high speed milling; significantly this occurs across the strain rate range generated in each of these testing methods. Confidence that deformation behaviour is comparable between low and high strain rates also validates the approach of using axisymmetric compression testing to analyse high speed machining. Use of the orthogonal cutting test will allow bridging of the disparate analysis techniques employed in this chapter and Chapter 4.

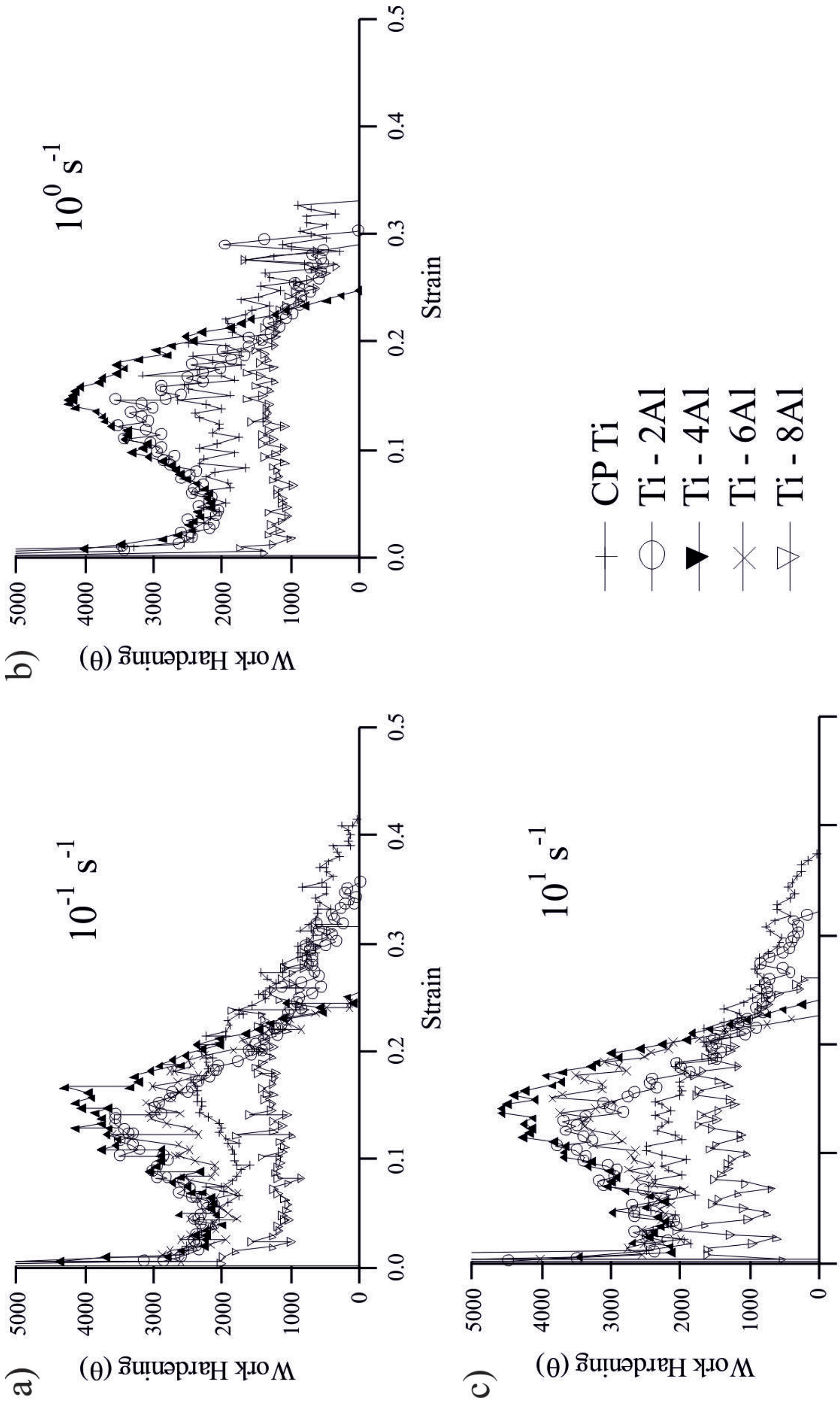

Figure 5.19: Graph showing work hardening ($\theta = \frac{d\sigma}{d\epsilon}$) vs strain behaviour of axisymmetric compression tests for titanium alloys containing 0 - 8 wt.% Al at strain rates a) 10^{-1} s^{-1} b) 10^{0} s^{-1} and c) 10^{1} s^{-1}. $\epsilon = 0.7$.

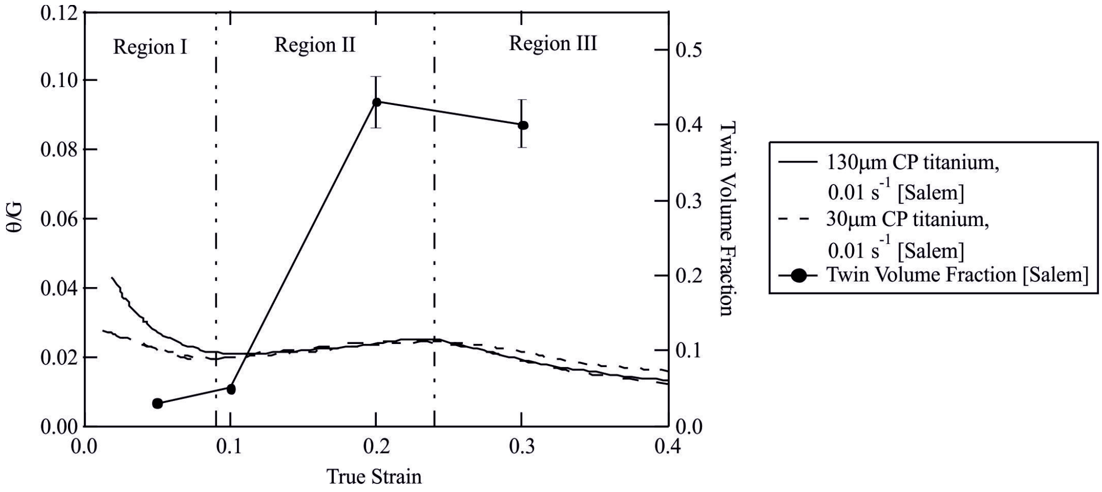

Figure 5.20: Plot showing twin volume fraction relative to regions of normalised work hardening. θ/G plots [59], twin volume fraction [40].

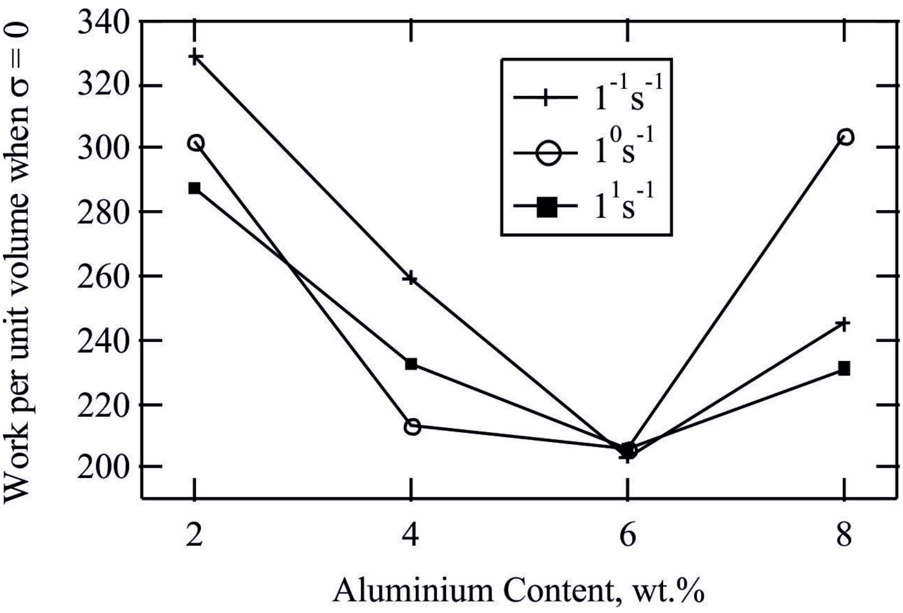

Figure 5.21: Graph showing the Cockcroft - Latham parameter as a function of aluminium content for a range of strain rates 10^{-1} - 10^{1} s^{-1}. $\epsilon = 0.7$.

5.8 Deformation Behaviour

As the key to 'machiniabilty' lies in increased tool life or increased tool speed it can deducted that the key metric by which we perhaps should measure 'machinability' is through the Cockcroft - Latham parameter as this is a measure of the work imparted in a system, and therefore a reflection of the work being imparted into the tool. Figure 5.22 shows three graphs that plot the relationship between the Cockcroft - Latham parameter and the three main contributing material characteristics; the yield strength, the strain at onset of failure and the work hardening. As can be observed from a) and b) neither the yield strength or the strain at onset of failure show and strong correlation to the Cockcroft - Latham parameter, even if Ti - 8 wt.% Al is discounted due to the short range ordering [50] no correlation is apparent. However, Figure 5.22c) shows a correlation between the Cockcroft - Latham parameter and the work hardening. This suggests that dominant mechanism to determine the 'machinability' of a given alloy could lie in understanding the dominant deformation mechanism, as the high work hardening rate in Ti - 4 wt.% Al is a result of the rapid saturation of the material by twinning, as demonstrated by Salem [40]. It is possible that this rapid saturation of twins in the material which leads to a reorientation of the material with a higher Schmid factor for slip, as observed in Figure 4.10, allows a large amount of slip, and therefore strain accommodation, to occur for a relatively low amount of work when compared to a material orientated less favourably for slip, ie. the parent grain. This would potentially facilitate failure through a mechanism comparable to twin softening, described in Seciton 2.7.5.

5.9 Experimental Axisymmetric Compression Vs Literature Strains

Figure 5.23 suggests that it takes approximately 0.8 strain locally for failure to occur. This hypothesis is based upon two dimensional FEM models of an axisymmetric compression using materials data obtained experimentally, described in Section 3.10.2. This approximation is based upon two assumptions: the first that the friction coefficient, μ, between the material and the tool is 0.3, and the second that any adiabatic shear bands that form initiate at the location of highest strain, the edge of the surface in contact with the tool. Comparison to data collected by Shankar [93] for CP titanium, where strain measurements were made *in situ* of the machining process, observed a value of approximately 0.7 strain, illustrated in Figure 5.24. This shows a reasonably good agreement with the estimation made from the FEM model, leading to the conclusion that adiabatic shear band formation is heavily dependent upon the effective strain. Effect of strain rate on adiabatic shear band formation is unclear but results obtained here from compression testing suggests that it may not be of significant importance as the curves are comparable past the known initiation of shear bands.

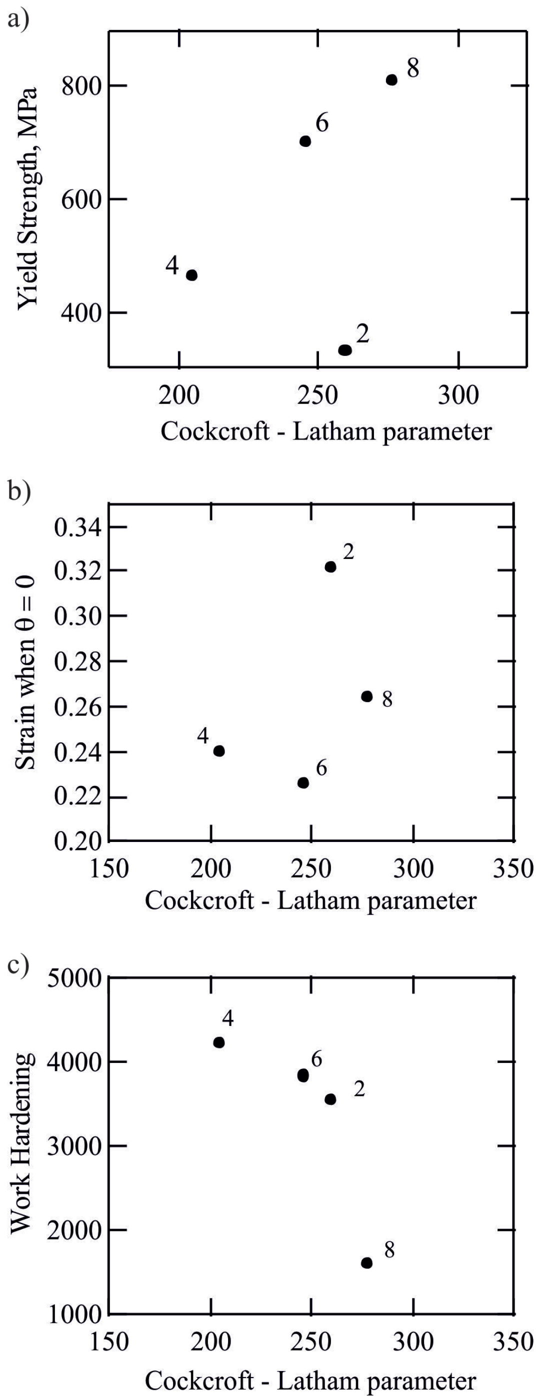

Figure 5.22: Plots showing a) Cockcroft - Latham parameter vs yield strength b) Cockcroft - Latham parameter vs strain at onset of failure and c) Cockcroft - Latham parameter vs peak work hardening.

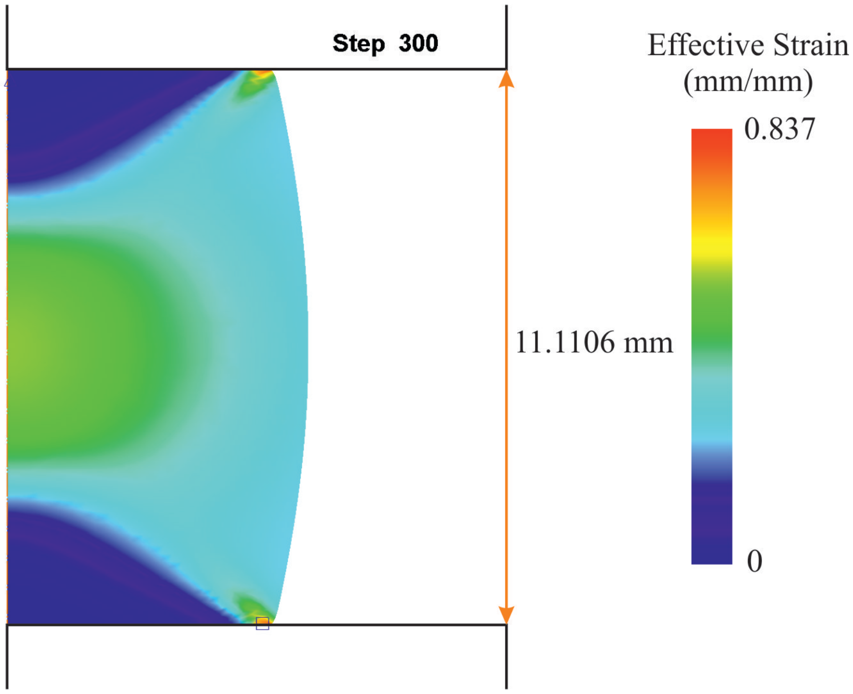

Figure 5.23: FEM model illustrating approximation of strain distribution and levels in specimens compressed to 0.3 true strain.

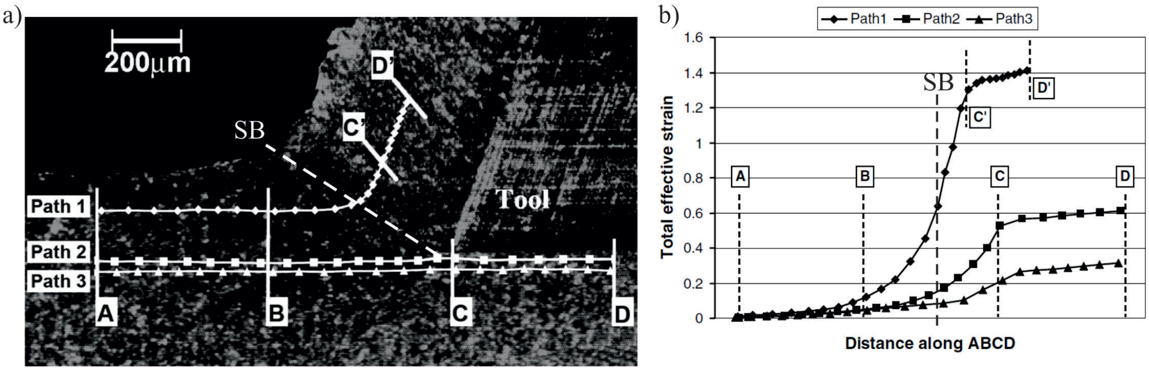

Figure 5.24: a) Micrograph showing particle paths for determination of effective strain values b) Showing particle trajectories for the paths indicated in a) [93].

5.10 *Shear Band Failure*

As discussed in Section 2.7.1 multiple potential propagation mechanisms for shear band failure could be present; ex-situ analysis of specimens showed characteristics from a number of mechanisms. Upon examination of the shear bands it is clear that a variety of propagation mechanisms occur within a specimen, depending on location and by extension its strain profile. Figure 5.25 shows two alternate shear band morphologies, a) being almost fibrous in appearance whereas b) shows a shear band comparable to that generated in industrial alloys, for example Ti-6Al-4V [103] in Figure 2.41. The cause of this is not immediately clear and investigation of the literature shows no occurrences of a fibrous shear band comparable to that observed in Figure 5.25a); all depict a shear band similar to that in Figure 5.25b).

While many of the conclusions drawn during this section have not been comprehensively verified, enough has been observed to achieve the following: one, that the material presented here accurately represents the commonly observed mechanical and deformational behaviour widely observed not just in titanium alloys but CPH materials in general. Two, the consistency of results from the axisymmetric compression to the high speed milling, and therefore by extension the low and high strain rate deformations, continue to support the potential for determining ‘machinability’ behaviours of high speed cutting operations from much slower, and therefore lower strain rate, testing methods that possess much higher levels of control.

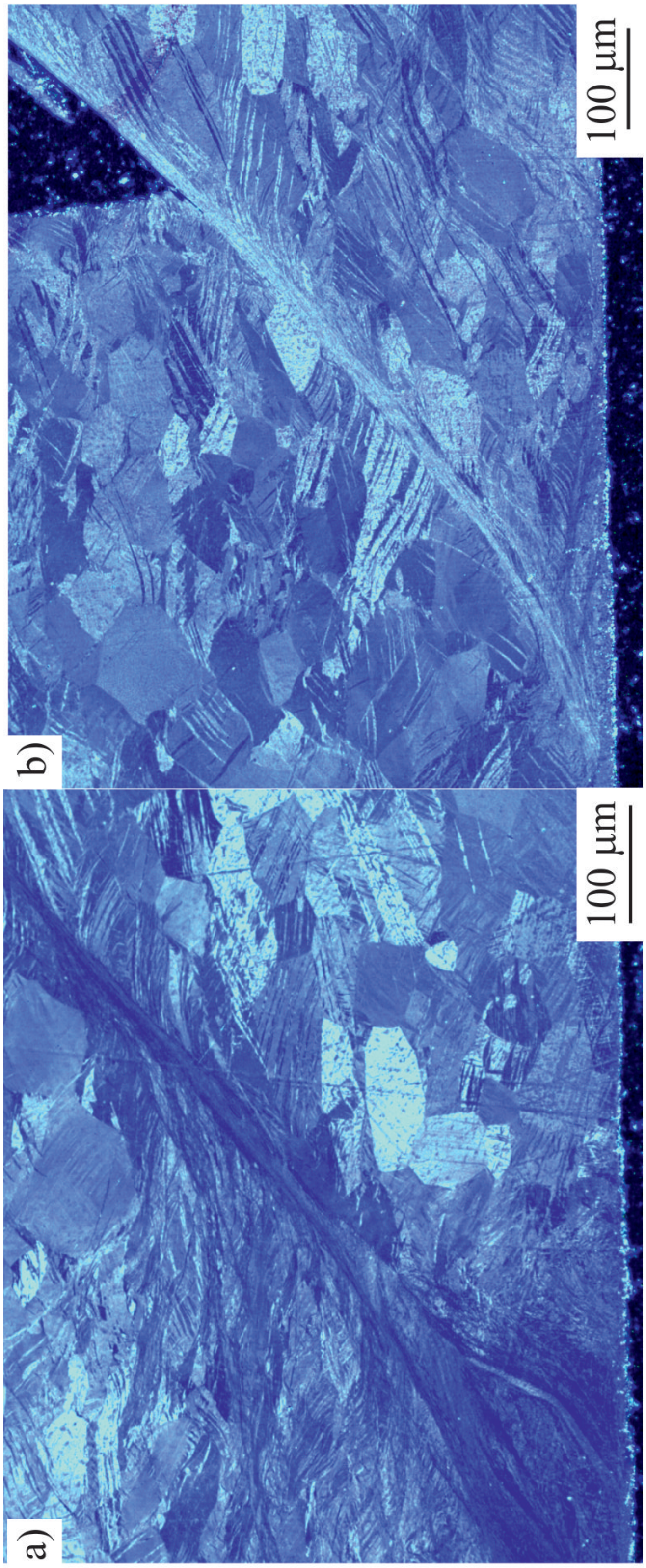

Figure 5.25: Light micrographs showing shear banded regions in Ti - 4 wt.% Al $\dot{\epsilon} = 10^2$ s^{-1}, $\epsilon = 0.7$ a) in the middle of the specimen and b) in the chip generated on the compression surface.

6. ORTHOGONAL CUTTING TEST RESULTS AND DISCUSSION

6.1 Tool Damage

After performing orthogonal cut experiments on the Ti - 4 wt.% Al specimen it was observed that the cutting face of the tool was fractured, illustrated in Figure 6.1, a phenomenon that occurred for 6 and 8 wt.% Al also. Measurements of the fracture area normalised by the cut area versus aluminium content were plotted, and depicted with macrographs in Figure 6.2. This shows that the softest material of the four alloys, Ti - 2 wt.% Al, did not cause the tool to fracture. Tool damage increased up to Ti - 6 wt.% Al before decreasing for Ti - 8 wt.% Al, where Ti - 4 wt.% Al demonstrates slightly larger fracture surface than that observed in the Ti - 8 wt.% Al tool. This behaviour is comparable to that observed by the strain to failure in the axisymmetric compression tests, Figure 5.13. The usefulness of this as a quantification method is difficult to measure, as much of the observed damage could have been induced by the friction of the chip along the tool face and away from the cut itself. But in the Ti - 8 wt.% Al specimen as chips were being generated they were fracturing into individual segments shortly after being generated, which would cause the frictional forces experienced by the tool to be greatly reduced compared to specimens where chip segments remained connected. This observation is expected as specimens demonstrated increasing severe shear band formation with increasing aluminium content.

6.2 Chip Formation and Load Displacement

In the 2, 4 and 8 wt.% Al specimens it was observed that during cutting a small number of chips were generated and that there were a number of peaks observed on the load displacement plots. Further investigation showed that there were equal numbers of peaks and chips generated, illustrated in Figure 6.3. The cause of Ti - 6 wt.% Al not adhering to this trend was due to experimental error: misalignment of the sample with regard to its position between the two tools meant that one side had a much larger depth of cut compared to the other. This led to the plot in Figure 6.4c) showing much lower values as the loads generated by each side, each cut, combine on a single sample to form a ‘beat’ wave observed in acoustics, which is defined as the interference of two waves of differing frequency. This was in contrast to the 2, 4 and 8 wt.% Al specimens which have two waves, therefore cuts, consisting of similar frequencies, which result in much higher levels of constructive interference, enabling reasonable prediction of shear stresses.

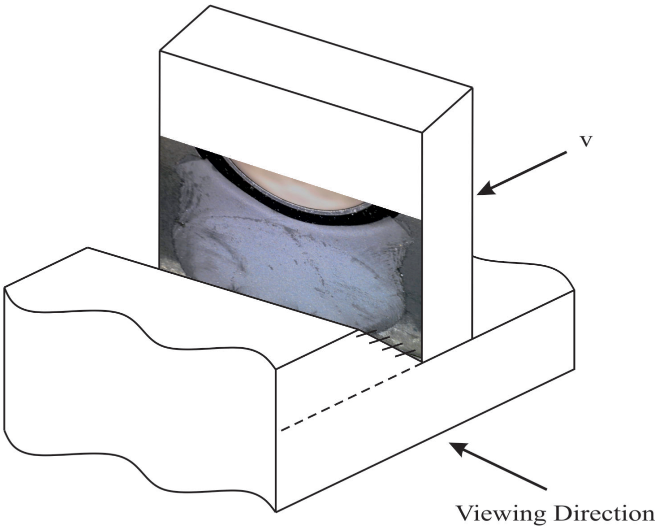

Figure 6.1: Schematic diagram showing region of tool fracture relative to the cutting orientation.

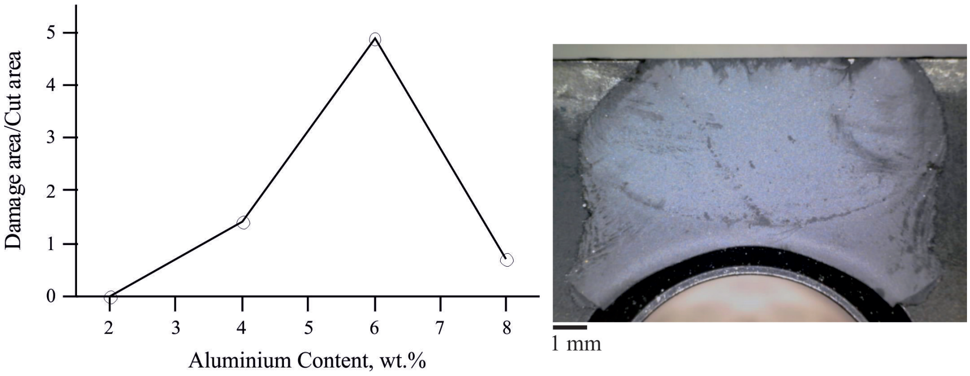

Figure 6.2: Graph showing tool fracture area normalised by cut contact area as a function of aluminium content and a macrograph of the tool fracture surface from Ti - 6 wt.% Al, V_c 0.01 m.min^{-1}.

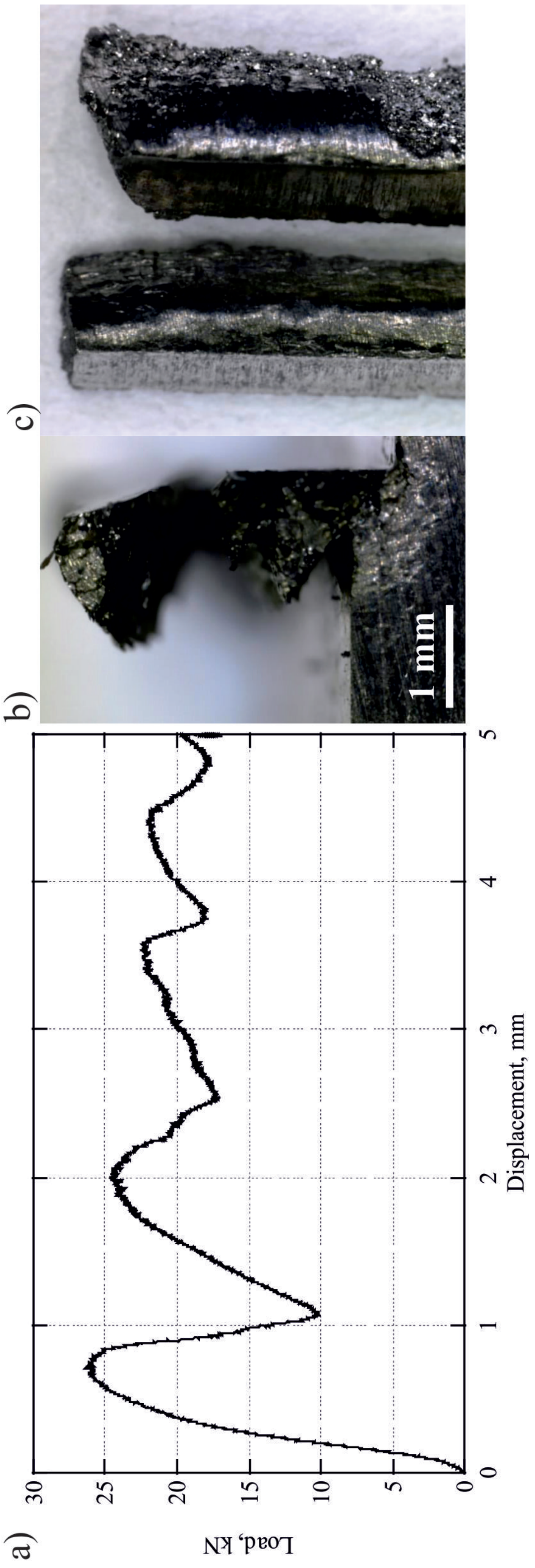

Figure 6.3: Load - displacement plots for binary alloys a) Ti - 2 wt.% Al, b) Ti - 4 wt.% Al, c) Ti - 6 wt.% Al and d) Ti - 8 wt.% Al, V_c 0.01 m.min^{-1}.

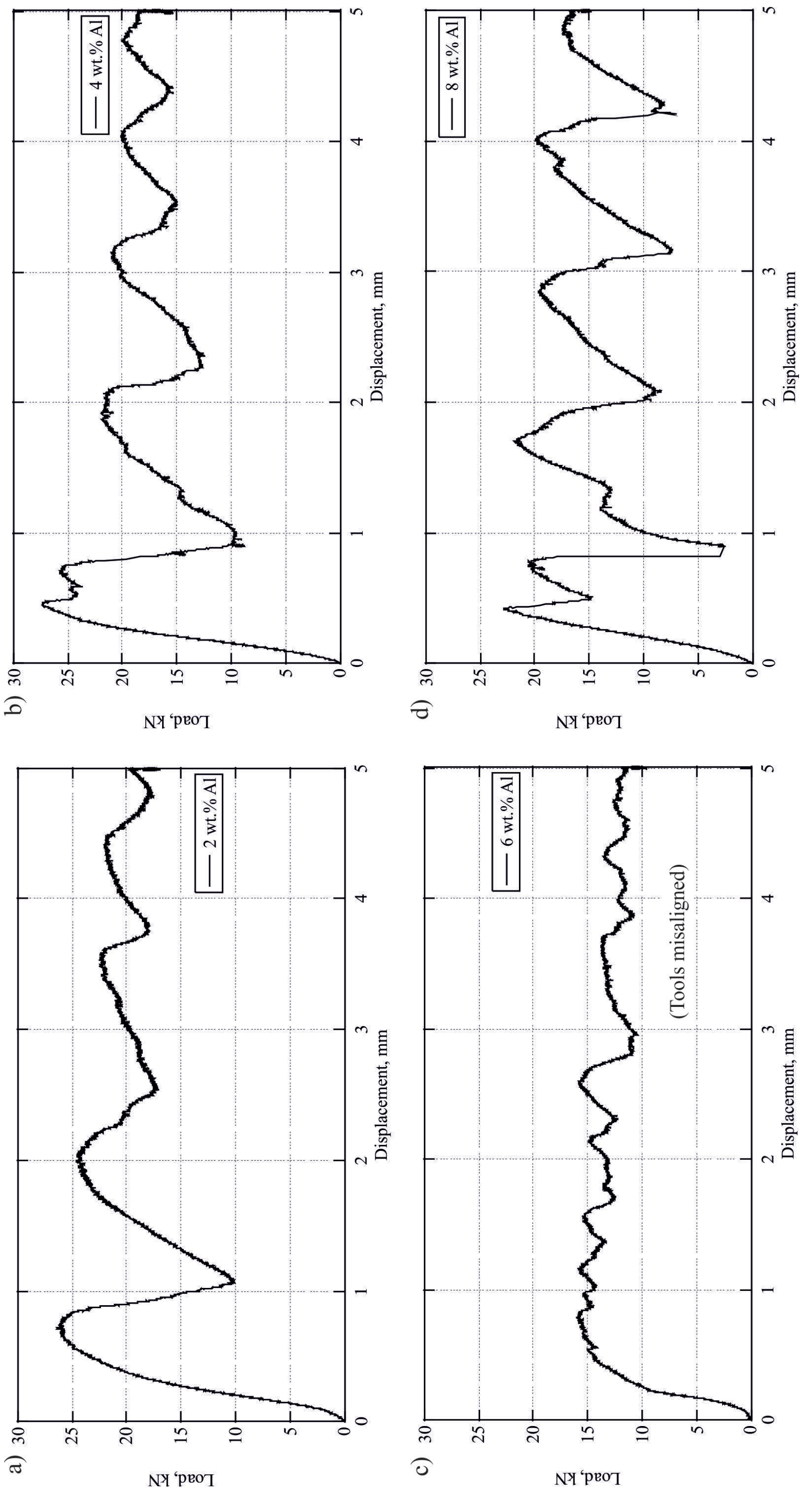

Figure 6.4: Graph showing load displacement plots and two macrographs of test specimen with still attached chip and fractured chip from Ti - 2 wt.% Al, V_c 0.01 m.min^{-1}.

TABLE 6.1: TABLE CONTAINING SHEAR BAND ANGLE AND DEPTH OF CUT MEASUREMENTS FOR ORTHOGONALLY CUT BINARY ALLOYS

Alloy	Ti-2Al *II*	Ti-4Al *II*	Ti-6Al *II*	Ti-8Al *II*
Shear band angle, ^{o}	38	32	38	39
Error, ± ^{o}	1.5	2	5.5	0.5
Total depth of cut, μm	1250	1270	1070	1100

6.3 Shear Band Angle

Each of the specimens exhibit a partially formed chip at the chip - cut interface and measurements of the shear band angle were made. It was assumed that the angle measured had remained constant throughout the chip forming process irrespective of the taper, which causes a reduction in depth of cut and influences the forces generated, according to Equation 6.1. The measured angles for each of these are listed in Table 6.1 and examples illustrated in Figure 6.5. Table 6.1 shows that the measured shear band angle is largely consistent, with only Ti - 4 wt.% Al showing a variation of 32^o compared to 38 or 39^o in the 2, 6 and 8 wt.% Al. Examination of this specimen using light microscopy shows that some cutting irregularities have occurred, whereby the cutting process appears to have struggled to achieve steady state manifesting as the high surface roughness of the new surface and the acute angle of the new cut surface when compared to the cut direction, Figure 6.6b), which should be almost parallel. This is in contrast to the other three binary alloys which demonstrate almost parallel new cut surface when compared to the cut direction, as seen in Figure 6.5. The cause for this could be a number of parameters. The most likely is that the specimen, while appearing even and square, was actually off-square, exhibiting rotation around the axis of movement during the cut. This means that on the back face the depth of cut initially was very large, compared to the front, and as the cut progresses the tangential force generated is correspondingly large and has caused the tool to move away from the cut. A method for detecting this in future would be to measure the separation of the two cutting tools immediately *pre* and *post* experiment, thereby identifying whether tool movement has occurred.

$$\tau_s = \frac{F_s}{A_s} \tag{6.1}$$

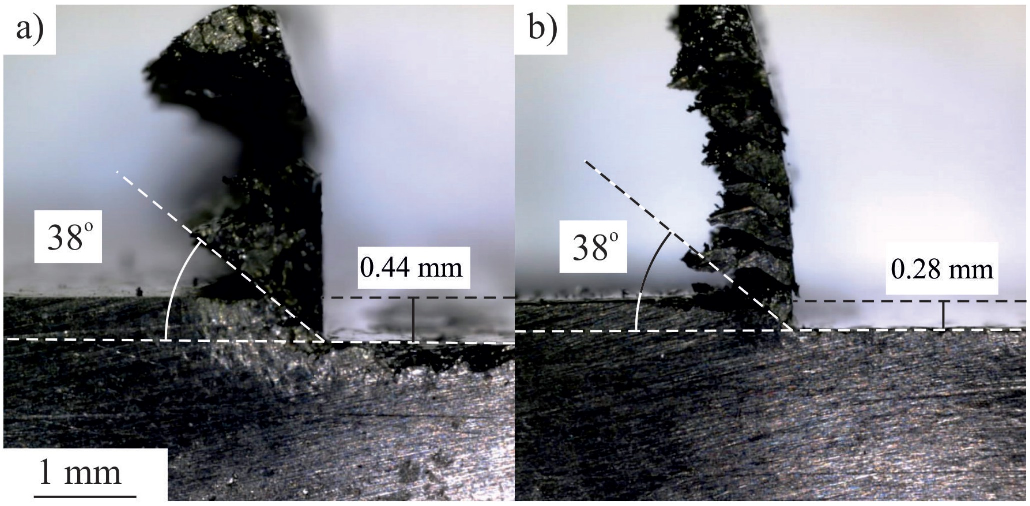

Figure 6.5: Macrograph of the specimen with still attached chip and determined shear band angle from a) Ti - 2 wt.% Al and b) Ti - 6 wt.% Al, V_c 0.01 m.min^{-1}.

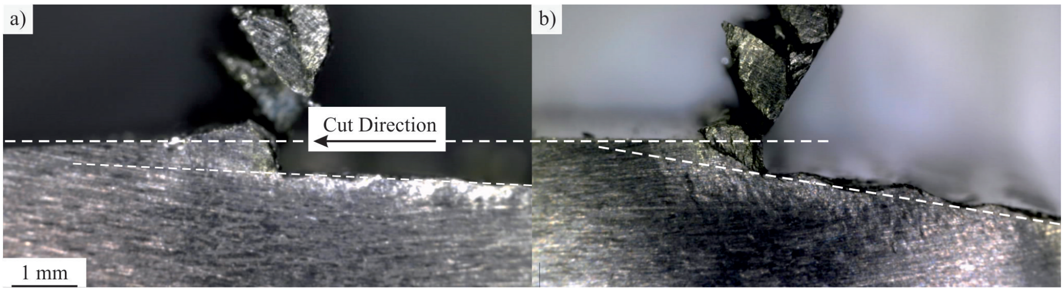

Figure 6.6: Macrograph showing non-parallel cut resultant in Ti - 4 wt.% Al, V_c 0.01 m.min^{-1} a) showing the near face b) the far face (image flipped in horizontal plane).

6.4 Shear Stress and Strain

Using the load data generated during the experiments, calculations were made to determine the shear stress generated in the shear band using the method described in Section 3.9.3, previously described in Section 3.9.3. Initially, determination of shear strain was not possible without the use of Digital Image Correlation (DIC) techniques, to make comparison possible with the flow curves generated from the axisymmetric compression. The strain of maximum stress from these flow curves was assigned to the peak load value of a selected chip, from Figure 6.7a), in this case chip 2. Assuming that the maximum load coincides with the failure and the minima from the load displacement plot is equivalent to 0 strain, a stress strain plot is generated, Figure 6.7b). At this point the generated result compares favourably to work performed by Shankar [93], which shows that the strain values observed in the shear band of an orthogonal cut are comparable to those observed in the FEM model. Each binary was subjected to these calculations and plots were generated, Figure 6.8a). As can be observed in Figure 6.8a) there appears to be no elastic region present when comparing the stress - strain curves generated for the axisymmetric compression tests, Figure 5.7. The curves generated appear comparable in shape to the plastic region of the flow curves, Figure 6.8b), with increased noise, which is a natural part of all machining force data. The shear stress does not exhibit a linear increase in the maximum shear stress as a function of aluminium content, in agreement with the observations made in Chapter 5. This would be expected if, as hypothesised, that the flow behaviour can be determined from the orthogonal cutting test. Qualitatively the trend observed is the same as in the axisymmetric compression tests, with Ti - 4 wt.% Al exhibiting the steepest initial rise due to work hardening, followed by Ti - 2 wt.% Al and Ti - 6 wt.% Al, then Ti - 8 wt.% Al. It can also be observed that 2, 4 and 6 wt.% Al show a variation in gradient, therefore in work hardening, prior to reaching maximum shear stress. This is not the case with Ti - 8 wt.% Al, which exhibits a very linear increase in the shear stress to maximum. Both of these observations are in line with the axisymmetric compression testing. The likely reason for Ti - 6 wt.% Al being so much lower than 2 and 4 wt.% Al has already been discussed, but for Ti - 2 wt.% Al the reason is not clear. Figure 6.9 shows a direct comparison of the pseudo shear stress curves with shear stress curves using the three most common equations for calculating shear stress in compression; Von-Mises, Octahedral and Tresca, Equations 6.2-6.4 respectively.

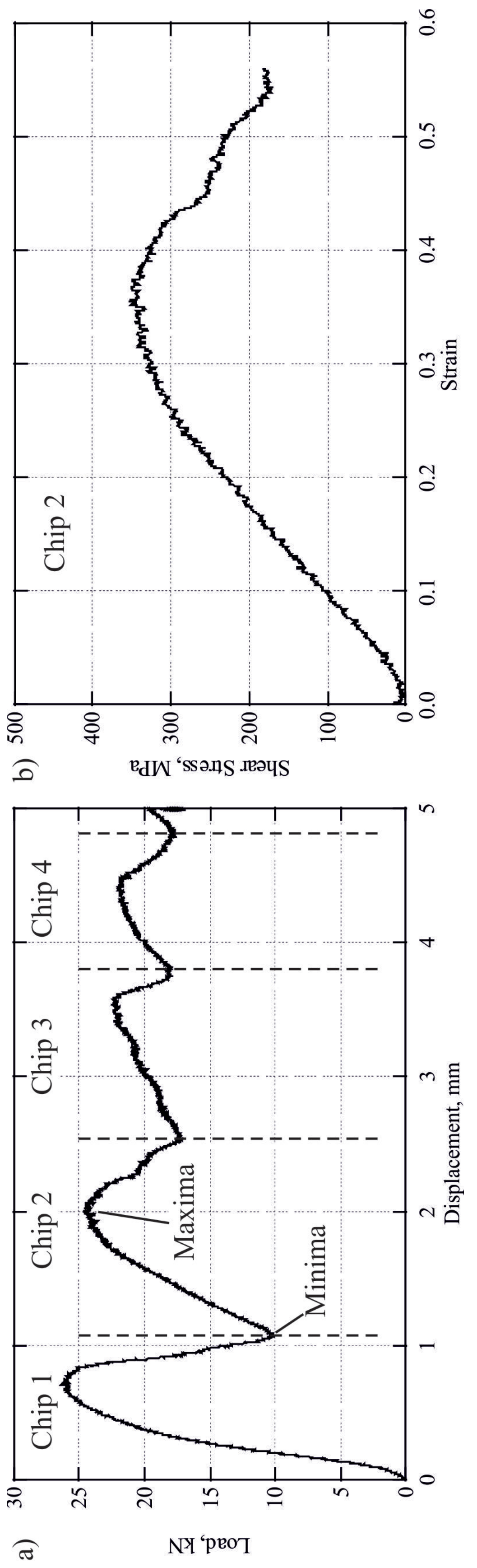

Figure 6.7: Plots of a) the load - displacement curves from orthogonal cut experiments, Ti - 2 wt.% Al cut at 0.01 m.min^{-1}, indicating regions of the plot corresponding to individual chips forming and b) pseudo shear stress vs strain curve for chip 2.

Figure 6.9 shows plots of the calculated orthogonal shear stress with corresponding shear stress plots determined from axisymmetric compression tests. The first observation is the good agreement achieved in 4 and 8 wt.% Al between the curves of the two methods. From this point Ti - 6 wt.% Al will not be included in discussion for orthogonal cut experiments as the 'beat' nature of the load displacement plots has led to great discrepancy in behaviour compared to the other three binary alloys. However, Ti - 2 wt.% Al shows a marked increase in the calculated shear stress; yield is 20 % higher in the orthogonal cut tests. The curves show good correlation both qualitatively, in the shape of the curve and quantitatively, in terms of the shear stress values calculated; this leads to the conclusion that comparable deformation is occurring in both experiments. Ti - 8 wt.% Al shows particularly good correlation with the Tresca shear stress and Ti - 2 wt.% Al showing a clear variation in gradient, similar to the axisymmetric compression test flow curves, indicating comparable work hardening behaviour.

$$k = \frac{\sigma_0}{\sqrt{3}} \tag{6.2}$$

$$\sigma_{oct} = \frac{\sqrt{2}\sigma_0}{3} \tag{6.3}$$

$$k = \frac{\sigma_0}{2} \tag{6.4}$$

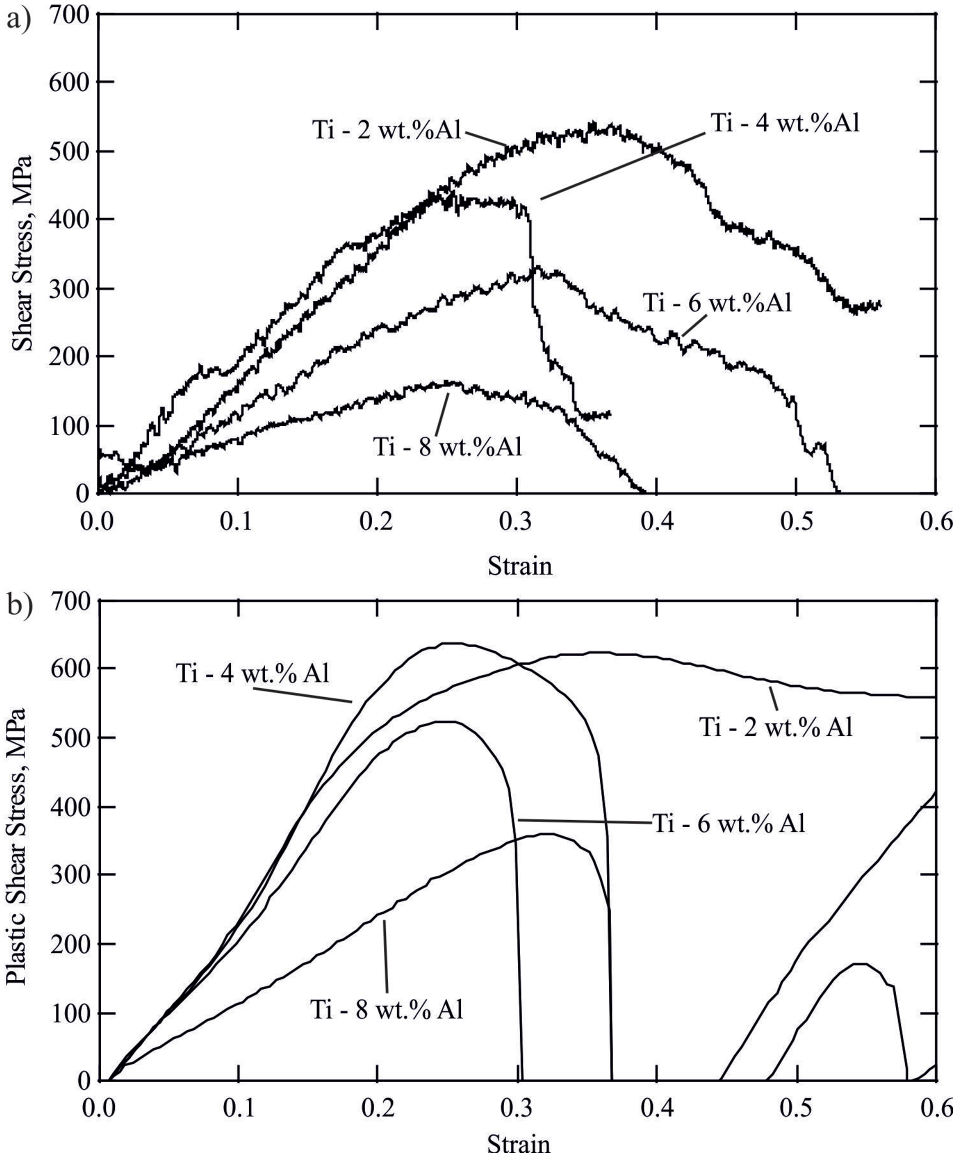

Figure 6.8: Plots of a) the shear stress - strain curves from orthogonal cut experiments, 0.01 m.min^{-1}, and b) the plastic shear stress strain curves of the compression specimens, $\dot{\epsilon} = 0.1$ ϵ=0.7.

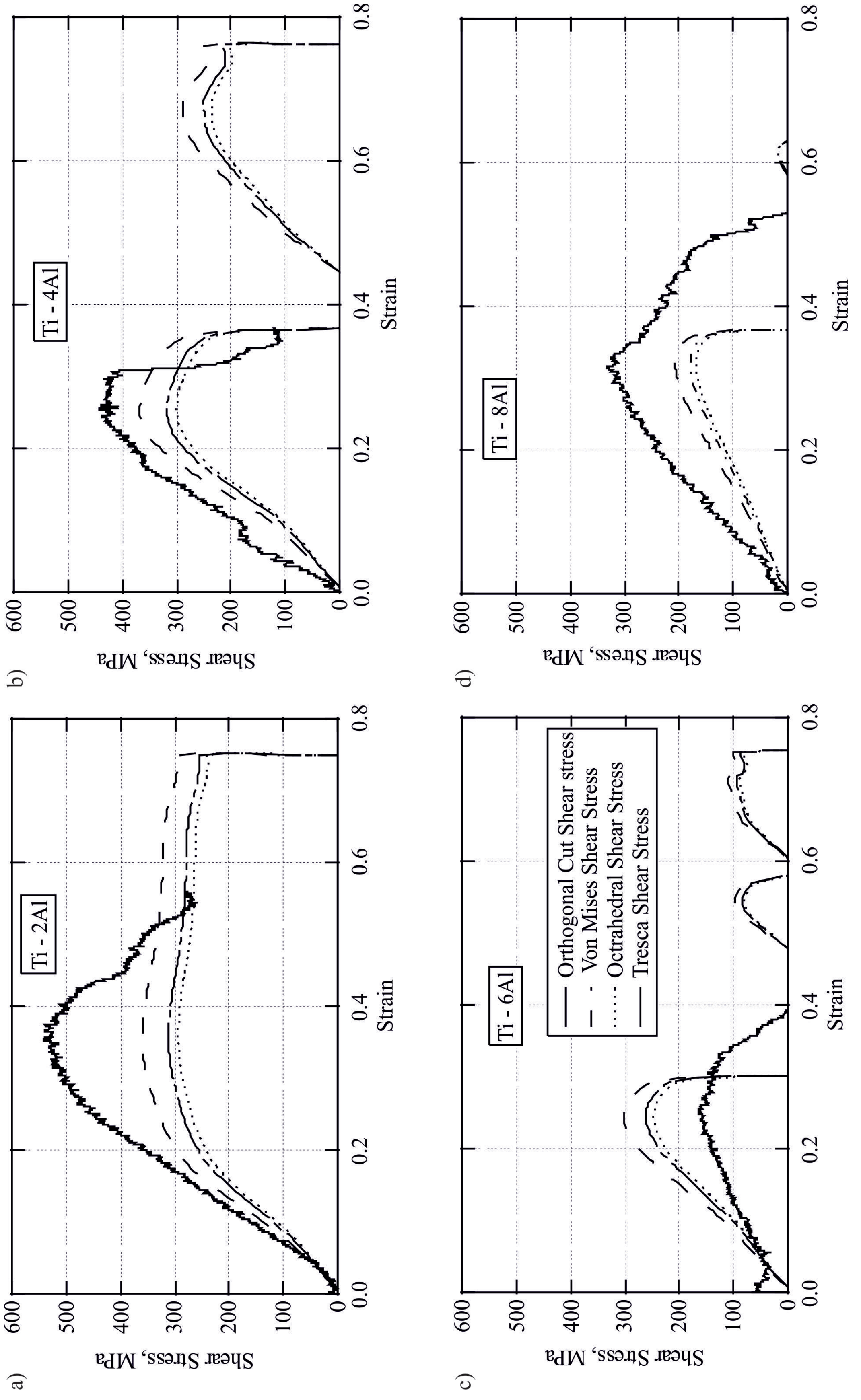

Figure 6.9: Plots of the shear stress strain curves from orthogonal cut experiments, 0.01 m.min^{-1}, and the three plastic shear stress strain curves of the compression specimens, $\dot{\epsilon} = 0.1$ ϵ=0.7, for a) Ti - 2 wt.% Al b) Ti - 4 wt.% Al c) Ti - 6 wt.% Al d) Ti - 8 wt.% Al.

Examination of the cause for elastic region not being present in the stress - strain curves generated from the orthogonal cut experiments was made. Examination focused on the minima value observed after the completion of chip one, as subsequent minima have increasing absolute values, which is likely caused by increased friction forces generated as the chip length increases, resulting in a larger contact area between the tool and the chip. Redefining the assumption used previously, that the minima is equal to zero shear stress, so the absolute load values are used rather than normalising curves based upon the minima, generates the curves in Figure 6.10. These curves show a strong correlation to the shear stresses calculated from the axisymmetric compression tests. The quantitative correlation is less than with the plastic stress but still shows that the pseudo yield strength from the orthogonal cut experiments is comparable to the axisymmetric compression tests. Ti - 2 wt.% Al shows the closest alignment with axisymmetric compression test shear stress. The potential cause for this is that as Ti - 2 wt.% Al generated the fewest chips, Figure 6.3, the chip forming processes had greater probability of being synchronized between the two individual cuts.

Due to the similarity of generated pseudo flow curves compared to the real flow curves examination of work hardening curves followed. Figure 6.11 illustrates the pseudo work hardening curves of the orthogonal cut binaries. Due to the significant noise resulting from the cutting operation, the shear stress curves were passed through a low pass filter. This was not ideal as it ‘smoothed’ out the influence of the pseudo elastic region generated previously, resulting in the work hardening increasing from near zero values at low strains, as opposed to decreasing from values in the order of 10^4, illustrated by Figure 5.14 in Section 5. As a result all three of the plots in Figure 6.11 show some correlation with the data from the axisymmetric compression tests but not enough to analyze the generated curve in the same manner as previously with the axisymmetric compression data in Section 5.6. Attempts to perform less smoothing resulted in the work hardening curves containing large amounts of noise making analysis impossible.

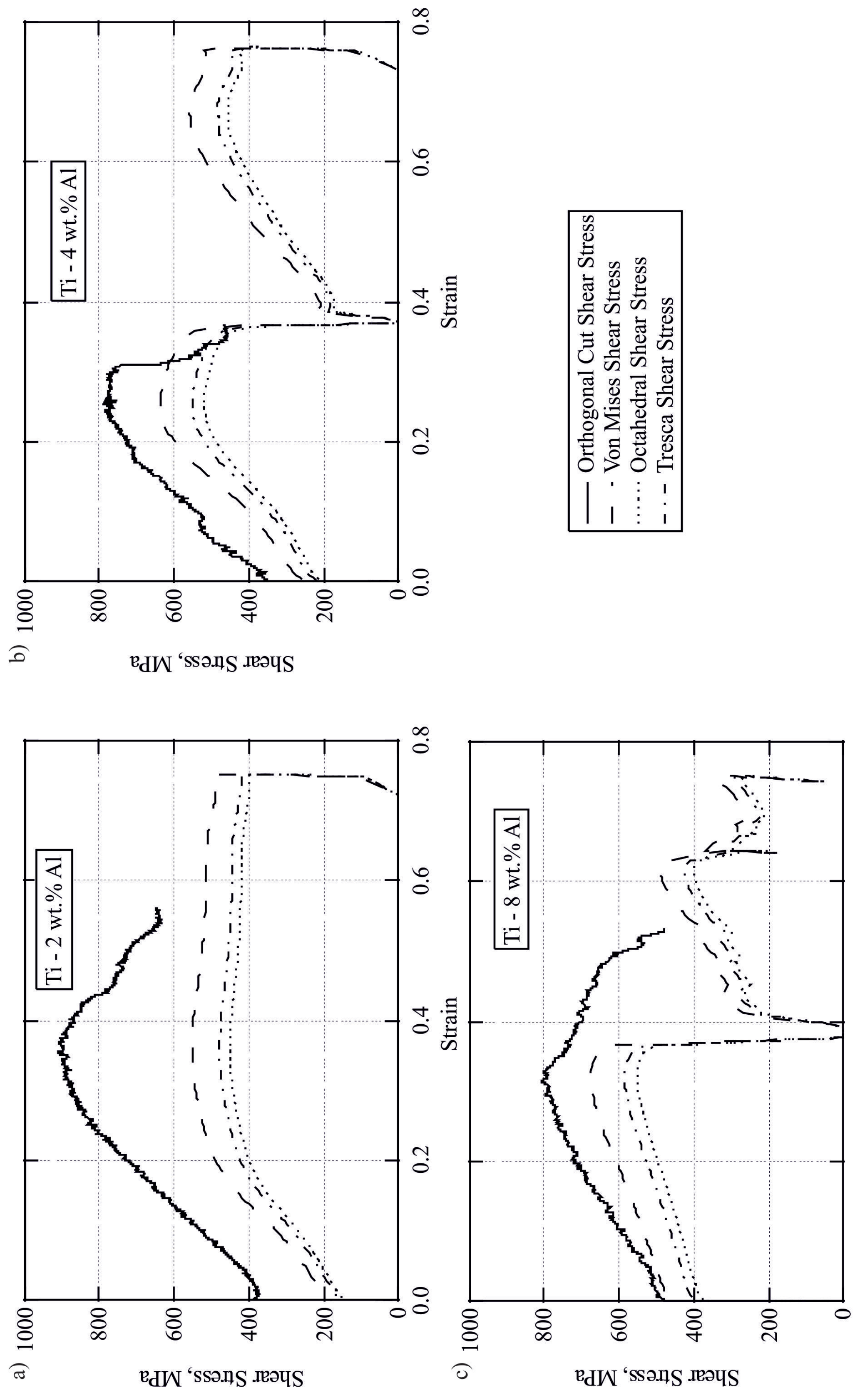

Figure 6.10: Plots of the pseudo shear stress - strain curves with pseudo elastic region from orthogonal cut experiments, 0.01 m.min^{-1}, and the shear stress strain curves of the compression specimens, $\dot{\epsilon}$ = 0.1 ϵ=0.7, for a) Ti - 2 wt.% Al b) Ti - 4 wt.% Al c) Ti - 8 wt.% Al.

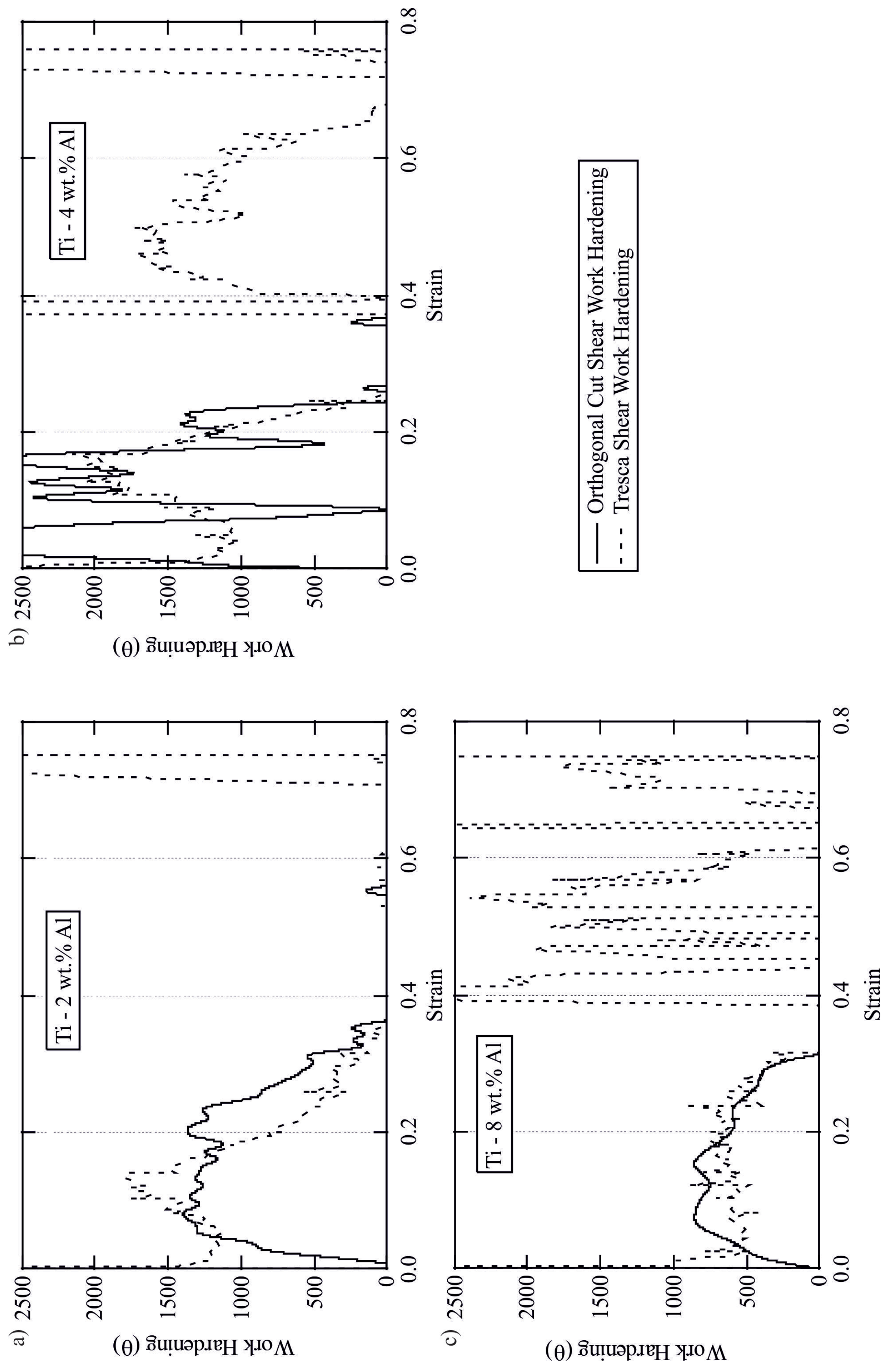

Figure 6.11: Plots of pseudo work hardening curves from orthogonal cut experiments, 0.01 m.min^{-1}, and the work hardening plots of the compression specimens, $\dot{\epsilon}$ = 0.1 ϵ=0.7, for a) Ti - 2 wt.% Al b) Ti - 4 wt.% Al c) Ti - 6 wt.% Al d) Ti - 8 wt.% Al.

6.5 Subsurface Damage

6.5.1 Backscatter Electron Imaging

Backscatter electron images of the subsurface damage induced by the orthogonal cutting are illustrated in Figures 6.12-6.15. Figure 6.12 shows the subsurface damage induced by cutting: Figure 6.12 a) and d) represent 2 and 8 wt.% Al and demonstrate rough cut surfaces and exhibit subsurface voids. This is in contrast to Figure 6.12b) and c), 4 and 6 wt.% Al respectively, which exhibit smooth and much less severe voids or cracking, with only one isolated void being observed away from the very near surface in Ti - 6 wt.% Al, Figure 6.12c). The level of subsurface deformation shows qualitative variation in the density and depth in line with observations made during high speed milling, analysed in Section 4.6. Ti - 4 wt.% Al, Figure 6.12b), exhibits the highest level of penetration and Ti - 8 wt.% Al, Figure 6.12d), shows the least, creating a parabolic with Ti - 4 wt.% Al at the peak.

Figure 6.13 illustrates the bulk - chip interface. Figure 6.13a) illustrates the large SPD region generated adjacent to the shear band, represented by the fracture face. This region is significantly larger than that observed in the subsurface, Figure 6.12a); the cause for this is that the majority of this material moves into the chip rather than remaining in the bulk. It is also observed that Ti - 2 wt.% Al exhibits a much larger SPD region than observed in 4, 6 and 8 wt.% Al, Figure 6.13b) - d). The cause for this has previously been hypothesised, in Section 2.3, whereby increasing the aluminium content increases the CRSS for all the deformation mo des, which effectively decreases the number of operational deformation modes. This results in higher energy for deformation, higher adiabatic heating and increasingly confined, or 'intense', shear banding. The other most significant observation to be made is the angle at which fracture occurs, relative to the cutting direction. It appears that the fracture angle is approximately 30 - 45^o for 2, 4 and 6 wt.% Al, which is in the range usually observed [105]. This is contrast to Ti - 8 wt.% Al, Figure 6.13d), which exhibits a chip fracture parallel to the cut direction. This is most significant, not only as it is anomalous with the fracture angle of the 2, 4 and 6 wt.% Al, but also because it differs from the shear band angle measured within Ti - 8 wt.% Al, shown in Table 6.1. This is investigated in Section 6.6 as, as previously discussed, the potential presence of α_2 particles may cause cutting behaviour comparable to free cutting steel.

The amount of damage generated ahead of the tool is illustrated in Figure 6.14. In all four alloys there is a substantial amount of damage generated in front of the cutting tool. In 2, 4 and 8 wt.% Al damage is manifested in the form of extensive twinning, whereas in Ti - 6 wt.% Al there appears very little twinning but extensive crack formation, with the cracks propagating along grain boundaries. It is also possible to distinguish high levels of grain distortion in the grains adjacent to those that have cracked. The cause of this discrepancy is not clear; it is possible that the grains have a 'hard' orientation meaning that deformation mechanisms have high CRSS values, making them unfavourable, leading to cracking in order to accommodate the generated strain.

This possibility is supported by Wang [63] who observed in magnesium alloys that if the orientation is such that the work hardening curve is characterised by an exponential decay and does not exhibit the work hardening rate associated with twinning, discussed by Salem [59], that the orientation is unfavourable for twinning. EBSD analysis of the subsurface was unsuccessful, showing indexing rates below 10%; this is likely due to the extreme amount of lattice distortion caused by the less than ideal cutting parameters used for the orthogonal cutting.

The final observations made from the backscatter electron imaging were a series of interesting microstructural features induced by the cutting process. Firstly, in the subsurface of the Ti - 2 wt.% Al, Figure 6.15a), which shows a grain that has experienced deformational twinning and, as the cut has progressed, a series of cracks have propagated across the twins, with the cracks exhibiting high levels of regularity in terms of separation and directionality. This is significant as it suggests that the cause of these cracks is consistent. A possible cause is that as the twin has formed, when the induced strain level is relatively low, 0.1 - 0.15, and as the cut progresses, the strain not only increases but the direction of the strain alters. This change in direction would be critical because when the twin is first generated the orientation of the material inside the twin is such that it will be ‘soft’ for strain direction experienced when formed; however, as the cut progresses the direction changes, meaning the orientation of material inside the twin changes and becomes a ‘harder’ orientation in relation to the new strain direction. This harder orientation would lead to increased CRSS values for the deformation mechanisms and mean that homogenous deformation is increasingly difficult, resulting in a corresponding increase in the likelihood of microcracks nucleating. However, as this is an isolated occurrence, confirming this theory would require further testing, which is beyond the scope of this work. Figure 6.15b), Ti - 4 wt.% Al, also illustrates microcrack formation in the subsurface. In this case the cracks have nucleated and begun to propagate along the grain boundary between two grains. The presence of these cracks is likely caused by the occurrence of twins that have transected the grain boundary and generated a ‘twinning shear’, which causes the cracks to open. This has been observed previously in γ TiAl [129,130] and molecular modelling of the cubic system [131].

Figure 6.15c), depicts a series of parallel subsurface deformation twins appearing to be propagating out of the heavily deformed SPD region, illustrating a phenomenon that was observed in the high speed milled material, Figure 4.2 in Section 4. It appears that twins are forming ahead of the tool and as the tool passes the SPD region, which does not penetrate to the same depth as the twins, it causes the section of twin nearest to the surface to deform to the point where it is no longer possible to distinguish under backscatter electron imaging. Upon closer examination, it appears that the right side of Figure 6.15c) show a series of narrow, secondary, twins inside a series of wider, primary twins; the unexpected aspect is that both sets of twins, narrow and wide, have parallel long axes. This is contradictory to what is usually observed [132], illustrated in Figure

6.16, where the secondary twins are orientated with the long axis perpendicular to the primary twin as opposed to parallel to the long axis.

Examination of the cut surface in Ti - 8 wt.% Al shows where a chip has not been completely removed from the surface as the cut has progressed. The cause of this appears to be a result of two factors. Firstly, this material exhibits shear band formation in the chip at an angle of 39^o, as measured previously in Table 6.1; secondly the fracture that forms causing the chip and the bulk to separate is parallel to the cut direction, Figure 6.13d), which is in contrast to the other three binary alloys which demonstrate this fracture along the shear band, Figure 6.13a) - c). This means that the angle between the shear band and the fracture will just be equivalent to the shear band angle, 39^o, and measurement of the angle of this feature, shown in Figure 6.17, shows the fracture divergence to be approximately 40^o. This suggests that as the fracture was propagating parallel to the surface, the loading on the shear band increased to a point making fracture along the shear band become preferred. Application of DIC would allow an insight into the strains being generated and if this fracture behaviour is captured then it would be possible to confirm the validity of this hypothesis.

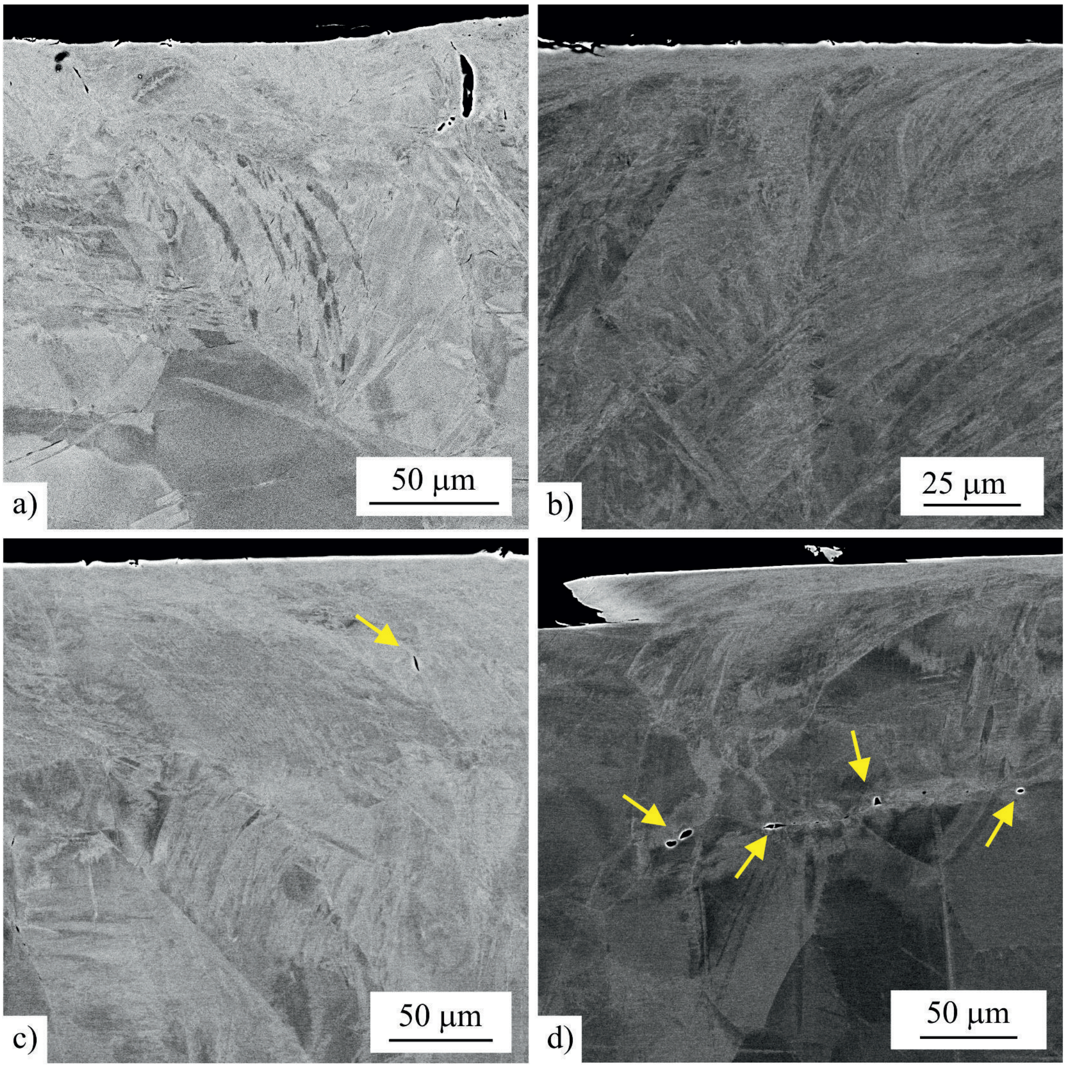

Figure 6.12: Backscatter electron images of orthogonally cut, at 0.01 m.min^{-1}, showing subsurface damage induced in a) Ti - 2 wt.% Al, b) Ti - 4 wt.% Al, c) Ti - 6 wt.% Al and d) Ti - 8 wt.% Al.

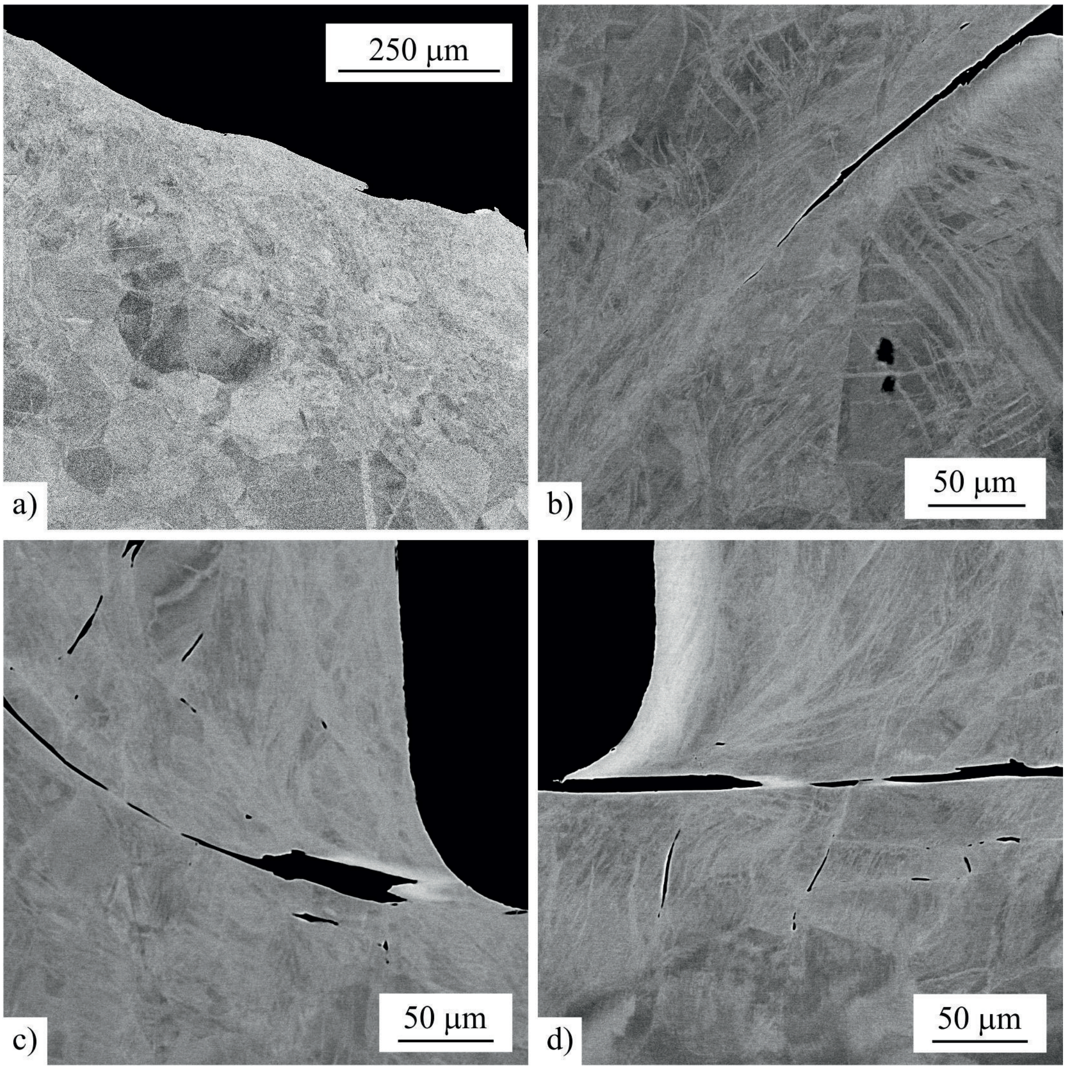

Figure 6.13: Backscatter electron images of orthogonally cut, at 0.01 m.min^{-1}, showing chip fracture and shear band location in a) Ti - 2 wt.% Al, b) Ti - 4 wt.% Al, c) Ti - 6 wt.% Al and d) Ti - 8 wt.% Al.

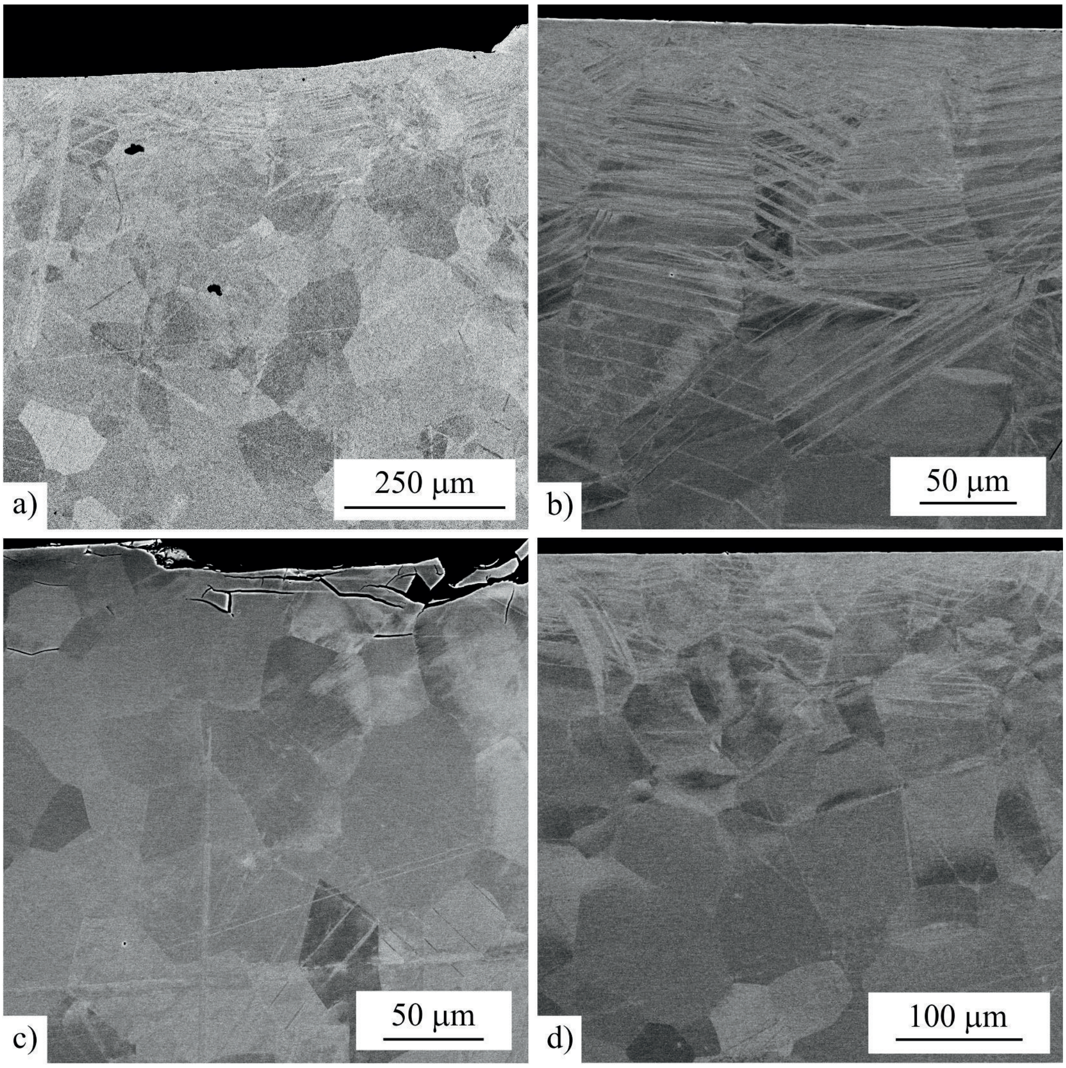

Figure 6.14: Backscatter electron images of orthogonally cut, at 0.01 m.min^{-1}, showing damage induced at the uncut surface in a) Ti - 2 wt.% Al, b) Ti - 4 wt.% Al, c) Ti - 6 wt.% Al and d) Ti - 8 wt.% Al.

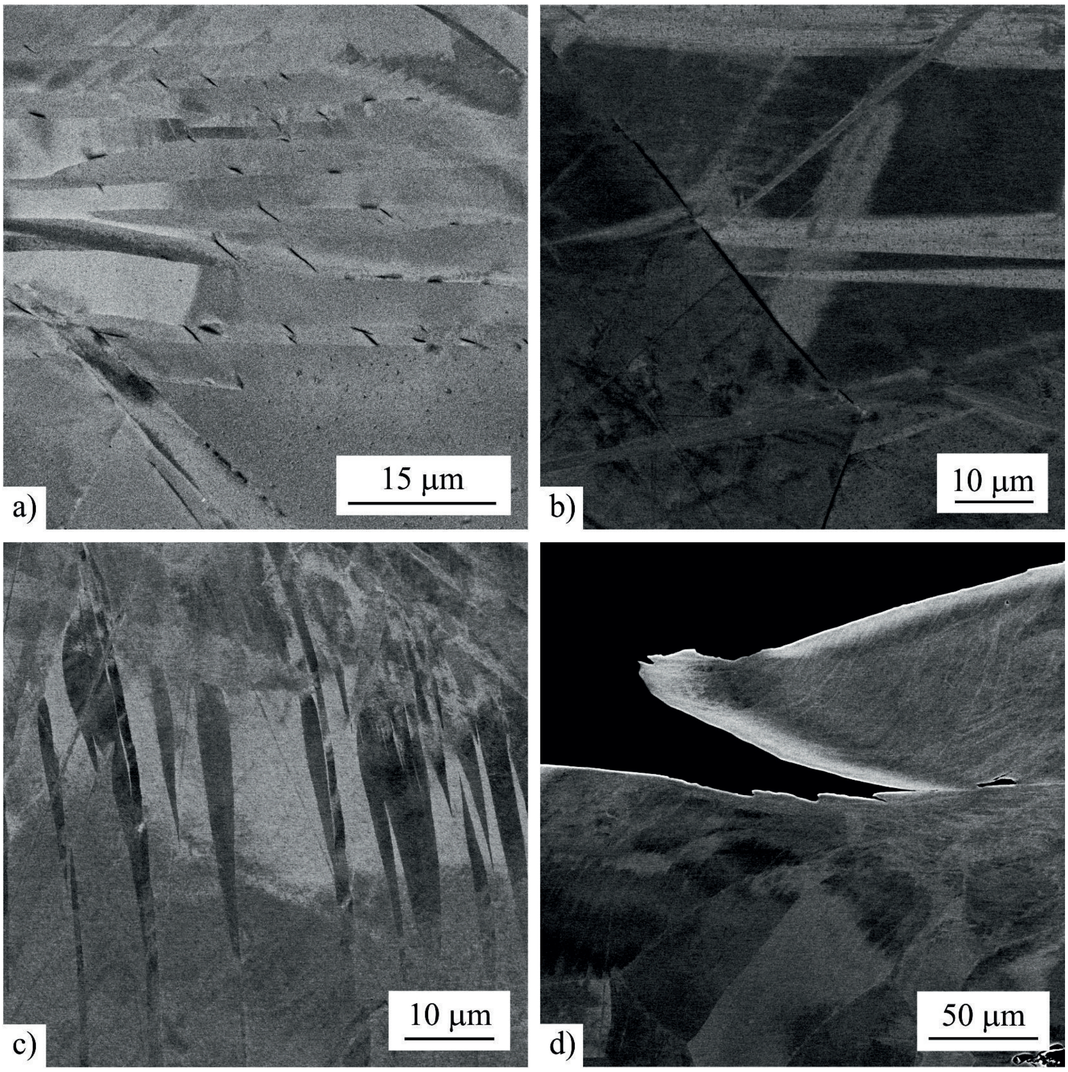

Figure 6.15: Backscatter electron images of orthogonally cut, at 0.01 m.min^{-1}, features induced a) set of parallel microcracks in subsurface twin in Ti - 2 wt.% Al, b) grain boundary cracking and trans granular twinning in Ti - 4 wt.% Al, c) Ti - 6 wt.% Al and d) cut chip fragments on cut surface on Ti - 8 wt.% Al.

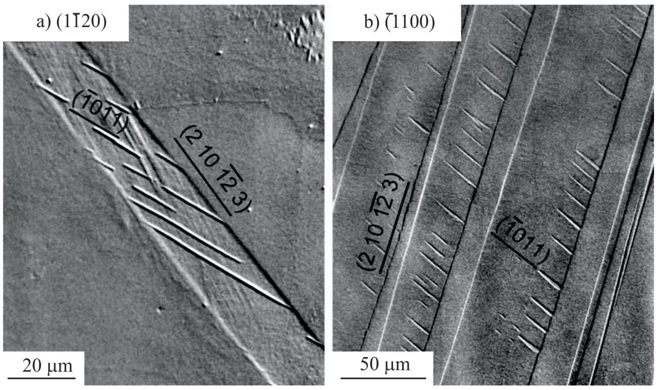

Figure 6.16: Optical micrographs of twins containing secondary twins found in Ti - 24.5 wt.% Al [132].

TABLE 6.2: CHEMISTRY OF STEEL GRADE A15 AND FREE CUTTING EQUIVALENT GRADE EN1A.

Grade	C, %	Mn, %	S, %	Si, %	P, %
A15	0.165	0.75	0.03	0.24	0.012
EN1A	0.07-0.15	0.8-1.20	0.20-0.30	0.10 Max	0.07 Max

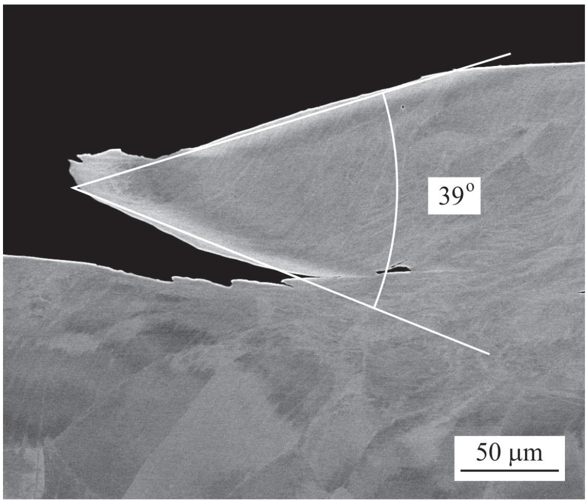

Figure 6.17: Backscatter electron image of Ti - 8 wt.% Al, orthogonally cut at 0.01 m.min^{-1}, with measurement of the diverging fractures generated during cutting.

6.6 Free Cutting Steel Comparison

Orthogonal cutting experiments were performed on a free cutting steel, grade EN1A, and compared to a non-free cutting steel of comparable chemistry, grade A15, with the chemistries of the two listed in Table 6.2. For a suitable comparison to the binary alloys to be made, a binary alloy that does not exhibit free cutting characteristics was analysed. Ti - 4 wt.% Al represents the best opportunity as it has the nearest alloy composition, structure and lattice parameters to Ti - 8 wt.% Al, which is the most likely to contain α_2 particles, while having had a successful orthogonal cut performed. Each of the steel alloys were subjected to orthogonal cutting at 0.01 m.min^{-1} and the chip fracture was examined.

Figure 6.18 illustrates the chip fracture behaviour captured from the two steel grades tested, Figure 6.18 a) and b), with comparison images of the corresponding Ti - 4 wt.% Al alloys below, Figure 6.18 c) and d). It can be observed that the two steel compositions fracture in comparable ways, Figure 6.18 a) and b), with both exhibiting a fracture direction parallel to the cutting direction. This is comparable to the Ti - 8 wt.% Al specimen and in contrast to the Ti - 4 wt.% Al, which exhibits fracture along the shear band plane.

This means the hypothesis that the change in fracture direction is a direct consequence of the presence of α_2 particles remains unconfirmed from a shear band standpoint. The cause of the contrasting fracture behaviour of Ti - 8 wt.% Al led to closer examination of the cuts present on each side of the specimen. Figure 6.19 shows that the fracture behaviour on each side of specimen differed, with the side in Figure 6.19a) showing the parallel fracture, compared to b) which shows fracture occurring along the shear band plane. Examination of these contrasting behaviours highlights that the most likely cause is the depth of cut, with a) and b) showing a depth of cut of approximately of 700 μm and 180 μm, respectively. Measurement of the Ti - 4 wt.% Al depth of cut in Figure 6.18 falls in between the two depths measured on the Ti - 8 wt.% Al suggesting the possibility that the parallel fracture present in the Ti - 8 wt.% Al specimen could be caused by 'ploughing', when the tool edge is insufficiently sharp to cut, which is influenced by the depth of cut and the tooling geometry, i.e. corner radius. This means that no direct inference on the presence of α_2 particles can be made based on the fracture behaviour of the orthogonally cut specimens.

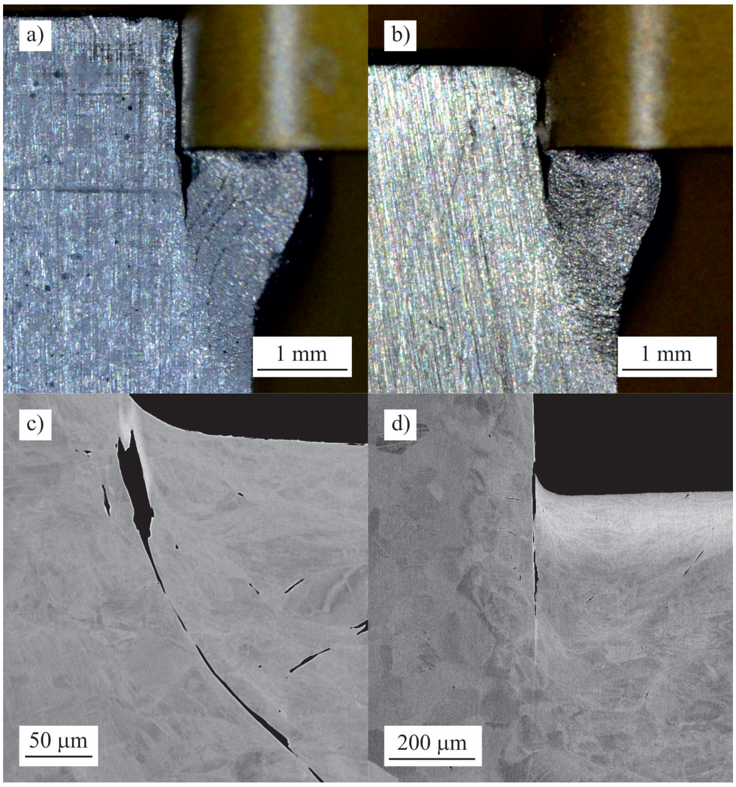

Figure 6.18: Macrograph from during orthogonal cut experiments, at 0.01 m.min^{-1}, on a) steel grade A15, b) steel grade EN1A, and backscatter electron images taken afterwards on c) Ti - 4 wt.% Al and d) Ti - 8 wt.% Al.

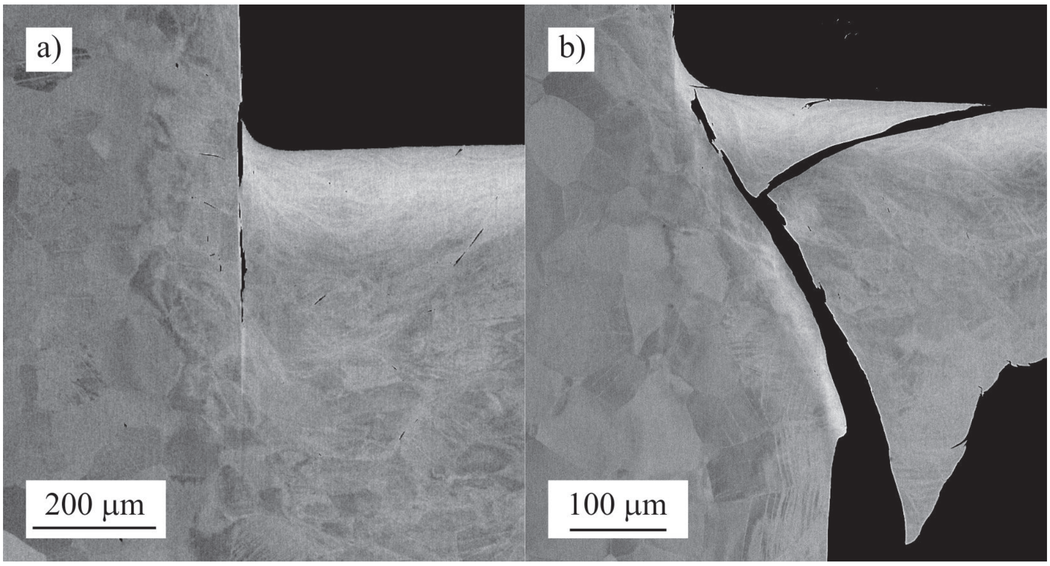

Figure 6.19: Backscatter electron images taken of Ti - 8 wt.% Al, orthogonally cut at 0.01 m.min^{-1} showing a) fracture parallel to cutting direction and b) fracture occurring along the shear band plane.

Examination of the load - displacement plots of the steel grades EN1A and A15, Figure 6.20, shows that both steel grades generated two chips. Firstly, the A15 (non-free cutting) grade generates a higher maximum load. Examination of the depth of cut shows that both materials experienced comparable depths of cut, approximately 0.2 mm. Secondly, the amount of displacement that has been required to form the first chip in the steel grade A15 is considerably more than for the steel grade EN1A. Comparison with the load - displacement plots for 4 and 8 wt.% Al shows that both of these generate the same number of chips, i.e. five, in contrast to the two steel grades, which show two chips being formed. EN1A has formed two complete chips and A15 only just started forming the second chip. The observations of the two steel grades show contrasting behaviour when compared to the two binary alloys, which leads to the conclusion that the free cutting effect of α_2 observed in the literature [55,56] has not occurred. This is supported by work currently being undertaken by Fitzner [133], who has Ti-8Al produced by the same route as the material in this work and has generated TEM diffraction, Figure 6.21a), which shows that there is no evidence for the presence of α_2 particles compared to Ti-6Al-4V aged at 500^{o}C for 20 weeks in Figure 6.21b), which shows clear reflections correlating the presence of α_2 particles.

The results described in this chapter show that there is a strong correlation between the shear stresses generated by this novel testing method and axisymmetric compression. While the microstructural damage observed in this chapter is significantly higher, both in frequency and depth of penetration, than that observed in industrial machining [39], comparable trends are present. It is likely that with use of more appropriate tooling for titanium alloys, the level of subsurface damage would be more comparable to what is observed in the literature using industrial machining parameters and conditions. The

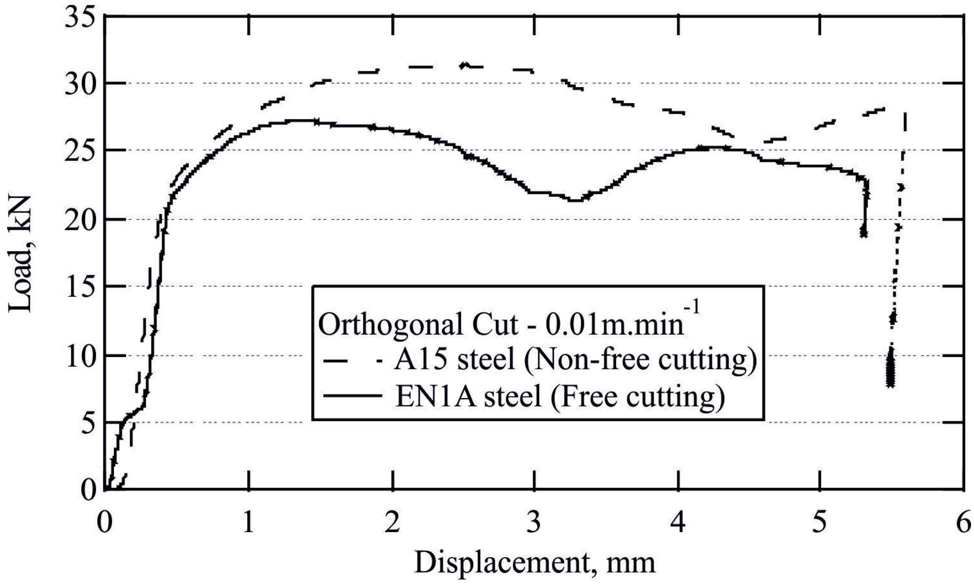

Figure 6.20: Load displacement plot for steel grades A15 and EN1A having been orthogonally cut at 0.01 m.min^{-1}.

fracture behaviour of the Ti - 8 wt.% Al specimen was most likely caused by the depth of cut, by a transition from cutting to ploughing; the apparent lack of α_2 particles means comparison to MnS particles is inconclusive. The result that a flow curve can be generated with a high degree of accuracy when compared to an axisymmetric compression test is the most significant result in this chapter and highlights that the key properties in predicting the 'machinability' of established and novel alloys can readily be assessed without the cost associated with traditional machining trials. The economic significance of this is discussed in Section 8.

The next step to further validating this process is to perform a case study, outlining how axisymmetric compression testing could be used to predict the cutting forces generated in the orthogonal cutting test and comparing that to load - displacement data generated during conventional machining operations. This will also allow further examination, using DIC, of the validity of assuming that the strain of maximum stress from the axisymmetric compression tests is a suitable value to assign to the maxima from the load displacement data from the orthogonal cut experiments.

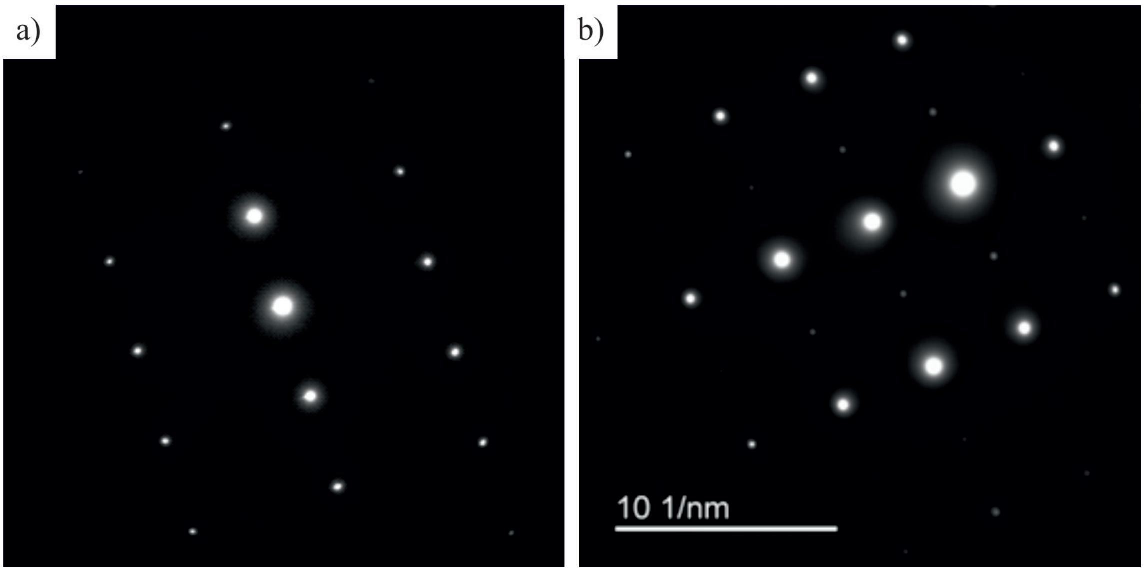

Figure 6.21: TEM Diffraction patterns on the zone axis $\langle 10\bar{1}0\rangle$ for a) Ti - 8 wt.% Al and b) Ti-6Al-4V aged at 500^{o}C for 20 weeks.

7. ORTHOGONAL CUTTING TEST VALIDATION RESULTS AND DISCUSSION

This chapter aims to examine three areas. Firstly, to examine whether the DIC methodology, proposed in Section 3.9.5, can determine the effectiveness of DEFORM™ FEM models compared to experimental results. Secondly, to use FEM models to compare load - displacement data generated by existing materials data for Ti-6Al-4V to experimental results, then using experimentally obtained data for one of the binary alloys to establish the suitability of three flow stress models: Tabulated data, Power Law and Johnson-Cook equations. Thirdly, to apply the shear stress methodology, formulated in Chapter 6, and DIC method to generate pseudo flow curves and compare axisymmetric compression tests and the previously generated flow shear stress results.

7.1 Established and Emerging Industrial Alloy Validation

In Section 6.4 the generation of a pseudo flow curve showed some of the potential use of the proposed testing method on alloys of varying degrees of industrial readiness, Ti-6Al-4V which is widely available, Ti-575 (Ti-5.3Al-7.7V-0.5Si) which is close to high volume production and Ti-407 (aluminium lean titanium alloy) which is under development. This section aims to enhance the validity of this method while adding experimentally obtained strain values from the orthogonal cut experiments, as opposed to the application of strain values obtained through axisymmetric compression testing. Figure 7.1a) - f) shows six frames taken during the orthogonal cutting of Ti-6Al-4V, these images correspond to the chip used to determine the shear stress generated during the experiment, Figure 7.2 shows the specimen, at the point of maximum strain during the formation of the chip used to generate the pseudo shear stress, with the strain profile generated from the DIC analysis overlaid. The approach used to apply the DIC determined strain values to the chip shear stress values is to assume that the maximum strain value occurs at the point of maximum shear stress and assuming that the minimum shear stress value of the selected chip corresponds to a strain of zero, this approach is comparable to the approach used when applying the axisymmetric compression strain values.

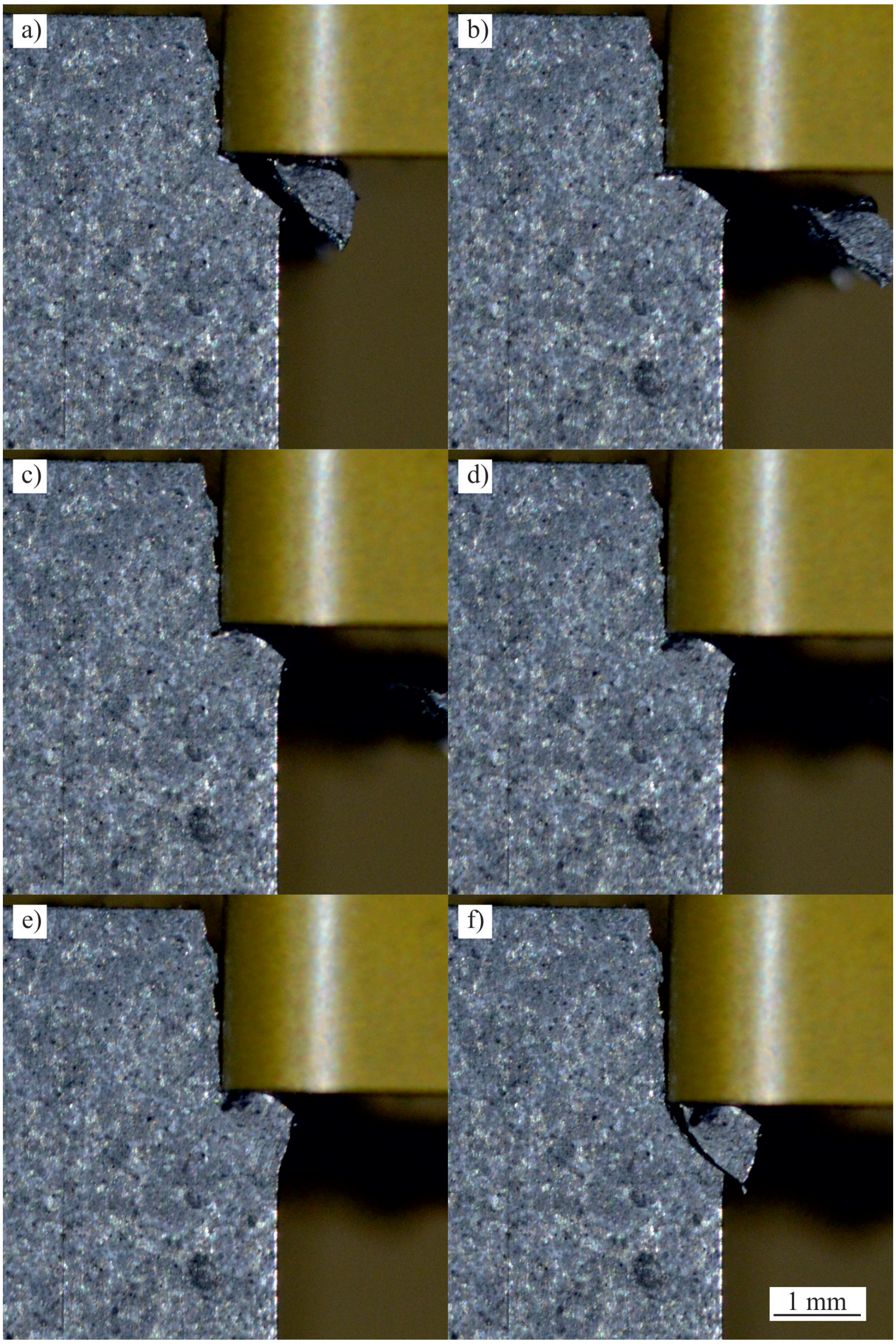

Figure 7.1: Macroimages of Ti-6Al-4V orthogonally cut at 0.01 m.min^{-1}, a) - f) showing progressive stages during the formation of the chip used to generate the pseudo flow curve.

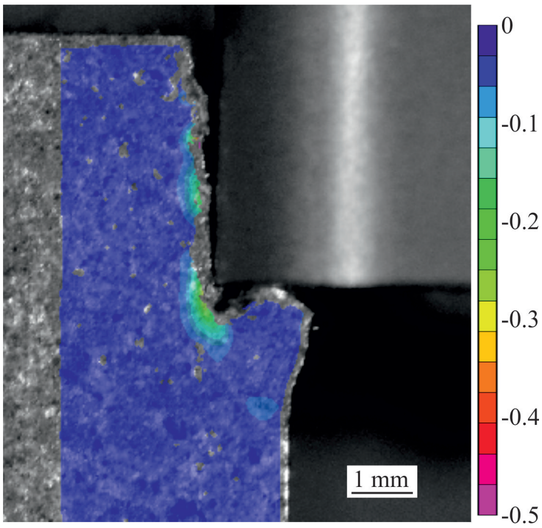

Figure 7.2: Macroimage of Ti-6Al-4V orthogonally cut at 0.01 m.min^{-1} with strain profile overlay at the point of maximum strain during the formation of the chip used to generate the pseudo flow curve.

In Figure 7.3 the pseudo flow curves for the three industrial alloys are presented. There are several observations to be made; the first is that the DIC determined strain values for Ti-6Al-4V and Ti-575 appear to show failure, i.e. a large drop in shear stress. These are comparable to the failure strains obtained from the axisymmetric compression tests. Due to the lack of true failure for the axisymmetric compression test for Ti-407 it is difficult to determine the accuracy of the DIC determined strain; however, as can be observed from Figure 7.4c) the frequency of load oscillation in the initial chip is low for Ti-407 compared to Ti-6Al-4V and Ti-575, in Figure 7.4a) and b), respectively. This suggests that a larger strain is being generated in Ti-407 than in Ti-6Al-4V and Ti-575.

For the pseudo flow curves the largest discrepancy is the magnitude of the calculated shear stress when compared to the axisymmetric compression flow curves. Examination of the DIC images shows that the likely cause is horizontal movement of the cutting tools. Figure 7.5 shows this movement for Ti-575, which demonstrates the amount of tool movement observed for three industrial alloys. This movement is significant because this influences the shear stress values because as the depth of cut reduces, as the cut progresses, the shear band angle, cutting force, and the coefficient of friction all change. All of these parameters, using Equations 3.20 - 3.17 in Section 6.4, influence the shear stress value, meaning this tool movement has a triple influence on the magnitude of the shear stress. Figures 7.6 and 7.7 show the tool movement that occurred during orthogonal cutting of Ti-6Al-4V and Ti-407. As the difference between shear stress values from the orthogonal cuts and the axisymmetric compression tests for the binary alloys, when compared to the industrial alloys, is significantly lower it is assumed that the level of tool movement is much less. This led to comparison of the loads generated during all the orthogonal cut test, Figure 6.9 in Section 6.4, for the binary alloys and Figure 7.4.

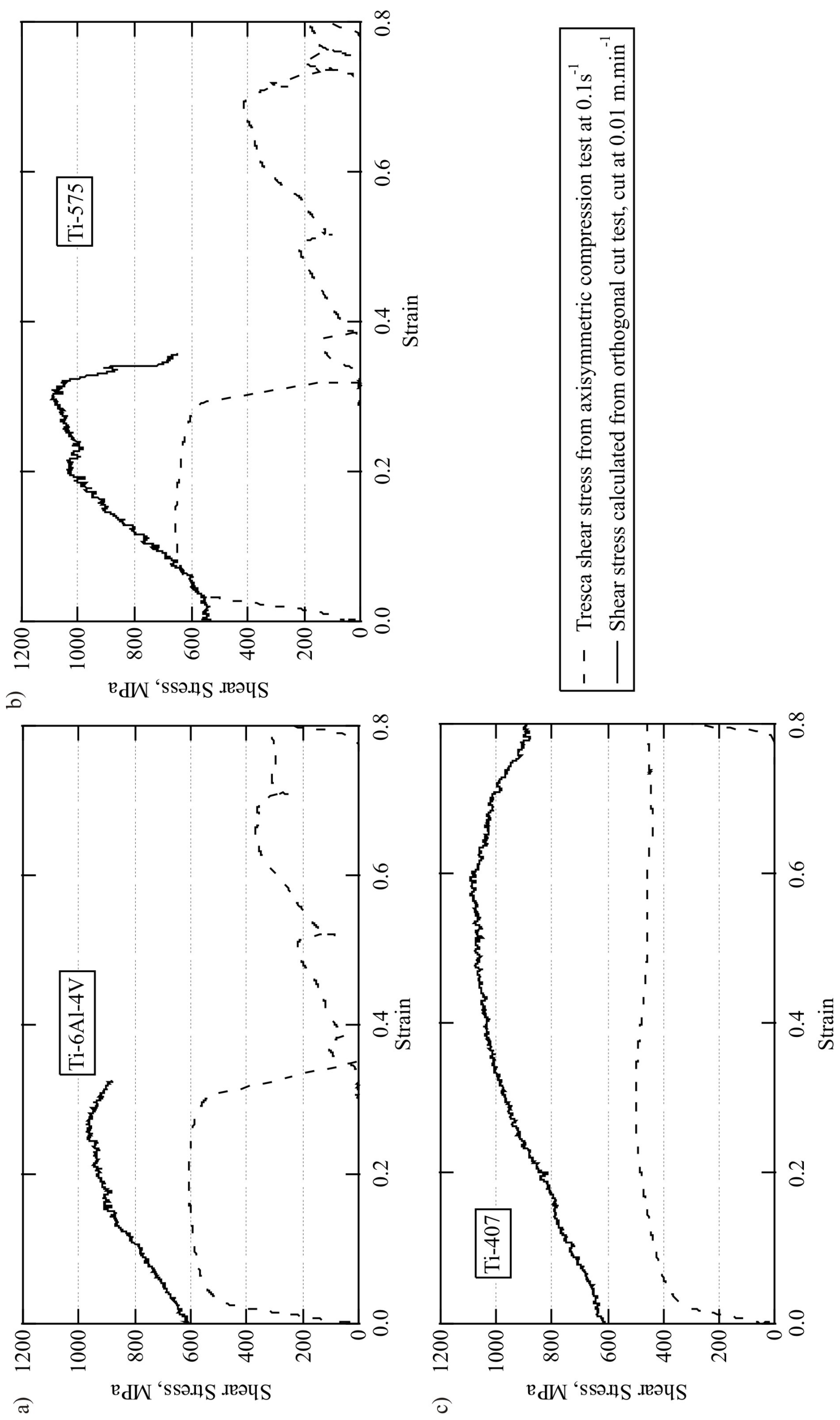

Figure 7.3: Graphs showing the pseudo flow curves of a) Ti-6Al-4V, b) Ti-575 and c) Ti-407 orthogonally cut at 0.01 m.min^{-1}.

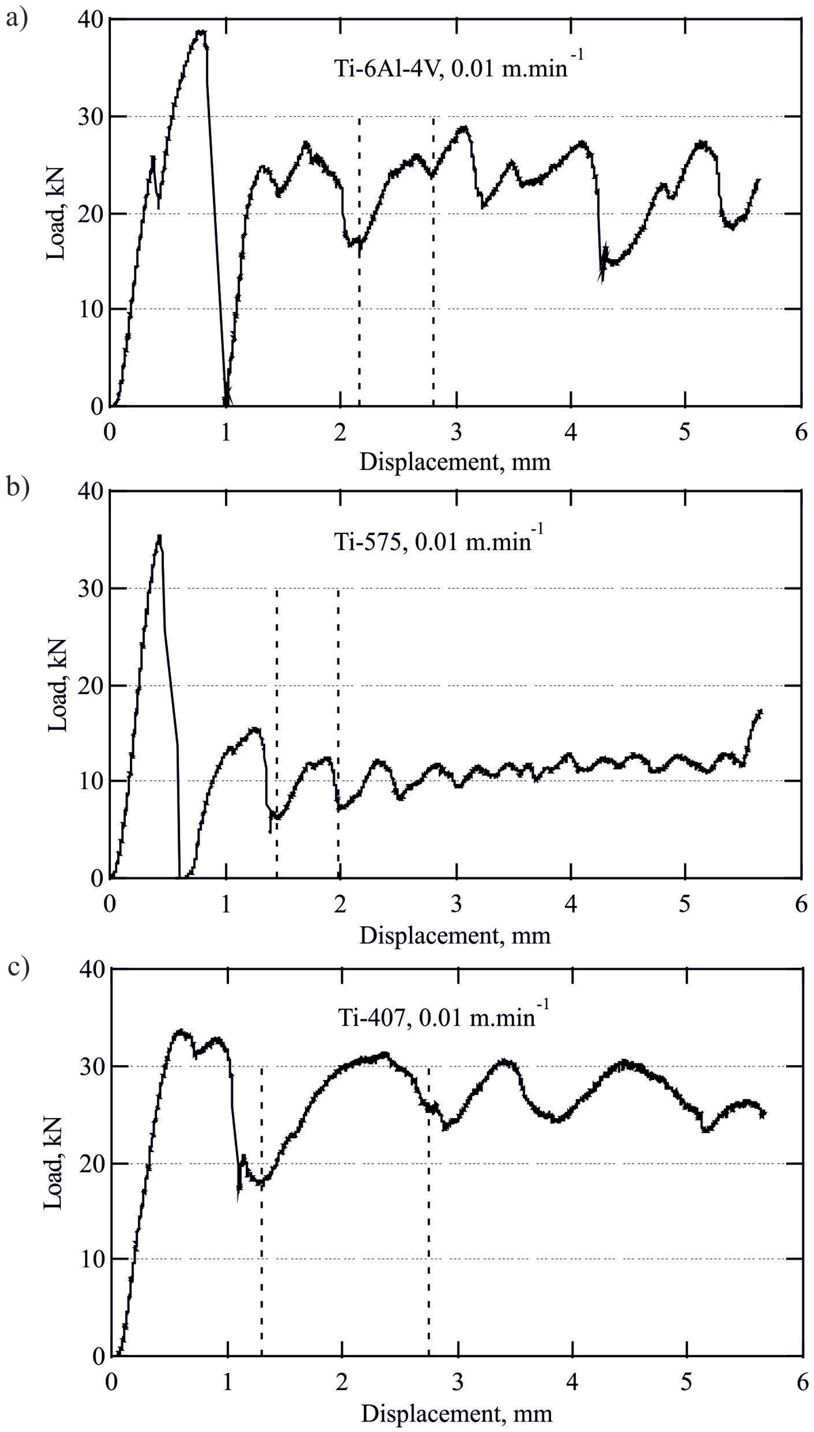

Figure 7.4: Graphs showing the load - displacement plots of a) Ti-6Al-4V, b) Ti-575 and c) Ti-407 orthogonally cut at 0.01 m.min^{-1}.

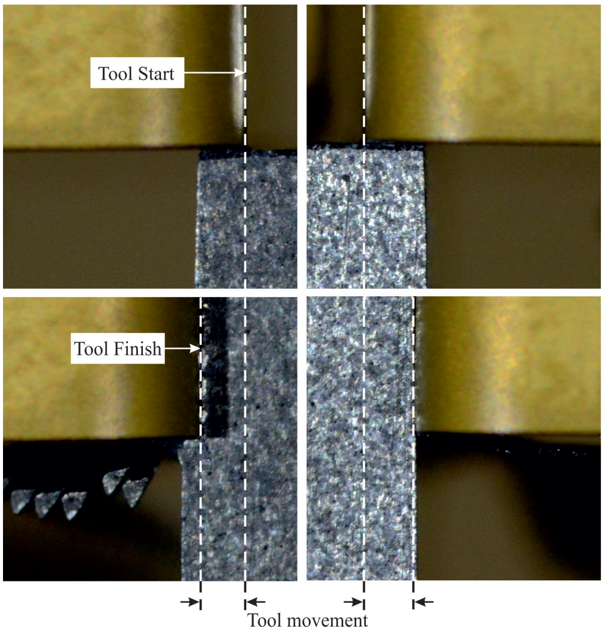

Figure 7.5: Macroimages showing the horizontal tool movement that occurred during orthogonal cut of Ti-575, cut at 0.01 m.min^{-1}, at the start and end, top and bottom respectively.

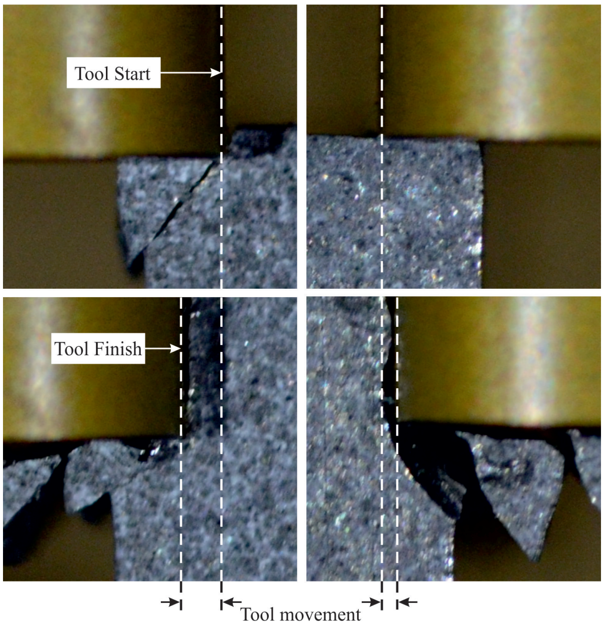

Figure 7.6: Macroimages showing the horizontal tool movement that occurred during orthogonal cut of Ti-6Al-4V, cut at 0.01 m.min^{-1}, at the start and end, top and bottom respectively.

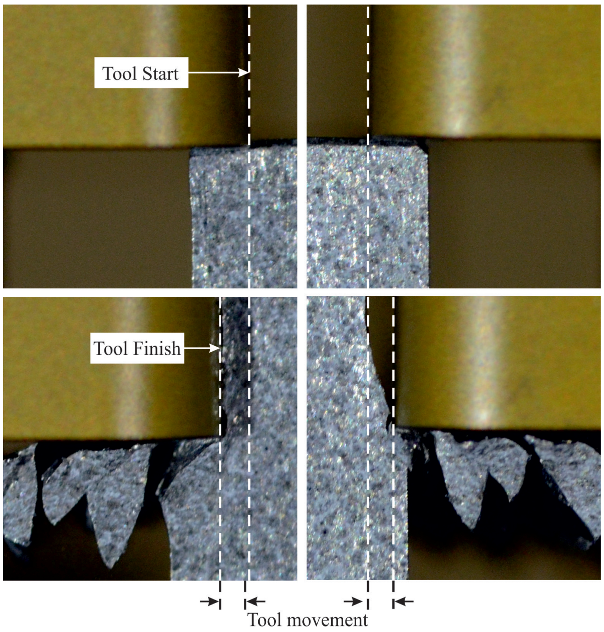

Figure 7.7: Macroimages showing the horizontal tool movement that occurred during orthogonal cut of Ti-407, cut at 0.01 m.min^{-1}, at the start and end, top and bottom respectively.

7.2 Finite Element Model and Orthogonal Cut Experiment Comparison

Using the pre-existing Ti-6Al-4V materials database on the DEFORM™ software, a 2D model of the orthogonal cutting processes was produced. A load - displacement plot was generated from the model and compared to the load - displacement data obtained experimentally, shown in Figure 7.8. Extraction of load data from 2D models is not ideal, as calculations are made from contact lengths and a nominal depth, as opposed to contact areas.

Figure 7.8a) illustrates a comparison of the model and experimentally obtained data and shows there is close to an order of magnitude difference in the magnitude of the loads. Making the assumption that results are generated based on unit width of 1 mm, and multiplying this by specimen width, 13 mm, generates Figure 7.8b). The reason for the assumption that the 2D simulation has a sample width of 1 mm is that the load values generated from DEFORM™ are for a unit depth and in DEFORM™ the default unit of distance is millimetres.

The comparison of Ti-6Al-4V led to the generation of 2D orthogonal cutting models using experimentally obtained material's data. FEM models for Ti - 4 wt.% Al were generated using the Power Law, Johnson-Cook and tabulated data and, using the same assumptions and calculations as used for Ti-6Al-4V, load - displacement plots were generated and compared to the orthogonal cut experiment. As the Johnson-Cook model did

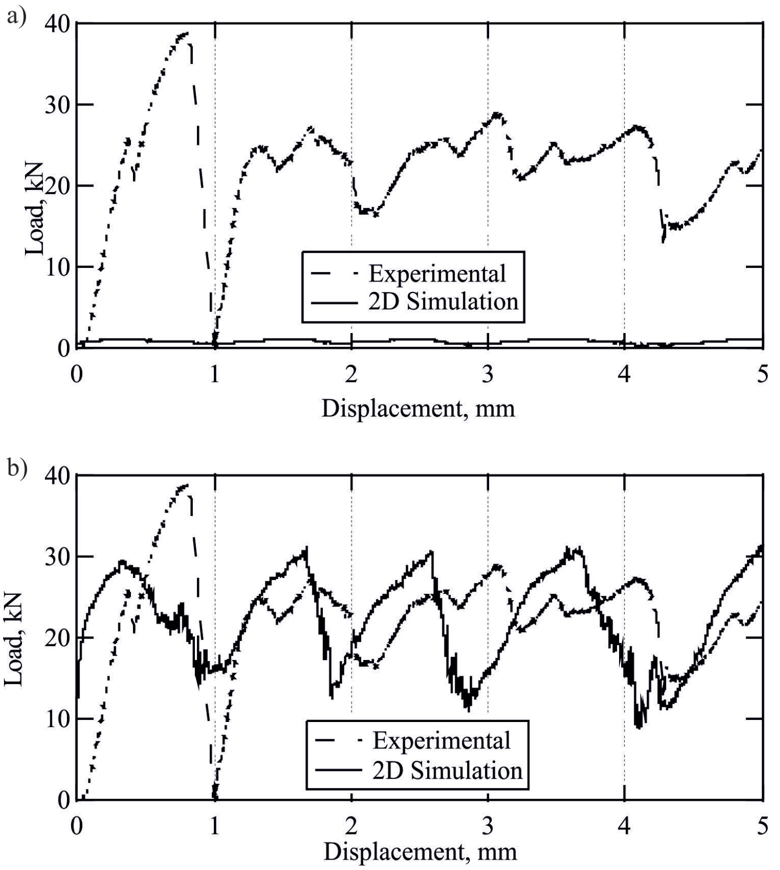

Figure 7.8: Load - displacement plot comparing model and experimentally obtained data of orthogonal cutting of Ti-6Al-4V, cut at 0.01 m.min^{-1}. a) Model data for a single cut of assumed width of cut of 1 mm and b) Model data for two cuts of 13 mm width.

not run successfully, comparison of results was not possible. Further interrogation of the materials database and the model parameters were required, which is beyond the scope of this current work. This left comparison with tabulated data and Power Law, Figure 7.9a) and b) respectively.

Figures 7.9a) and b) both show that the loads generated by FEM are comparable to those generated experimentally. Both the tabulated data and the Power Law predict peak loads of approximately 20 kN, which is comparable to that observed experimentally. The largest difference between both FEM models and the experimental data occurs during generation of the first chip; the FEM models show a much lower peak stress and a much larger displacement to fully form the first chip. A possible cause for this is that in both models, upon reaching the damage criterion, the yield falls to 10%. This, based upon the axisymmetric compression data obtained in Section 3.6.3, shows that the load initially drops to zero. This is impractical for the models to simulate so 10% was used, as it generates a significant flow drop without incurring the impracticalities associated

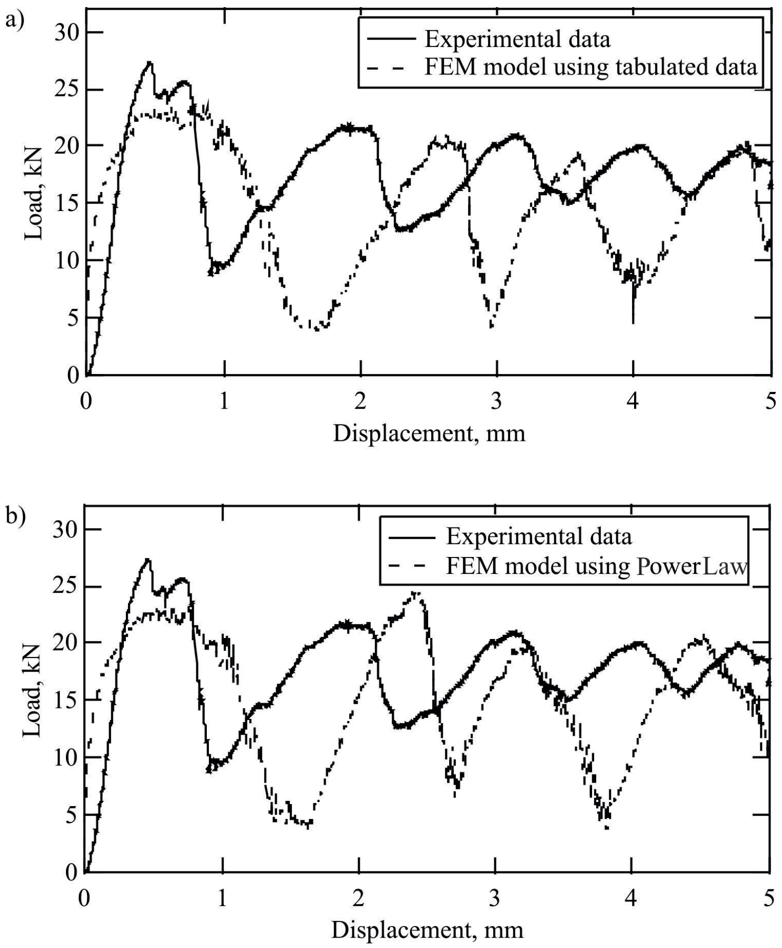

Figure 7.9: Load - displacement plot for two cuts of 13 mm cut width comparing a) data generated by Power Law model and b) tabulated data models with experimentally obtained data of orthogonal cutting of Ti - 4 wt.% Al, cut at 0.01 $m.min^{-1}$.

with using 0%. Another difference is the magnitude of the minima: in the FEM models the minima occur at approximately 5 kN, which is in contrast to the experimental data when the first minima occurs at 10 kN, but then has increasingly large minima up to 15 kN for the final chip. The cause for this appears most likely due to the morphology of the chip after forming; in the FEM models the chip curves back over itself, as illustrated in Figure 7.10a). This is in contrast to what occurs experimentally, where the chip remains in contact with the tool throughout cutting, illustrated in Figure 7.10b), suggesting that the larger contact area results in an increased friction force than occurs in the model. Examination of which of the two approaches yields the best result are inconclusive as both are equally close to experimental results. This favours the Power Law for future models for two reasons. Firstly, the speed at which data can be extracted and inserted into DEFORM™materials databases compared to tabulated data and the Johnson-Cook equation. Secondly, inclusion of a temperature dependent variable, changing from the Power Law to the Norton-Hoff equation, requires limited experimental testing and would help account for temperature rises generated when performing higher cutting speed models. Thirdly, models that go beyond the confident range, the range parameters were extracted from that in this case is 0.1-10 s^{-1}, would be more reliable than those generated by the more restrictive tabulated data; however, the accuracy of the model is still significantly lower for both models when operating outside the confident range.

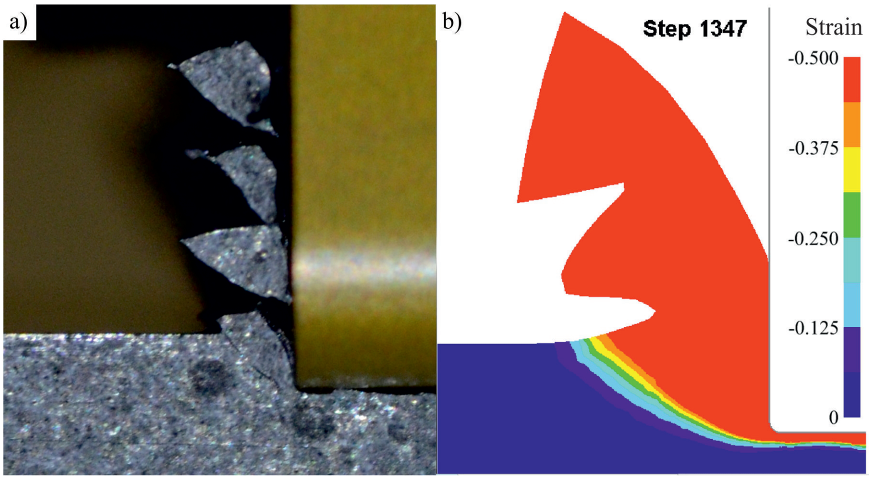

Figure 7.10: a) Macroimage showing chip/tool interaction of Ti-6Al-4V during orthogonal cutting and b) chip/tool interaction in FEM model of Ti-6Al-4V orthogonal cut, both cut at 0.01 $m.min^{-1}$.

The final comparison to be made from the orthogonal cut experiments and FEM models is to compare the strain value obtained experimentally to those obtained from the corresponding FEM model. Figure 7.11a) shows a macroimage with strain values overlaid next to, b), a screen shot at the corresponding point of chip formation in the FEM model. This shows that there is a discrepancy in the distance in front of the tool that the strain field is generated, the model shows projection of the strain field to the surface whereas the DIC image shows the field terminating a short distance into the material. However, as can be observed, in the regions where both model and DIC show a strain field the shape and magnitude of the field are comparable, both showing an initial flat section projecting in the cutting direction followed by a curving towards the uncut material surface. Closer examination of the strain field also shows that there is a similar level of gradation from zero strain up to 0.25, the maximum observed strain in the DIC image. This helps support the potential of FEM models to successfully predict machining behaviour. The biggest difference in magnitude comes in the chip and very near subsurface, two regions where the DIC has not generated results. Howvever, this result continues to demonstrate the suitability of FEM modelling for the prediction of machining behaviour.

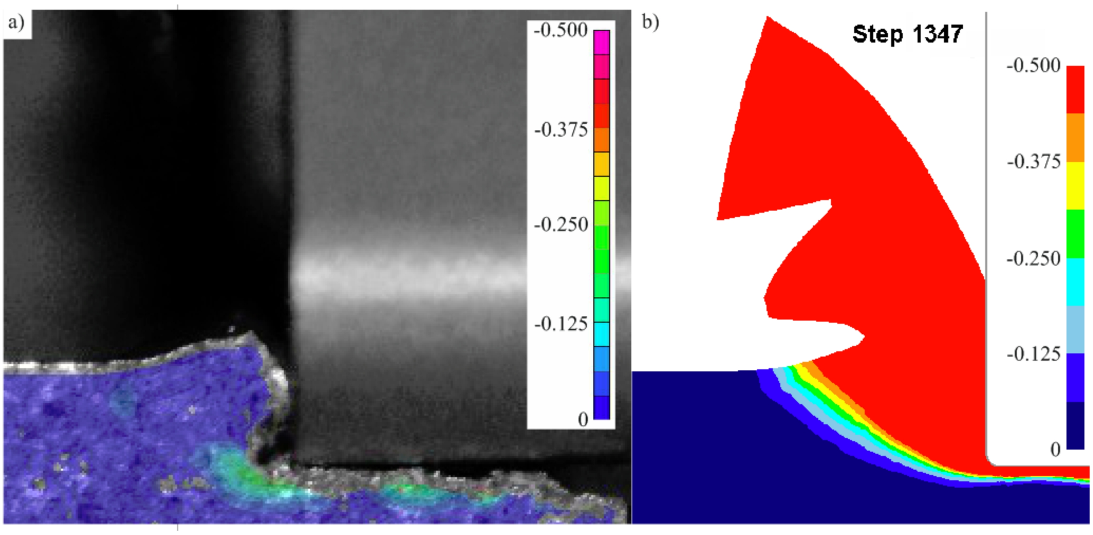

Figure 7.11: Comparison of the strain field generated during orthogonal cutting of Ti-6Al-4V at 0.01 m.min^{-1} at corresponding points in the chip forming process, in a) DIC macroimage with strain overlay and b) DEFORM™FEM model.

The generation of a pseudo flow curve shows promising results; however, the lack of rigidity in the tool housing has influenced the result. The strain values obtained from the DIC show comparable values to those of the axisymmetric compression test, but at this early stage of development highlights the potential of this technique. Most significant is the ability to generate accurate data directly from FEM models using axisymmetric compression testing. This further highlights the possibility to accurately predict the machining behaviour of a material without performing the expensive traditional machining trials.

8. CONCLUSIONS, SUMMARY AND FUTURE WORK

8.1 Summary

In view of the results made in each chapter of this work, it is necessary to place these results in a wider context. This work has proved in principle that the ‘machinability’ of an alloy can be inferred from a simple orthogonal cut test and axisymmetric compression test. The orthogonal cutting test method would not be a direct replacement for conventional, expensive, machining trials; it would be exploited early on in the alloy design stage and would accelerate the downselection of compositions and microstructures, and would generate a new piece of information for a materials data sheet allowing the ‘machinability’ for different alloys to be compared. For example, the reported mechanical properties of TIMETAL®54M are similar to those of Ti-6Al-4V but the ‘machinability’ is improved, as reported by Armendia [6]; however, currently it is not possible to distinguish this from the data sheet because the relevant data is not included.

As the orthogonal cut test has not been optimised for any particular material it makes an ideal first comparison for new alloy systems, but also microstructural variants of a single new alloy. The potential time and cost savings in being able to eliminate alloys systems or microstructure variants is outlined below and offers a much more time and cost effective method for determining ‘machinability’:

1. Conventional machining trials; (Costings are typical market values for Ti-6Al-4V)

    - Aerospace quality billet material: £40/kg
    - Material required for conventional machining trial: 240 kg

    Weight required × Material cost/kg = Total material cost → 240 × 40 = 9600 (£)

    - Machine time (including cost dynamometer): £12,000

    Total material cost + Machine time = Total trial cost → 12,000 + 9,600 = 21,600 (£)

2. Orthogonal cut tests; (one axisymmetric compression test and one orthogonal cut test)
    - 14 mm^2 bar: £400
    - Specimen machining cost: £36
    - Machine time (Axisymmetric Compression test): £490
    - Machine time (Orthogonal Cut test): £420
3. Material cost + Specimen machining + Total machine time = Total trial cost
   $\rightarrow 400 + 36 + (490 + 420) = 1346$ (£)

The method proposed in this work, combining axisymmetric compression test and orthogonal cut test, represents a saving of over 93 % for a single alloy and microstructural condition. This is a significant saving, one that would allow testing of 15 unique chemistries and/or microstructures for the cost of one conventional machining trial. This provides great scope for exploration of new alloy systems or microstructural variations.

During the course of this work a series of microstructural and deformation behaviours have been characterised using a series of established analysis techniques, and a novel testing method developed. The key findings from the work are:

- High speed milling on 2, 4, 6 and 8 wt.% Al binary alloys generated levels of subsurface damage, both SPD and twin depth penetration, that showed a maxima in the Ti - 4 wt.% Al alloy. In contrast, the level of subsurface damage was independent of cutting speed in the range tested, 25 - 188 $m.min^{-1}$. The dominant twinning mechanism observed was $\{10\bar{1}2\}$ but with occurrences of $\{10\bar{1}0\}$ and $\{10\bar{1}1\}$ as the secondary and tertiary twin mechanisms respectively. This order of propensity leads to the suggestion that temperatures in the near-surface could be reaching 500^{o}C.
- Axisymmetric compression testing of the binary alloys shows an increasing propensity for shear band formation by increasing strain rate and aluminium content. Analysis of work hardening curves showed that 2, 4 and 6 wt.% Al showed a comparable flow curve shape, in contrast to Ti - 8 wt.% Al, which showed a much lower hardening rate, that continued to just prior to failure. This indicated that Ti - 8 wt.% Al was deforming via a different mechanism compared to the 2, 4, 6 wt.% Al. Examination of other work shows that α_2 particles are not present and comparisons with a free cutting steel and a non free cutting equivalent showed failed to any significant similarities, but further examination into the effect of short range ordering is required as that does occur in the Ti - 8 wt.% Al and possibly Ti - 6 wt.% Al to a lesser extent.

- The shapes of the 2, 4 and 6 wt.% Al binaries work hardening curves show a distinct three region shape. Regions *I* and *III* indicate dynamic recovery and Region *II* deforming by mechanical twinning. Region *II* shows the biggest variation across the three alloys as the rate of work hardening, Ti - 4 wt.% Al demonstrates the highest Region *II* work hardening and lowest Cockcroft - Latham parameter, indicating that it has undergone the highest amount of deformation by mechanical twinning but requires the lowest "damage" to induce failure. This result is significant as in the high speed milled material, Ti - 4 wt.% Al demonstrated the larger twin penetration depth of the four binary alloys leading to the possibility the Cockcroft - Latham parameter could be used to determine the 'machiniability'.

- Load data from orthogonal cutting experiments has been successfully used to generate pseudo shear stress curves. These curves were close to those calculated from axisymmetric compression testing. This was achieved using force circle relationships for orthogonal cut data and well established shear stress formula, Von Mises, Tresca and Octahedral, for axisymmetric compression data.

- Work hardening behaviour, therefore mechanical twinning behaviour, could not be extracted successfully from the pseudo shear stress curves as the load data contained significant levels of noise and could not be smoothed as loss of detail in the work hardening curve occurs.

- Comparisons of the influence of α_2 particles and MnS particles in free cutting steels are inconclusive via the chip fracture behaviour of the high aluminium, 6 and 8 wt.% Al, content binary alloys. However, this led to examination of the influence of depth of cut, showing that while a reasonably large depth of cut, >350 μm, is needed to be able to obtain strain results from DIC in the chip during formation, too large a depth of cut leads to a change in material removal mechanism from cutting to ploughing.

- Analysis of the DIC images taken during the orthogonal cutting of the industrial alloys showed the level of tool movement that occurs. This result highlights the lack of rigidity in the current system, which in turn led to changes in the force diagram, leading to an increased discrepancy in the pseudo flow curves compared to the axisymmetric compression flow curves. This appears not to have occurred with the binary alloys, based on the pseudo and axisymmetric compression flow curve comparison, although there is no evidence to further support this. However, the magnitude of the peak loads between the orthogonal cut tests of the binary alloys and the industrial alloys, 28 kN and 38 kN respectively, suggests the possibility that the increased loads resulted in increased tool movement. This does not just have an effect on the depth of cut but also a triple influence on the shear stress through the shear band angle, calculated friction coefficient and cutting force, which are parameters when calculating shear stress.

- Comparison of DEFORM 2D simulation with the pseudo shear stress-strain curves generated from experimental data, for Ti-6Al-4V highlights the application of FEM models to predict experimental behaviour with very good correlation between real and predicted load-displacement behaviour. Further examination using experimentally obtained parameters for the Power Law equation and tabulated data show positive correlation for binary alloys. However, use of Johnson-Cook equation requires further development of simulation conditions and parameters.
- Proof of concept of analysis on Ti-6Al-4V, which is a well researched alloy, and the less researched Ti - 575 and Ti - 407, have shown the validity of the orthogonal cutting test on industrial alloys, further emphasising the validity of the orthogonal cutting test as a method to aid development of new machinable alloys.

To summarize, this work has highlighted the potential of a new and novel testing method to aid alloy development; further study of the reliability and validity of this testing method would lead to it becoming an essential part of materials testing in future generation materials, not just titanium. Further examination of this test method, in conjunction with conventional machining trials, with axisymmetric compression testing could lead to a situation where subsurface damage could be accurately predicted from axisymmetric compression behaviour.The orthogonal cutting experiment could also aid tooling setup design, such as rake and clearance angles, chip breakers, tool coatings etc., through knowledge of shear band and microstructural damage information obtained from the axisymmetric compression tests and chip formation information, such as shear band angle and strain field size and orientation, being obtained from orthogonal cut tests.

8.2 Conclusions

The work in this thesis has developed a new approach to machining research, one that incorporates the fundamental materials understandings and analysis with the traditional large scale mechanical approach to machining, switching the focus away from the machining process to the ultimately more important influence on the material damage.

The influence of aluminium additions on machinability has shown that the behaviour is a parabolic function of aluminium content, with the observed subsurface deformation twinning showing a comparable parabola also. These results are significant as both parabolas show 2 and 8 wt.% Al as the minima and 4 wt.% Al at the peak. This result leads to the conclusion that the observed level of subsurface deformation twinning is directly linked to the machinability of the material. This will allow estimations of a materials ‘machinability’ at a much earlier stage of the development process, allowing for ‘machinability’ to be included in the design process. This combined with the cost saving of the test method developed in this work will allow more exploration of new materials and the specimen size will allow examination of laboratory quantities of material.

Corroboration of results from the orthogonal cut experiments, the axisymmetric compression tests, and FEM models highlights the robustness of the proposed testing technique. Once material data is acquired experimentally for new alloy systems, materials databases can be generated. It then becomes possible to use the same database and have confidence in simulating more industrial machining processes, using complex tool geometries, tool coatings and cutting speeds all pushing traditional machining trials towards the final confirmation of simulated behaviour as opposed to a testing method to determine these behaviours. All of this reduces cost to alloy development and further allows exploration of exotic processing parameters to optimise industrial processes.

8.3 Future Work

Through the course of this work several new and developing theories and techniques have been suggested and performed, all of which require further investigation for full validity. The future work can be broken into two main areas, orthogonal cut test method and materials behaviour during testing.

With regard to the testing method itself, the main area for improvement is the rigidity of the tool housings. As was observed in Section 7.1, the movement of the tools means the geometry and force magnitudes of the system alter. This, combined with the change in the shear band angle, means improvement in the rigidity of the tool housing is required, as change in these characteristics could be responsible for the discrepancy in the pseudo flow curve compared to the axisymmetric compression flow curve, as discussed in Section 8.2.

The testing in this work has centred around four binary alloys. Initial examination of the material took in basic characteristics, e.g. grain size, global composition. In this thesis an understanding of the influence of aluminium content on titanium alloys has been presented. For this to be more complete an in-depth analysis of the ordered phase, α_2, and short range ordering for high aluminium content is required. This would take place in the form of TEM study of 4, 6 and 8 wt.% Al in particular and examining how the formation, growth and distribution of α_2 alters with increasing aluminium and, ideally, oxygen content. Once characterisation of this behaviour has been performed, a testing matrix would be required on these materials to identify which of the characteristics found in this work relate predominantly to aluminium or oxygen. The characterisation of this type has been performed [50] but further examination on how this influences machinability has yet to be performed, particularly with the net strengthening of oxygen above 1000 ppm in Ti - 8 wt.% Al being zero [50]. There are a number of issues that this work would encounter; firstly the control required during sample production to achieve compositions which vary only in the desired elements, and secondly, a testing method that has the accuracy and resolution to detect potentially very small variations in outputs, such as loads, with a high degree of confidence.

For investigating the influence of microstructure, the proposed approach would be to investigate a range of microstructures available for Ti-6Al-4V, such as mill annealed, β annealed, as-forged and solution treated and aged (STA). This material has been investigated extensively in large scale trials so the large amounts of data available, on the influence of these microstructures on properties, would enable a stronger understanding of the results generated during this proposed investigation. This would also aid FEM modelling, as most of the literature on modelling Ti-6Al-4V fails to identify the microstructural condition the data was generated from [65–67, 79, 134–136]. This has resulted in large variations in, for example, Johnson - Cook parameters reported, but means it is not possible to identify the appropriate parameters for a particular microstructural condition. The work to be performed in this study would be orthogonal cutting experiments and comparison of the generated pseudo flow curves with those generated through axisymmetric compression testing. This would mean that during future alloy development, microstructural suitability can be investigated as well as chemistry, meaning down stream, conventional, machining trials can be reduced further as unsuitable microstructures can be ruled out at an earlier stage.

As already stated the aim of all this future work is to develop a testing method that becomes integrated into the existing alloy development methods. All of the future work outlined is designed to enhance the understanding of the results that are generated so that the test can be used with confidence and enable an increased number of alloys and microstructures to be examined, while simultaneously reducing the financial and time cost of achieving this.

REFERENCES

[1] TIMET Ltd., Internal data.

[2] European Commision CORDIS, Seventh framework machining projects, `http://cordis.europa.eu/fetch?CALLER=FP7_PROJ_EN&QZ_WEBSRCH=machining&QM_PJA=&USR_SORT=EN_QVD+CHAR+DESC` (March 2014).

[3] Boeing, University partners, `http://www.boeing.co.uk/Boeing-in-the-UK/Research-and-Technology/Universities-Research-and-Technology` (March 2014).

[4] Rolls-Royce, Advanced manufacturing technologies, `http://www.rolls-royce.com/about/technology/manu_tech/ad_machining_technologies.jsp` (March 2014).

[5] S. Audion *et. al.*, Extending the use of titanium alloys on A350XWB.

[6] M. Armendia, A. Garay, L. Iriarte, P. Arrazola, Comparison of the machinabilities of Ti6Al4V and TIMETAL®54M using uncoatedWC-Co tools, J. Mater. Proc. Tech. 209 (2009) 2223–2230.

[7] M. Thomas, S. Turner, M. Jackson, Microstructural damage during high-speed milling of titanium alloys, Scripta Mater. 62 (2010) 250.

[8] W. Kroll, A contribution to the history of ductile titanium and zirconium, Journal of Less-Common Metals 8 (1964) 361.

[9] J. Barksdale, Titanium: Its Occurence, Chemistry and Technology, The Roland Press Company, 1966.

[10] K. Dring, M. Jackson, M. Dashwood, Electrochemical deoxidation mechanisms of titanium oxides, Cost-Affordable Titanium: Symposium Dedicated to Professor Harvey Flower (2004) 95–102.

[11] M. Peters, C. Leyens, Titanium and titanium alloys, Wiley-VCH.

[12] G. Lutjering, J. Williams, Titanium, Springer, 2007.

[13] H. Margolin, Slip band spacing in alpha titanium, Scripta Met. (1969) 561.

[14] H. M. Flower, Microstructural development in relation to hot working of titanium alloys, Mater. Sci. Tech. 6 (11) (1990) 1082.

[15] M. Tan, G. Chen, S. Thiruvarudchelvan, High temperature deformation of Ti-5Al-2.5Sn alloy, J. Mater. Process. Tech 192 (2007) 434–438.

[16] R. R. Boyer (Eds.) Richard Blockley, W. Shyy, Encyclopedia of Aerospace Engineering; Titanium and its Alloys: Processing, Fabrication and Mechanical Behaviour, John Wiley & Sons Ltd.

[17] M. Jackson, R. R. Boyer (Eds.) R. Blockley, W. Shyy, Encyclopedia of Aerospace Engineering; Titanium and its Alloys: Processing, Fabrication and Mechanical Behaviour, John Wiley & Sons Ltd.

[18] P. G. Partridge, The crystallography and deformation modes of hexagonal close-packed metals, Metall. Rev. 12 (1967) 169–194.

[19] K. R. Evans, Deformation mechanisms in titanium and titanium-aluminium alloys, Trans. Met. Soc. AIME 242 (1968) 648.

[20] A. T. Churchman, The slip modes of titanium and the effect of purity on their occurence during tensile deformaiton of single crystals, Proc. Roy. Soc. A226 (1954) 216.

[21] F. D. Rosi, C. A. Dube, B. H. Alexander, Mechanism of plastic flow in titanium - determination of slip and twinning elements, J. Met. (1953) 257.

[22] N. E. Paton, W. A. Backofen, Plastic deformation of titanium at elevated temperatures, Met. Trans. 1 (1970) 2839.

[23] D. Hull, D. Bacon, Introduction to dislocations, Butterworth-Heinemann.

[24] N. E. Paton, J. C. Williams, G. P. Rauscher, The deformation of α-phase titanium (1972) 1049.

[25] P. Bakarian, C. Mathewson, Slip and twinning in magnesium single crystals at elevated temperatures, Trans. Metall. Soc. AIME 152 (1943) 226–253.

[26] J. Williams, R. Baggerly, N. Paton, Deformation behaviour of HCP Ti-Al single crystal, Met. Mater. Trans. A 33 (3) (2002) 837–850.

[27] K. Piao, K. Chung, m. G. Lee, R. H. Wagoner, Twinning-slip transition in Mg AZ31B, Met. and Mater. Trans. A 43A (2012) 3300–3313.

[28] N. P. Gurao, R. Kapoor, S. Suwas, Deformation behaviour of commercially pure titanium at extreme strain rates, Acta Mater. 59 (2011) 3431–3446.

[29] H. S. Rosenbaum, in: R. E. Reed-Hill, J. Hirth, E. H. Rogers, Deformation Twinning, Gorden and Breach Science Publishers.

[30] E. Anderson, D. Jillson, S. Dunbar, Deformation mechanisms in alpha titanium, J. Met 197 (1953) 1191–1197.

[31] F. D. Rosi, F. C. Perkins, L. L. Seigle, Mechanism of plastic flow in titanium at low and high temperatures, J. Met. (1956) 115.

[32] O. E. Hall, Twinning, Butterworth Scientific Publications.

[33] E. Tenckhoff, Deformation mechanisms, texture and anisotropy in zircaloy, ASTM International.

[34] L. Wang, Y. Yang, P. Eisenlohr, T. R. Bieler, M. A. Crimp, D. E. Mason, Twin nucleation by slip transfer across grain boundaries in commercial purity titanium, Metall. Met. Trans. A. 41A (2010) 421–430.

[35] A. D. McQuillan, M. K. McQuillan, Metallurgy of rare earths 4 -Titanium, Butterworth Scientific Publications.

[36] G. E. Dieter, Mechanical Metallurgy, McGraw-Hill Book Company, 1961.

[37] A. Rohatgi, K. Vecchio, G. T. Gray *III*, The influence of stacking fault energy on the mechanical behavioiur of Cu and Cu-Al alloys: deformation twinning, work hardening and dynamic recovery, Met. and Mater. Trans. A 32A (2001) 135–145.

[38] S. Asgari, E. El-Danaf, S. Kalidindi, R. Doherty, Strain hardening regimes and microstructural evolution during large strain compression of low stacking fault energy FCC alloys that form deformation twins, Metall. Mater. Trans. A 28 (1997) 1781–1795.

[39] P. Crawforth, B. Wynne, S. Turner, M. Jackson, Subsurface deformation during precision turning of a near-alpha titanium alloy, Scripta Mater. 67 (2012) 842–845.

[40] A. A. Salem, S. R. Kalidindi, R. D. Doherty, Strain hardening of titanium: role of deformation twinning, Acta Mater. 51 (2003) 4225.

[41] R. L. Fleischer, E. D. Pecker, The strengthening of metals, Chapman and Hall.

[42] D. R. Chichili, K. T. Ramesh, K. J. Hemker, The high strain-rate response of α titanium: Experiments, deformation mechanisms and modeling, Acta Mater. 46 (3) (1998) 1025.

[43] M. J. Blackburn, J. C. Williams, Strength, deformation modes and fracture in titanium-aluminium alloys, Trans. ASM 62 (1969) 398–409.

[44] L. J. Swartendruber, L. H. Bennett, L. K. Ives, R. D. Shull, The Ti-Al phase diagram: the $\alpha - \alpha_2$ phase boundary, Mater. Sci Eng. 51 (1981) 1–9.

[45] E. W. Collings, J. C. Ho, Magnetic susceptibility and low-temperature scpecific hear of high-purity titanium, Phys. Rev. B 2 (1970) 235.

[46] E. W. Collings, Magnetic studies of phase equilibria in Ti-Al (30 to 57 at. pct) alloys, Metall. Trans. A. 10 (1979) 463.

[47] I. Ohnuma, Y. Fujita, H. Mitsui, K. Ishikawa, R. Kainuma, K. Ishida, Phase equilibria in the Ti-Al binary system, Acta. Mater. 48 (2000) 3113–3123.

[48] J. L. Murray, Phase diagrams of binary titanium alloys, ASM International.

[49] U. R. Kattner, J. C. Lin, Y. A. Chang, Thermodynamic assessment and calculation of the Ti-Al system, Metall. Trans. A. 23 (1992) 2081–2090.

[50] J. Y. Lim, C. J. McMahon, D. P. Pope, J. C. Williams, The effect of oxygen on the structure and mechanical behaviour of aged Ti-8 wt. pct Al, Metall. Trans. A 7A (1976) 139–144.

[51] F. Crossley, Effects of ternary additions: O, Sn, Zr, Cb, Mo and V on the $\alpha/\alpha+ti_3al$ boundary of Ti-Al base alloy, Trans. Metall. Soc. ASM 245 (1969) 1963–1968.

[52] S. Banerjee, P. Mukhopadhyay, Phase transformations, Pergamon Materials Series.

[53] M. J. Blackburn, The ordering transformation in titanium:aluminium alloys containing up to 25 at. pct aluminium, Trans. Metall. Soc. ASM 239 (1967) 1200–1208.

[54] J. C. Schuster, M. Palm, Reassessment of the binary aluminium-titanium phase diagram, J. Phase Equilib. Diff. 27 (3) (2006) 255–277.

[55] N. Singh, V. Singh, low cycle fatigue behaviour of Ti alloy IMI 834 at room temperature, Mater. Sci. Eng. A 325 (2002) 324–332.

[56] D. Lee, S. Lee, C. Lee, Quasi-static and dynamic behaviour of Ti-6Al-4V alloy containing fine α_2-Ti_3Al precipitates, Mater. Sci. Eng. A 366 (1) (2004) 25–37.

[57] H. Mecking, Description of Hardening Curves of FFC single and Polycrystals in: Work Hardening in Tension and Fatigue, American Institute of Mining, Metallurgical and Petroleum Engineers, 345 ast 47th Street, New York, New York, 1975.

[58] S. Nemat-Nasser, W. G. Guo, J. Y. Cheng, Mechanical properties and deformation mechanisms of a commercially pure titanium, Acta Mater. 47 (13) (1999) 3705.

[59] A. A. Salem, S. R. Kalidindi, R. D. Doherty, Strain hardening regimes and microstructural evolution during large strain compression of high purity titanium, Scripta Mater. 46 (2002) 419–423.

[60] A. A. Salem, S. R. Kalidindi, R. D. Doherty, S. L. Semiatin, Strain hardening due to deformation twinning in alpha titanium: mechanisms, Metall. Mater. Trans. A 37 (2006) 259–268.

[61] H. Mecking, U. F. Kocks, Kinetics of flow and strain-hardening, Acta Metall. 29 (1981) 1865–1875.

[62] W. P. H. Becker, Work-hardening stages and deformation mechanism maps during tensile deformation of commercially pure titanium, J. Comp. Mater. Sci. 76 (2013) 52–59.

[63] B. Wang, R. Xin, G. Huang, Q. Liu, Effect of crystal orientation on the mechanical properties and strain hardening behaviour of magnesium alloy AZ31 during uniaxial compression, Mater. Sci. and Eng. A 534 (2012) 588–593.

[64] G. L. Wulf, High strain rate compression of titanium and some titanium alloys, Int. J. Mech. Sci. 21 (1979) 713.

[65] H. W. Jr. Meyers, D. S. Kleponis, Modeling the high strain rate behaviour of titanium undergoing ballistic impact and penetration, Int. J Impact Eng. 36 (2001) 509–521.

[66] W. S. Lee, C. F. Lin, Plastic deformation and fracture behaviour of Ti-6Al-4V alloy loaded with high strain rate under various temperatures, Mater. Sci. Eng. A241 (1998) 48.

[67] J. Peirs, P. Verleysen, J. Degrieck, F. Coghe, The use of hat-shaped specimens to study the high strain rate shear behaviour of Ti-6Al-4V, Met. Trans. 1 (1970) 219–224.

[68] A. Kumaraswamy, V. V. Rao, High strain-rate plastic flow behaviour of Ti-6Al-4V from dynamic indentation experiments, Mater. Sci. Eng. A 528 (2011) 1238.

[69] S. P. Timothy, I. M. Hutchings, The structure of adiabatic shear bands in a titanium alloy, Acta Met. 33 (1985) 667–676.

[70] S. P. Timothy, I. M. Hutchings, Initiation and growth of micorfractures along adiabatic shear bands in Ti-6Al-4V, Mater. Sci. Technol. 1 (1985) 526–530.

[71] Y. Me-Bar, D. Shechtman, On the adiabatic shear of Ti-6Al-4V ballistic targets, Mater. Sci. Eng. 58 (1983) 181–188.

[72] G. Lutjering, J. Williams, Titanium, Springer, 2007.

[73] T. A. C. Stock, K. R. L. Thompson, Penetration of aluminium alloys by projectiles, Met. Trans. 1 (1970) 219–224.

[74] S. C. Liao, J. Duffy, Adiabatic shear bands in Ti-6Al-4V titanium alloy, J. Mech. Phys. Solids 46 (11) (1998) 2201.

[75] M. Zhou, A. J. Rosakis, G. Ravichandran, Dynamically propagating shear bands in inpact-loaded prenotched plates - I. experimental investigations of temperature signatures and propagation speed, J. Mech. Phys. Solids 44 (6) (1996) 981–1006.

[76] N. Ranc, V. Pina, P. Hévre, Optical measurements of phase transition and temperature in adiabatic shear bands in titanium alloys, J. Phys. IV 10 (2000) 347–352.

[77] N. Ranc, L. Taravella, V. Pina, P. Hévre, Temperature field measurement in titanium alloy during high strain rate loading - adiabatic shear bands phenomenon, Mech. Meter. 40 (2008) 255–270.

[78] P. Cotterill, P. R. Mould, Recrystallisation and Grain Growth in Metals, University Press, London, 1976.

[79] W. Lee, C. Lin, High-temperature deformation of Ti-6Al-4V alloy evaluated by high-strain rate compression tests, J. Mater. Proc. Tech. 75 (1998) 127–136.

[80] L. E. Murr, A. C. Ramirez, S. M. Gaytan, M. I. Lopez, E. Y. Martinez, D. H. Hernandez, E. Martinez, Microstructure evolution associated with adiabatic shear bands and shear band failure in ballistic plug formation in Ti-6Al-4V targets, Mater. Sci. Eng. A 516 (2009) 205–216.

[81] C. Che-Haron, Tool life and surface integrity in turning titanium alloy, J. Mater. Proc. Tech. 118 (2001) 231–237.

[82] K. Venugopal, S. Paul, C. A, Growth of tool wear in turning of Ti-6Al-4V alloy under cryogenic cooling, Wear 262 (2007) 1071–1078.

[83] R. Li, A. Shih, Finite element modeling of 3D turning of Ti-6Al-4V alloy, Int. J. Adv. Manuf. Tech. 29 (2005) 253–261.

[84] P. Arrazola, A. Garay, L. Iriarte, M. Armendia, S. Marya, F. L. Maître, Machinability of titanium alloys (Ti6Al4V and Ti555.3), J. Mater. Proc. Tech. 209 (2009) 2223–2230.

[85] M. E. Merchant, Mechanics of the metal cutting process I. orthogonal cutting and a type 2 chip, J. App. Phys. 16 (5) (1945) 267.

[86] S. Zhang, J. Li, J. Sun, F. Jiang, Tool wear and cutting forces variation in high-speed end-milling Ti-6Al-4V alloy, Int. J. Adv. Manuf. Tech. 46 (2009) 69–78.

[87] J. Hughes, A. Sharman, K.Ridgway, The effect of tool edge preparation on tool life and workpiece surface integrity, Proc. Inst. Mech. Eng., Part B: J. of Eng. Manuf. 218 (2004) 1113.

[88] H. Abdelaal, M. Nouari, M. Elmansori, Influence of thermal conductivity on wear when machining titanium alloys, Tribology International 42 (2009) 359–372.

[89] A. Ugarte, R. Saoubi, A. Garay, P. J. Arrazola, Machining behaviour of Ti-6Al-4V and Ti-5553 alloys in interupted cutting with PVD coated cemented carbide, Procedia CIRP 1 (2012) 202–207.

[90] S. Sun, M. Brandt, M. S. Dargusch, Characteristics of cutting forces and chip formation in machining of titanium alloys, Int. J. Mach. Tool Manuf. 49 (2009) 561–568.

[91] H. Schulz, High-speed machining, CIRP Annals - Manuf. Tech. 41 (1992) 637–643.

[92] C. Ohkubo, I. Watanabe, J. P. Ford, H. Nakajima, T. Hosoi, T. Okabe, The machinability of cast titanium and Ti-6Al-4V, Biomaterials 21 (2000) 421–428.

[93] M. R. Shankar, B. C. Rao, S. Lee, S. Chandrasekar, A. King, W. Compton, Severe plastic deformation (SPD) of titanium at near ambient temperatures, Acta Mater. 54 (2006) 3691–3700.

[94] J. D. P. Velásquez, A. Tidu, B. Bolle, P. Chevrier, J.-J. Fundenberger, Sub-surface and surface analysis of high speed machined Ti-6Al-4V, Mater. Sci. and Eng. A 527 (2010) 2572–2578.

[95] A. Sharman, J. Hughes, K. Ridgway, An analysis of the residual stresses generated in Inconel 718 when turning, J. Mater. Process. Tech. 173 (2006) 359–367.

[96] I. S. Jawahir, E. Brinksmeier, R. M'Saoubi, D. K. Aspinwall, J. C. Outeiro, D. M. amd D Umbrello, A. D. Jaya, Surface integrity in material removal processes: Recent advances, CIRP Annals - Manuf. Tech. 60 (2) (2011) 603–626.

[97] H. Ernst, Physics of metal cutting, Machining of Metals (American Society for Metals) (1938) 24.

[98] A. E. Bayoumi, J. Q. Xie, Some metallurgical aspects of chip formation in cutting Ti-6wt%Al-4wt%V alloy, Mater. Sci. Eng. A A190 (1995) 173–180.

[99] D. Ulutan, T. Ozel, Machining induced surface integrity in titanium and nickel alloys: A review, Int. J. Mach. Tools Manuf. 51 (2011) 250–280.

[100] N. Narutaki, Study on machining of titanium alloys, CIRP Annals - Manuf. Tech. 62 (1983) 65–69.

[101] S. Jeelani, K. Ramakrishnan, Subsurface plastic deforrmation in machining 6Al-2Sn-4Zr-2Mo titanium alloy, Wear 85 (1983) 121–130.

[102] J. A. Bailey, S. Jeelani, Determination of subsurface plastic strain in machining using an embossed grid, Wear 36 (1976) 199–206.

[103] S. P. Timothy, I. M. Hutchings, Influence of adiabitic shear bands on the fatigue strength of a titanium alloy, Fatigue Eng. Mater. Struct. 7 (1984) 223.

[104] M. S. Dargush, M.-X. Zhang, S. Palanisamy, A. J. M. Buddery, D. H. S. John, Subsurface deformation after dry machining of grade 2 titanium, Adv. Eng. Mater. 527 (2008) 2572–2578.

[105] G. Sutter, Chip geometries during high-speed machining for orthogonal cutting conditions, Int. J. Mach. Tools & Manuf. 45 (2005) 719.

[106] HKL Technology A/S, Channel 5 project manager (version 510.50315.0) [computer software].

[107] G. E. Dieter, Mechanical Metallurgy, McGraw-Hill Book Company, 1961.

[108] A. Ghaderi, M. R. Barnett, Sensitivity of deformation twinning to grain size in titanium and magnesium, Acta Mater. 59 (2011) 7824.

[109] B. Roebuck, J. D. Lord, M. Brooks, M. S. Loveday, C. M. Sellars, Measurement good practice guide no 3: Measuring flow stress in hot axisymmetric compression tests (2002).

[110] G. E. Dieter, Mechanical Metallurgy, McGraw-Hill Book Company, 1961.

[111] WaveMetrics Inc., IGOR pro (version 5.0.3.0) [computer software].

[112] Corel Corporation, Coreldraw®x5 (version 15.2.0.686) [computer software].

[113] Wayne Rasband, Nation Institute of Health, ImageJ 1.45s (version 1.6.0_20) [computer software].

[114] J. T. Black, ASM handbook: Machining.

[115] E. H. Lee, B. W. Schaffer, The theory of plasticity applied to a problem of machining, J. Appl. Mech. 73 (1973) 74–98.

[116] E. P. Rastogi, E. Hack, Optical Methods for Solid Mechanics: A Full Field Approach, Wiley-VCh, Weinheim, Germany, 2012.

[117] G. Crammond, S. W. Boyd, J. M. Dulieu-Barton, Speckle pattern quality assessment for digital image correlation, Opt. Laser Eng. 51 (2013) 1368–1378.

[118] D. Lacompte, A. Smits, S. Bossuyt, H. Sol, J. Vantomme, D. V. Hemelrijck, A. M. Hadraken, Quality assessment of speckle patterns for digital image correlation, Opt. Laser Eng. 44 (2006) 1132–1145.

[119] Correlated Solutions Inc., VIC 2D (version 2009.1.0, build 738:744M) [computer software].

[120] M. D. Cockcroft, D. J. Latham, Ductility and workability of metals, J. Inst. Metals 99 (1968) 33–39.

[121] E. Merchant, Basics mechanics of the metal cutting process, J. App. Mech. 11 (1944) A168–A175.

[122] J. Longbottom, J. Lanham, Cutting temperature measurement while machining - a review, Aircr. Eng. Aerosp. Tech. 77 (2) (2005) 122–130.

[123] D. Vakondios, P. Kyratsis, S. Yaldiz, A. Antoniadis, Influence of milling strategy on the surface roughness in ball end milling of the aluminum alloy Al7075-T6, Measurements 45 (2012) 1480–1488.

[124] C. K. Toh, Comparison of chip surface temperature between up and down milling orientations in high speed rough milling of hardened steel, J. Mater. Process. Tech. 167 (2005) 110–118.

[125] M. R. Barnett, Z. Keshavarz, A. G. Beer, D. Atwell, Influence of grain size on the compressive deformation of wrought Mg-3Al-1Zn, Acta Mater. 52 (2004) 5093.

[126] P. Crawforth, Towards a micromechanistic understanding of imparted subsurface deformation during machining of titanium alloys, Ph.D. thesis, University of Sheffield (April 2014).

[127] H. Conrad, On the strengthening of titanium by aluminium, Scripta Metal. 7 (5) (1973) 509–512.

[128] H. Oikawa, T. Oomori, Steady state deformation characteristics of α-Ti-Al solid solution, Mater. Sci. Eng. A 104 (1988) 125–130.

[129] B. A. Simkin, B. C. Ng, M. A. Crimp, T. R. Bieler, The role of mechanical twinning on microcrack nucleation and crack propagation in a near-γ TiAl alloy, Intermetallics 12 (2004) 1317–1323.

[130] B. A. Simkin, B. C. Ng, M. A. Crimp, T. R. Bieler, Crack opening due to deformation twin shear at grain boundaries in near-γ TiAl, Intermetallics 07 (2007) 55–60.

[131] Y. Zhang, P. C. Millett, M. Tonks, B. Biner, Deformation-twin-induced grain boundary failure, Scripta Mater. 66 (2012) 117–120.

[132] K. Kishida, Y. Takahama, H. Unui, c-axis compression twinning in an off-stoichiometric compound Ti_3Al with $D0_{19}$ structure, Mater. Sci. and Eng. A 400 (2005) 339–344.

[133] A. Fitzner, Effects of alloying elements on twinning in alpha-titanium (unpublished), Ph.D. thesis, University of Manchester (2015).

[134] A. S. Khan, Y. S. Suh, R. Kazmi, Quasi-static and dynamic loading response and constitutive modeling of titanium alloys, Int. J. Plasticity 20 (2004) 2233–2248.

[135] S. Seo, O. Min, H. Yang, Constitutive equation for Ti-6Al-4V at high temperatures measured using SHPB technique, Int. J. Impact Eng 31 (2005) 735–754.

[136] A. Dorogoy, D. Rittel, Determination of Johnson - Cook material parameters using the SC specimen, Exp. Mech. 49 (2009) 881–885.